**EPFL**

# Advanced Manufacturing and Characterization of Building-Integrated Photovoltaic Modules

## Alejandro BORJA BLOCK

■ École
polytechnique
fédérale
de Lausanne

2024

1. Do not panic
2. Let's not get depressed
3. Let's not get too excited

Alessandro Virtuani

# Acknowledgements

I would like to start by expressing my sincere gratitude to Prof. Christophe Ballif for allowing me to pursue my PhD at PV-Lab. We first met for an online interview and since the first moment, you transmitted me your passion about PV technology and your willingness to make a positive impact in the world. Your support and advice in my research have been a huge source of motivation throughout these years. Your guidance has deepened my dedication and enriched my academic pursuits.

I thank my co-supervisor for the last year of my thesis, Dr. Antonin Faes. Your motivation, excitement, and advice were the push I needed to conclude this journey. Thank you for being there in one of the most challenging stages always optimistic and with fruitful ideas.

Last but not least among my supervisors, I would like to thank Dr. Alessandro Virtuani, who supervised me during my first three years at PV-Lab and the last year continued to share his guidance, but more like a friend and life mentor. I could write another thesis about you, but I will apply your teachings ("KISS" keep it short and simple). Thank you for all the nice conversations, support, and advice in this adventurous journey. Without knowing, you have taught PV-Lab three crucial rules that helped everyone through their PhD journey.

I thank the members of the jury, Prof. Rachid Cherkaoui, Prof. Francesco Frontini, Dr. Björn Niesen, and Dr. Janne Halme for accepting being part of one of the most important moments in my thesis. I hope this event is just the beginning of beneficial collaborations between PV-Lab and your institutions, and that we find common grounds to tackle the challenges of the PV field.

Module group deserves a special big thanks for having the best members ever: Fabiana, Luca G., Olatz, Hugo, Andrew, Marie, Florian, Umang, and Kléber. Special thanks to Fabiana, the best office mate and friend I could have asked for. Luca, thank you not only for your friendship, but also for the mentorship in the PhD life. Jabata, thank you for the coffee breaks that were necessary to refill the motivation, tus consejos de arreba te los agradezco inmensamente. Hugo, thank you for existing, you make life in the lab way more enjoyable. Thank you guys for the amazing moments inside and outside of the lab!

I would like to thank the technicians and engineers of the lab, Xavier, Aymeric, Cédric, Sylvain, Joël and Nicolas. Without you the lab simply would not work. Special thanks to "el Capo" Aymeric for helping me with the Ribbon Coating Equipment and "el Bandido" Xavier that

## Acknowledgements

# Abstract

Photovoltaic (PV) technology is necessary for global decarbonization. However, one of the challenges of the technology is that its land use may conflict with other space demands (e.g. agriculture, pastures, forestry). Building-integrated photovoltaic (BIPV) is a solution to efficiently use the space and produce electricity with low $CO_2$ emissions where it is needed, even when it is installed in inadequate orientations. Nonetheless, this technology needs a number of requirements as well as innovative solutions.

First, we investigated the significance of installing PV from a carbon intensity (CI) perspective in sub-optimal orientations by comparing the CI values calculated for PV to the CI of European countries' electricity mix. We discovered that in most European countries, integrated PV in façades (including N-facing PV façades, which receive only about 15% of the insolation of an optimally oriented surface) would work as $CO_2$ sink by reducing the green-gases emission compared to the electricity mix. This suggests that PV could be installed on most buildings regardless of their orientation, and even colored PV, which would, on one side, penalize the $CO_2$ emissions, but on the other side, increase acceptability and market attractiveness, offers a promising dual benefit.

Architects and building owners may prefer greater flexibility in terms of size, shape, and color, as it results in improved aesthetics. We focused on black metallic interconnects because they play a significant part in the uniform appearance of BIPV modules. We designed and manufactured an unique prototype equipment capable of self-aligned masking of metallic interconnects with ink regardless of their shape, size, or orientation. The designed manufacturing step can automatically produce fully black PV modules while only reducing the maximum power output by 2%.

We designed and implemented a stability testing protocol for inks to be applied inside PV modules in glass/glass (G/G) and glass/backsheet (G/BS) configurations. An ultraviolet (UV) curable-inkjet-ink showed large color change ($\Delta$E) after UV accelerated aging caused by photodegradation of the main component of the ink, 2-phenoxyethyl-acrylate. Despite the color shift, PV module performance remained nearly stable, with less than 3% power loss after 360 kWh/m$^2$ of UV light exposure. We suggest a mitigation strategy based on the use of UV blocker encapsulants.

Finally, an innovative color characterization technique appropriate for BIPV modules or any

# Abstract

application in which the color layer is hidden behind a transparent material has been developed. The newly developed characterization technique surpassed benchmark techniques, including a portable colorimeter and an integrated sphere spectrometer to measure color behind a transparent cover. Without the transparent glass covering, all devices produced equivalent results. However, when a glass layer is above the colored layer, the novel colorimeter decreases the change in color ($\Delta$E) from 57 (commercial portable colorimeter) to 3 for an ivory colored glass laminate, obtaining better results.

In essence, this thesis links together the complex issues surrounding BIPV and the incorporation of black metallic interconnects into PV modules, covering topics from equipment manufacturing to the stability of the inks, besides investigating advanced characterization techniques for real-world use. By doing so, this research offers valuable insights into the challenges associated with introducing novel components into the bill of materials (BOM) of PV modules.

**Key words:** building-integrated photovoltaic, solar module, reliability, black metallic interconnects, inkjet printing, degradation, ultraviolet (UV), color characterization, stability, mitigation, carbon intensity (CI), black ribbons, automation, image processing.

# Résumé

La technologie photovoltaïque (PV) est nécessaire pour la décarbonisation. Cependant, l'un des défis majeur de cette technologie est que son utilisation extensive des surfaces qui peut entrer en conflit avec d'autres utilisation des terres (par exemple l'agriculture, les pâturages, et la foresterie). Le photovoltaïque intégré au bâtiment (BIPV) est une solution permettant d'utiliser efficacement l'espace et de produire l'électricité à faible impact environemental là où elle est nécessaire, même lorsqu'elle est installée dans des orientations non-idéales. Néanmoins, cette technologie nécessite un certain nombre d'exigences ainsi que des solutions innovantes.

Tout d'abord, nous avons étudié l'importance des installations du photovoltaïques du point de vue de l'intensité carbone (IC) dans des orientations sous-optimales en comparant les valeurs d'IC calculées pour le PV à l'IC du mix électrique des pays européens. Nous avons découvert que dans la plupart des pays européens, l'intégration du PV dans les façades (y compris les façades PV orientées au nord, qui ne reçoivent qu'environ 15% de l'ensoleillement d'une surface orientée de manière optimale) fonctionnerait sur leur durée totale comme un puit à $CO_2$ en comparaison au mix électrique. Cela suggère que le PV pourrait être installé sur la plupart des infrastructures quelle que soit leur orientation, et même le PV coloré, qui, d'un côté, pénaliserait les émissions de $CO_2$, mais d'un autre côté, augmenterait l'acceptabilité et l'attractivité du marché, offre une perspective prometteuse.

Les architectes et les propriétaires de bâtiments préféreront une plus grande flexibilité en termes de taille, de forme et de couleur, car cela se traduit par une esthétique améliorée. Nous nous sommes concentrés sur les interconnexions métalliques noires car elles jouent un rôle important dans l'apparence uniforme des modules BIPV. Nous avons conçu et fabriqué un prototype capable de masquer automatiquement les interconnexions métalliques grâce à une reconnaissance visuelle et une impression jet d'encre, quelle que soit leur forme, leur taille ou leur orientation. Le prototype peut produire des modules PV entièrement noirs tout en réduisant la puissance maximale seulement 2%.

Nous avons conçu et mis en œuvre un protocole de tests de stabilité des encres pour l'application en utilisant des configurations de modules PV standard en configuration, verre/verre (G/G) et verre/feuille arrière (G/BS). Nous nous sommes concentrés sur une encre pour jet d'encre durcissable aux ultraviolets (UV) qui présentait un changement de couleur ($\Delta$E) après vieillissement UV accéléré en chambre climatique. Nous avons découvert que le jaunissement

est causé par la photodégradation du composant principal de l'encre, le 2-phénoexyéthyl-acrylate. Malgré le changement de couleur, les performances du module photovoltaïque sont restées presque stables, avec moins de 3% de perte de puissance après 360 kWh/m$^2$ d'exposition aux rayons UV. Nous avons suggéré une stratégie afin de limiter la degradation basée sur l'utilisation d'encapsulants avec bloqueurs d'UV.

Enfin, nous avons proposé une nouvelle technique de caractérisation des couleurs appropriée aux modules BIPV ou à toute application dans laquelle la couche de couleur se trouve derrière un matériau transparent. Nous avons comparé différents appareils, dont un colorimètre portable et un spectromètre avec sphère d'intégration, au nouveau colorimètre. Sans le verre, tous les appareils mesuraient des résultats équivalents. Cependant, lorsqu'un verre se trouve au-dessus de la couche colorée, le nouveau colorimètre diminue l'erreur de mesure de couleur ($\Delta$E) de 57 pour le colorimètre portable commercial à 3 (le nouveau colorimètre) pour un stratifié de verre de couleur ivoire, offrant ainsi de meilleurs résultats.

Essentiellement, cette thèse relie les problèmes complexes entourant le BIPV et l'incorporation d'interconnexions métalliques noires dans les modules PV, couvrant des sujets allant de l'intégration de nouveaux équipements à la chaîne de production à la stabilité des encres, en plus de proposer une technique innovante de caractérisation avancées des couleurs pour une utilisation sur le terrain. Ce faisant, cette recherche offre des informations précieuses sur les défis associés à l'introduction de nouveaux matériaux dans la composition des modules photovoltaïques.

**Mots clefs :** photovoltaïque intégré au bâtiment, module solaire, interconnexions métalliques noires, jet impression d'encre, dégradation, ultraviolet (UV), caractérisation des couleurs, stabilité, atténuation, intensité carbone, rubans noirs, automatisation, reconnaissance d'images.

# Contents

**Contents**

# Contents

# List of acronyms and symbols

| | |
|---|---|
| APIs | Application programmable interfaces |
| ATR | Attenuated total reflectance |
| BAPV | Building-applied Photovoltaic |
| BIPV | Building-integrated Photovoltaic |
| BOM | Bill of materials |
| BS | Backsheet |
| CI | Carbon intensity |
| CI(%) | Carbonyl index |
| CIE | International Commission on Illumination |
| CIJ | Continuous inkjet |
| $CO_2$ | Carbon dioxide |
| c-Si | Crystalline silicon |
| DCP | Digital ceramic printed |
| DH | Damp heat |
| DOD | Drop on demand |
| DPI | Drops per inch |
| EL | Electroluminescence |
| EVA | Ethylene vinyl acetate |
| FF | Fill factor |
| FTIR | Fourier-transform infrared spectroscopy |
| G/BS | Glass/backsheet |
| G/G | Glass/glass |
| $gCO_2$-eq | Grams of carbon dioxide equivalent |
| GHG | Green house gas |
| HALS | Hindered amine light stabilizer |
| $I_{SC}$ | Short-circuit current |
| IEC | International Electrotechnical Commission |
| IIPV | Infrastructure integrated photovoltaic |
| $I-V$ | Current-voltage |
| LCOE | Levelized cost of electricity |
| LV | Low voltage |
| $MPP$ | Maximum power point |

**List of acronyms and symbols**

| | |
|---|---|
| MS | Mass spectrometry |
| MSE | Minimum square error |
| MV | Medium voltage |
| NIR | Near infrared |
| NZEBs | Nearly zero-energy buildings |
| $P_{max}$ | Maximum power |
| PERC | Passivated emitter and rear contact |
| PID | Proportional, integral, derivative |
| POE | Polyolefin elastomer |
| PV | Photovoltaic |
| $R_{sh}$ | Shunt resistance |
| $R_s$ | Series resistance |
| RCE | Ribbon coating equipment |
| RGB | Red, green, blue |
| STC | Standard test conditions |
| TDGC | Thermo-desorption gas-chromatography |
| UI | User interface |
| UV | Ultraviolet |
| $V_{OC}$ | Open-circuit voltage |
| VIS | Visible |
| 2-PEA | 2-phenoxyethyl acrylate |
| $\Delta E$ | Color change |
| $\eta$ | Energy conversion efficiency |

# 1 Introduction

## 1.1 Motivation

Global warming is one of the biggest challenges that humanity faces. If we fail to mitigate it, the consequences could be disastrous and irreparable. Some of the catastrophic changes that will occur are increasing sea level rise, extreme weather conditions and biodiversity loss [1]. Therefore, governments across the world have committed to reduce green house gases emissions to maintain the global warming below a 2 °C increase in the Paris Agreement [2], [3]. In order to decarbonize society, all sectors, including heating, power, and transport, could benefit from electricity coming from renewable sources.

Our current electricity generation relies mainly on the burning of fossil fuels, while renewable technologies, unfortunately, only have contributed to 28% of the worldwide total in 2020 [4]. These technologies have the enormous potential to produce clean energy, reducing the green house gases released into the atmosphere and securing the energy supply without relying on uncertain imports. However, to tackle the challenge of climate change, further technological, economical, social and political actions are needed. In a potential situation where we limit the temperature rise to 1.5 °C by 2050, it is estimated that renewable sources will need to make up 91% of the total electricity supply. This shift would result in an increase of the electricity generation by three times compared to 2020 levels, as projected [4].

One of the most optimal technologies to produce clean electricity is the solar photovoltaic (PV). It harnesses the energy from the sun to convert it, without the movement of any mechanical part, directly into electricity. Throughout the years, the price reduction coupled with the impressive technological advances have made it one of the cheapest, if not the cheapest in some countries, source of electricity. Therefore, photovoltaic technology experienced a significant global rise in installed capacity, with a substantial growth rate of nearly 18% in 2022 [5].

Multiple reports emphasize the significant expansion that photovoltaic installations have experienced and will continue to undergo (see Figure 1.1)[5]–[7]. This growth is attributed

not only to the remarkable economic benefits attained by this technology but also to the high urgency of fulfilling international commitments aimed at mitigating climate change. However, more efforts are needed and a massive production and installation is necessary [8]. In some countries where space is limited, such as Switzerland, one of the main issues of PV is the land use. Large-scale PV systems dispute with agriculture and livestock the ground exploitation. Hence, new technologies have emerged such as agrivoltaics or building-integrated photovoltaics (BIPV) where the space constraints are addressed. However, these novel technologies demand several requirements and innovative solutions.
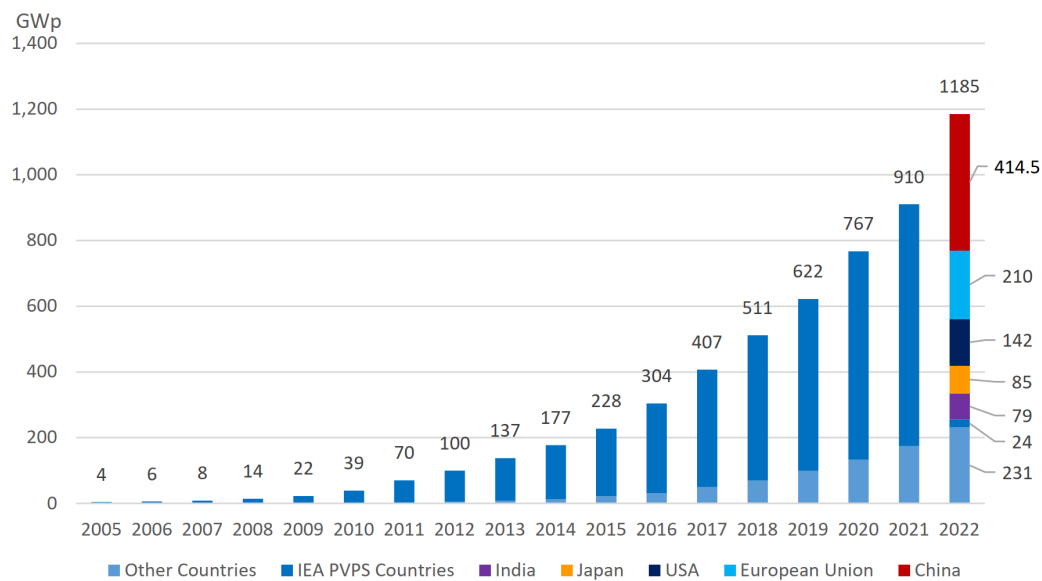


**Figure 1.1:** Evolution of cumulative PV installations worldwide from 2005 to 2022. It is expected to continue with exponential trend. Image taken from [9].

## 1.2 Building integrated photovoltaics

Residential solar photovoltaic (PV) systems have experienced an increment in popularity in recent years, thanks to new political and economic measures. In the European Union, the implementation of the Building Energy Performance Directive [10] and the Directive on Renewable Energy [11] has established a minimum requirement for nearly zero-energy buildings (NZEBs) to fulfill international commitments in mitigating global warming. These requirements emphasize the use of renewable energy, and solar PV is an ideal technology for building integration.

There are two primary approaches to incorporating PV modules into buildings. The first is known as building-applied photovoltaics (BAPV), where PV modules are mounted onto existing structures. The second approach, called building-integrated photovoltaics (BIPV), involves integrating PV modules directly into the building as an active element (see Figure 1.2). The BIPV elements should form or replace a construction element. They should be

multi-functional and aesthetically pleasant. The BIPV product should fulfill both construction and PV requirements.



**Figure 1.2:** (A) BIPV installation and (B) BAPV installation, we can notice more efficient use of space of the BIPV installation and enhanced aesthetics. Image courtesy of 3S Swiss Solar Solutions AG.

BIPV offers significant economic advantages in new construction or renovation projects, as many studies highlight [12]–[15]. However, it is true that BIPV systems can be more expensive in terms of module cost and installation, resulting in higher capital expenditure (CAPEX) than ground-based PV systems. Besides, the fact of being installed as part of the construction can cause larger stresses to the modules by increasing shading and temperature [16], [17].

Additional requirements for BIPV modules arise from architects' increasing desire for customization in their building designs, as you can see in Figure 1.3. As each building is distinct, BIPV manufacturers face the challenge of producing solutions with varying shapes, sizes, and even colors. These factors significantly impact the production process, demanding high degree of flexibility and leading to increased prices. Consequently, there is a growing need for advanced manufacturing techniques to effectively reduce manufacturers' costs.

### 1.2.1 Levelized cost of electricity

In the field of BIPV, the overall cost of manufacturing is predominantly influenced by customization requirements and specialized installation needs. These factors directly impact the levelized cost of electricity (LCOE), which serves as a benchmark for comparing electricity costs across different technologies (refer to the formula). Several considerations have been implemented to the LCOE formula [18], [19], but we refer to the concept [20]:

$$\text{LCOE} = \frac{\text{Lifecycle Cost}}{\text{Lifetime Energy Yield}} \tag{1.1}$$

**Figure 1.3:** BIPV projects carried out by 3S Swiss Solar Solutions AG. (A) The Umweltarena in Zürich, Switzerland, depicts specific geometries required for BIPV modules. (B) A building with terracotta-colored BIPV modules. (C) Residential BIPV installations also make use of special sizes and geometries, often experience extra shading from trees and chimneys. Images courtesy of Swiss Solar Solutions AG.

The formula 1.1 primarily involves the life cycle cost, related to expenses incurred by the system owner, such as initial investment, operation, and maintenance. Additionally, it considers the lifetime energy yield, which represents the total energy output delivered by the BIPV system. In most part of Europe, the units of the LCOE are naturally given in €/kWh. A more comprehensive version of the formula incorporates capital expenditures (CAPEX) and

operational expenditures (OPEX), and it can be found in [21]:

$$\text{LCOE} = \frac{CAPEX + \sum_{n=1}^{N} \frac{OPEX - RV}{(1+r)^n}}{\sum_{n=1}^{N} \frac{Y_0 \cdot (1-D)^n}{(1+r)^n}} \tag{1.2}$$

where:

$N$ is the number of years in operation [years];

$CAPEX$ is the total initial investment [€];

$OPEX$ is the sum of the annual operation and maintenance expenses [€];

$RV$ is the residual value [€];

$r$ is the discount rate [%];

$Y_0$ is the initial energy yield [kWh];

$D$ is the system annual degradation rate [%].

When directly compared to conventional PV modules, BIPV modules typically exhibit a higher LCOE. This is primarily due to increased CAPEX [22], as mentioned earlier, as well as a lower lifetime energy yield caused by harsher environmental conditions and aesthetic modifications that reduce the maximum power output ($P_{max}$). BIPV modules may be 25% to 30% more expensive than conventional modules [23]. The price would be highly dependent on the materials and customization, however, it is challenging to do a general price estimation since product vary considerably and the BIPV modules replace building elements which also have a wide range of prices. In order to reduce costs and become more competitive, the BIPV industry should rely on highly automated production lines with flexible capabilities, develop standard processes of installation and module fabrication, and use customization techniques that minimize the loss in $P_{max}$ of their products with long durability.

### 1.2.2 BIPV market

The market for BIPV remains relatively niche, with its installations representing only a small fraction of the total PV market. Nevertheless, the potential growth of this industry is very considerable [24], [25]. It is not easy to perform estimations about the BIPV market since many definitions exists and there are still many small players [7]. However, governments across the globe are considerably supporting the BIPV industry. For example, recently, China unveiled a plan with the goal of implementing 50 $GW_p$ of rooftop and BIPV installations by the conclusion of 2025 [26]. Besides, other governments support new constructions that integrate PV with significant subsidies. Nowadays, the main driver for the BIPV market is still public

policy.

In Switzerland alone, the market could have a potential of 6 $GW_p$, and in Germany as high as 81 $GW_p$, and this is a conservative analysis [27]. Despite its potential, the BIPV market has not grown as expected in recent years [28]. Several factors have limited the widespread integration of BIPV into the built environment. These include the absence of supportive policies such as construction and safety codes tailored to BIPV, limited awareness and expertise among architects regarding BIPV technology, the lack of implementation tools like Building Information Modeling (BIM), high manufacturing costs, and concerns about the appearance of BIPV elements [29], [30]. Aesthetics customization is one of the main drivers to increase the incorporation of BIPV into the market. The aesthetics of BIPV elements are necessary not only to attract building owners and architects but also to comply with construction codes. Overcoming these barriers requires a multi-faceted approach that addresses these various challenges simultaneously.

## 1.3 PV module technology

PV modules can be manufactured using various types of solar cell technologies. However, this thesis specifically focuses on crystalline silicon (c-Si) PV modules, as they currently dominate the market [7], [31]–[33]. The primary objective of a PV module is to protect the delicate solar cells, which possess an approximate thickness of 200 μm. Additionally, the module aims to ensure installer safety by isolating potential electrical or fire hazards, protect the solar cells from weather-induced stressors, and minimize cell-to-module losses (CTM) to the greatest extent possible. A typical c-Si solar module has multiple arrays of solar cells, encapsulants, and, depending on the module type, either two sheets of glass (front and rear) or a front glass and rear backsheet. These components work in synergy to achieve the desired performance and durability of the PV module.

### 1.3.1 c-Si solar cell

Solar cells, the active components of the module, are responsible for converting light into electricity. Their operational principle relies on a semiconductor material's ability to convert photon energy into a pair of electrons and holes, followed by the extraction of these charge carriers with minimal resistance losses to prevent recombination. Typically, the procedure involves two major steps. First, generating electron-hole pairs through photon absorption (photogeneration) and, subsequently, separating and selectively extracting the generated charge carriers. Figure 1.4 showcases the typical solar cell configurations.

Aluminium back surface field (Al-BSF) had the highest market share until recent years, when the passivated emitter and rear contact (PERC) solar cell surpassed it. Nowadays, technologies such as tunnel oxide passivated contact (TOPCon) and bifacial silicon heterojunction (SHJ) are entering the market.
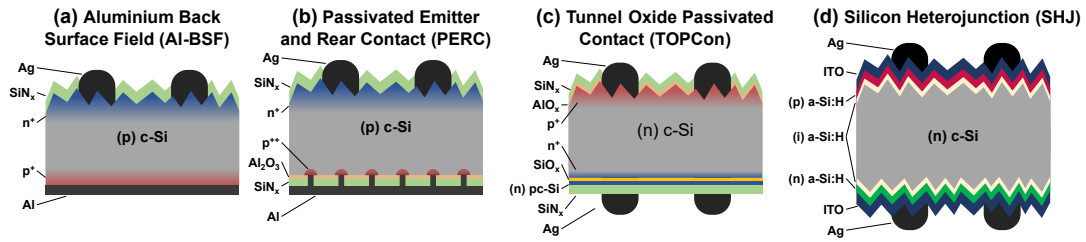
**Figure 1.4:** Schematics of solar cell technologies in the market: (a) aluminium back surface field (Al-BSF), (b) passivated emitter and rear contact (PERC), (c) tunnel oxide passivated contact (TOPCon) and (d) bifacial silicon heterojunction (SHJ). The solar cells are not drawn to scale. Image taken from [34].

### 1.3.2  c-Si solar cell metallization and interconnection

The electrical interconnections of PV modules are present in three main levels. On the c-Si solar cell, the metallization is usually performed with screen printing techniques. The cells are placed under a screen composed of a mesh supporting an emulsion locally opened to form a mask with the busbars and/or fingers array. The squeegee presses into the mesh to flow the metallization paste accurately onto the cell. The second level consist on connecting several solar cells to produce strings of cells. This is done with metallic interconnects called cell connectors, ribbons or even wires, depending on the number of busbars of the solar cells they can range from 0.9 mm wide to lower values. Currently, there is a growing trend to increase the number of busbars in solar cells and therefore the number of cell connectors with a reduced width [35]–[39]. The third level involves connecting the different string of solar cells, to perform the soldering metallic ribbons known as string connectors, interconnects or cross-connectors are used. They are usually 4-6 mm wide and also used to produce the connection with the junction box. Figure 1.5 provides an example of one soldered solar cell and depicts the fingers, cell connectors and string connectors. The nomenclature used in this thesis also involves calling all metallic connectors, metallic ribbons, interconnects or connectors interchangeably, as this is the case in academy and industry.

### 1.3.3  PV module packaging

The packaging of common PV modules typically comprises a sandwich-type structure consisting of multiple materials, such as glass, encapsulants, backsheet, and junction box (refer to Fig. 1.6). There are two primary configurations known as glass/glass (G/G) or glass/backsheet (G/BS). Both configurations feature a front glass sheet, but at the rear side, they can either have another rear glass providing mechanical support or transparency for bifacial solar cells, or a backsheet made of a polymeric material that protects the rear side of the module from moisture ingress (when the backsheet has an aluminum layer), provides electrical insulation and mechanical stability. While G/BS configuration currently dominates the market, there is a growing trend towards the adoption of G/G configuration [40].
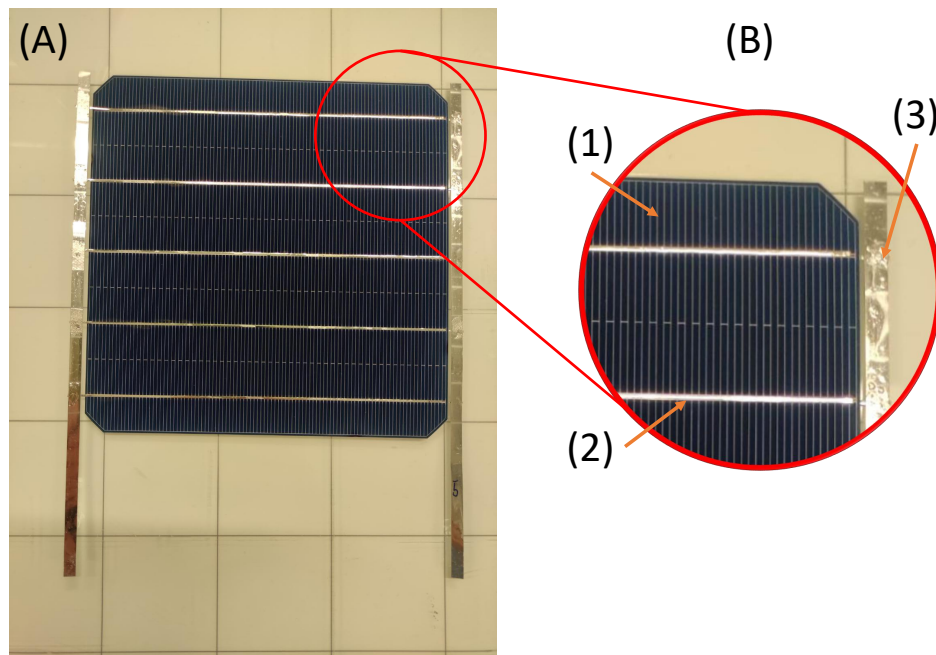
**Figure 1.5:** (A) Soldered solar cell. (B) c-Si solar cell metallization and interconnection. (1) Fingers, (2) cell connectors and (3) string connectors.
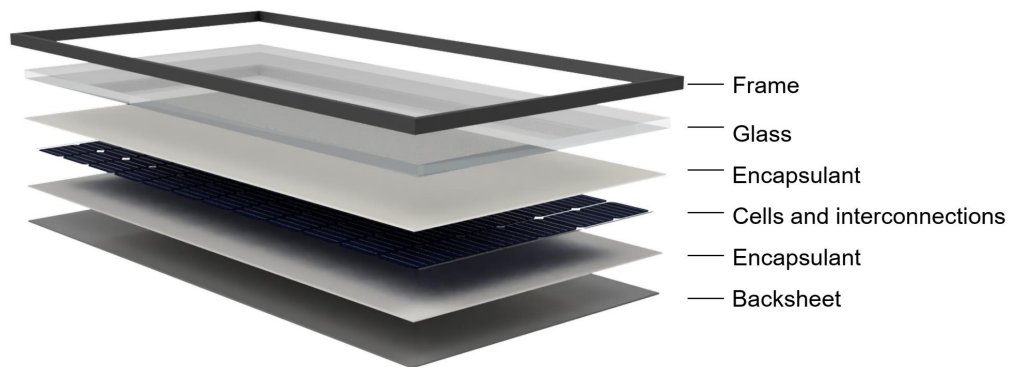


**Figure 1.6:** Common PV module with glass/backsheet configuration. Image taken from [34].

The encapsulant is placed on the front and rear sides of the array of solar cells within the PV module. This encapsulant serves the purpose of bonding all the module's materials together, protecting the solar cells from weather-induced stressors, and insulating the electrical components to prevent short-circuits. The encapsulant must possess important characteristics for effective performance and solar cell protection [41]–[43]. These characteristics include high

optical transmittance to maximize sunlight penetration, thermal and UV stability to resist degradation and yellowing over time, weather resistance to endure various environmental conditions, strong adhesion to all parts of the module (glass, cell, interconnects, backsheet, etc...) for secure bonding, thermal conductivity for efficient heat dissipation, electrical insulation to prevent electrical hazards, and mechanical strength and flexibility to withstand mechanical stresses.

The glass employed in PV needs to exhibit excellent transparency while offering adequate weather protection against elements like wind, snow, and hail. To minimize light absorption, the glass has low iron content. Additionally, it should have strong bonding capabilities with the encapsulant material and maintain a uniform thickness. In certain situations, specialized coatings can be applied to the glass. Examples of these coatings include anti-reflective coatings to diminish surface reflections and enhance light transmission, as well as hydrophobic coatings to repel water and minimize soiling [44]–[50].

Finally, the junction box contains bypass diodes that help address partial shading on the module. It is key for the junction box to be properly isolated and equipped with a secure and efficient connector, enabling the formation of PV installations with arrays of modules. To enhance the safety of the junction box, a process called potting is performed. During potting, the junction box is filled with a liquid polymer that solidifies to provide essential electrical safety, fire resistance, and weather protection. This potting process ensures that the junction box maintains its functionality and safeguards the electrical connections and components within.

### 1.3.4 Modifications for improved aesthetics

Aesthetics play a relevant role in BIPV, and the decreasing cost of solar cells has opened up opportunities for creative and unconventional module designs [51]. Examples of installations and aesthetic modifications can be found in [52]–[55]. In common cases, modifications focus on altering colors, geometries, and textures (see Figure 1.7). EPFL, in collaboration with other Swiss institutions such as EMPA, ETH, and SUPSI, has made significant contributions to BIPV aesthetic solutions and advancements in this field. These contributions include projects such as the Archinsolar project [56], among others. Notably, CSEM has played a key role in the design and manufacturing of some of the initial high-end colored PV solutions.

Glass, a key component of PV modules, can undergo various modifications to achieve desired aesthetics. These include surface treatments to control reflection patterns, the use of tinted or digital ceramic printed (DCP) glass to alter the color. Other components in the module can also be added or modified, for instance, the incorporation of colored foils or backsheets. While less common, modifications to solar cells themselves, such as using colored cells or altering their geometries, are also possible [57]–[62].

Pelle et al. [64] categorize colored BIPV solutions into two main categories. The first category,

**Figure 1.7:** Winter World project made by SUNAGE in Wallisellen, Switzerland. It has BIPV modules with tinted glass and special geometries. (A) Full building and (B) closer view. Image retrieved from [63].

referred to as "integrated or embedded," involves implementing color changes directly into the active layer or solar cells themselves. On the other hand, the second category, known as "added," involves modifications made to the glass, encapsulant, or the addition of a new colored layer to achieve the desired color effects. Figure 1.8 depicts possible arrangements of color layer positioning in BIPV. It is important to notice that a combination of them is also possible.
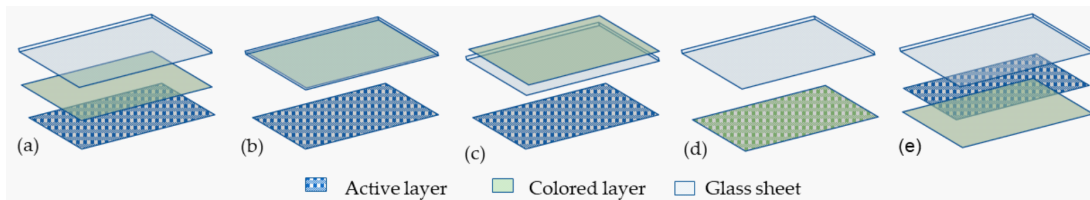


**Figure 1.8:** Colored layer positioning options within the BIPV module assembly: (a) Colored interlayer or colored encapsulant; (b) Colored coated front glass; (c) Colored layer placed on top of the front glass; (d) Colored or coated active layer; (e) Colored backsheet. Image taken from [64].

Architects may often prefer BIPV modules that do not resemble typical PV modules (dark blue solar cells, white backsheet, and visible interconnects), making it necessary to find ways to mask the metallic interconnects (cell and string connectors). One approach involves manually placing black colored strips over string connectors, although this process can be expensive. Another option implies using black tapes to hide cell connectors during the stringing process, however, it may lead to cell cracks and decreased power output. Industrial application of inks to mask cell connectors is also possible, but the process currently lacks efficiency and flexibility, and there is a lack of data on suitable coatings for this purpose. This thesis explores

possible solutions for this topic.

## 1.4 BIPV production line

### 1.4.1 Manufacturing process

The BIPV production line is continuously evolving, with significant changes in technologies and module designs occurring in recent years. The manufacturing process is influenced by the specific technologies used and the production arrangements adopted.

BIPV modules stand apart from conventional PV modules due to their ever-changing geometries. As a result, the key distinction between PV and BIPV manufacturing lies in the incorporation of manual steps to achieve the required flexibility. Currently, the geometric flexibility of BIPV products cannot be fully achieved through automated means. However, there is a collective effort between academia, research institutes, and industry to enhance automation in the BIPV assembly line in the near future. Figure 1.9 depicts a standard manufacturing line for PV modules, including the primary process stations:
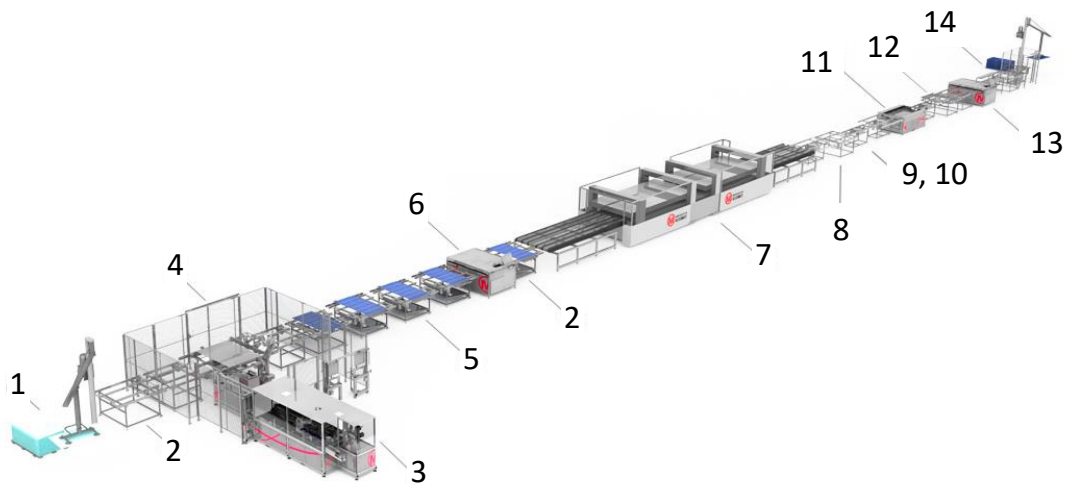


**Figure 1.9:** Example of a 100 MW production line from Mondragon Assembly. Image retrieved from [65].

1. Glass handling: A piece of glass of the desired dimensions is positioned in the conveyor belt.

2. Encapsulant cutter: An encapsulant layer is cut directly from the roll to match the glass size and placed on top of it. This step is repeated when the rear encapsulant and backsheet are added after the in-line electroluminescence (step #6).

3. Stringer: In a parallel process, solar cells are soldered together using cell connector ribbons to form strings. The rolls of metallic ribbons are fed into the stringer machine, where they are cleaned, to then be cut and solder automatically.

4. Lay up: The previously soldered strings are positioned on top of the glass with encapsulant. The solar cells active side is facing down.

5. Busing system and final layers: The full strings of solar cells are soldered in a manual or automated process producing the full active layer. Another layer of encapsulant is added on top of the array of solar cells, followed by a layer of backsheet or glass, depending on the module configuration. The stack of materials, forming the module, is prepared for lamination.

6. In-line electroluminescence (EL): Before lamination, EL is performed to assess the possibility of defects such as cracks in the solar cells. At this step, the materials can still be recovered if a defect is found.

7. Lamination: This process involves melting the encapsulant, while removing air to avoid bubble formation, to bond all the materials together and provide protection for the module's internal components. It consists on three main steps

   (a) Pre-Heating: It gently heats the module materials, specially the glass, to avoid any breakage.

   (b) Curing: The cross-linking of the encapsulant occurs, it bonds the stack of materials and becomes transparent.

   (c) Cooling: The module temperatures decrease to be able to be handled for further steps.

8. Edge trimming: In some cases, after lamination, there may be excess encapsulant on the module's exterior. The surplus encapsulant is trimmed. Edge trimming is also very important for glass-backsheet modules as the backsheet is larger than the glass the trimming adjust the backsheet size to the glass.

9. Contacting: The string-connectors are connected to the electric wires in the junction box by soldering or mechanically using springs.

10. Potting: A silicone material is used to fill the junction box, providing better protection for its electronics (bypass diodes) and connection between string-ribbon from the module and the electric wires. Some junction boxes do not require potting as the box is sealed against moisture.

11. Framing: If the modules have a frame, they can be automatically placed in this step with aluminum profiles that provide more mechanical stability to the modules.

12. Visual inspection: Visual inspection is performed manually or automatically to assess bubbles, backsheet wrinkles, or other defects.

13. Testing: The modules undergo testing by measuring the current-voltage (IV) curve under standard light source and also performing electroluminescence.

14. Classification: Once the results of the testing are processed the modules are classified according to their power output and aesthetics.

These manufacturing steps relate to standards PV modules, however, each production line main have small variations having the steps not in the exact same configuration. The main difference for BIPV modules would be the implementation of "new materials" related to aesthetical modifications and the use of various module shapes and sizes.

### 1.4.2   Metallic ribbons handling

The handling of metallic ribbons varies depending on the module design. Cell connectors are typically fully processed by stringer machines, where they are soldered using heating lamps and pins, depending on the solar cell type. On the other hand, string connectors are often soldered manually for BIPV manufacturing which increase the cost and reduce the yield of production.

One drawback of these metallic ribbons is their highly reflective surface, which may be considered aesthetically unappealing. To overcome this, manufacturing companies choose to mask them with black tapes, a costly and labor-intensive manual process. Although precoated black ribbons are available, they pose limitations when bent at 90° angles or other configurations. Selectively coating the sides of the ribbons is difficult to manage and undoubtedly expensive to process, since it is not possible to solder on the coated side. Additionally, precoated ribbons need to withstand all the production line steps, especially the stretching, soldering processes and lamination processes.

To address these challenges, a possibility would be coating the metallic ribbons after the soldering process using a highly automated and efficient printing step. This approach offers several advantages. First, it allows using standard soldering equipments and processes. Second, it offers a better control over the coating process, ensuring uniform coverage on the ribbons. Then, automating the coating step reduces the reliance on manual labor, thereby minimizing production costs and improving efficiency. Finally, by applying the coating after the soldering process, it eliminates the need for the coating to endure the stretching and soldering steps, reducing the risk of damage to the black coating. Additional elaboration on this subject can be found in Chapter 4.

## 1.5 Reliability in photovoltaics

### 1.5.1 BIPV module degradation modes

In the preceding sections, we have emphasized the significance of extending the lifetime of BIPV modules, as doing so would directly lead to a decrease in the LCOE and prove advantageous for key stakeholders involved. However, it is essential to acknowledge that BIPV modules are often installed in suboptimal orientations and environments (topic developed in Chapter 3), which can result in various challenges affecting their performance [66].

One prominent issue faced by BIPV modules is higher operating temperatures compared to standalone PV systems caused by inadequate rear-side ventilation. Shade exposure is also common and may give rise to hotspots within the modules, leading to potential power losses and reduced operational lifespans. Moreover, BIPV modules are constantly subjected to various environmental stressors, including humidity, strong winds, snow loads, and other typical weather-related factors, which are common stressors experienced by traditional PV systems.

Reliability engineering in PV industry aims to prolong the operational lifetime of components or systems by delaying or mitigating failures, caused by the previously mentioned stressors, throughout their operation. One effective way to represent the failure characteristics of components or systems is through the use of the bathtub curve (see Figure 1.10) [67], [68].
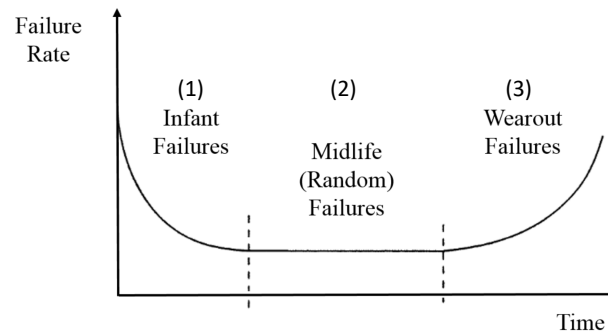


**Figure 1.10:** The bathtub curve. Image taken from [69].

The bathtub curve is divided into three main sections, each describing distinct failure phases:

1. Infant Failures: These failures are often caused by defects in the manufacturing process or defective components, and they tend to be more catastrophic in nature. To prevent or minimize these failures, rigorous qualification testing and quality control measures are implemented during the production phase.

2. Mid-life Failures: The middle section of the bathtub curve is characterized by a relatively flat failure rate. These failures are considered random events and are usually not

influenced by initial defects. During this phase, the component or system operates with a relatively stable and low failure rate.

3. Wear-out Period: In this phase, the failure rates begin to increase again as the components or systems experience end of life failures. This increase in failures is attributed to aging mechanisms, cumulative stress, and deterioration of materials. To manage this phase effectively, maintenance and replacement strategies are employed to extend the useful life of the component or system.

In the context of PV modules, extensive research has led to the identification of various failure mechanisms, as depicted in Figure 1.11, summarizing the observed failures and their occurrence in real-world conditions. The effect of these failures in PV modules is typically quantified as a loss in power output. However, when considering BIPV, the analysis becomes more intricate due to its dual-purpose nature as both an energy-producing component and a building element.
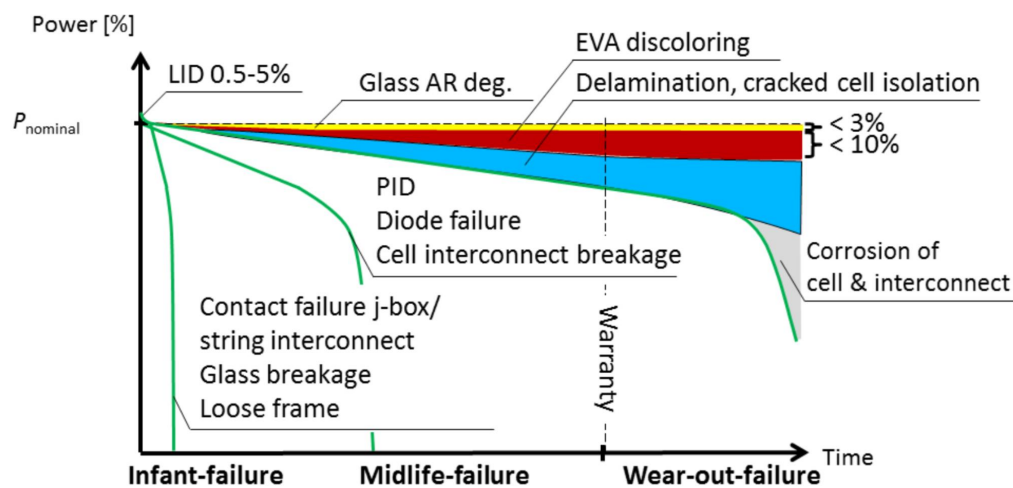


**Figure 1.11:** Typical instances of failure observed in field-installed c-Si modules. Image retrieved from [70].

While BIPV modules may experience failures as those described in Figure 1.11 when evaluated solely as PV modules, their unique combination with building materials introduces the possibility of new failure modes. For instance, issues related to aesthetics, such as discoloration or visual changes, could be considered as additional failure criteria in BIPV systems (even if they are not affecting the power output). These aesthetic concerns arise from the use of innovative materials, like colored glass, foils or coatings, which can lead to alterations in the module's appearance over time.

It is important, not only to assess the power output of the BIPV modules, but also the impact of these aesthetic changes and understand their significance. While they might not directly

affect the power generation capacity, they could still have implications for the overall building aesthetics and design integrity.

Currently, the absence of standardized guidelines for BIPV poses challenges in determining an acceptable threshold for color changes. Addressing this gap is essential to provide clear criteria for assessing the visual impact of BIPV modules on building aesthetics. Developing industry-wide standards would enable designers, architects, and developers to make informed decisions, striking a balance between functional energy generation and maintaining the desired visual appearance of buildings.

In this thesis, we explore the use of materials that are not commonly employed in traditional PV systems. Specifically, we investigate the application of ink coatings to mask the metallic interconnects in BIPV modules. It is worth noting that these ink-coated metallic interconnects, when exposed to weather stressors, could potentially lead to significant color changes across the BIPV module's appearance. As a result, handling this issue becomes important to maintain both the optimal performance and visual appeal of the BIPV installations.

Addressing the concern of color modification in building aesthetics, we recognize the importance of finding an appropriate balance between energy generation efficiency and the overall appearance of the building. Therefore, one of the key contributions of this thesis is an in-depth exploration of these issues, particularly in Chapter 5, where we investigate the implications of using ink coatings to mask metallic interconnects and how such modifications can affect the appearance of BIPV modules over time.

### 1.5.2 Qualification standard tests

Accelerated aging tests serve, first to evaluate the product safety and requirements [71], [72], and in a second step it can give some initial ideas about reliability of PV modules by increasing failure modes potentially observed during the product's operational life [73]. By definition, the objective is to assess the module's ability to perform as required [74] , particularly as defined by product warranties, which are typically based on power output performance. In essence, these warranties ensure that the module's power output will remain above a specified percentage of its nominal value for a certain duration.

By subjecting PV modules to accelerated aging tests, manufacturers can validate their reliability under harsher conditions and analyse potential failure scenarios. These tests aid in identifying weaknesses, design flaws, or material degradation that could impact the module's performance over time, allowing for improvements and ensuring a potential longer operational life.

Qualification standards tests are instrumental in establishing trust between manufacturers and customers regarding the quality and reliability of PV products. The International Electrotechnical Commission (IEC) has developed various test sequences, including accelerated aging tests, to thoroughly assess the reliability of PV modules. One such critical standard is the IEC 61215 [72], which outlines specific requirements for the design qualifications and

**Table 1.1:** Examples of the primary aging tests outlined in IEC 61215. Each test is associated with specific failure modes it aims to replicate. Table adapted from references [75] and [76].

| Test | Conditions & Description | Potential Effects and Field Failure Modes |
|---|---|---|
| Damp Heat | Exposure to constant 85°C temperature and 85% relative humidity for 1000 hours to assess prolonged high humidity effects and water penetration potential. | Delamination Solder bonding failure Encapsulant discoloration |
| Hail Test | The module is subjected to impacts from ice balls with diameters ranging from 25 to 75 mm and velocities of 23 to 39.5 m/s to evaluate hail resistance. | Cell breakage Glass damage |
| Humidity Freeze | Temperature cycling between 85°C with 85% relative humidity and -40°C to assess resistance to temperature and humidity variations, with continuous current flow. | Delamination Junction box failure Broken interconnections Solder joint failure Cell breakage |
| Mechanical Load | Front side loaded with 2400/5400 Pa for 1 hour, followed by -2400/-5400 Pa for 1 hour (repeated 3 times) to evaluate stability under snow or wind conditions. | Structural failures Glass damage Broken interconnections Cell breakage Solder bonding failure |
| Thermal Cycling | Exposure to 200 temperature ramp cycles from 85°C to -40°C to evaluate thermal mismatches between components. Maximum power point current ($I_{mpp}$) during temperature ramping-up and 1% of $I_{mpp}$ during the rest of the cycle. | Delamination Junction box failure Broken interconnections Solder joint failure Cell breakage |
| UV Preconditioning | Constant temperature of 60 ± 5°C with UV light exposure (specific intensity and spectrum) accumulating a UV dose of 15 kWh/m$^2$. Testing UV-sensitive components. | Encapsulant discoloration, Backsheet discoloration Delamination |

type approval of PV modules. By adhering to this standard's stringent pass or fail criteria, manufacturers can demonstrate a minimum level of quality and assure customers of the modules' durability and potential long-term performance. Complying with such comprehensive standards not only benefits manufacturers but also provides confidence for customers, driving the widespread adoption of cleaner and more reliable solar energy solutions. Table 1.1 describes some of the most-demanding aging tests contained in IEC 61215.

In this thesis, we focus on testing materials that are not commonly used in PV modules, such as inks. Inks are mixtures, often made of polymeric materials, and we provide more detailed information about them in Chapter 5. As a result, our main testing procedures are based on the standard tests that are typically used for PV polymeric materials.

Currently, there are no established standard tests specifically designed for the inks used to mask the metallic ribbons in PV modules. Therefore, we have developed a new testing approach to evaluate these novel elements. The primary test we conducted involves subjecting the materials to UV exposure, following the guidelines outlined in IEC 62788 [77]. Additionally, we have explored the effects of temperature and humidity on these materials, which adds

another layer to our investigation. The used protocol is described deeply in Chapter 5 and Annex B.

### 1.5.3   Limitations of qualification tests

As previously mentioned in this chapter, qualification tests play a relevant part in finding design weaknesses and finding solutions to improve the quality of PV modules. However, they are not very effective in predicting the lifetime of PV modules [78]. The actual lifespan of PV modules depends on various factors such as their design, operating conditions, and the environment they are installed in. The IEC standards only provide guidelines to determine whether modules meet the basic requirements, but they are sometimes mistakenly seen as predictors of overall lifetime expectancy. Although a passing qualification tests could imply effective module designs, it is a common practice to test only a relatively small number of modules from the overall production. This limits the ability to accurately predict the overall performance of the entire production batch [79]. The main limitations of qualification tests can be divided in several points:

- **Not defined for specific climates:** The tests lack climate specificity. Although modules might successfully pass the distinct IEC 61215 test sequences, their long-term performance will ultimately be dependent on the specific climatic conditions of the installation site, including factors such as temperature, humidity, UV exposure, and soiling.

- **No test-reality correlation:** The relationship between the test parameters (like duration and stress levels) and actual stress conditions remains ambiguous. In essence, these tests are unable to forecast the actual module lifespan.

- **Risk of unrepresentative failures:** Altering or extending the intensity of one or more acceleration factors can result in the emergence of impractical failure modes. For instance, excessively high UV intensity can induce degradation modes that would not naturally occur in standard operational field conditions. Another example involves Damp Heat (85% RH and 85°C), which conditions do not exist on Earth and could trigger failures that will never occur in reality.

## 1.6   Objectives and structure

### 1.6.1   Goal of this work

In this chapter, we have highlighted the challenges faced by the BIPV industry, emphasizing the significance of automation and aesthetics for BIPV modules. It was mentioned that BIPV modules resembling common building materials are preferred, and hiding the metallic cross connectors is crucial. However, currently, there are no automated solutions available for this

process, and there is a lack of understanding and data regarding the use of new materials, such as inks, for the masking task. Additionally, specific protocols to assess possible degradation modes observed in BIPV modules have not been defined, and suitable characterization techniques are yet to be established. Finally, no equipment can measure correctly the color of a BIPV element so it is difficult to quantify the specification for color change in production and over time during outdoor exposure.

In this context, the primary objectives of this thesis are as follows:

1. To investigate the viability of implementing PV systems in suboptimal orientations from a carbon intensity (CI) perspective focusing on European locations. Our study involved comparing the CI of PV installations with the carbon intensity associated with the electricity mix of each European country. Based on our findings, we present recommendations to guide decision-making in this context.

2. To understand the state-of-the-art challenges and limitations faced by the BIPV industry in terms of automation for aesthetic purposes. The key aim is to design and develop a prototype tool, as a proof-of-concept, that can automatically coat the strings and interconnects of solar cell arrays, irrespective of their orientation, size, or type of cell connectors and cross connectors. The proposed automated tool will serve to prepare samples for future research and have the potential for seamless integration into the BIPV production line.

3. To identify and characterize the effects of employing new materials, such as UV-curable inkjet inks, to conceal the metallic ribbons within the bill of materials (BOM) through accelerated aging tests. To achieve this objective, we utilize the developed customized ribbon coating equipment to create samples comprising various materials used in BIPV modules. These samples are meticulously analyzed to gain valuable insights into the observed degradation modes and effective mitigation strategies. Additionally, we propose, analyze, and explain novel characterization techniques that can contribute significantly to the field.

### 1.6.2   Structure of the thesis

The thesis is structured as follows:

1. **Chapter 2** shows the materials, sample configurations and characterization techniques used in this work. We also provide a description of the experimental setups utilized and methods followed.

2. **Chapter 3** provides an overview of the meaningfulness of installing solar photovoltaic modules in buildings from a carbon intensity perspective. It presents an analysis based on the installation orientation and the national electricity mix of European countries. A deeper overview of the BIPV potential, challenges and future perspectives is described.

3. **Chapter 4** elaborates on the automation solutions developed to enhance the aesthetic appeal of BIPV modules. It describes the design process and manufacturing of a customized tool specifically aimed at improving the appearance of stringed solar cells by coating the metallic interconnects with ink. The chapter provides a meticulous description of the tool's functioning, outlining its capabilities and limitations in detail.

4. **Chapter 5** is dedicated to examining the degradation caused by the inks employed to mask the metallic interconnects. Various typical PV module configurations, incorporating ink components, undergo exposure to different cumulative UV doses. The primary objective of this chapter is to conduct a thorough investigation and gain understanding of the effects of UV curable inkjet inks on PV modules, particularly under the influence of weather stressors. Moreover, this chapter seeks to propose viable alternatives to mitigate the observed degradation modes, offering potential solutions for improving the long-term performance and reliability of BIPV modules.

5. **Chapter 6** introduces a novel characterization tool designed to accurately quantify the color coordinates of PV modules, serving relevant purposes such as quality control, color design assessment, and color degradation evaluation. The equipment is subjected to thorough analysis and is also compared against conventional characterization techniques, including a portable colorimeter and a spectrometer based on an integrated sphere. One of the standout features of this equipment is its capability to measure the color of surfaces even under transparent layers, providing valuable insights into the visual properties of BIPV modules that were previously challenging to assess.

6. **Chapter 7** offers a concise summary and a discussion of the primary findings obtained in this research, along with providing practical recommendations and suggesting future activities to further enhance and build upon the study.

### 1.6.3 Contribution to the research field

This thesis makes significant contributions to the research field of BIPV, focusing specifically on carbon intensity, automation, long-term performance, and characterization, as follows:

1. Through an examination of the carbon intensity (CI) of PV systems in buildings and a comparative analysis with the CI of national electricity mixes across Europe, we conclusively demonstrate that the installation of PV, even in sub-optimal orientations (including north-facing facades), would not incur penalties in the majority of European countries. However, we acknowledge that PV in optimal orientations is more effective in reducing GHG emissions. To complement our study, we formulate a series of insightful recommendations for policy makers. These guidelines are aimed at optimizing the widespread adoption of PV in the building environment, with the ultimate goal of achieving a massive and rapid diffusion of PV technology.

2. We present an innovative manufacturing tool that uses image processing and inkjet technology to flexibly coat the metallic interconnects of solar cell arrays. This device guarantees accurate coating, independent of the interconnects' diverse dimensions or varying orientations. We are the firsts to fabricate fully black inkjet coated ribbons, with a process that ensures the power output to remain nearly constant after the entire coating procedure. We provide the design process, manufacturing requirements, limitations and scalability possibilities into the BIPV production line.

3. We demonstrate the effects of UV-curable inkjet inks on typical PV module configurations by subjecting them to accelerated aging tests. A testing and characterization protocol is developed specifically for evaluating the performance of inks used to mask metallic interconnects, with a particular focus on their aesthetic applications in PV modules. The degradation effect observed in a specific case is subjected to in-depth analysis and explained. Furthermore, practical mitigation strategies are proposed to reduce the observed degradation, thereby enhancing the long-term aesthetics, reliability, and overall performance of BIPV modules. This research represents an effort to address the importance of ink design and selection in the context of BIPV module technology, contributing to valuable insights that can potentially lead to more durable and visually appealing BIPV systems.

4. We propose, for the first time, a color characterization technique and a specialized device tailored specifically for the assessment of BIPV colored modules and more general color measurement below a glass or any other transparent materials. The novel colorimeter demonstrates exceptional precision in measuring reflectance within the visible spectrum range, even beneath the glass layer of typical PV laminates, with minimal signal reduction. Through a critical analysis, we explore the limitations commonly associated with portable and integrated sphere spectrometers in the context of color characterization for BIPV modules. Furthermore, we offer an explanation of the functioning of the newly developed technique, accompanied by a detailed examination of its constraints. This research significantly contributes to the advancement of color characterization methodologies for BIPV modules, contributing to enhanced color quality control in the production line and in the field.

These findings have significant implications in the field of BIPV, providing beneficial information to increase automation, improve characterization, and extend the long-term lifetime of BIPV colored solutions. These work aims to boost the incorporation of solar PV into the built environment. Currently, three papers are published [80]–[82], and one is under review [83], highlighting the academic impact of this research. Moreover, the work presented in this thesis has been shared through presentations at four international conferences and through two conference proceedings [84], [85]. For a complete list of publications, please refer to the end of this thesis. Our findings address BIPV industry challenges and benefit both the scientific community and major players such as BIPV manufacturers. This work bridges research and real-world applications, promoting BIPV technology integration into sustainable building

practices. In the upcoming chapter, we will present the characterization techniques and experimental methods employed in this thesis.

# 2 Experimental Methods

The following chapter presents the materials, sample configurations, and characterization techniques used in this work. It includes detailed information about the materials we used and the processes we employed to manufacture the samples. Additionally, we provide a description of the experimental setups employed and the methods we followed in this research.

## 2.1   Sample design and materials

The samples used in this thesis are divided in three main categories (see Figure 2.1):

1. 5 cm by 5 cm glass/backsheet (G/BS) and glass/glass (G/G) coupons were manufactured to understand the interplay between ink-coated metallic ribbons and PV module materials. The choice of this specific size was performed by considerations surrounding the sample quantity, manufacturability, and spatial constraints within the climatic chambers. The metallic ribbons were cut into 3 cm-long strips and placed in the PV stack containing a front glass cover, encapsulant layer, the coated ribbon, another encapsulant sheet and a backsheet or glass rear cover. The same kind of samples were manufactured but instead of encapsulating the coated ribbon pure ink components were laminated.

2. One solar cell G/BS mini module samples of 20 cm by 20 cm were prepared with and without coated ribbons to characterize the effects of ink in the PV module in terms of electrical performance and appearance.

3. G/BS coupons of 7 cm by 7 cm with a wide variety of colored foils ranging from bright white to dark clay with various glass thicknesses were used to characterize the color coordinates with several techniques.

The section below provides the characteristics of the main raw materials used to prepare the samples.
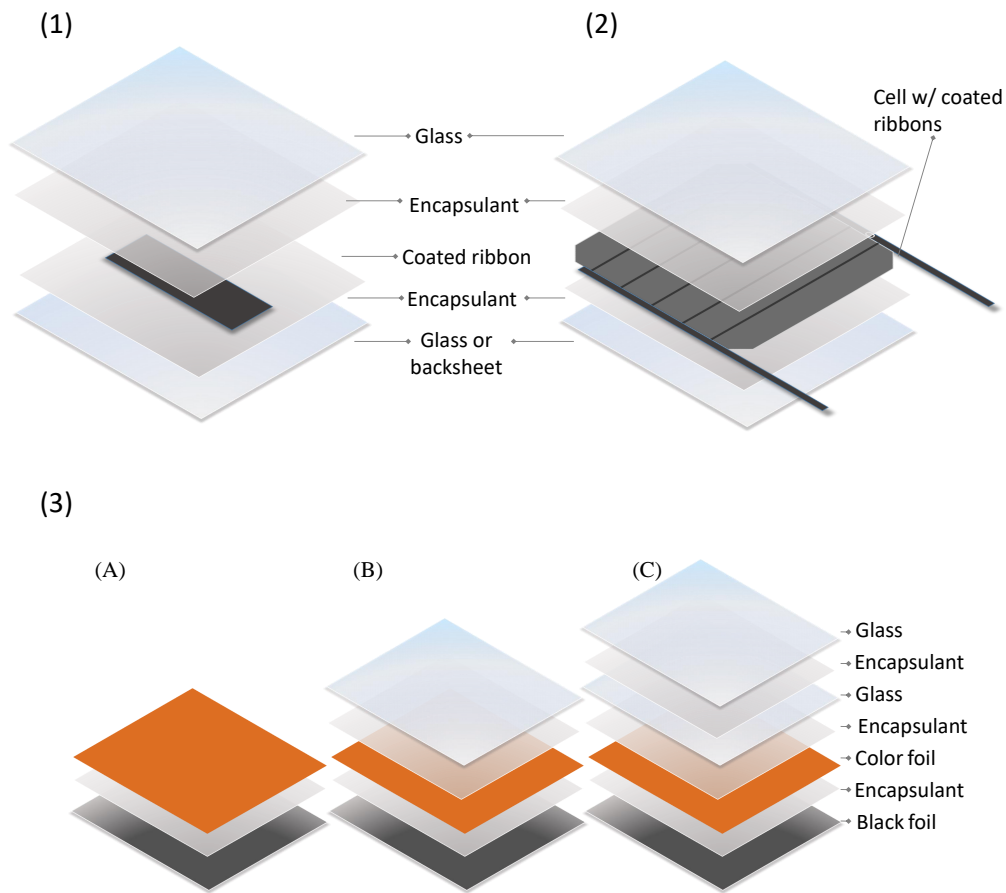
**Figure 2.1:** Schematic of the main samples used in this thesis. (1) 5 cm by 5 cm coupons with encapsulated coated ribbon. (2) 20 cm by 20 cm one solar cell mini module. (3) Colored samples (A) without glass, (B) with 0.5 mm encapsulant + 3.2 mm glass and (C) with 2 times encapsulant + glass = about 1 mm encapsulant + 6.4 mm glass.

### 2.1.1 Glass covers

The glass covers used in this work had the following characteristics:

- Contain a flat surface in both sides.

- Free from the presence of heavy metals.

- Glass measurements: 600 mm in length, 600 mm in width, and 3.2 mm in height.

- Optical transmittance: Approximately 91% with a variance of 0.5% within the range of 350 to 1200 nm.

The low iron glass used was SOLARFLOAT soda-lime glass, characterized by a standard composition containing 70–75 wt% $SiO_2$, 12–16 wt% $Na_2O$, and 10–15 wt% CaO. The glass was untempered, enabling us to cut it into smaller fragments using a glass diamond cutter. Several glass layers were used to cover colored layers as represented in Figure 2.1. The properties of these glass layers appear in Figure 2.2.
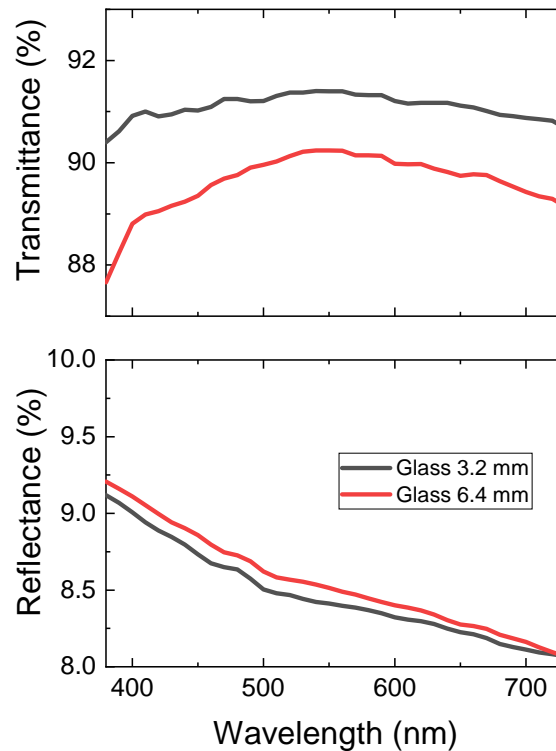
**Figure 2.2:** Transmittance and reflectance in the visible spectrum of the two glass layers with varying glass thickness: 3.2 and 6.4 mm. The 6.4-mm-thick glass (made by two 3.2 mm thick glasses bonded by a layer of encapsulant) has a lower transmittance than the 3.2-mm-thick glass by 1.5% to 2%. The 3.2-mm-thick glass has a transmittance between 90% and 91% while the 6.4-mm-thick glass has a transmittance between 88% and 90%. The reflectance is only slightly higher for the 6.4 mm glass. These reflectances data include reflection from both sides of the glass.

### 2.1.2 Encapsulants

Four different encapsulants were used in this work. Two primary types of encapsulant materials took center stage: ethylene vinyl acetate (EVA) and polyolefin elastomer (POE), with and without UV blockers. All these materials were conveniently sourced from the Chinese manufacturer Hangzhou First with the commercial names:

- F406 PS: EVA without UV blocker

- F806 PS: EVA with UV blocker

- TF4: POE without UV blocker

- TF8: POE with UV blocker

Notably, the encapsulant with UV blockers exhibited a transmittance rate of 30% or lower for wavelengths spanning from 290 nm to 380 nm. In contrast, the counterparts without UV blockers displayed significantly higher transmittance rates, surpassing 70% within the same wavelength range. They were all laminated according to the manufacturer specifications in the process described in section 2.2.1.

### 2.1.3 Inks

All inks studied in this work were commercially available and black colored. No laboratory inks were manufactured. The investigated inks were suggested by ink manufacturers considering the following characteristics:

1. Interaction of the ink with the metallic interconnects.

2. Stability capabilities under weather stressors.

3. Dispensing technique, which needs to be paired with the ink itself.

The ink choice was rather challenging due to the lack of commercial available coatings and dispensing techniques designed for coating the metallic interconnects of PV solar cell arrays. The main process to retrieve the commercial inks consisted on contacting ink and dispensing companies, share the requirements needed by the BIPV industry (see points above) and select the most suitable inks from the commercial feedback. This thesis gives special focus on UV-curable inkjet inks. The ink types used are specified when mentioned during the thesis, mainly in Chapter 5 and Annex B, however, no company, product codes, and full components lists are given due to non-disclosure agreements.

### 2.1.4 Solar cells

Only one type of solar cell was used in this investigation.

- Monofacial PERC with an area of 156.75 × 156.75mm ± 0.25mm, a thickness of 210 ± 20 μm (regardless of the front silver), and 5 bus bars of 0.7 mm width, fabricated by DMEGC Solar.

### 2.1.5 Metallic ribbons

The metallic ribbons employed were commercially available made of a core copper with a soldering coating composition of 60% Sn 40% Pb or 62%Sn 36%Pb 2%Ag. The soldering of solar cells was performed in two main ways, manually in the laboratory at 370°C or in the industrial production line. In both cases the electrical continuity was confirmed. The cross sectional dimension of the string interconnects was of 5 mm by 0.2 mm and 0.9 mm by 0.2 mm for the cell connector. The supplier companies were Sunby, YourBest, and Bruker-Spaleck.

### 2.1.6 Backsheets

The samples with backsheet in this investigation served multiple purposes:

1. Investigate the impact water ingress into the samples.

2. Facilitating the ability to dissect the samples in order to analyze the chemical composition of the polymeric materials in the interior.

Two distinct colors of backsheet were employed – black and white, produced by Cybrid. This deliberate selection aimed to evaluate the visual appearance of the samples under varying degrees of contrast. Particularly, conventional polymeric backsheets with permeable qualities were employed for this investigation.

## 2.2 Processes

### 2.2.1 Lamination

During the lamination process, the encapsulant undergoes a melting phase that binds together the various layers in the PV modules' sandwich structure. It is important that the process is tuned to the encapsulant properties to ensure proper encapsulation of the solar cells. After the lamination process, the encapsulant adopts a transparent and solid state. The equipment employed for this encapsulation procedure within the industry is called laminator. This device typically has two distinct chambers separated by a membrane. The lower chamber integrates a heating plate and adjustable pins to control height (up or down), while the upper chamber, linked to the membrane, possesses the capability to ascend or descend, thereby opening or closing the chamber.

In the context of this study, a 3S laminator without a cooling plate was used. Before initiating the lamination, the samples are arranged as the previously mentioned sandwich structure. These samples are positioned onto a metallic plate featuring a silicone frame, relevant for maintaining precise alignment and preventing material misalignment or breakage. The lamination process, governed by two primary parameters, temperature and pressure, is segmented into three key stages (refer to Fig. 2.3):

1. Preheating: The stack of module materials is introduced into the preheated laminator, with the pins elevated to avoid sudden thermal shocks. The materials within the samples experience gradual heating. Simultaneously, a vacuum is created in the sample chamber (lower chamber) and in the upper chamber so no pressure is exerted, allowing any bubbles present to dissipate from the sample materials with the help of the vacuum.

2. Curing: The pins are lowered, inducing full contact between the glass and the heating plate, causing a raise in temperature. Additionally, a pressure equivalent to 1 atmosphere is applied via the membrane. For thermoset encapsulants like POE and EVA, this phase produce the crosslinking of the encapsulant's polymeric chains, resulting in enhanced thermal and mechanical stability, and the desired transparent appearance, needed for optimal optical transmittance.

3. Cooling: In industrial settings, laminators typically incorporate an additional chamber housing a cooling plate to expedite the cooling process. However, in the laboratory environment, the samples are cooled beneath a membrane at room temperature.

The duration of the lamination process varies depending on the encapsulant and sample configuration employed, typically with a duration of 15 to 20 minutes, and maximum temperatures ranging from 145°C to 160°C. For this study, the lamination process was executed in accordance with the recommendations provided by the encapsulant manufacturers, with lamination temperature of 145°C for EVA F406 and 150°C for POE TF4, respectively. The parameters should be modified depending on the sample configurations.
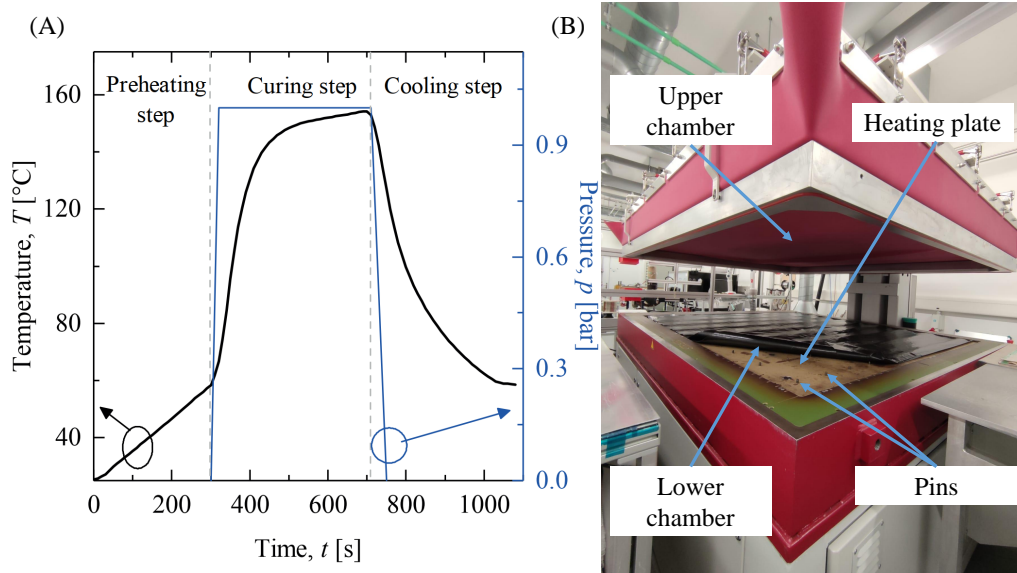


**Figure 2.3:** (A) Three main lamination steps: (1) preheating, (2) curing and (3) cooling. Image taken from [75]. (B) 3S laminator depicting the different parts of it.

### 2.2.2 Coating

Initially, the ribbons were cut and then subjected to a cleaning using isopropanol. The coating process encompassed three primary methods:

1. Manually: The ribbons were coated with a clean brush.

2. Laboratory inkjet: Using the ribbon coating equipment (RCE) described in Chapter 4, the ribbons were coated with inkjet ensuring that the full surface was covered.

3. Industrial techniques: The ribbons were already coated with industrial techniques (e.g. inkjet, screen printed, unknown) by companies, the raw ribbons were sent and returned coated.

The coating process was dependent on the ink's specific characteristics, its availability, and its compatibility with the dispensing equipment. The primary technique employed within this thesis was inkjet technology. This field encompasses two main categories: Drop on Demand (DOD) and Continuous Inkjet (CIJ). Within the DOD framework, two principal mechanisms for droplet generation exist.

The first mechanism is known as DOD thermal inkjet, where an elevation in temperature induces the formation of bubbles within the coating material. These bubbles, by the characteristic of the volume they occupy, increase the pressure within the chamber, producing the expulsion of droplets from the system. The second approach involves a piezoelectric actuator that bends under the influence of a voltage signal, known as waveform, thereby generating pressure within the chamber and expelling the coating in a controlled manner, resulting in the formation of droplets.

One of the primary advantages of the inkjet DOD dispensing method lies in its cleanliness. This is due to its controlled drop-by-drop mechanism, which is contingent upon the frequency of the signal. The operational speed of the system is closely tied to the mechanism responsible for ejecting the droplets. An additional benefit of this method is its inherent simplicity.

On the other hand, Continuous Inkjet (CIJ) employs a continuous flow of coating material, influenced by an electrostatic field to guide the discharge of ink and facilitate printing. While CIJ offers certain advantages, including its continuous flow nature that reduces the likelihood of clogging and its status as a well-established technology, it tends to involve a messier process. Common occurrences include leakages of the coating material. For a visual representation of the primary inkjet types, refer to Figure 2.4.
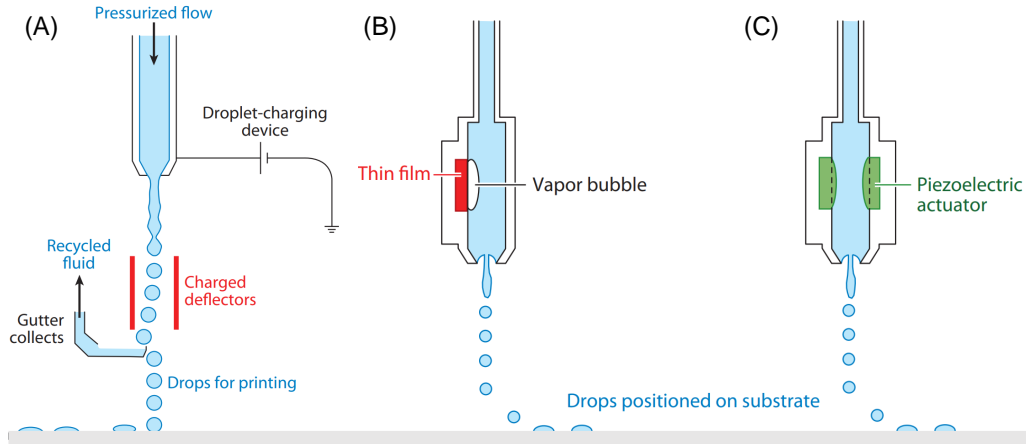
**Figure 2.4:** Inkjet main technologies: (A) Continuous, (B) thermal, and (C) piezoelectric inkjet. Image adapted from [86].

## 2.3 Characterization

### 2.3.1 Current-Voltage measurements

The primary electrical characteristics of PV modules can be derived from the current-voltage (IV) curve, illustrated in Figure 2.5. This curve is generated by systematically adjusting the voltage across the solar cell at specific intervals and recording the corresponding current. This process takes place under defined illuminating conditions known as Standard Test Conditions (STC), which facilitate effective comparison among PV modules. These conditions are detailed in the IEC 60904-3:2019 standard [87] and include:

- Maintaining the device at a temperature of 25°C.

- Subjecting the device to simulated light with an intensity of 1000 W/m².

- Using AM1.5G as the reference solar spectrum.

The main parameters that can be retrieved from the IV curve are the following:

- Short-circuit current ($I_{sc}$) refers to the highest current that flows through solar cells when there is no voltage difference present.

- The open-circuit voltage ($V_{OC}$) represents the highest voltage attainable across the PV module, occurring when the current within the solar cell is non-existent.

30
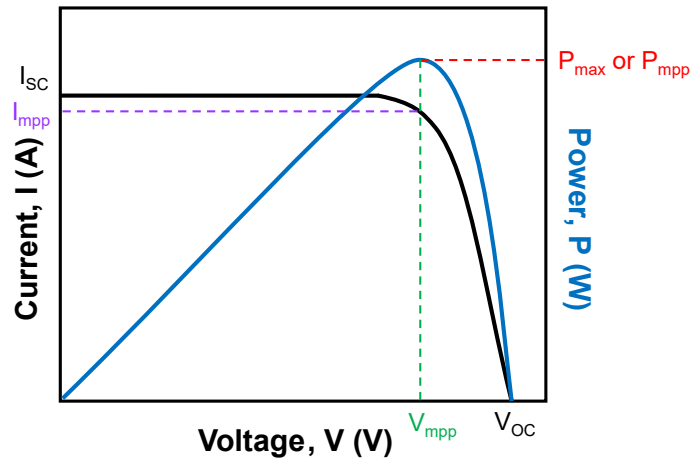
**Figure 2.5:** IV curve with the main parameters that can be obtained from it. Image taken from [34].

- Current ($I_{mpp}$) and voltage ($V_{mpp}$) characterize the point of maximum power output in solar cells.

- Fill Factor (FF), expressed as a percentage, represents the deviation of the recorded I-V curve from the ideal square-shaped I-V curve. Its calculation involves: FF = ($I_{mpp}$ / $I_{sc}$) × ($V_{mpp}$ / $V_{oc}$).

- Power conversion efficiency ($\eta$) quantifies the ratio of the measured electrical output power to the incident light power input under STC. This efficiency is computed as: $\eta$ = ($P_{max}$ / $P_{in}$).

Modifications observed in the IV curve can provide valuable insights, as shown in Figure 2.6. These insights are described through the following points:

1. Reduction in $V_{OC}$ indicate a loss of passivation of the cell.

2. Reduction of the $I_{sc}$ is linked to shading losses (i.e. encapsulant discoloration, degradation of the anti-reflective coating, less light reaching the solar cell) or disconnected cells area (cell breakage, ribbon detached).

3. When cell and string interconnects degrade, typically due to corrosion, it often results in a lower FF.

4. Corrosion tends to lead to more pronounced slopes in the proximity of $V_{OC}$, resulting in a higher series resistance ($R_s$).

5. A slope near $I_{sc}$ indicates the formation of shunt paths within the cell, resulting in a lower shunt resistance ($R_{sh}$).
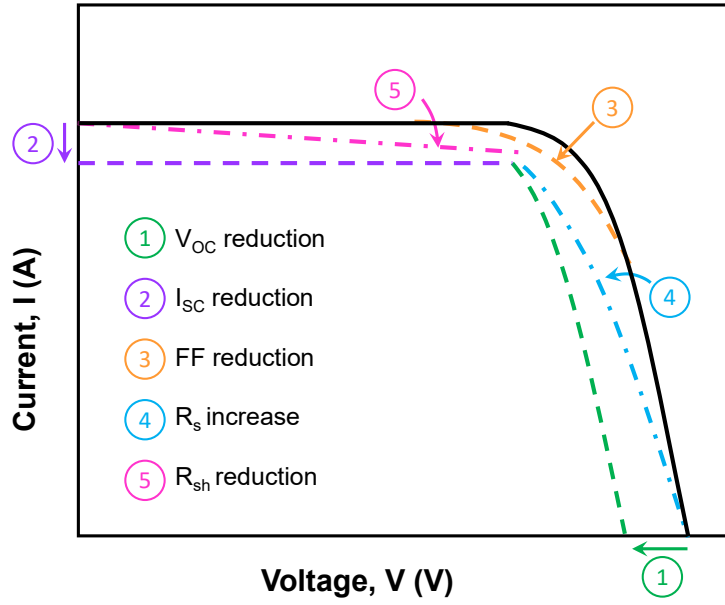
**Figure 2.6:** Possible modifications to the IV curve upon degradation of the module. Image obtained from [34].

The solar cell mini-modules were subjected to measurements within the controlled environment of a horizontal PASAN solar simulator, using both LED and halogen lamps to replicate the AM1.5G spectrum indoors. The measurement process was initiated by measuring a calibrated module, which allowed for the determination of equipment sensitivity while accounting for temperature variations. Subsequently, the mini-modules were measured, applying the established sensitivity value, and employing a thermocouple to adjust the temperature to standard test conditions (STC) through the equipment's software. The measurement setup carries an estimated uncertainty of ±3% and a reproducibility of ±1%.

### 2.3.2 Electroluminescence (EL)

Electroluminescence (EL) imaging offers a rapid and non-destructive approach for the qualitative inspection of photovoltaic (PV) modules. By injecting a direct current into the module, it prompts radiative recombination of generated electrons and holes, thus facilitating the detection of defects like shunts, cell cracks, and shading. Captured by a charge-coupled device (CCD) camera, the emitted photons are recorded under low-light conditions to minimize noise. This work leveraged EL imaging to assess modules both prior to and during aging tests, effectively exposing shading and other potential impacts on solar cells, as visualized in Figure 2.7.

For this study, a Sensovation SamBa Ci model charge-coupled device (CCD) camera, equipped with a Nikon lens boasting a fixed focal length and operating at a pixel resolution of 1660 x 1252, was used. Measurements were consistently carried out in the dark. Throughout the aging

tests, ongoing monitoring of mini-modules provided insights into the evolving performance of the modules over time.
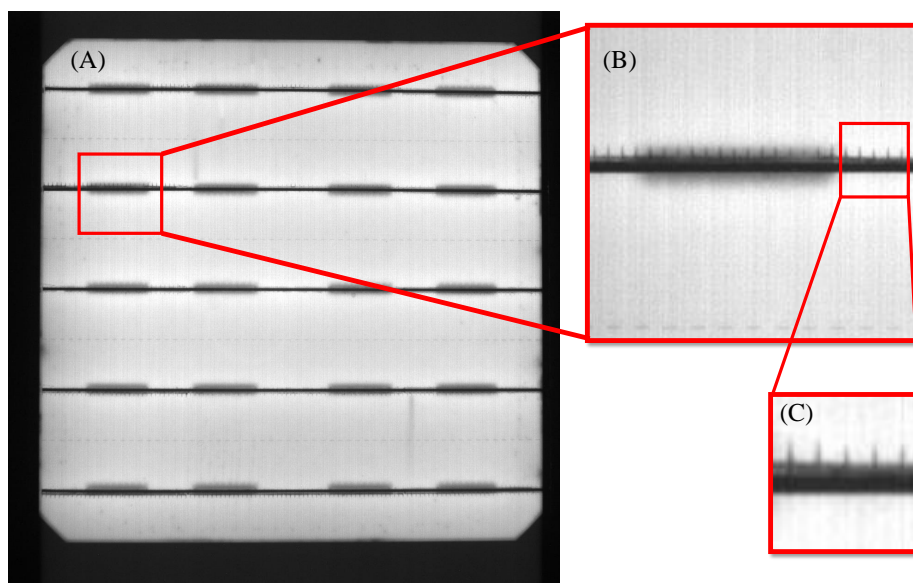


**Figure 2.7:** (A) EL image of a solar cell with coated metallic ribbons. (B) The closer view provides insights that the ink flew into the fingers of the cell. (C) Closer view of the ink flow into the fingers.

### 2.3.3   Colorimetry

This section describes the characterization techniques used to measure the color of the samples. More information about colorimetry theory can be found in Chapter 6 and Annex C.

**Visual inspection**

In photovoltaic research, visual inspection is a prevalent method for evaluating the appearance of samples. This technique proves valuable in identifying potential changes like bubbles, cracks, and delamination. Small-area samples can be subjected to visual inspection using digital scanners similar to those found in printers. These scanners are favored due to their consistent resolution and lighting, enabling the comparison of small samples before and after accelerated aging tests. Typically, scanner devices employ arrays of light sources, such as LEDs, in a linear arrangement to capture images while the sensors traverse the entire sample surface.

When using a scanner for visual inspection on a glass laminate, it is common to observe a darkening of the image due to the shift with the glass thickness. Manufacturers might apply diverse color corrections through internal processes, which remain undisclosed to users. If color assessment is involved, the output is provided in RGB coordinates using an unknown illuminant. To address this concern, a software tool was developed employing image processing to quantify color alterations between a reference color and the pixels or region of

interest. The software uses image registration techniques to align the digital images of the same sample and calculated with CIELAB DE2000 standard [88] the change in color ($\Delta$E) of pixel by pixel of the image array, as depicted on Figure 2.8. In this study, a conventional Canon imageRUNNER ADVANCE DX C5860i scanner was employed to measure the samples.
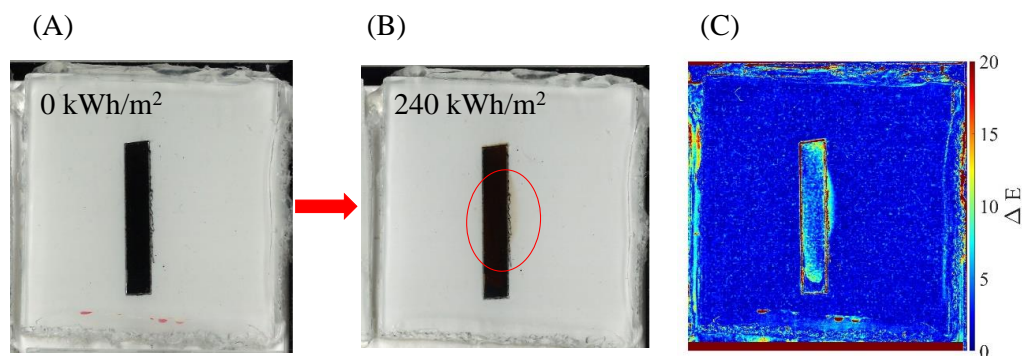


**Figure 2.8:** Example of the output of the advanced visual inspection software on G/BS samples before and after UV exposure. It compares images (A) and (B) to produce image (C). Each pixel of image (C) represents a value of color change ($\Delta$E).

**Portable colorimeter**

The colorimeter employed in this study was the portable X-Rite i1Pro Rev E, capturing data across the 380 nm to 730 nm range with a 10 nm sampling interval. This device uses a brief illumination of the sample by a light source, followed by the detection of its reflectance. Variations in parameters like color space, reflectance data range, observer angle (2° or 10°), illuminant, and sampling interval are common. Commercial colorimeters are typically compact and portable, allowing measurements to be taken in a matter of seconds. Initial calibration against a white reference sample is a prerequisite step with this tool, ensuring a maximum reflectance value of 100%.

**UV-Vis spectrometer**

Reflectance data for this study were gathered using an integrated sphere UV/VIS/NIR spectrometer, namely the Perkin Elmer Lambda 950. This equipment is proficient in assessing transmittance and reflectance across the 250 nm to 2500 nm spectrum. However, our analysis primarily centered on the visible range. Employing an integrating sphere, this device captures the reflected light from the sample. In contrast to the colorimeter's approach of generating a light probe with varying wavelengths and swiftly recovering reflectance, the spectrometer generates a wavelength scan with a selected sampling interval, recording reflection data for each wavelength.

Prior to data collection, a calibration procedure is executed using a white reference (spectralon)

and a dark reference (no sample lid placed) to establish the uppermost and lowest reflectance values. This reference data subsequently aids in rectifying the reflectance of the measured samples. To conduct a measurement, the sample is positioned within the integrated sphere's aperture and covered using the device's lid. It's important to note that integrated sphere spectrometer measurements take longer than colorimeter measurements, potentially lasting up to 3 minutes per measurement depending on the wavelength range and sample interval. In our study, the focus remained on the visible range, and a 10 nm sampling interval was utilized. This equipment was used as a reference to compare innovative proposed techniques.

### 2.3.4 Attenuated total reflectance Fourier transform infrared spectroscopy (ATR-FTIR)

Fourier-transform infrared (FTIR) spectroscopy is a non-destructive technique to characterize changes in the chemical composition of materials. The functioning is the following, a beam with several frequencies of infrared light is directed to the sample and the system measures how much of it is absorbed. This process is repeated with many ranges of frequencies and then the software processes the data to calculate the absorption at each wavelength. The technique was implemented in this work only in reflectance mode due to the nature of the analyzed samples.

In this thesis, ATR-FTIR was mainly used to characterize encapsulants and ink components. A Bruker Vertex 80 spanning the 400-4000 $cm^{-1}$ range with 64 scans in absorbance mode was used to retrieve the data. The background was collected on a clean ATR diamond crystal. Several measurements of each sample were taken in various spots to then process the data and normalize it.

### 2.3.5 Thermo-desorption gas-chromatography coupled to mass-spectrometry (TD-GCMS)

Gas chromatography (GC) was the preferred separation technique for smaller volatile and semi-volatile organic molecules, such as ink components. This technique, when paired with the detection capabilities of mass spectrometry (MS), empowers GC-MS to effectively separate complex mixtures, identify unknown peaks, and even quantify them.

This approach was applied to examine the chemical processes within samples with ink components and encapsulants. Approximately 1 mg of both reference and contaminated encapsulant, containing ink component materials, were extracted from the G/BS laminates. This qualitative investigation aimed to uncover changes in additive composition and the formation of potential degradation products that occurred during exposure.

TD-GCMS experiments were conducted using a GC-MS QM2010 Ultra from Shimadzu, equipped with a Pyrolyzator 3030D from Frontier Laboratories at the Polymer Competence Center Leoben GmbH (PCCL). For the encapsulant samples, the pyrolyzator's furnace was employed

to heat them from 60 °C to 320 °C, employing a heating rate of 20 °C/min, and then maintained at 320 °C for 3 minutes. Gases released from the encapsulants during this phase were directed into the GC using helium as the carrier gas. The GC, outfitted with an Optima-5-Accent column (30 m length and 0.25 mm inner diameter), effectively separated the evolved substances. The interface between the GC and pyrolyzator was maintained at 300°C. The GC's thermal protocol comprised the following steps: (I) warming from 50 °C to 90 °C at 10 °C/min, (II) a 2-minute isotherm at 90 °C, (III) warming from 90 °C to 300 °C at 10 °C/min, and (IV) a 10-minute isotherm at 300°C. Subsequent to column elution, each substance underwent ionization using an ionization energy of 70 eV, with mass spectra recorded across the m/z 50 – 800 range. Identification of mass spectra was accomplished through comparison with the NIST database. These measurements were performed at the Polymer Competence Center Leoben (PCCL).

### 2.3.6 Raman spectroscopy

In this study, Raman spectroscopy was used as an additional non-destructive technique for the identification of ink components and modifications within the encapsulant. The process involves directing a laser beam onto the sample under investigation. The energy or frequency of the scattered photons is quantified. During inelastic interactions with vibration modes within the sample, certain photons can undergo energy changes. The resulting alteration in energy, and consequently in frequency, provides insights into the chemical bonds present within the material. A significant advantage is that samples can be examined without the need for peeling, although this presents a challenge.

Similar to the approach used in ATR-FTIR, the G/BS laminates underwent manual peeling to assess chemical changes within the encapsulant. The Raman spectra were acquired using two Renishaw InVia confocal spectrometers, both equipped with a 785 nm laser for excitation. Generating a line map of the Raman spectra required a 100x Leica objective (numerical aperture NA = 0.90), accompanied by a dielectric rejection filter and a 1200 grooves/mm diffraction grating. As a calibration reference, the Raman line of crystalline silicon at 520.5 cm-1 was employed. These measurements took place at the Institute of Physics of the Czech Academy of Sciences (FZU).

### 2.3.7 Ultraviolet (UV) fluorescence imaging

Ultraviolet (UV) fluorescence imaging is an analytical technique that uses ultraviolet illumination to induce fluorescence responses in materials. This imaging method uses the phenomenon of fluorescence, where certain materials absorb UV light and emit visible light, enabling the visualization of specific compounds or structures with enhanced contrast.This technique is particularly advantageous for investigating compounds with intrinsic fluorescence properties, facilitating non-invasive analysis and visualization of small details or specific components within a sample. In this investigation the technique was employed to visualize

material alterations on ink component and encapsulants. Images were taken indoors in a dark room, illuminated only with a 365 nm, 20 W UV LED flood light, and photographed with a digital camera.

## 2.4 Indoor accelerated aging tests

### 2.4.1 Damp Heat (DH)

The Damp Heat (DH) aging is an important indoor test in the PV field, constituting a relevant element within the test sequences proposed by the IEC 61215 standard [72]. As discussed earlier, this test is designed to offer insights of the impact of humidity and temperature on the materials of PV modules. This evaluation revolves around two main parameters: relative humidity (RH) and temperature. Within a controlled setting, using a Weiss C180/-40 climatic chamber, the testing conditions were established at 85°C and 85%RH. While the standard test protocol stipulates a duration of 1000 hours, this study diverged by implementing varying test durations to the different configurations of samples. More information about the test duration employed can be found in Annex B.

### 2.4.2 UV indoor exposure

The UV indoor exposure was conducted in accordance with the IEC 62788-7-2 standard under A3 conditions [77]. Employing a Q-Sun Xenon chamber (Q-SUN Model Xe-3) equipped with a noon summer sunlight filter, the following conditions were adhered to:

- Irradiance: 0.8 W/m$^2$ at 340 nm

- Relative humidity: 20%

- UV dose (UV-A + UV-B): 60 W/m$^2$

- Chamber air temperature: 65 °C

- Black panel temperature: 90 °C

This exposure regimen aimed to replicate indoor sunlight consistently through the use of Xenon arc lamps.

The major findings of this thesis are presented in the following chapters. In the next one, we start by comparing the carbon intensity (CI) values derived for PV to the CI of European nations' power mix to assess the impact of installing PV from a CI perspective in sub-optimal orientations.

# 3 Carbon Intensity of Integrated-Photovoltaics: Solar Electricity Everywhere

The work in this chapter is based on the following article accepted by a journal:

## Abstract

To minimize land exploitation and to allow PV to play a major role in the decarbonization of Europe, a massive deployment of PV in Europe should occur through the integration of PV in buildings and infrastructures, including surfaces with a sub-optimal orientation. To assess the meaningfulness of installing PV under this constraint, we consider a carbon intensity balance perspective and assess, for all European countries, whether installing PV at different exposures acts as a net $CO_2$ sink or source, when compared to the same amount of carbon that would be generated over the same timeline using the local electricity mix. The mean values obtained for the carbon intensity of PV in buildings (for all orientations and all European countries) corresponds to 35.8 and 41 $gCO_2$-eq/kWh, respectively, for an optimally exposed surface or for a generic rooftop installation. The mean value of the distribution for façades corresponds to: 51.4, 71, and 214 $gCO_2$-eq/kWh, respectively, for south-, west-/east-, and north-facing façades. Notably, the potential to halve these figures by 2030 already exists. These figures must be compared to the mean value for the CI of national electricity mixes in Europe which is 374.5 $gCO_2$-eq/kWh with a much broader distribution, reflecting the wide difference in the generation technologies adopted by the different countries. These results indicate that for most European countries the integration of PV in façades (including most of the times N-facing PV façades, which receive on average approximately 15% only of the insolation of an optimally oriented surface) would not penalize - and conversely would still support- a transition towards a carbon-neutral electricity mix. Our analysis is complimented by a list of recommendations to policymakers to foster and maximize in the shortest possible time a massive diffusion of PV in the built and urban environments.

## 3.1 Introduction

The global commitment to reduce greenhouse gas (GHG) emissions and achieve the 2015 Paris Agreement to keep global warming below 2 °C – while pursuing efforts to limit the increase to 1.5 °C – is not on track. Hence, the European Commission is setting ambitious targets to achieve climate neutrality by 2050, requiring a massive electrification of the mobility and heating sectors, coupled with a major shift towards renewable energy generation sources, among which solar photovoltaic (PV) electricity is deemed to play a pivotal role. By this horizon European member states may have to install, according to some scenarios, from 5 to 10 $TW_p$ of PV power across the Old Continent [89], corresponding to yearly installation rates of 100-300 $GW_p$/y (for a comparison, 173.5 GW of new solar capacity was installed globally in 2021, with projections of 260 GW for 2022). This urgency - in the middle of an energy crisis and with the need to become energy independent from third countries - has presently become even more pressing.

In countries with limited availability of land (e.g. the Netherlands, Malta, Switzerland), however, the full deployment of PV on land conflicts with other land uses, such as agriculture, pastures, forestry. Also in larger countries, the deployment of large solar parks on agricultural land is nowadays increasingly facing resistances from national and local administrations because of land use conflicts. A situation, which in some countries (e.g. Italy) creates serious bottlenecks in the permitting phase, leading to considerable delays in the execution of solar projects and the adoption of national targets. For these reasons, the adoption of PV projects leading to a double land or space use - as for example so called agri-PV (i.e. on agricultural land) or floating-PV (on water reservoirs) projects – are highly welcomed and presently becoming targeted applications with a considerable market potential.

Nevertheless, a massive deployment of PV in Europe should primarily occur through the integration of PV in urbanized settings and into the built environment [30], [90], [91], including residential, terziary, commercial and industrial buildings and warehouses, and more in general all the available infrastructures. The latter may include: noise barriers along roads and railways, car-parks, water treatment plants, bus and train stations, harbors, and many others. Two examples of building-integrated PV are given in Figure 3.1, whereas examples of infrastructure-integrated PV (IIPV or IPV) and landscape-integrated PV are given in Annex A.

However, as opposed to large utility-scale plants, for which it is generally easier to have an optimal (or close to optimal) PV array exposures, this becomes more difficult when integrating PV in buildings or infrastructures, as the constraints will typically be set by the physical arrangement of the building skin or surface. Hence, the energy yield potential of a "solar active skin" will be impacted by the sub-optimal orientation [92], [93].

To assess the meaningfulness of installing PV in surfaces with sub-optimal orientations, we do not take an economical perspective - a topic recently reviewed by Gholami and Rostvik [94] - but that of a carbon intensity (CI) balance. To do this, we first asses the generating potential (insolation and PV energy yield) of non-optimally exposed surfaces in buildings (and

**Figure 3.1:** South and north-facing BIPV façades: The top row shows the south- (left) and shaded north-(right) facing BIPV façades of a high-rise office building in Milan (Italy). The building has undergone a major renovation process in year 2020. The bottom row shows the east- and north-facing façade (left) of a building of the life-science department at the University of Neuchâtel (Switzerland), renovated in 2021 and (right) cladded on all surfaces with integrated solar panels.

elsewhere) for different European cities distributed at different latitudes (from 35° to 60° N); and then assess for all European countries whether – on a time horizon of 30 years – installing PV at different exposures acts as a net $CO_2$ sink or source, when compared to the same amount of carbon that would be generated over the same timeline using the local electricity mix. Since the solar electricity generated in buildings is generally consumed on site (or on its proximity), for a fairer comparison we focus here on country's electricity consumption - rather than generation - figures at the low-voltage (LV) grid, therefore including transmission and distribution losses.

Both CI figures for PV and the national electricity mixes make use of the most updated life cycle estimates available in the literature. For solar PV, we make as well use of a greener-PV scenario, which is consistent with a further reduction of the carbon embedded in the construction of solar PV expected in the coming years. In short, our primary research question can be summarized as follows: *is the integration of PV in sub-optimal orientations justifiable from a carbon-balance perspective?*

The results are somehow surprising for most countries - at least for the less favorable exposures - and clearly laydown the pathway for a massive adoption of solar electricity into the built environment. In addition, we come out with indications and recommendations for the policy

maker to help them achieve this target. The perspective adopted in this manuscript is primarily European, but could easily be transferred to other countries and regions in the world. As per the solar PV potential in European buildings (not including infrastructures), figures vary between studies. In a publication form 2012, Defaix and coworkers [95] estimate this potential to be 951 $GW_p$ for EU-27 countries (corresponding to an annual yield of 840 TWh/y, or more than 22% of the expected European electricity demand by 2030), lower than the potential previously reported in a 2002 IEA-PVPS report [96].

A recent study from the Swiss Federal Office of Energy focusing on Switzerland, however, estimates the annual solar power production potential of roofs and façades in Switzerland to be 67 TWh/y (split between 50 and 17 TWh/y for rooftops and façades, respectively), potentially exceeding the current country's electricity demand by over 10% [97]–[100]. By considering the latest numbers for Switzerland, it is realistic to assume that the 951 $GW_p$ potential for PV in buildings in EU-27 countries is largely underestimated, even by a factor of three to five. Estimates for the solar PV potential in infrastructures at the European level do not exist. Preliminary figures may be available at the country level, as in the case of Switzerland for which recent studies review the potential for PV on roads, highway embankments and open alpine spaces [101]–[103].

## 3.2 Approach, data and method

### 3.2.1 Solar resources and energy yield of PV systems for different orientations

Insolation (H, [kWh/m$^2$·y]) and yearly energy yield (EY, [kWh/kW$_p$·y]) data for PV as a function of different exposures are obtained by JRC's (Joint Research Center – European Commission) PV-GIS, a free on-line tool, which uses satellite-derived data to estimate the availability of solar resources [104]. The EY values are obtained for PV systems made with conventional crystalline-silicon (c-Si) and fixed system losses set at 14% (a default PV-GIS value). H and EY for south-facing surfaces at optimal tilt angle (S-opta) - the orientation that maximizes the annual energy yield of a PV plant in the Northern atmosphere- are shown in Table 3.1 for the capital cities of EU 27-member states and other European countries.

### 3.2.2 Carbon intensity of solar PV electricity

Life cycle analysis (LCA) is a well-established methodology to evaluate the environmental impact caused by products or processes throughout their entire life cycles [106]. The relevant ISO (International Standard Organization) standard 14040–44 [107], [108] is supported by European guidelines [109] and by PV-technology specific best practices [110], [111]. LCA figures for PV are, however, often outdated, as they do not often reflect the large progress made for this technology in recent years all along the value chain, as well as the massive manufacturing shift to Asia (mostly China) in the last decade. The limits of existing carbon inventories for PV and differences between databases (e.g. electricity mixes, material consumption and energy

**Table 3.1:** Carbon intensity CI of the national electricity mixes (i.e. consumption figures at the low-voltage grid [105], insolation and energy yield for a S-facing PV system at optimal tilt (S-opta, [104]) located in the capital cities of EU27-member states and other European countries.

| Country | Country code | Capital | CI elect. Mix [gCO$_2$-eq/kWh] | S-opta Insolation [kWh/m$^2$·y] | S-opta Energy Yield [kWh/kW$_p$·y] |
|---|---|---|---|---|---|
| Austria | AT | Vienna (48.2N, 16.4E) | 264 | 1477.5 | 1179.9 |
| Belgium | BE | Brussels (50.8N, 4.4E) | 230 | 1287.1 | 1034.1 |
| Bulgaria | BG | Sofia (42.6N, 24E) | 544 | 1701.3 | 1343.7 |
| Cyprus | CY | Nicosia (35.1N, 33.2E) | 791 | 2168.2 | 1623.2 |
| Czechia | CZ | Prague (50N, 14.5E) | 564 | 1357 | 1082.7 |
| Germany | DE | Berlin (52.5N, 13.4E) | 422 | 1325.3 | 1061.7 |
| Denmark | DK | Copenhagen (55.7N, 12.6E) | 158 | 1254 | 1041.4 |
| Estonia | EE | Tallinn (59.4N, 24.8E) | 472 | 1117.7 | 900.2 |
| Greece | EL | Athens (38N, 23.7E) | 780 | 1932.5 | 1587 |
| Spain | ES | Madrid (40.4N, 3.7W) | 279 | 2098.9 | 1625.8 |
| Finland | FI | Helsinki (60.2N, 24.9E) | 141 | 1188.9 | 972 |
| France | FR | Paris (48.9N, 2.3E) | 98 | 1437.2 | 1151.3 |
| Croatia | HR | Zagreb (45.8N, 16E) | 372 | 1553.6 | 1214.3 |
| Hungary | HU | Budapest (47.5N, 19.1E) | 338 | 1573.2 | 1245 |
| Ireland | IE | Dublin (53.3N, 6.3W) | 384 | 1191.1 | 975.5 |
| Italy | IT | Rome (41.9N, 12.5E) | 356 | 1912.6 | 1499.7 |
| Latvia | LV | Riga (56.9N, 24.1E) | 325 | 1214 | 980.7 |
| Lithuania | LT | Vilnius (54.7N, 25.3E) | 321 | 1191 | 959.8 |
| Luxembourg | LU | Luxembourg (49.7N, 6.1E) | 338 | 1299.6 | 1042.9 |
| Malta | MT | Valletta (35.9N, 14.5E) | 463 | 2097.4 | 1659.8 |
| Netherlands | NL | Amsterdam (52.4N, 4.9E) | 450 | 1276.7 | 1033 |
| Poland | PL | Warsaw (52.2N, 21E) | 805 | 1312.9 | 1051.8 |
| Portugal | PT | Lisbon (38.7N, 9.1W) | 324 | 2007.3 | 1585.4 |
| Romania | RO | Bucharest (44.4N, 26.1E) | 464 | 1648.5 | 1287.2 |
| Slovakia | SK | Bratislava (48.1N, 17.1E) | 346 | 1508.7 | 1197.7 |
| Slovenia | SI | Ljubljana (46N, 14.5E) | 307 | 1419.8 | 1114.3 |
| Sweden | SE | Stockholm (59.3N, 18.1E) | 40 | 1219.7 | 988.6 |
| Iceland | IS | Reykjavik (64.1N, 21.9W) | 26 | 1091.8 | 892.3 |
| Norway | NO | Oslo (59.9N, 10.6E) | 31 | 1130.5 | 915.2 |
| Switzerland | CH | Bern (46.9N, 7.4E) | 78 | 1502.3 | 1195.5 |
| United Kingdom | UK | London (51.5N, 0.1E) | 304 | 1287.4 | 1050.8 |
| Ukraine | UA | Kiev (50.4N, 30.5E) | 492 | 1364.5 | 1095.3 |
| Serbia | RS | Belgrade (44.8N, 20.4E) | 900 | 1606.3 | 1254.8 |
| Albania | AL | Tirana (41.3N, 19.8E) | 24 | 1835.3 | 1416.4 |
| Montenegro | ME | Podgorica (42.4N, 19.3E) | 663 | 1840.1 | 1409.5 |
| Turkey | TR | Istanbul (41N, 29E) | 588 | 1754.9 | 1382.5 |

requirements) is reviewed by Müller and coworkers in Ref. [112].

Several technological improvements have in fact allowed a remarkable reduction in the carbon footprint (per installed W$_p$ or generated kWh of electricity) of crystalline silicon (c-Si) based PV, the dominant PV market technology. This has been achieved over the years through a considerable increase in solar cell and module efficiencies, reduction in material consumption (thanks for example to the use of thinner wafers, reduced wafering losses and lower silicon and

silver consumption), and the adoption of more efficient manufacturing processes, including polysilicon production, as recently reviewed by [51]. Just to make two examples, over the last thirty years (1990 to 2020), Si wafer thicknesses have been reduced by at least a factor of two (from 400 to 180 µm) and Si usage per watt-peak by a factor of four (from 16 to around 3 g/$W_p$). In parallel, with module prices today in the range of 0.2 \$/$W_p$, the combination of technological innovation and economies of scales have led to a cost reduction of the PV technology larger than a factor of 100 since the early 80's of the last century, making solar photovoltaic electricity a major and cost-effective enabler of the ongoing energy transition towards a low-carbon-emission society.

A direct comparison of the different figures available in the literature about the global warming potential ($GW_p$) or CI of PV is further complicated by several factors:

(a) Some authors report estimates about the $GW_p$ of PV referring to the system capacity (g$CO_2$-eq/$W_p$) and others to the electricity generated by the PV plant (g$CO_2$-eq/kWh).

(b) Estimates for the CI of PV per kWh require assumptions about the electricity generated by a PV plant over its guaranteed lifetime (including assumptions about service lifetimes and degradation rates) and largely depend on the installation site, particularly on the local availability of solar resources. This figure is however the most adequate for comparing the $GW_p$ of different power generation technologies.

(c) Some authors report CI numbers for the full PV system (including inverters and other BOS components) and others about solar modules only;

(d) The methodology and the $GW_p$ inventories adopted by the different authors to estimate the CI and energy yield of PV during its entire life-cycle may largely affect the outcomes of the analysis.

Fortunately, some novel contributions (listed in Table 3.2) have recently appeared in the literature for the CI of PV allowing a more accurate and reliable analysis. In this work we decided to use the estimates reported by Frischknecht et al. in a recent factsheet report from the IEA (International Energy Agency) [113], [114]. This are relative to a 3 k$W_p$ residential rooftop PV system located in Switzerland. The assumptions used by the author are briefly summarized at the bottom of Table 3.2 and are based on a strong carbon mix for the electricity used for the sand to module manufacturing, reflecting manufacturing in China. Under these worst-condition assumptions, PV has a CI of 42.5 g$CO_2$-eq/kWh for an energy-yield of 975 kWh/k$W_p$ and assuming a 30-year-long lifetime for the PV plant with an average annual degradation rate of - 0.7%/y. According to the same report, the environmental impact – in terms of GHG emissions - of PV systems made with c-Si modules has been reduced from 2011 to 2018 by a factor of 40%.

The green-house gas (GHG) emissions associated with the generation of 1 kWh of solar electricity from PV systems are far lower than the emissions from fossil fuel generators, which can

**Table 3.2:** Carbon intensity CI of the national electricity mixes (i.e. consumption figures at the low-voltage grid [105], insolation and energy yield for a S-facing PV system at optimal tilt (S-opta, [104]) located in the capital cities of EU27-member states and other European countries.

| Source | PV module or system | CI of PV per capacity [kgCO$_2$-eq/kW$_p$] | CI of PV per kWh of electricity [gCO$_2$-eq /kWh] | Notes |
|---|---|---|---|---|
| **Fthenakis et al. [115]** | System | 1000 (mono, 2020) | 40 23 17 | Three insolation levels: 1000, 1700, 2300 kWh/m·y (from top to bottom) |
| **Frischknecht et al. [113]** | System | | **42.5** | **Data used in this work.** Details given below: (*); |
| **Golsdchmidt et al. [116]** | System | 1270 (mono, 2021) | | |
| **Müller et al. [112]** | Module | 810 580 | | (G/BS, China, 2021) (G/BS, EU, 2021) |

*G/BS = glass/back-sheet panel structure, mono: mono-crystalline Si, EU: manufacturing in Europe.*

**(*) Starting assumptions for the CI of PV**: 42.5 gCO$_2$-eq /kWh for a residential 3 kW$_p$ rooftop PV system (including panels, inverters, cabling, mounting structures) installed in Switzerland (46°N), yearly PV energy yield of 975 kWh/kW$_p$·y (corresponding to 83% of the energy yield of a S-facing system installed at the optimal angle in Bern i.e. 1175 kWh/kW$_p$·y); Service life: PV modules 30 years (with an annual degradation rate of -0.7%/y); inverter 15 years. Origin of polysilicon/ingots/cell/modules; CI of Chinese electricity mix: 1190 gCO$_2$-eq /kWh; Energy pay-back time of PV system: 1.2 years (Switzerland). Breakdown of emissions: 63.5% (panels), 23.5% (inverter), 11.7% BOS, 1.2% (other).

emit up to 1000 gCO$_2$-eq /kWh in the case of coal-fired power plants. Almost all the emissions from the life cycle of PV originate from the manufacture of the different components. There is little impact from end-of-life activities and almost no impact at all from their operation. This is in direct contrast to fossil and nuclear power plants which release the majority of emissions through their ongoing operation and fuel supply. For all the works reported in Table 3.2, modules (as well as metallurgical-grade Si, ingots, wafers, cells and the aluminum frame [117]) are assumed to be manufactured in China, reflecting the fact that over 80% of global module shipments presently originate from this country.

Despite the fact that this share has been decreasing over the last decade, still 65% of Chinese electricity comes from burning coal [92], [118]). This fact is reflected in the CI of the Chinese electricity mix (i.e. 1190 gCO$_2$-eq /kWh on the medium-voltage grid; the value used in the Ref. [113], [119]–[121]), which is more than three times higher when compared to the European average ( 374.5 gCO$_2$-eq /kWh on the low-voltage grid tough, see Table 3.3). Since the energy yield (kWh/kW$_p$) of a PV plant over its lifetime is strongly site-dependent (primarily depending on the availability of solar resources) and, for a given site, will largely be affected by the plant's orientation and tilt, we use the starting assumption of 42.5 gCO$_2$/kWh for the CI of PV systems in 2022 (975 kWh/kW$_p$, see details in Table 3.2) and correct these values to reflect the energy

yield of PV plants installed in different locations in Europe and for different orientations (see Table 3.3). This is done by using the same assumptions: a plant service lifetime of 30 years with an annual performance degradation rate of -0.7%/y [122]. Understandably, the CI of solar electricity will highly depend on the lifelong generation of a PV plant, which is highly site-dependent and highly impacted by the system exposure.

In the following (Section 3.3), we similarly make use of a scenario ("greener-PV") in which the CI of PV is reduced by a factor of 2 (i.e. 21.2 $gCO_2$-eq/kWh, as base value; see Table 3.2). This is a realistic scenario for 2030 and beyond reflecting two main drivers: (1) further reduction of $GW_p$ of PV following additional technological evolution and innovation; (2) manufacturing of PV panels and other components outside of China: in countries with a low-carbon electricity mix. This includes the possibility of reshoring manufacturing back to some European countries, presently a highly-discussed and sensitive topic at the European level.

As previously shown in Table 3.2, in the breakdown of emissions for PV systems (and under the same assumptions), the manufacturing of PV panels (silicon, wafer, cell and module) accounts for over 63% of overall GHG emissions. According to Ref. [112], detailing the overall and breakdown contributions of GHG emissions of solar PV modules, this value could already be reduced today – for modules in a glass/foil structure - from 810 $gCO_2$-eq/kWh (for manufacturing in China; i.e.100%) to 580 (72%) and 480 (60%) $gCO_2$-eq/kWh for manufacturing, respectively, in Germany and more in general in the European Union (EU).

Very recently a full "made-in-Europe" 566 $W_p$ module with a carbon footprint of 317 $kgCO_2$-eq/$kW_p$ only has been reported by CEA (see Ref. [123]). This record has been achieved by using silicon-heterojunction solar cells, thinner glass and cells, a wooden frame (replacing the conventional aluminum frames) and sourcing most materials (including poly-silicon) in Europe. These numbers, clearly demonstrating the large potential that already today exists for the further reduction of the $GW_p$ of PV, tell us that a carbon tax on the imports of Asian solar panels would be fully justified in this perspective and could serve as a basis to support the reshoring of solar module manufacturing to Europe. Noticeably, many stakeholders of the PV value chain nowadays are engaging in using cleaner electricity in their production (in Asia as well) to address this issue.

### 3.2.3 Carbon intensity of European countries energy mixes

As the electricity generated by PV in buildings is generally consumed by or close to the end-user and it is injected into the LV or the medium voltage (MV) grid (depending on the size of the plant), to have a fairer comparison we make use - for CI figures of the local electricity mix - of consumption (rather than generation) figures at the LV grid.

CI figures for power generation, rather than consumption ones, are much easier to retrieve and can be generally accessed through European statistical databases (see e.g. Ref. [124]).

The existing literature, however, shows a clear gap in the knowledge of the real green-house gas (GHG) emissions associated with the production and the use of electricity. In particular, there is a lack of studies clearly addressing GHG emissions produced across the whole life cycle of electricity production and use, including upstream emissions, operational and use-related emissions. In addition, few evaluations are available for the construction and decommissioning related emissions of the electricity generation facilities.

In the present work we use recently published (i.e. 2022) consumption figures by Scarlat and coworkers [105], who adopt a Well-to-Wheel (WTW, see Ref. [125]) methodology considering all the emissions that occur along the entire pathway, from fuel supply to the power plant, construction of the electricity generating facility, operational phase, plant decommissioning and waste management.

Further, the methodology proposed by the authors considers the impact of electricity trade (intra-country electricity imports and exports) on the carbon intensity that can impact considerably the CI of the electricity used, but which is in general not considered so far in existing assessments of the CI of electricity (see also Ref. [125] and [126]). Furthermore, the proposed methodology considers all sources of electricity, including renewable energy sources, type of plants, conversion efficiencies, own electricity consumption in the power plant, as well as transmission and distribution losses in the grid. The CI figures for the electricity consumption at the LV grid used in this work are listed in Table 3.1 and 3.3 for all EU27 member states and other European countries. These numbers reveal significant variations between countries.

### 3.2.4   Caveats: BIPV and moving targets

In this section, and before presenting the results, we want to highlight a few shortcomings of our analysis. Firstly, when considering the integration of PV in buildings (or more in general in infrastructures), we generally differentiate between Building-Applied PV (BAPV) and Building-Integrated PV (BIPV). This distinction is generally not clear to the layman. In the case of a rooftop installation, for example, a BAPV system is added on top of an existing roof. In the case of BIPV, the PV system is fully integrated into the building envelope, therefore replacing (and providing the functionalities) of a building element, as tiles in a roof.

In the case of full integration (i.e. BIPV), the PV modules are therefore replacing some building elements (the roof tiles of our example) that have an embedded carbon-footprint related to the materials and processes used in manufacturing them. This should ideally be considered and balanced by offsetting the CI of the PV system with that of the replaced building element. Therefore, allowing to further reduce the CI of actual BIPV systems. On the other hand, BIPV modules may often have a lower total-area efficiency (depending on cell and edge spacing) or in some cases (mostly in façades, to become complaint with building regulations) may require the adoption of much thicker cover glasses, which would successively require the adoption of more robust mounting structures, in turn partly penalizing the carbon-footprint of BIPV when compared to conventional PV modules and systems. The energy yield of BIPV solutions

(and consequently the CI of the electricity generated by them) may also be penalized by the adoption of coloring techniques (or other transformative approaches).

In addition, the full integration of PV in the building skin generally exposes the modules to higher operating temperatures that to a given extent penalize the energy yield of the PV system, if compared to a free-standing or to a partly-ventilated BAPV system. Similarly, the operation of PV systems in the built environment (which statistically are more affected by the presence of shading, compared to ground-mounted plants) may in some cases considerably penalize the energy yield of the system [127].

In this work, to avoid adding excessive complexity and keep the right focus on our primary research question (i.e. is the integration of PV in sub-optimal orientations justifiable from a carbon-balance perspective?), we do not differentiate between BAPV or BIPV systems. We are therefore: (1) neither offsetting the carbon-footprint of BIPV modules when they are replacing other building elements; nor, when applicable, (2) penalizing the energy yield of the PV system due to a full building integration.

Secondly, the numbers on which our analysis relies on (i.e., the CI of PV and of the national electricity mixes) are both understandably moving targets. It is important to note that while the reference data is sourced from recent publications, it is derived from information more than 5 years old. Consequently, we anticipate that the CI values will likely be lower than those presented in this work.

In Section 3.2.2 we have discussed how the CI of PV can be reduced in the future by further technological progress or -already today -by moving PV manufacturing - particularly the most upstream processes of silicon, wafer and solar cell manufacturing - in countries using electricity with low carbon (C) footprints. This has led us to propose in this work a "greener-PV" scenario for 2030 or beyond, in which the present CI of PV is halved. This scenario is within reach, but will highly depend on: (a) the ability of moving a considerable portion of global PV manufacturing outside of China, in countries using electricity mixes with a much lower C footprint than that presently used in China today; or (b) rely on a very rapid transition in China towards a low-carbon electricity mix, a target that does not presently seem to be in sight, despite the considerable progresses made in the country in the last decade.

Analogously, the carbon intensity of electricity shows on average a clear reduction trend since 1990 for most European countries. In the European Union (EU27), the carbon intensity of the electricity used at low voltage decreased from 641 $gCO_2eq/kWh$ in 1990 to 334 $gCO_2eq/kWh$ in 2019 [105]. This trend is expected to continue in the coming years, particularly in view of the 2050 carbon-neutral targets presently under discussion.

We are therefore aware that with this analysis, we are taking a snapshot of the current situation and that the estimates presented in this work will have to be fine-tuned at regular intervals in the coming future. Nevertheless, in view of the massive integration of PV in the built environment, the outcome of this work clearly indicates that already today in the vast majority

of European countries solar electricity is certainly a cost-effective and reliable technology that can be a key enabler for full decarbonization of the energy sector.

## 3.3 Results

### 3.3.1 Solar resources and PV system energy yield

For three different cities spanning most latitudes in Europe (Malta, Milan, Oslo), Figure 3.2 shows the ratio of H and EY for different PV system exposures, normalized over the same parameters calculated for an optimal exposure, i.e. south-facing at S-opta. This includes values for a flat roof (flat), for an average rooftop PV installation (Avg roof), and for installation facing the different cardinal points at 45°- and 90°- (façades) tilt, respectively. Avg roof values represent an average value for PV systems integrated or applied onto rooftops applying a constant 17% loss rate, which accounts for misalignment with respect to an optimal exposure (i.e. S-opta). This loss rate is computed by averaging the yearly EY of a south-, west-, and east-facing PV system at 45°-tilt.

With respect to an optimal PV energy yield, as can be observed in Figure 3.2, the potential of façades in Europe varies from 60% to 76% for Malta (35°N) and Oslo (60°N), respectively, for S-facing façades; from 46% to 49% (idem) for façades with a W and E orientation; and from 13.1% to 17.6% (idem) for N-facing façades. The corresponding values for Milan (45°N) lie between these two extremes. Differences between E and W orientations are generally low and, for a given location, may be due to the presence of different horizons, weather conditions or far-shading. Similarly, for a mid-latitude city as Milan, the difference in the yearly electricity generated of a PV system installed in a flat roof or for an avg-roof is negligible. This difference is slightly larger in Oslo or in Malta, but as a first approximation, we can consider the two values to correspond. In the following, for conciseness we will present data for flat roofs only.

### 3.3.2 Carbon balances

Out of the different capital cities listed in Table 3.1, we select three cities representative of three different cases:

(a) Oslo: a high-latitude city (60°) with a low insolation (1'130 kWh/m$^2$·y) and a very low CI of the national electricity mix (31 gCO$_2$-eq/kWh);

(b) Bratislava: a mid-latitude city (48°) with the insolation of a typical Central European location (1'509 kWh/m$^2$·y) and the CI of the national electricity mix (346 gCO$_2$-eq/kWh) close to the European average (i.e. 374 gCO$_2$-eq/kWh);

(c) Athens: a Mediterranean city (38°) with relatively high insolation (1'932 kWh/m$^2$·y) and high CI of the national electricity mix (780 gCO$_2$-eq/kWh);
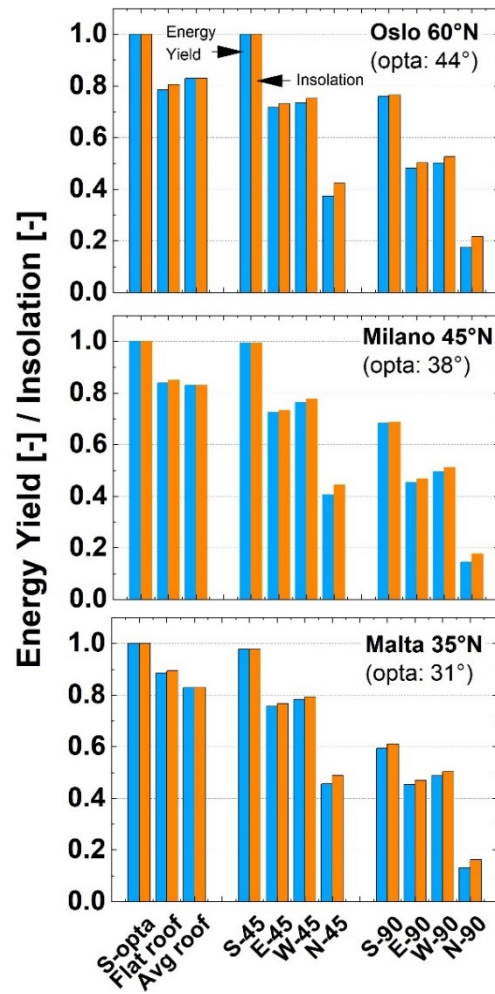
**Figure 3.2:** Solar resources and PV energy yield (three cities). Ratio of the insolation H [kWh/m$^2$·y] (orange) and the yearly energy yield EY [kWh/kW$_p$·y] (blue)) of a PV system for different exposures normalized over the same parameters calculated for an optimal orientation (S-opta) for three cities in Europe located at different latitudes.

Understandably, as can be inferred by the data in Table 3.1, Oslo and Athens represent two extreme cases, whereas the results for Bratislava are representative of a large number of European cities and countries. For these three cities we compute:

1. The cumulative energy yield (MWh/kW$_p$) generated by a PV plant under the assumption of a 30-year-long service lifetime (and an annual degradation rate of -0.7%/y);

2. The amount of $CO_2$ that would be emitted by the same plant over the same lifespan using current PV CI figures (PV-2021) and under a scenario with reduced PV GHG emissions (greener-PV). These values are compared to - and normalized over - the amount of $CO_2$ that would be emitted to generate the same amount of electricity using the present CI of the local electricity mix.

The results are presented in Figure 3.3 for these three cities. For Oslo it becomes obvious that a carbon intensity balance is not in favor of PV, not even for good system exposures (i.e. S-opta, flat, S-90°). This situation would change in the greener-PV scenario with a reduced CI of PV, for which only E-, W- and N-facing façades would not be fully justifiable from a carbon-balance perspective.

On the contrary, in Bratislava, and understandably even more in Athens, the carbon balance is largely in favor of PV, even - and not without a surprise - for the N-facing façade. In the case of S-opta and N-90° PV installations in Bratislava, the carbon emissions would correspond to only 10% and 62% of that that would be emitted over the same lifespan using the present CI of the national electricity mix. In Athens the corresponding ratios would be only 3% and 24%, respectively, and in Oslo 146% and 830%.

In the previously mentioned greener-PV scenario, a reasonable target for 2030, all these figures would be halved. Therefore, in Bratislava, Athens and the vast majority of European countries (as demonstrated in the next section), even a N-facing PV façade (receiving on average only approximately 15% of the yearly cumulative irradiance received by a surface with an optimal exposure) can be fully justified if a carbon-balance perspective is considered.

### 3.3.3   Carbon intensity of PV vs national electricity mixes

By adopting the same methodology and dividing the lifetime $CO_2$ emissions of a PV system (which are nearly entirely attributable to the manufacturing of the different components, with a smaller contribution from their shipment) over the energy yield [kWh/kW$_p$·y] of the PV system installed at different exposures, we are able to compute the CI of PV for the different capital cities of Table 3.1.

The carbon intensity of PV in the different capital cities as a function of the CI of national electricity mixes for all European countries is presented in Figure 3.4 for different orientations and tilts: i. south orientation at optimal tilt (S-opta); ii. flat roof; iii. 90°-tilt façades with orientation to the south (S-90°), to the west (W-90°) and to the north (N-90°). Results for east-facing façades are generally very similar to west-facing ones and are therefore omitted. The dashed line corresponds to a CI of PV = CI of electricity mix. For the points (i.e. countries and orientations) lying above or below the dashed line, PV has a larger or lower CI, respectively, when compared to the current electricity mix of the specific country.

Figure 3.4 (a) is divided into three sections, which are then magnified for more clarity. Fig. 3.4 (b) shows the low end of the abscissa scale (0-300 gCO$_2$-eq/kWh). In this chart a restricted subsection of countries (AL, IS, NO, SE) lies above the straight line for all orientations, although only slightly for the S-opta orientations. These countries (with the exception of Albania) are all high latitude countries with low CI electricity mixes due to a large use of renewables (and some nuclear in the case of Sweden). For another restricted group of countries (CH, FR, FI, DK) with low CI electricity mixes, PV is below the threshold (dashed line) for all orientations
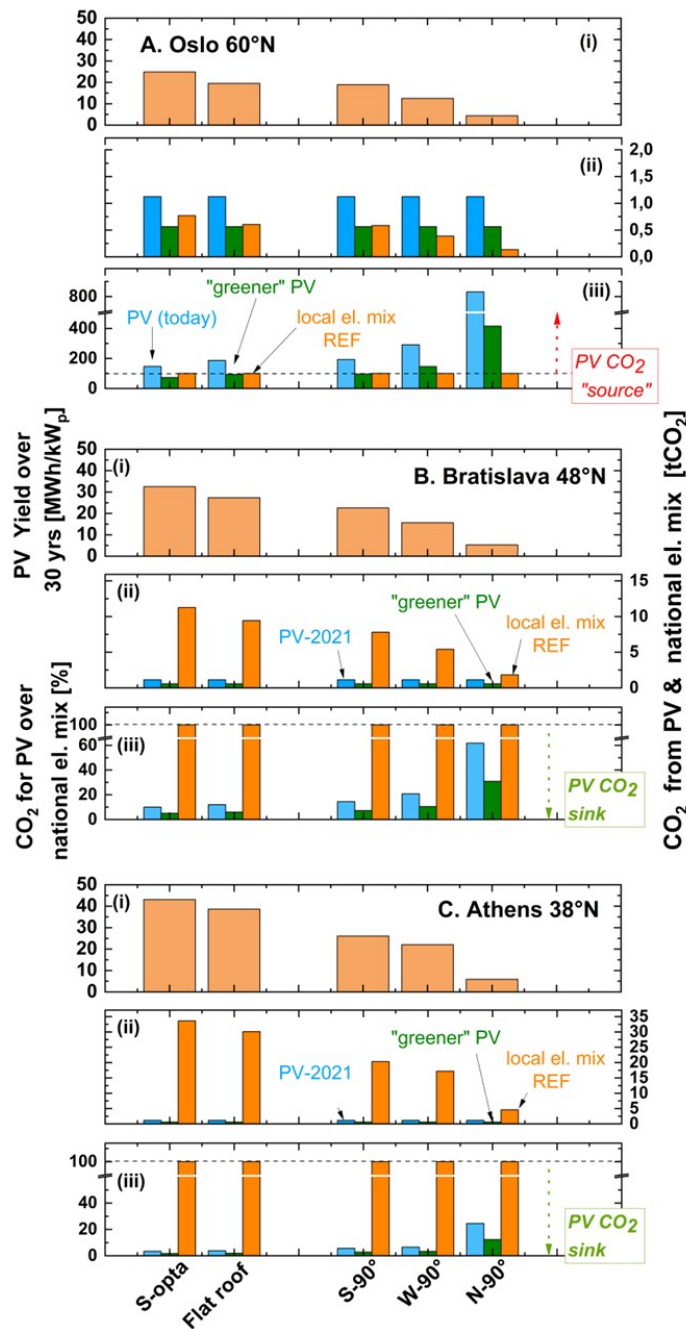
**Figure 3.3:** Carbon emission of PV vs local electricity mix (three emblematic cases). A. Oslo (60°N); B. Bratislava (48°N); C. Athens (38°N). (i) Cumulative energy yield (kWh/kW$_p$) over 30 years – as a function of different orientations - for a PV system; (ii) shows the amount of $CO_2$ that would be emitted by the same plant over its service lifetime using current PV CI figures (PV-2021) and under a scenario with a reduced (i.e. 50%) PV CI (greener-PV). The amount of $CO_2$ that would be emitted to generate the same amount of electricity using the CI of the national electricity mix is shown as well for a comparison (orange bars), and is used to normalize the corresponding values in (iii). The results for an E-facing facade are well aligned to the case of a W-facing façade and are therefore omitted.

with the exception of the N-facing façade. The other countries in this portion of the original chart (BE, AT, ES) all lie below the dashed line for all orientations, including N-facing façades. Meaning that in these countries the carbon footprint of the electricity generated by a N-facing PV façade over its entire life span (i.e. 30 years) is already lower than that of the local electricity mix.

This is the same situation for all the countries lying in Figure 3.4 (b) (abscissa: 300-600 $gCO_2$-eq/kWh), where most countries are represented, and (c) (abscissa: 600-1000 $gCO_2$-eq/kWh), which represents countries with very large CI of electricity mixes, largely due to an extensive use of coal.

The same values of Figure 3.4 are listed in Table 3.3 and - normalized over the CI of the national electricity mixes - summarized in Table A.1.
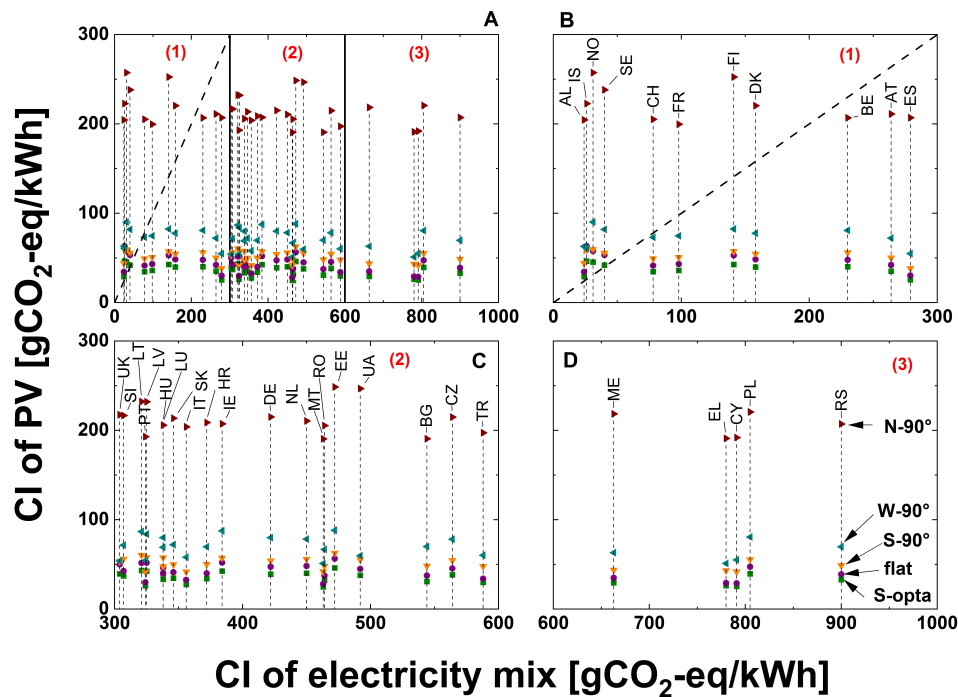


**Figure 3.4:** Carbon emission of PV vs local electricity mix (all Europe). Carbon intensity of PV in the different capital cities vs the CI of national electricity mixes for all European countries as a function of different exposures (orientation and tilt): i. south orientation at optimal tilt (S-opta); ii. flat roof; iii. 90°-tilt façades with south- (S-90°), west- (W-90°) and north-orientation (N-90°). Results for E-facing façades are very similar to W-facing ones and are therefore omitted. Fig. 3.4 (a) is divided into three sections (1, 2, 3), which are magnified for more clarity. The dashed line corresponds to a f(x)=x line: i.e. for the points lying above or below the straight line, PV has a larger and lower CI, respectively, when compared to the electricity mix of the same country. Note that the four charts have the same scale in the ordinates but differ in the abscissas. In the greener-PV scenario (for 2030 and beyond) all values for the CI of PV would be halved (see Figure 3.5 (A)).

**Table 3.3:** Carbon intensity of the national electricity mixes (i.e. consumption figures at the low-voltage grid), compared to that of PV in the different capital cities of EU-27 member-states and other European countries as a function of different exposures (orientation and tilt): i. south orientation at optimal tilt (S-opta); ii. flat roof; iii. 90°-tilt façades with orientation to the south (S-90°), to the west (W-90°) and to the north (N-90°). Results for E-facing façades are very similar to W-facing ones and are therefore omitted. The last row presents the mean values of the distributions. The same values – normalized over the CI of the national electricity mix – are listed in Table A.1. In the greener-PV scenario all values for the CI of PV would be halved. The same values – normalized over the CI of the national electricity mix – are listed in Table A.1.

| Country code | Capital | CI elect. mix [gCO$_2$-eq/kWh] | S-opta [gCO$_2$-eq/kWh] | Flat roof *[idem]* | S-90° *[idem]* | W-90° *[idem]* | N-90° *[idem]* |
|---|---|---|---|---|---|---|---|
| AT | Vienna (48.2N, 16.4E) | 264 | 35.1 | 42 | 50.2 | 72.2 | 211 |
| BE | Brussels (50.8N, 4.4E) | 230 | 40.1 | 47.9 | 56 | 80.8 | 206.9 |
| BG | Sofia (42.6N, 24E) | 544 | 30.8 | 37.4 | 48.1 | 69.9 | 190.6 |
| CY | Nicosia (35.1N, 33.2E) | 791 | 25.5 | 28.9 | 41.8 | 55.1 | 192 |
| CZ | Prague (50N, 14.5E) | 564 | 38.3 | 45.5 | 54.4 | 78.1 | 214.8 |
| DE | Berlin (52.5N, 13.4E) | 422 | 39 | 47.3 | 54.2 | 79.9 | 215.1 |
| DK | Copenhagen (55.7N, 12.6E) | 158 | 39.8 | 48.3 | 54.5 | 77.6 | 220.5 |
| EE | Tallinn (59.4N, 24.8E) | 472 | 46 | 56.5 | 62.8 | 88.1 | 248.6 |
| EL | Athens (38N, 23.7E) | 780 | 26.1 | 29.1 | 43.2 | 51.1 | 191.1 |
| ES | Madrid (40.4N, 3.7W) | 279 | 25.5 | 30.4 | 38.3 | 54.8 | 207 |
| FI | Helsinki (60.2N, 24.9E) | 141 | 42.6 | 52.9 | 57.3 | 82.5 | 252.5 |
| FR | Paris (48.9N, 2.3E) | 98 | 36 | 43.2 | 50.7 | 74.7 | 199.7 |
| HR | Zagreb (45.8N, 16E) | 372 | 34.1 | 40 | 50.2 | 69.8 | 208.8 |
| HU | Budapest (47.5N, 19.1E) | 338 | 33.3 | 39.9 | 47.6 | 69.2 | 205.8 |
| IE | Dublin (53.3N, 6.3E) | 384 | 42.5 | 52 | 57.1 | 87.5 | 207.4 |
| IT | Rome (41.9N, 12.5E) | 356 | 27.6 | 32.6 | 41.8 | 58.1 | 204 |
| LV | Riga (56.9N, 24.1E) | 325 | 42.3 | 51.8 | 57.7 | 83.8 | 232 |
| LT | Vilnius (54.7N, 25.3E) | 321 | 43.2 | 51.5 | 60.5 | 86.7 | 232.2 |
| LU | Luxembourg (49.7N, 6.1E) | 338 | 39.7 | 46.2 | 57.6 | 79.9 | 205.7 |
| MT | Valletta (35.9N, 14.5E) | 463 | 25 | 28.2 | 42 | 51.1 | 190.4 |
| NL | Amsterdam (52.4N, 4.9E) | 450 | 40.1 | 48.2 | 55.9 | 78.2 | 210.6 |
| PL | Warsaw (52.2N, 21E) | 805 | 39.4 | 47.3 | 55.3 | 80.7 | 220.5 |
| PT | Lisbon (38.7N, 9.1W) | 324 | 26.1 | 30 | 41.8 | 54.3 | 193 |
| RO | Bucharest (44.4N, 26.1E) | 464 | 32.2 | 37.5 | 48.2 | 66.9 | 205.4 |
| SK | Bratislava (48.1N, 17.1E) | 346 | 34.6 | 41.2 | 49.9 | 72 | 213.6 |
| SI | Ljubljana (46N, 14.5E) | 307 | 37.2 | 42.6 | 56.2 | 71.5 | 216.6 |
| SE | Stockholm (59.3N, 18.1E) | 40 | 41.9 | 53.2 | 55.6 | 81.9 | 238.2 |
| IS | Reykjavik (64.1N, 21.9W) | 26 | 46.4 | 63.3 | 58.7 | 60.6 | 222.8 |
| NO | Oslo (59.9N, 10.6E) | 31 | 45.3 | 57.7 | 59.6 | 90.2 | 257.4 |
| CH | Bern (46.9N, 7.4E) | 78 | 34.7 | 41.3 | 49.4 | 73.1 | 205.2 |
| UK | London (51.5N, 0.1W) | 304 | 39.4 | 50 | 53.5 | 54 | 217.5 |
| UA | Kiev (50.4N, 30.5E) | 492 | 37.8 | 45 | 55.4 | 59.7 | 246.7 |
| RS | Belgrade (44.8N, 20.4E) | 900 | 33 | 38.9 | 48.7 | 69.7 | 207.1 |
| AL | Tirana (41.3N, 19.8E) | 24 | 29.3 | 34.3 | 44.1 | 62.9 | 204.4 |
| ME | Podgorica (42.4N, 19.3E) | 663 | 29.4 | 34.9 | 43.7 | 63.1 | 218.5 |
| TR | Istanbul (41N, 29W) | 588 | 30 | 34 | 47.9 | 60.3 | 197.4 |
| Mean (all) | - | 374.5 | 35.8 | 43.1 | 51.4 | 70.8 | 214.2 |
| Mean (greener-PV, 2030+) | | | 17.9 | 21.5 | 25.7 | 35.4 | 107.1 |

The data of Table 3.3 (and Figure 3.4) are rearranged in Figure 3.5 showing the probability distribution (and box and whisker plots) of the CI of PV systems for all exposures and all European countries. These distributions are primarily affected by the different availability of solar resources in the different capital cities and are largely symmetric. The mean values of the distributions are listed in the last line of Table 3.3. For the same countries, Figure 3.5 (b) compares the same set of values to the present distribution of the CI of national electricity mixes. In the greener-PV scenario – a target potentially at reach for 2030 (see Section 3.2.2) - all values for the CI of PV would be halved.

Finally, for the different European countries Figure 3.6 shows the CI of the national electricity mixes plotted as a function of the yearly cumulative irradiance for an optimally oriented PV system (S-opta) in the capital city of that country. In the plot, the two dashed lines correspond to the mean values (taken from Table 3.3) of the CI distributions for PV in a West- (70 $gCO_2$-eq/kWh) and North-facing façade (214 $gCO_2$-eq/kWh) and help us divide the chart into three sub-sections: (1) a very restricted pool of countries (four and labeled: (PV) not in the first place) for which the CI of PV is slightly higher (even at the optimal exposures) when compared to the CI of the national electricity mix; (2) a similar number of countries for which only an installation in N-facing façades would lead to a higher CI for PV (i.e. No N-facing (PV)); (3) the vast majority of the countries (i.e. PV everywhere) or which PV would act as a net carbon sink irrespective of the exposures (including N-facing façades).

These results clearly indicate, not without surprise, that for the vast majority of European countries a N-facing PV façade would not penalize a transition towards a carbon-neutral electricity mix and would therefore be fully justified if a carbon balance perspective is considered.
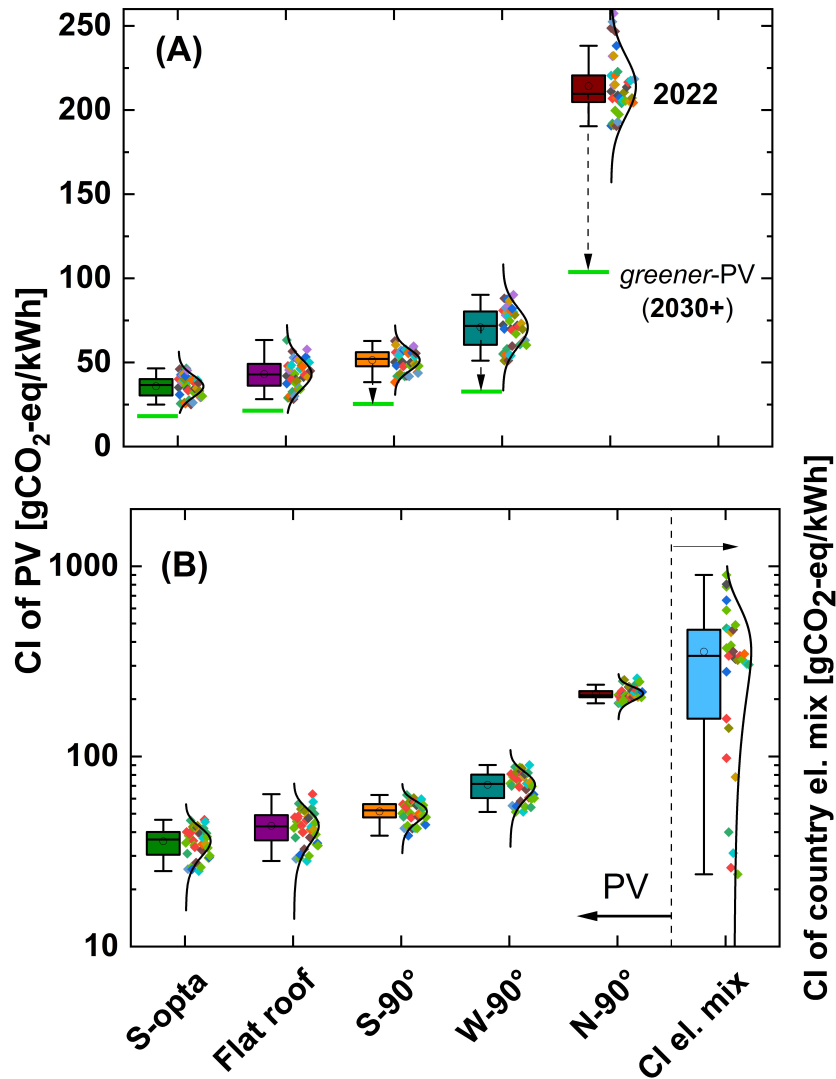
**Figure 3.5:** Carbon emission of PV vs local electricity mix (all Europe). (A) Probability distributions (and box and whisker plots with mean, median, and quartiles) of the CI of PV systems for all orientations and all European countries. The distribution is largely affected by the different annual insolation levels of the different capital cities. In the greener-PV scenario all values for the CI of PV would be halved (for more clarity only the mean values of the distributions are shown). The same values are compared in (B) to the distribution of the CI of national electricity mixes (note: the scale of the y-axis is here logarithmic).
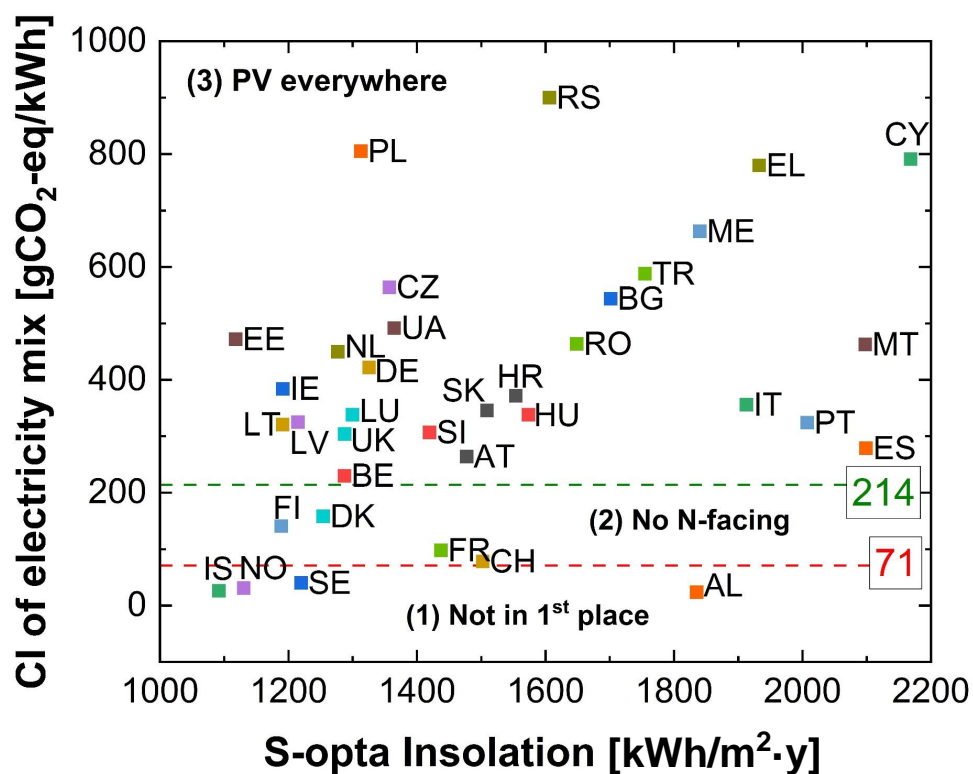
**Figure 3.6:** Where does PV go first? CI of the national electricity mix as a function of the yearly cumulative irradiance for an optimally oriented PV system (S-opta) in the capital city of that country. The two dashed lines correspond to the mean values for European countries of the CI distributions for PV in a W- (71 gCO$_2$-eq/kWh) and N-facing façade (214 gCO$_2$-eq/kWh), highlighting three sections: (1) (PV) not in the 1st place; (2) No N-facing (PV); (3) PV everywhere.

## 3.4   Discussion and recommendations

### 3.4.1   PV at sub-optimal orientations

Massive integration of solar electricity in buildings and infrastructures will need to be pursued through the integration of PV onto/into surfaces with sub-optimal orientations, as the availability of ideal surfaces will understandably be limited, or not possible because of the presence - for example - of persisting shading. If we focus on buildings or infrastructures, several reasons may lead us to promote the integration of PV in façades:

1. South-facing PV façades (or high-tilt orientations) have a more stable generation profile throughout the year, as shown in Figure 3.7 (a) which plots the monthly generation profile – as a function of different orientations and tilts - for a 1 kW$_p$ PV system located in Milan (Italy, 45° N). This helps maximizing PV production in winter [128] – a season in which several mid- or high-latitude countries may have shortages of supply from renewable energies – and prospectively reduce the impact of high PV generation in summer months during the central hours of the day.

2. East- or west-facing PV façades may help shaving and shifting peaks of PV generation throughout the day, generating power during periods of the day when the electricity may be more valuable, due to supply-demand imbalances, and potentially alleviating stresses to the grid that may arise during the periods of high PV electricity injection into the grid (i.e., summertime at midday). The hourly generation profile on the 21st of March of a 1 kW$_p$ located in Milan is shown in Figure 3.7 (b), clearly highlighting that, despite the lower daily electricity production, E- and W- facing façades maximize the generation of electricity in the early and late hours of the days, respectively.

3. North-facing PV façades: as shown in the previous Section, carbon footprint considerations for PV tell us that solar electricity today is fully justifiable in the vast majority of European countries and for most orientations, including – most of the time – north-facing façades, which receive on average only approximately 15% of the yearly cumulative irradiance received by a surface with an optimal exposure.

Finally, if we consider the countries that are placed in the two lowest quadrants of Figure 3.6, the CI of PV compared to the CI of local electricity mix, may serve as a first (but not unique) discriminant to incentivize the adoption of PV in buildings and infrastructures, pointing out that in countries with a low CI of the national electricity mix - and massively relying on nuclear power for their electricity supply (e.g. France, Switzerland, Sweden, . . .) - other elements should simultaneously be weighted. Citizens in these countries may in fact oppose the use of a technology (nuclear fission), which will leave a huge burden and dangerous legacy to the coming generations in terms of disposal of nuclear fuels and infrastructures and of the costs needed for the decommissioning of the nuclear power plants. In addition, in countries planning nuclear phase-outs (e.g. Germany, Switzerland,. . .) PV will clearly be in the future a
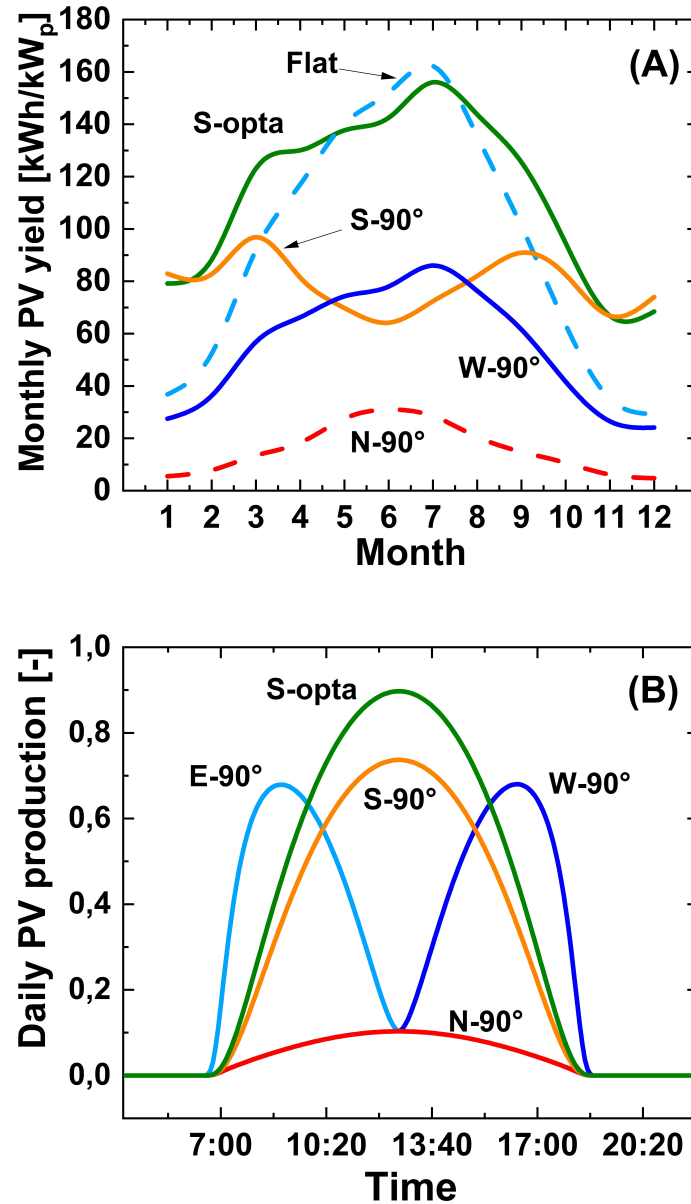
**Figure 3.7:** Monthly and daily generation profiles of PV for different orientations. (a) Average monthly electricity generation of a 1kW$_p$ PV system installed in Milan (Italy, 45° N) as a function of different orientations and tilts; (b) hourly generation profile (in arbitrary units) on the 21st of March for the same plant as a function of different orientations and tilts (source: JRC's PV-GIS [104]).

valid alternative to other energy sources to lower or preserve a low CI budget of the national electricity mix.

Finally, we should mention the abundant material availability for photovoltaics. Hence, installations penalizing energy-yield should not be avoided. This understandably would not be the case if the production of silicon or panels was limited. However, we should optimize the PV production and only install the amount needed. The cleanest source of electricity is the one that is not produced.

### 3.4.2 Colored PV

Colored PV can increase the acceptance among building owners and aid in meeting construction codes. As proposed in this chapter within the context of a greener PV scenario, we anticipate a further reduction in the carbon intensity of PV as the electric grid decarbonizes. This provides additional reasons, from a CI perspective, to consider adopting colored PV solutions. While these solutions may, on one hand, penalize $CO_2$ emissions compared to higher efficiency technologies, they, on the other hand, increase acceptability and market attractiveness.

For instance, in an extreme case, a white PV system typically experiences a 40% reduction in efficiency [129], leading to a roughly 35% decrease in energy yield due to less heating. This results in an approximate 54% increase in CI. For PV systems with low-intensity colors, such as a terracotta, which may reduce the efficiency by 20% and the energy yield by 18%, the carbon intensity would increase by 22%. These increases in CI remain reasonable for most scenarios, making colored PV a viable solution for implementation.

Furthermore, ongoing developments in colored PV technologies aim to reduce $CO_2$ emissions and mitigate power losses in PV modules, as discussed in this thesis.

### 3.4.3 Challenges and solutions

We would simultaneously like to put some emphasis on the fact that the massive integration of PV in urban and building contexts will pose some threats in terms of:

1. PV system design;

2. Potential grid imbalances and infrastructure investment costs.

**PV system design**

A massive integration of solar PV in the built environment may require the adoption of different PV plant design practices, such as:

(a) The adoption of micro-inverters or power optimizers (i.e. DC-DC converters) to minimize the impact of shading on the energy yield of PV arrays: Despite the impact on the

energy yield, the constant solicitation of by-pass diodes may lead to diode failures and potentially lead to the generation of hot-spots in modules that are exposed to frequent or persisting shading. The integration of module-level electronics or the development of shading-tolerant modules may therefore allow a smoother operation of solar arrays installed in buildings or more in general in urban contexts.

(b) Because a PV array rarely produces power close to its STC (standard test conditions) DC rating, it is common practice and economically advantageous to size the AC power of the inverter to be lower than the DC power of the PV array. This ratio of PV array to inverter power is called the DC/AC ratio and it is a good practice to vary it from 1.1 to 1.25. If the PV array generates more energy than the inverter can handle, the inverter will reduce the voltage of the electricity and limit the power output. This mechanism and the consequent power loss are known as clipping. Certainly, the DC/AC ratio for the integration in surfaces with a sub-optimal orientation may be much more aggressive and speculatively vary from 1.5 to 2 for east/west facing and north facing façades, respectively.

**Potential grid imbalances and infrastructure investment costs**

The full coverage of roofs in residential areas is expected to require, in many cases, an important and costly reinforcement of the LV grid infrastructure. The latter is in general dimensioned to cope with the potential maximum electric load, but is not designed to sustain high PV generation peaks, especially when the electric consumption is low. High reverse power flows at the MV to LV transformer, exceeding the latter rated limits, and overvoltage situations are emblematic effects of large PV penetration [130]–[132]. Installation of PV on most façades is expected to exacerbate the situation and further stress LV grid operation. Fortunately, as shown in Figure 3.7 (a), roof-top and façade PV systems do not exhibit their maximum power at the same time, reducing the magnitude of the grid impact. S-facing façade production maximum takes place during the winter season when roof-top production is reduced. W- and E- facing façades show their maximum in the afternoon, respectively in the morning, when again roof-top production is lower.

On the other hand, the detrimental effect of the high PV penetration on the LV operation and needs for grid reinforcement can be mitigated by different solutions. Curtailments of the PV production by limiting the power that can be injected in the LV grid at all time is the cheapest measure to implement [133]; a relatively severe curtailment can be implemented without affecting too much the yearly production of a PV system. A limit of the injection set at 50% of the PV nominal power only affects the yearly production, in many cases, by less than 10% [131], [134]. Reactive power control is another solution to increase PV hosting capacity [131], [135]. As an alternative solution, electricity tariffs, on the import and export (i.e. feed-in tariff), can be tailored to reduce PV surplus injection, improving the self-consumption and, incentivizing the deployment of local electricity storage [136]. The latter can be provided by a central grid battery, but this option is currently costly and does not alleviate all grid limitations (beside the

one set by the MV to LV transformer) or using distributed storage systems at the building level [131], [137]. Storage can be provided by electro-chemical batteries or in the form of thermal storage (e.g. water tanks for the domestic hot water) or by using thermal inertia of building when heating or cooling [138]].

Additionally, other form of demand-side management can be implemented to use PV surplus [131], [134]. As an example, the deployment of electric mobility is expected to offer much of the flexibility needed for a large penetration of PV. As most of the cars are idle most of the time, their large battery capacity could be used for the storage of excess PV production and therefore use to minimize the impact on the grid [139], [140].

Renewable energy communities [11], [141] and microgrids have also been proposed to help integrate PV at the level of LV grids [142], [143].  Energy communities help increasing self-consumption by balancing production and consumption, benefiting of the aggregation of the latter. While such communities offer an easier management of the energy flows to balance production and consumption and potentially attractive economics (for these communities), they do not offer considerable advantage in terms of PV hosting capacity (in comparison to the solutions already mentioned) and marginally reduce exchanges at the transformer level. Nevertheless, they reduce the overall size of energy storage or flexible assets (total capacity for the LV grid) for optimized operation.  In short, they modify the grid operation without modifying substantially the total energy exchanged between LV and MV grids.

In addition, one should note that the impact of a large PV deployment on façades is expected to be low on MV grid. PV systems in façades are in general smaller than the ones on rooftops and connected to LV grids. Large system connected to MV include mostly industrial or large commercial sites with large self-consumptions and reduced grid injections.


### 3.4.4   Recommendations for policy makers

With over 90% of European rooftops and façades unused, a strong need for regulations that encourages all new and renovated residential, tertiary, commercial, and industrial buildings - including infrastructures - in the EU to include PV systems is necessary. By 2050 (or better earlier) these systems need to be installed on every appropriate rooftop (or façade) to enable all citizens to become active consumers. At the European level, policy drivers, such as the Energy Performance of Building Directive (EPBD) - amended in 2018 and for which an additional revision is pending to reflect higher ambitions and the more pressing needs for Europe on how to achieve a zero-emission and fully decarbonized building stock by 2050 [10] - already exist, and are presently boosting the adoption of renewable electricity generation sources (mainly solar PV electricity) in the built environment. Particularly, in the case of new buildings and in the case of deep renovations. Member states impose directives at the national level, and the requirements are implemented (and can become more stringent) at the regional or municipal levels.

For this reason, based on the analysis presented in this work, we come out with a list of recommendations that should help local authorities adopting favorable building codes and the right policies (including proper incentive schemes) to foster and maximize the diffusion of PV in buildings and infrastructures. These include:

1. In most European countries, PV installations should be mandatory (in the case of new buildings and renovations) and incentivized by different means (being investment tax credits, feed-in tariffs, direct contributions or net metering schemes, etc.) for all the cases (building or infrastructure) when a surface is exposed to an insolation higher than 40-50% (net of shadows) of that of a south-facing surface exposed at an optimal tilt for a given location. This threshold should be country, or even region-dependent and should be tailored to allow the inclusion of E- and W- facing façades. Particularly, incentives are urgently needed for all the situations where such solar systems cannot contribute significantly to self-consumption (an incentive per-se), which considerably increases the return on investments for this kind of projects.

2. Exceptions to the mandatory installations of PV in buildings/infrastructures should be granted if the above criterium is not met, as well as in the case of impossibility for urban, architectural, or heritage reasons.

3. Installations in surfaces with less optimal orientations (e.g. N-facing façades) should possibly not be incentivized in the first place, but not expressly "prohibited" (or abandoned), as we have demonstrated that, in several countries, they are fully justifiable from a CI perspective. In addition, this may still help in promoting and creating PV-awareness among citizens, help architects in preserving building harmony/aesthetics, and push market deployment for BIPV and integrated PV (I-PV). Furthermore, they could still make sense from an economical perspective (not considered in this work) in the case of a new building or major renovation project, as they may avoid the adoption of different mounting structures and cladding elements for the different surfaces of the building. With consequently the possibility to simplifying and streamlining the overall building project. Economic considerations for sub-optimal orientations in buildings can be found in Ref. [94].

4. Finally, we firmly take a firm position against minimum requirements, as they are usually set in local codes. A recurrent limitation in existing municipal building codes is that of referring to minimal requirements expressed in terms of nominal capacity per building ground area (e.g. 2 kW$_p$ per 100 m$^2$). These requirements sometimes lead to the absurd situations where only limited-size PV systems are deployed in surfaces with a much greater potential. This situation is well represented in Figure 3.8, which shows an aerial view of a newly-built residential housing project recently realized in Canton Vaud (Switzerland). In this specific case, only 10 m$^2$ of solar PV was installed on most single-family houses when in reality 100+ m$^2$ (of well oriented PV) could have been installed on most roofs. The situation of such roofs will likely be locked-up for the next 30 years,

despite the optimal orientations and solar yield potential of all the neighbourhood. This image is therefore emblematic of a situation in which the integration of PV in a building project (or infrastructure) could have been maximized - due to the clear potential of the area - to avoid an unnecessary exploitation of land elsewhere. The philosophy behind requiring minimal requirements is fully understandable, but relevant incentives should be put in place – as discussed earlier - to consider this as a minimum threshold and incentivize citizens to maximize, whenever possible, the adoption of PV in the built environment.



**Figure 3.8:** Against minimal requirements. Aerial view of a newly built residential housing project recently realized in Bussigy (Switzerland). In this specific case, only 10 m$^2$ of solar PV was installed on most single-family houses – being fully compliant with the local building requirements - when in reality 100+ m$^2$ (of well oriented PV) could have been installed on most roofs (credits: Thomas Söderström).

## 3.5 Conclusions

To assess the meaningfulness of installing PV in surfaces with sub-optimal orientations, we consider a carbon intensity (CI) balance perspective and assess, for all European countries, whether – on a time horizon of 30 years – installing PV at different exposures acts as a net $CO_2$ sink or source, when compared to the same amount of carbon that would be generated over the same timeline using the local electricity mix.

The mean values obtained for the probability distributions of the carbon intensity of PV systems for all orientations and all European countries tell us that the CI of PV in buildings corresponds to 35.8 g$CO_2$-eq/kWh for an optimal exposure (i.e. south-orientation at optimal tilt). This value is slightly higher for an average rooftop installation (assuming a 17% loss factor for the energy yield for misalignments compared to the optimal exposure): 43 g$CO_2$-eq/kWh. The mean value of the distribution for façades corresponds to: 51.4, 71 and 214 g$CO_2$-eq/kWh

for, respectively, south-, west-/east-, and north-facing façades. The distribution (and the corresponding values for each city or country) is affected by the different annual insolation levels experienced by the different capital cities. These figures must be compared to the mean value of the distribution of the national electricity mixes, which is 374.5 $gCO_2$-eq/kWh (for all European countries in 2021) with a much broader distribution, reflecting the wide differences in the generation technologies adopted by the different countries.

These results clearly indicate, not without surprise, that for most European countries the integration of PV in façades (including most of the times N-facing PV façades) would not penalize - and conversely would still support - a transition towards a carbon-neutral electricity mix. It would, therefore, be fully justified taking a carbon balance perspective. Understandably, the numbers on which our analysis relies (the CI of PV and of the national electricity mixes) are both moving targets. This has led us to propose a greener-PV scenario in which the present CI of PV is halved by 2030 (or beyond). This scenario is not just a futuristic concept; it is already within our grasp for several compelling reasons. Primarily, the PV industry is rapidly transitioning to higher efficiency and thinner wafers, such as 130 microns for TOPCON solar cells, a significant departure from the base scenario's 170-180 micron thick PERC cells. Additionally, advancements in wafer sawing (with kerf loss now approaching 50-55 microns) and improvements in energy-intensive processes (like the Siemens process and crystal pulling) have rendered the originally used values outdated by potentially 20% to 30%.

Simultaneously, China is surpassing expectations in decarbonizing its electricity mix, particularly through the extensive deployment of wind and solar technologies, with an estimated capacity exceeding 230 GW by 2023. We are hence aware that with this analysis we are taking a snapshot at the current situation based on original life cycle assessment (LCA) values, which were likely accurate three years ago but have since become outdated. Consequently, the estimates presented in this work should be viewed as a worst-case scenario, with a need for periodic adjustments in the future as technology and industry practices evolve.

Based on this analysis, we come out with a list of recommendations that should help national and local authorities adopting favorable building codes and the right policies to foster and maximize the diffusion of PV in buildings and infrastructures. We also emphasize the fact the system design practices for façades may have to be adapted and that strategies like promoting self-consumption or adopting smart-tariffs may be a way to mitigate imbalances (and infrastructure investment costs) to the local medium- and low- voltage grids, in view of a massive penetration of solar electricity in urban environments.

We have shown in this chapter that PV systems with sub-optimal orientations are reasonable from a carbon intensity perspective for most European countries, and that colored solutions can also be justified. In the following chapters, we study the complexities of adding new elements into PV modules for aesthetic purposes, a fundamental topic for the incorporation of PV into the built environment. In particular, we investigate several aspects related to black metallic interconnects, how to manufacture fully black PV modules, their stability

under weather stressors, and color characterization under glass layers. Next, in Chapter 4, we will present the design, manufacturing, and performance of an equipment capable of automatically producing black-colored metallic interconnects, regardless of their size, shape, or orientation.

# 4 Customized Inkjet Equipment for Coating Metallic Interconnects of BIPV Modules

The work in this chapter is based on the following article submitted to a journal:

- A. Borja Block, A. Faes, A. Virtuani, C. Ballif, *Customized Inkjet Equipment for Coating Metallic Interconnects of BIPV Modules,* submitted to the Journal of Manufacturing Processes, 2023 [83].

## Abstract

The production of building integrated photovoltaic (BIPV) modules demands a combination of flexibility, automation, and precision engineering to create customized modules that replicate the aesthetic qualities of traditional building materials. Among the critical factors influencing the aesthetics are the metallic interconnects, including cell connectors and cross connectors, as they strongly reflect the light compared to solar cells and dark backsheet. However, there is currently a lack of manufacturing equipment capable of coating all metallic interconnects. In this study, we present the design and development of a specialized flexible inkjet equipment specifically designed for laboratory applications with the potential for scalability. This equipment enables the coating of metallic interconnects using UV-curable ink, regardless of their orientation, size, or position. The implemented vision system allows for precise locating and dispensing at a printing speed of 100 mm/s with a resolution of 1440 drops per inch (DPI). The equipment effectively modifies the appearance of all metallic interconnects with a position accuracy of 160 μm. Furthermore, the electrical performance of the inkjet coated solar cells strings is reduced by only 2% in the maximum power output ($P_{max}$) compared to reference strings, mainly due to a decrease of 1.5% in the short circuit current ($I_{sc}$). Increasing the surface energy of the metallic cross connectors with plasma gun treatment allows improved printing quality reducing the ink required to 1080 DPI. This study highlights the design process, calibration using software image processing techniques, potential enhancements, and scalability considerations, offering valuable insights into the manufacturing of inkjet printers with integrated vision systems. While the focus is primarily on BIPV applications, the findings

are relevant not only to this specific domain but also extend to other areas of application where dynamic printing flexibility is required.

## 4.1 Introduction

A production line for building integrated photovoltaic (BIPV) modules may differ significantly from a standard photovoltaic (PV) module production line. While both involve manufacturing PV modules, the BIPV production line focuses mostly on modules designed for seamless integration into building structures. In contrast, a regular PV module production line primarily produces standalone modules for installation on rooftops or in the field. The BIPV modules prioritize aesthetics and architectural integration, with today's designs that mimic traditional building materials such as glass, roofing tiles, facades [144], or at least often materials with dark appearance. This allows for visually appealing and harmonious integration with the overall building design. In comparison, regular PV modules prioritize standardization, efficiency and cost reduction.

The BIPV production line incorporates additional manufacturing processes to facilitate panel integration into building structures. This includes the use of specialized components not typically employed in standard PV production lines, such as colored glass, encapsulants, foils, and coating ribbons (see Figure 4.1). Close collaboration with architects, designers, and construction professionals is often required in BIPV manufacturing lines to ensure a perfect blending with the building's overall design. This necessitates customization, precision engineering, and flexibility in panel size, shape, and color variations that impact manufacturing costs [145]. In contrast, products and processes in conventional manufacturing lines are much more standardized requiring nearly no level of customization and allowing a true mass series production.

(A)  (B)
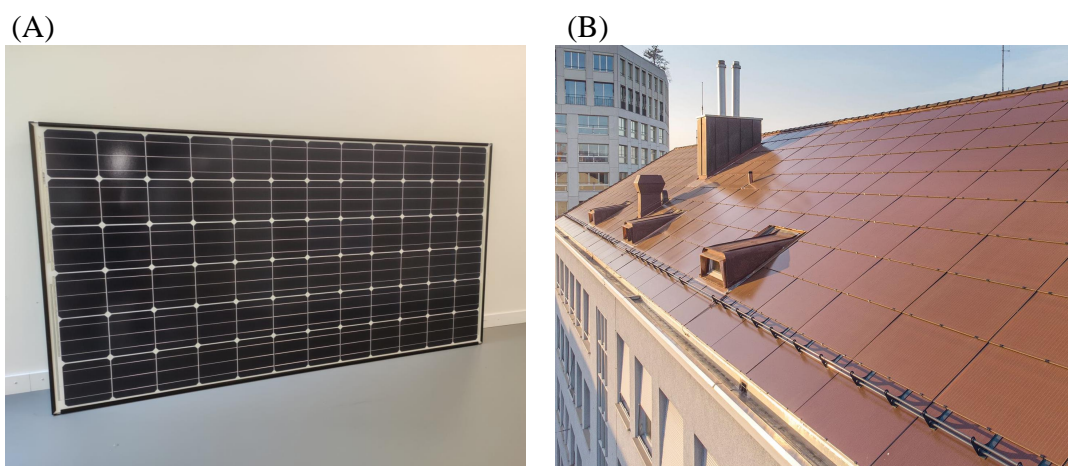


**Figure 4.1:** (A) PV module at EPFL PV-Lab with the common classic white rear side, striking blue solar cells and highly reflective metallization. (B) Terracotta BIPV modules installation installed in Zürich. Image courtesy of 3S Swiss Solar Solutions AG.

Metallic ribbons, also known as interconnects, may impact the visual appearance in PV modules construction and their aesthetics. These thin metal strips connect the arrays of solar cells within the module, extracting the current from the PV module. Two kinds of metallic ribbons exist, the cross connectors, which connect neighboring strings of solar cells, and the cell connectors that connect cells in series (see Figure 4.2). In general, the cell connectors are thin (approximately 1 mm) and placed on the top and rear side of solar cells while the cross connectors (approximately 5 mm wide) connect the string and eventually converge into the junction box. In addition to their functional role, metallic ribbons can contribute to the module's aesthetic appeal. Traditionally, interconnect hiding techniques involved manual application of colored strips or bands, which can be costly and cumbersome. However, coating metallic ribbons with ink can offer a solution to modify their appearance. Inkjet technology is well-suited for accurate and flexible printing [146]–[148], coating the bright metallic ribbons, even on the cell connectors [149]. Coating metallic ribbons with ink allows the uniform appearance architects often seek.
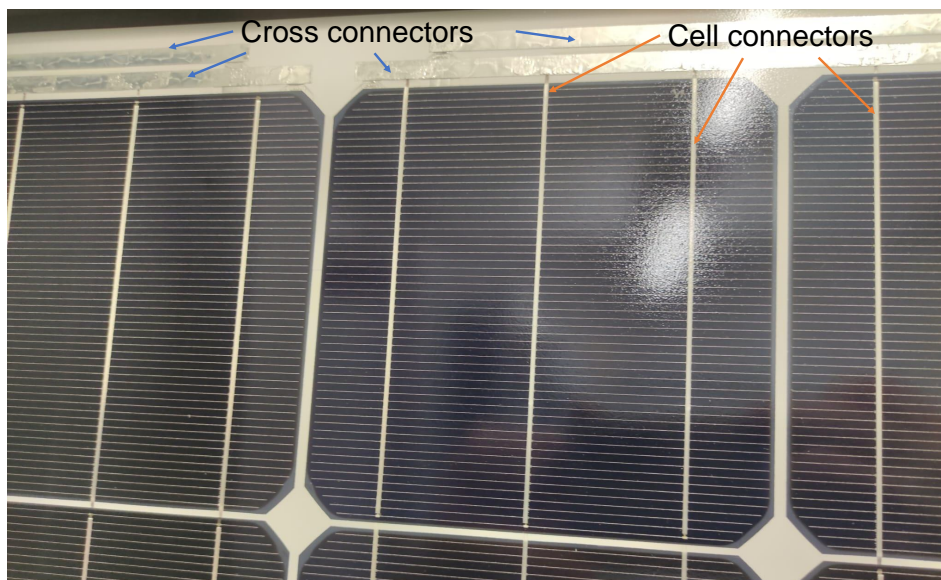


**Figure 4.2:** Typical PV module with white backsheet and dark blue solar cells. Two types of metallic ribbons appear, the cross connectors, indicated by blue arrows, and the cell connectors, highlighted by orange arrows.

Precoated black ribbons could be a suitable alternative. Nevertheless, using precoated black ribbons on the production line poses challenges. These ribbons undergo stretching, bending, soldering, and lamination processes at high temperatures (>300°C and 150°C, respectively), necessitating the black coating's ability to withstand such conditions while maintaining the production line's speed. An alternative approach involves the advanced inkjet printing of interconnects using UV-curable inks after the stringing and soldering of the solar cell array. Swift curing of the ink is essential, making UV curable inks an appropriate choice for this application.

Presently, there is a lack of manufacturing equipment capable of meeting the requirements of flexibility, speed, automation and accuracy of BIPV production. In this chapter, we introduce the design and construction of a customized equipment specifically designed for laboratory applications but with scalability potential, enabling the coating of metallic interconnects regardless of their orientation, size or position. We demonstrate its performance in terms of printing quality, accuracy, and power of solar cells after the inkjet coating step. Additionally, we discuss in Section 4.4, the challenges, areas for improvement, and potential for industrialization.

## 4.2 Material and methods

### 4.2.1 Design and manufacturing process

The design process, as illustrated in Figure 4.3, follows a well-defined methodology outlined by V. Borja and A. Ramírez [150]. It begins with the identification of the need, which may arise from either the customer or the industry. Afterwards, the conceptual design stage is initiated, where the initial product specifications are carefully considered. This stage involves multiple iterations to refine the design until a final prototype is achieved.

Following the conceptual design phase, the detailed engineering stage is undertaken to establish precise thresholds and values for the parameters associated with the conceptual design. This step bridges the gap between the theoretical concept and the practical implementation, ensuring that the design is feasible and can be effectively executed.



**Figure 4.3:** Conceptualization and design process flow used in the development of the prototype of the customized inkjet printer. Blue boxes indicate achieved milestones. Green-boxes prospective follow-up steps. The product specifications are iterated throughout the full process. What is relevant is that with the realization of a prototype (step 4) we have achieved the proof-of-concept.
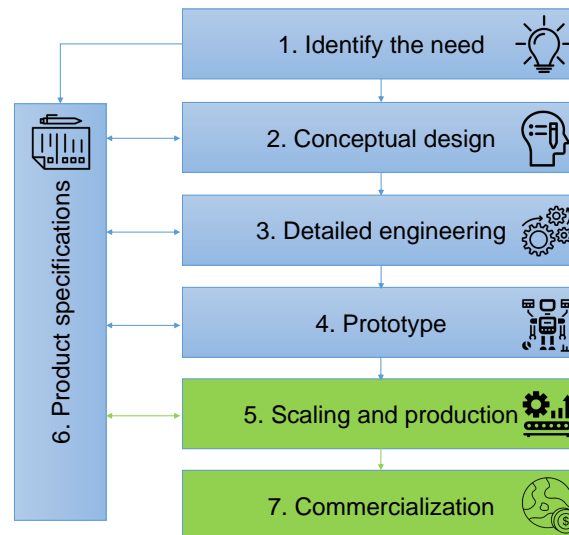
In this work, the primary objective was to enhance the appearance of the metallic interconnect (cell connectors and cross connectors) in order to achieve uniform black color in BIPV modules. The proposed solution needed to meet several critical requirements, including ease of scalability for production line integration, cost-effectiveness, and reliability.

The requirements and ranking, outlined in Table 4.1, were recognized during the initial stage of need identification. They were provided based on feedback from manufacturers of BIPV modules. It is important to note that some of these requirements may not be initially clear due to inherent trade-offs. For example, prioritizing fast coating could potentially compromise accuracy. Therefore, careful consideration and prioritization were necessary to define the product specifications. This constant feedback loop ensured that the requirements remained closely aligned with the final product specifications. In this work, we define accuracy as the distance of the target dispensed pixel with respect to the actual coated pixel after camera calibration.

**Table 4.1:** Main requirements for the prototype, ranked on a scale from 1 to 5. A rating of 1 indicates low importance, while a rating of 5 indicates high importance. These requirements are identified at the beginning of the design process.

| No | Requirement | Description | Importance |
|----|-------------|-------------|------------|
| 1 | Flexibility | Ability to work and adapt to variable numbers of solar cells, orientations and sizes | 5 |
| 2 | Speed | Full process execution time | 5 |
| 3 | Dispensing accuracy | Tolerance of the coating target | 5 |
| 4 | Automatic operation | How independent is the system from manual intervention | 4 |
| 5 | Clogging | Failure of the dispensing sub-system | 4 |
| 6 | Working space | Area of the module the machine could coat | 4 |
| 7 | Maintenance | Preventive repairs | 3 |
| 8 | Space | Volume or floor occupancy | 2 |

Following the identification of the need and the initial specifications (see Table 4.2), the design process advanced to the conceptual design phase, which marked the second step of the process. In this phase, gathering relevant information played a crucial role in evaluating and selecting the most suitable solutions. Various alternatives, such as mini spray, screen-printing, and additive manufacturing, were considered. However, none of them matched the desired combination of flexibility, speed, and accuracy that inkjet technology offered.

Inkjet technology offers valuable advantages when it comes to modifying the appearance of metallic interconnects in BIPV modules. Its flexibility allows for intricate and customizable designs, while its speed and efficiency ensure rapid ink deposition, boosting productivity in many fields [151]–[153]. The accuracy and precision of inkjet systems result in high-quality patterns with minimal errors [154]. Additionally, the cost-effectiveness of inkjet technology, achieved through efficient ink usage and reduced material waste, makes it an appealing choice.

**Table 4.2:** Main product specifications. The product specifications give to each requirement a qualitative or quantitative value and helps clarifying the objectives. Even though the product specifications can change during the design process, it is useful to start with a summary of them to have an idea of the targeted orders of magnitude.

| No | Specification | Unit | Nominal value | Tolerance | Possible values |
|----|---------------|------|---------------|-----------|-----------------|
| 1 | Flexibility | # of cells | 4 | ±3 | 6,1 |
| 2 | Speed | Modules/min | 1 | ≥ 1 | 1.5, 1.3, 1.1 |
| 3 | Dispensing accuracy | mm | 1 | ±0.03 | 1.025, 0.997 |
| 4 | Automatic operation | - | Low | Low, none | High, medium, low, none |
| 5 | Clogging | - | None | Low, none | High, medium, low, none |
| 6 | Working space | $cm^2$ | 2500 | ±400 | 2600, 2300 |
| 7 | Maintenance | Months | 12 | ±6 | 6, 18 |
| 8 | Space | $m^2$ | 1 | ±0.5 | 1.5, 0.8 |

When selecting an inkjet printer, it is crucial to make certain considerations. Specifically, evaluating the printer's resolution capabilities is relevant to ensure it can achieve the desired level of fine pattern details. Additionally, careful assessment of the printer's compatibility with various surfaces and materials becomes important, including the selection of appropriate ink and substrate, in order to achieve optimal results [155]. While inkjet printing is generally fast, it may not match the speed of other methods. Moreover, the initial investment and ongoing costs, including specialized inks, should be considered. By addressing these considerations through proper equipment selection and maintenance practices, the limitations of inkjet technology can be managed, enabling the desired modifications to metallic interconnect appearance in BIPV modules.

### 4.2.2   Hardware

The equipment was designed with modularity in mind, incorporating various subsystems to optimize performance, as shown in Figure 4.4. The power system supplies energy to ensure all systems function effectively. Different voltage sources were used to meet the specific requirements of each component in the customized inkjet printer. The control system primarily relies on a PC, which runs a C# software responsible for managing the ink delivery system, printhead, camera, and motors. This is achieved through the use of different application programmable interfaces (APIs). Additionally, the printhead controller, located externally to the PC, receives information from the software and translates it into printing signals.

The lighting system operates independently and is isolated from other components. It consists of diffuse white LED lamps, strategically placed to enhance the detection of metallic interconnects. To capture high-resolution images of the printing area, a dedicated camera

with a focused lens is employed. Subsequent image processing techniques are then used to generate the necessary input for the printhead controller. Several examples of vision systems for enhancing manufacturing processes can be found in references [156]–[160]. The equipment incorporates two linear slides equipped with stepper motors, boasting an impressive resolution of 10 μm. These slides facilitate movement along a single plane. Overall, it is important to note that printing is limited to a single axis. However, this axis effectively enables the movement of the printhead, curing UV lamp and camera, while the other axis supports the full printing linear slide. Table 4.3 provides a description of all systems.
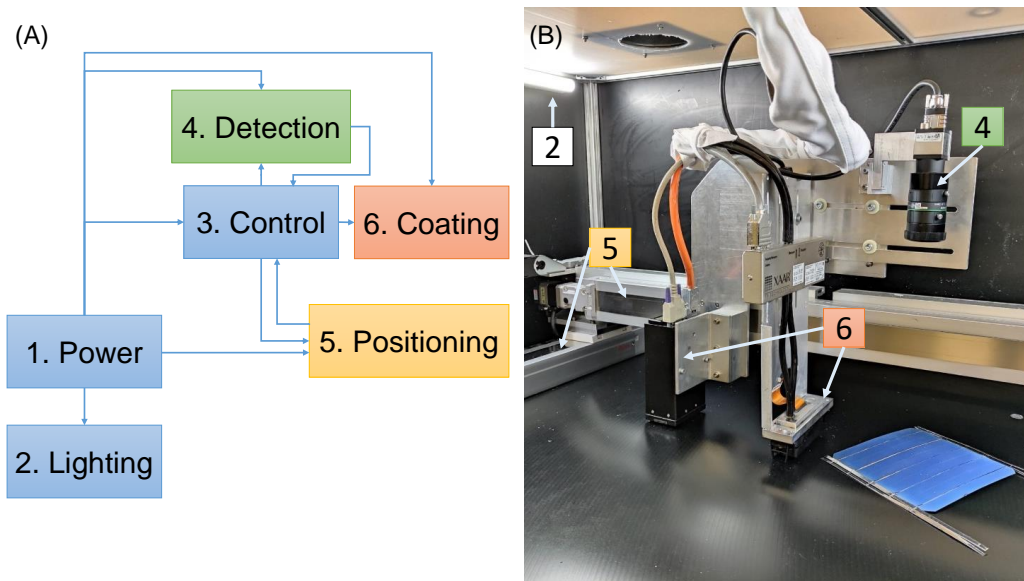


**Figure 4.4:** (A) Subsystems that constitute the customized inkjet printer and their interactions. Specifically, two feedback interactions are considered: one between the control and positioning, and another between the control and detection. These feedback loops are implemented to retrieve essential information necessary for accurately printing in the desired locations. (B) Photograph of the customized inkjet printer highlighting different systems.

### 4.2.3   Software

The customized inkjet printer relies on two main software components. The first software controls the ink delivery system, while the second software interfaces with all the previously mentioned subsystems through APIs. These software components operate independently of each other. The ink delivery system software uses a proportional, integral, derivative (PID) control mechanism to establish optimal temperature, pressure, and ink flow rates for optimal ink dispensing. The primary software, described in Figure 4.5, initiates with a user interface (UI) where connections to the actuators, camera, and printhead are established.

Once the communication is established, the printing process follows a specific sequence: (1) A picture of the array of cells is taken, and through image processing techniques, the metallic interconnects are isolated to generate an image with the coordinates where printing

**Table 4.3:** Purpose and solution for every subsystem. All subsystems interact the make the customized ribbon coating equipment.

| Subsystem | Purpose | Solution |
|---|---|---|
| **1. Power** | Power the full system | Voltage source |
| **2. Lightning** | Help the detection system to facilitate the recognition | LED diffuse light |
| **3. Control** | Generate and send the signals/instructions to the systems | Microcontroller |
| **4. Detection** | Recognize the coordinates of the metallic ribbons | Vision sensor |
| **5. Positioning** | Move the dispensing head to the correct coordinates | Planar gantry |
| **6. Coating** | Cover the ribbons with the desired material | Inkjet DOD (Drop on demand) |

is required. (2) The processed image is transmitted to the printer. The controller sends a signal to the printhead, which prepares to receive encoder signals from the actuators to dispense ink on demand. (3) The curing UV-lamp is activated, and as the motors move, the printing process takes place. Once printing is complete, the curing lamp is turned off.

Since the printing is performed in a single pass, to repeat the process, the same procedure must be followed in a different area. By following this sequence, the customized inkjet printer achieves accurate and efficient printing results.

Accurate printing requires the calibration process to be highly effective. A calibration protocol was implemented comprising several steps using image processing techniques from OpenCV [161] to modify the input image for correct printing, as depicted in Figure 4.6. Initially, a known geometry with a print width 'X' and a chosen distance of 'Y' was printed. The print width 'X' represents the maximum distance the printhead can cover in a single pass, while 'Y' denotes a preselected known distance. Then, a photograph was taken of the printed output. The raw image obtained exhibits various lens distortions that introduce optical imperfections. To rectify these distortions, the image undergoes a calibration process. The checkerboard calibration method was employed, involving the capture of multiple images of a calibrated checkerboard with known geometries to calculate the intrinsic and extrinsic parameters of the vision system to rectify the captured image [162]–[165].

Following this procedure, as depicted in Figure 4.6, it can be observed that the printed rectangle was not flawless. This was attributed to misalignment caused by mechanical tolerances, which prevented the printhead from achieving complete alignment. Some authors have proposed systems to align trajectories for dispensing applications application [166], [167], but to address this issue, a warping process was carried out, transforming the coordinates of the rectangle to align with the ideal rectangle. The same image transformations were implemented when printing on soldered metallic interconnects (see Figure 4.7).
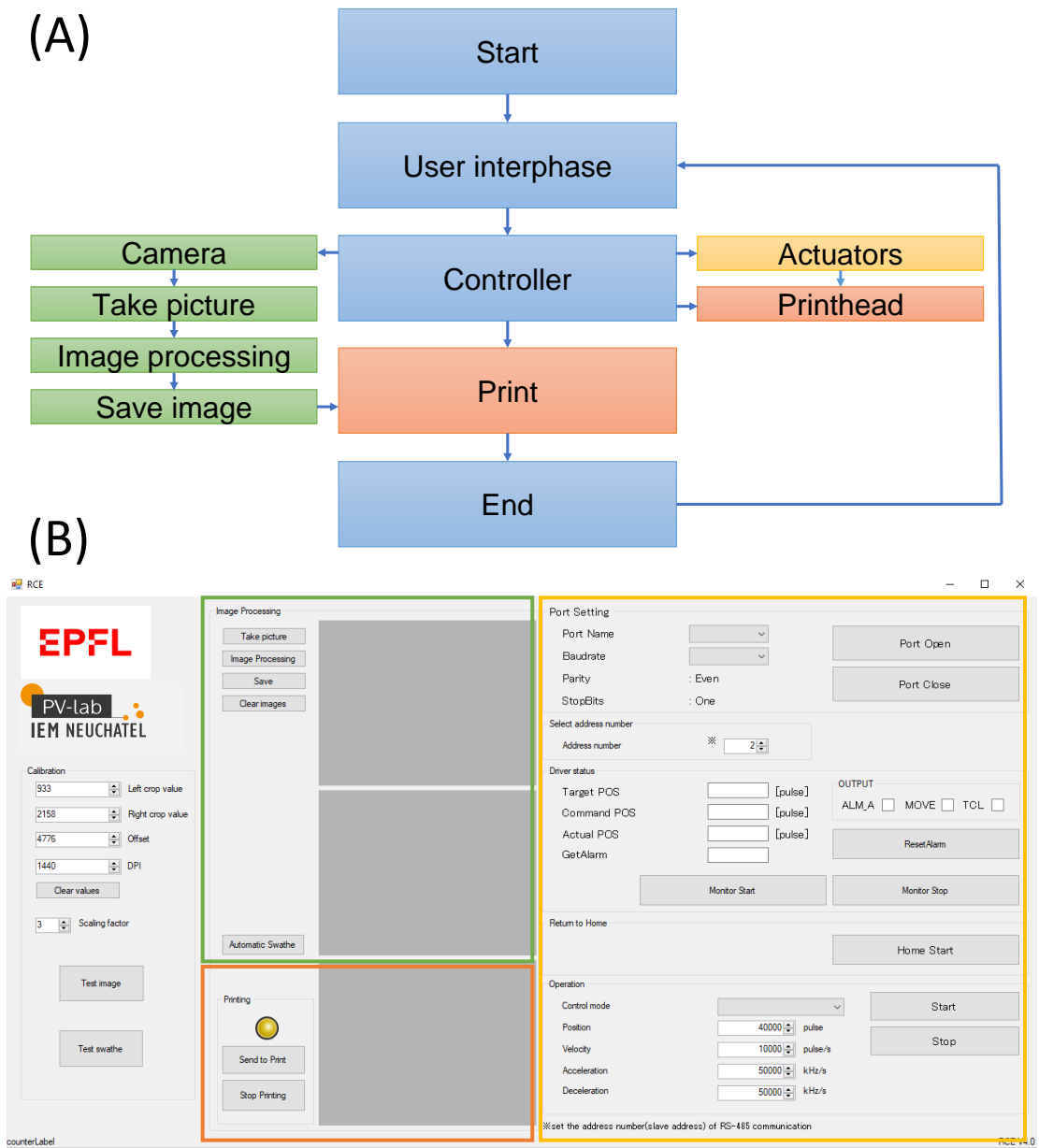
**Figure 4.5:** (A) The software process flow for the customized inkjet equipment involves several key steps. It begins with the user interface (UI), which provides control over the camera, printhead, and actuators. Once the input image is captured by the camera, it undergoes processing and is eventually sent for printing. During this process, the actuators are positioned, and their encoder signals ensure accurate printing by the printhead. This sequential flow can be repeated as needed, allowing for consistent and precise printing on different areas or with different input images. (B) Representation of the UI, with the different sections highlighted in color.

To ensure accurate droplet placement, the input image must undergo several processing steps tailored to the printing system, taking into account the specific hardware and printing char-
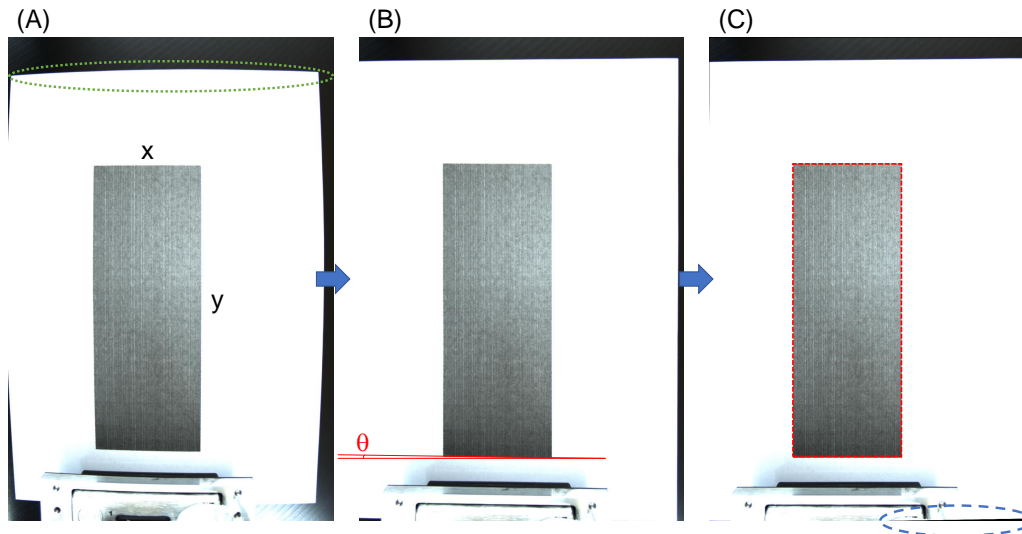
**Figure 4.6:** Calibration protocol implemented. A rectangle with known dimensions 'XY' was printed on a flat surface. (A) Raw image with lens distortions. (B) Lens distortions were corrected with checkerboard image processing technique, notice that the curve lines in the edge of the image are rectified, but the rectangle is not fully aligned (see angle $\theta$). (C) Warped and final image to align the rectangle to the position where it should be. The blue dashed line shows the angle at which the image is bent, this is due to mechanical misalignment's in the equipment. Finally, the image could be cropped according to the print width and print offset.

acteristics. Considering the customized inkjet printer equipped with a printhead consisting of 1000 nozzles, resulting in an input image width of 1000 pixels. Firstly, the raw image was subjected to calibration, warping, and cropping procedures, as shown in Figure 4.7. These steps aim to correct any distortions, align the image properly, and eliminate unwanted areas. Once calibrated, the image was converted to gray-scale to simplify further processing and prepare it for resizing. Resizing the image is the following step, ensuring it matches the desired dimensions for the printhead controller. This process involves adjusting the image's width and height while maintaining its aspect ratio to fit the printing medium and loading the image with the correct file format.

Following the resizing, the image was analyzed to isolate the presence of the metallic ribbons. This was performed using common image processing techniques [168]–[171] and was crucial for generating a printing mask, which determined where the ink was deposited during printing. By identifying and separating the metallic ribbons, the printing system could precisely deposit ink in the targeted regions, resulting in a refined and accurate printing output.

Figure 4.7D illustrates the process of increasing DPI by elongating the image. This adjustment involved modifying the image with the specific requirements of the printing system. By elongating the image, we aimed to enhance drop density during the printing process, ensuring optimal ink coverage. Additionally, the system's configuration was calibrated to increase the number of DPI during the printing process. This adjustment could enhance the level of detail

and sharpness in the final print, resulting in a more visually appealing output. However, increasing the DPI uses larger amount of ink and it is harder to cure. By following these image processing steps, the input image was transformed and optimized for the specific requirements of the customized inkjet printing system.
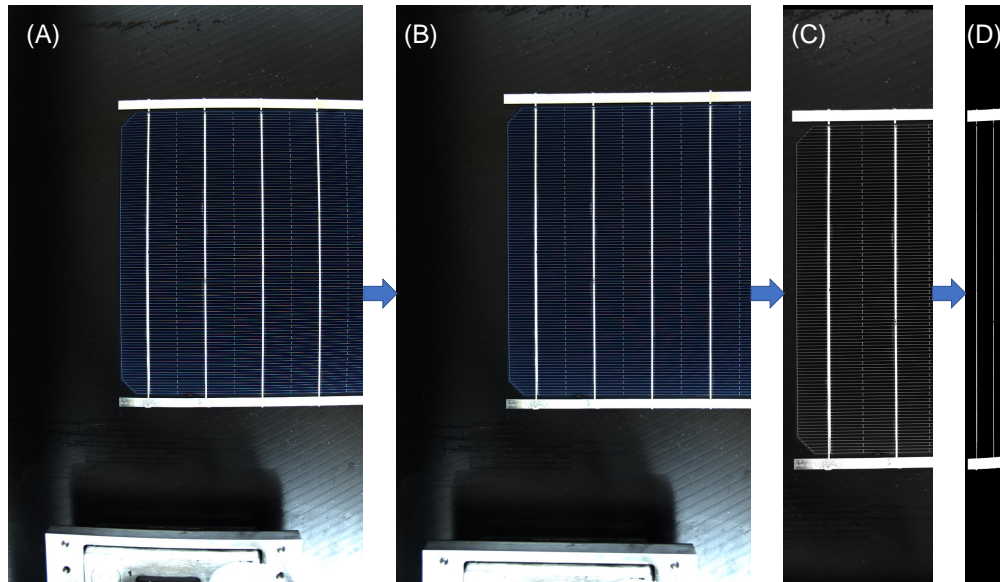


**Figure 4.7:** (A) Raw image of a stringed solar cell. (B) Undistorted image. (C) Warped and cropped image converted to greyscale. (D) The metallic interconnects are isolated using image processing techniques and the image is processed for be used as an input for the printhead controller. Note that the image is not to scale, it is elongated to increase the drops per inch (DPI) and the white pixels are the regions where ink droplets are dispensed.

### 4.2.4 Sample preparation

To evaluate the quality of the printing, we conducted several tests comparing printed reference images using different parameters, such as drops per inch (DPI) or printing speed. Our focus was on metallic ribbons, and we explored various DPI settings while considering the effects of plasma surface treatment at fix speed. Through these experiments, we aimed to identify the optimal printing parameters that would yield the highest quality results on metallic ribbons. After selecting one of the most suitable inks for this application considering dispensing systems manufacturers' feedback, we coated soldered single cells with the equipment. Furthermore, Figure 4.8 presents the samples with and without the application of a black ink on soldered solar cell ribbons, enabling us to evaluate the influence of this manufacturing step on the performance of the solar cells.

**Image processing**

Image processing techniques were used to determine the printing quality with various parameters. The minimum square error (MSE) was calculated between a checkerboard reference
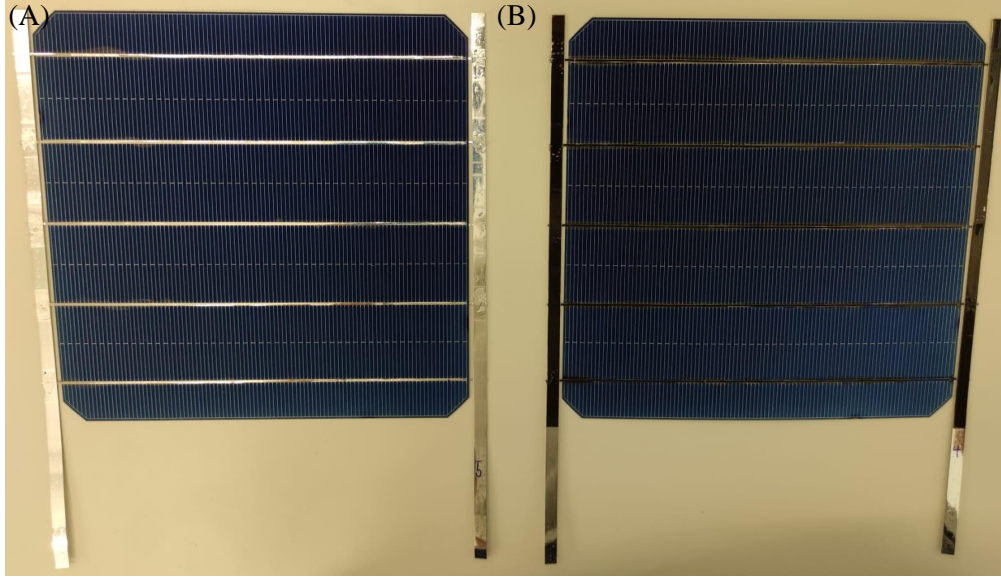
**Figure 4.8:** (A) Solar cell with uncoated ribbons, where the high reflection of the uncoated ribbons can be observed and (B) solar cell with black ink coated ribbons.

image $\hat{f}$ and the printed image $f$ using the following equation [172]:

$$MSE = \frac{1}{MN} \sum_{x=0}^{M-1} \sum_{y=0}^{N-1} [f(x,y) - \hat{f}(x,y)]^2 \tag{4.1}$$

Where $M$ and $N$ are the width and height of the images in pixels and $(x, y)$ are the pixel coordinates of the images. The printed images were taken with high resolution and equal illumination and then post processed to match the size of the reference image. To retrieve the printing accuracy the reference corner coordinates of the checkerboard image were found and compared with the printed images at different speeds using the distance between two points equation:

$$d = \sqrt{(x_2 - x_1)^2 + (y_2 - y_1)^2} \tag{4.2}$$

**Microscopy**

A Hirox microscope was used in the low and mid-range to photograph the coated metallic interconnects and find printing defects. The illumination, magnification and working distance parameters were fix for all the samples.

**IV curve and electroluminescence (EL)**

IV curves are used to determine the power and other PV parameters (e.g. open circuit voltage, short circuit current, etc.) and EL to visualize defective regions in solar cells/modules. A PASAN solar simulator was used to measure the illuminated IV (current-voltage) curve and electroluminescence (EL) images were performed on individual solar cell mini modules. The goal was to compare the performance of coated and uncoated PV modules. The measurements were conducted under standard test conditions (25 °C, Air Mass 1.5g, 1000 W/m$^2$), and corrections for sensitivity and temperature were applied during calibration.

## 4.3 Results

The results are categorized into three primary sections. The first section focuses on printing accuracy, evaluating the precision of the customized inkjet printer. The second section entails visual inspection of the coated metallic interconnects, assessing their appearance. Lastly, the third section analyzes the electrical performance of the coated solar cells produced using the customized inkjet printer.

### 4.3.1 Accuracy

The accuracy of the customized inkjet printer was evaluated through a series of experiments involving the printing of a reference image with a constant DPI while varying the printing speed, and vice versa. In this study, we characterize accuracy as the measure of the distance between the target-dispensed pixel and the corresponding actual coated pixel following camera calibration.

In Figure 4.9A, it is evident that increasing the printing speed leads to an increase in the distance to the target pixel. This can be attributed to the vibrations generated by the machine, which adversely affect the accuracy of the printing process.

Furthermore, the Mean Squared Error (MSE) calculated with Equation 4.1, exhibits a similar trend (see Figure 4.9C). When the printing speed remains constant, increasing the DPI results in a reduction of MSE. This implies that higher DPI settings contribute to improved print quality, as indicated by lower error values in the MSE metric as shown in Figure 4.9D.

### 4.3.2 Visual inspection

Microscope images were captured on the black ink-coated cross-connectors using various DPI settings while maintaining a printing speed of 100 mm/s. The metallic interconnects were cut into 8 cm stripes, followed by a cleaning process with isopropanol and by the printing process. In one set of experiments, an additional step involving plasma treatment was introduced using the Relyon piezo brush PZ3 plasma gun at maximum power for 30 seconds throughout the
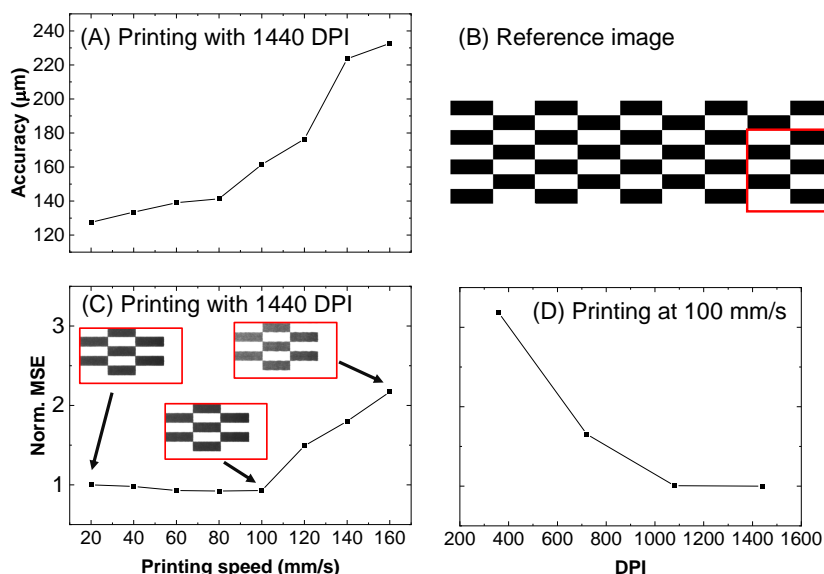
**Figure 4.9:** (A) Accuracy across different printing speeds. The device is less accurate as the printing speed increases, highlighting the inverse relationship between speed and accuracy. (B) Checker board pattern used as a reference image. In red the corresponding cropped area of the image to be visualized. (C) Variation of Normalized Mean Squared Error (MSE) with printing speed, as the printing speed increases, the MSE also increases, indicating a decrease in accuracy. (D) MSE at different DPI settings, the MSE decreases as the DPI increases, indicating that higher DPI settings result in lower error values.

full metallic stripe surface on one side. The treatment modifies the surface of the metallic interconnects by using plasma increasing its surface energy.

By analyzing Figure 4.10, it is evident that low DPI settings result in sub optimal interaction between the substrate and the ink, leading to ink reticulation. However, increasing the DPI significantly improves the coverage for the untreated metallic ribbons, requiring a resolution of 1440 DPI. Conversely, for the treated ribbons, a DPI setting of 1080 is sufficient to achieve full coverage. These findings highlight that the use of surface treatment enhances the printing quality while reducing ink consumption. The treatment not only further cleaned the surface of the metallic ribbons but also improved their wettability for printing. Contact angle measurements and surface energy calculations were not performed due to the availability of the equipment.

### 4.3.3 Electrical performance

The IV curve analysis was conducted on soldered individual solar cells both before and after the coating process. The samples underwent printing at a resolution of 1440 DPI and a speed of 100 mm/s. In addition to IV curve measurements, EL measurements were performed, (not shown here). The EL images demonstrated that, no resistive defects, nor cracks were induced in the cells during sample movement and processing. It is noteworthy that the coating process led to a mere 2% reduction in the maximum power output ($P_{max}$) of the solar cells. This
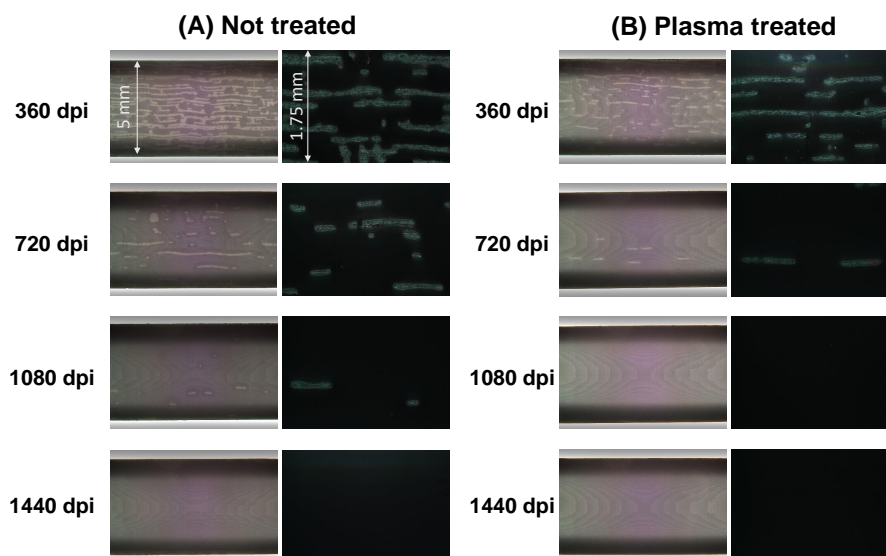
**Figure 4.10:** Coated metallic interconnects printed at 100 mm/s with various drops per inch (DPI). (A) Not treated metallic interconnects. Ink reticulation is clearly observed between the ink and the substrate, at 1440 DPI the metallic ribbon is fully covered. (B) Plasma treated metallic interconnects. An improvement in printing quality is observed at 1080 DPI, in which the ribbons are fully covered

reduction can be primarily attributed to a decrease in the short circuit current (see Figure 4.11), which is associated with the ink flowing into the solar cell (see Figure 4.12).
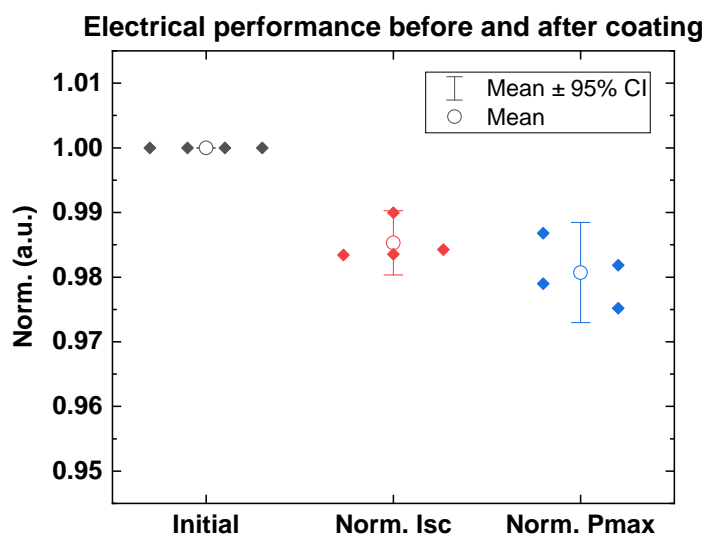


**Figure 4.11:** Normalized electrical performance of solar cells before and after inkjet coating. The short-circuit current ($I_{sc}$) and maximum power ($P_{max}$) showed a slight decrease of 1.5% and 2%, respectively, while the open-circuit voltage ($V_{oc}$) and fill factor (FF) remained relatively unchanged.
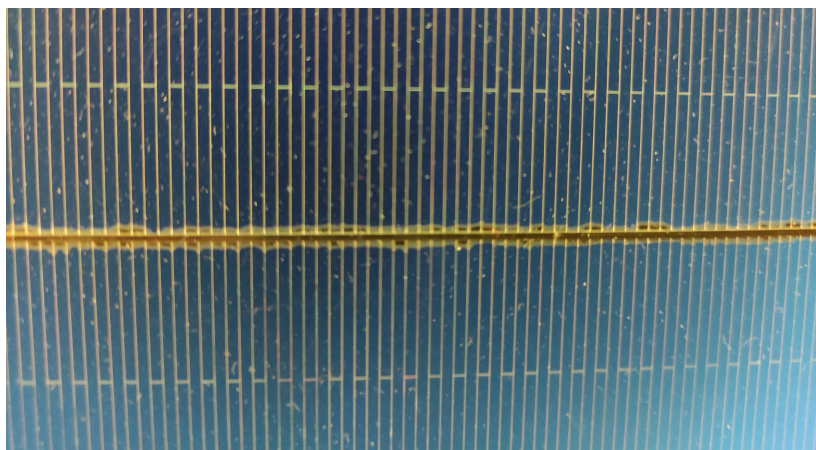
**Figure 4.12:** Coated cell connector on top of the solar cell.  The ink flows slightly into the solar cell causing a decrease in short circuit current, however, the ink is not fully opaque.

## 4.4   Discussion

Although the customized inkjet printer demonstrates suitable performance, there are several aspects that could be enhanced to achieve better printing quality. Firstly, the printer system currently treats all printing as if it was on a flat plane, assuming the solar cells to be very thin. However, once the cells are soldered, they can exhibit a curvature of a few millimeters. This curvature can adversely affect printing quality, considering that the optimal printing distance for the used printhead is 1 mm [155]. To address this issue, a viable solution would involve implementing suction vents on the cell plane to flatten them during the printing process.

The quality of printing is significantly influenced by the interaction between the ink and the substrate [86]. This interaction can be improved through surface treatments like plasma treatment.  In this study, we used only one ink recommended by the manufacturer.  It is crucial to emphasize that the ink must be compatible and appropriately matched with the printing equipment as well as compatible with the encapsulation materials over the lifetime of the PV module [80].  Further enhancements to the printing quality could be achieved by using printheads with higher resolution and capacity. Overall, equipment performance could be improved through hardware modifications, considering the optimization of different subsystems and their interrelations. Adequate maintenance practices are essential to prevent nozzle clogging and ensure optimal printing and curing processes.

Considering the scalability of equipment with such characteristics for the BIPV production line, various manufacturing approaches can be explored. One potential solution involves coating the cell connectors after the stringing process [149]. Alternatively, flipping the soldered array of solar cells and employing the flexibility of an inkjet printer with image detection can enable coating of the entire array (cell connectors and cross connectors). Multiple printheads can be positioned in parallel to achieve simultaneous coating within seconds. It is worth mentioning that, nowadays, due to changes in the technology and the ribbon number increase, the coating

of cell interconnects has become less crucial, however, the proposed equipment offers the flexibility to coat the string interconnects too, which are still relevant, and even other areas of the module, such as the glass itself.

Finally, we stress that the tool presented here demonstrates the proof-of-concept of an equipment capable of coating on a flexible manner metallic interconnect of any size of orientation. To adapt it for a production line, a more practical approach would involve maintaining the vision, printing, and curing equipment in a fixed position while moving the substrate on a conveyor belt for coating reducing vibrations. In terms of the ink, the most preferable approach would be to develop a customized coating that is specifically tailored for this application. This is relevant because the printing equipment must be compatible with the ink being used [173]. The forthcoming stages entail a focus on up scaling, necessitating an in-depth exploration of the integration into manufacturing processes through a meticulous feasibility study. This study will encompass a comprehensive assessment of costs associated with the implementation.

## 4.5 Conclusions

In this research, we successfully designed and prototyped a customized inkjet printer suitable for modifying the appearance of metallic interconnects in BIPV applications. We addressed important considerations in equipment design and highlighted the crucial calibration steps required for accurate printing, including the implementation of a vision system. The calibration process effectively corrected lens distortions and misalignments resulting from mechanical tolerances.

Our study has convincingly demonstrated that customized inkjet printer is a viable flexible equipment for modifying the appearance of metallic interconnects, even when applied directly into solar cells connectors, irrespective of their size, orientation, or position with the help of a vision system using image processing. Notably, the maximum power ($P_{max}$) output experienced a mere 2% decrease primarily attributed to shading losses leading to a reduction in the short circuit current ($I_{sc}$). This reduction can be further mitigated by using hardware with greater capacity. Inkjet printing has exhibited the desired flexibility, speed, and automation necessary for implementation in the BIPV production line.

Furthermore, our investigation has revealed that optimal printing parameters can be determined by considering the printing speed, DPI, and the specific hardware, printing fluid, and substrate employed. The presented equipment achieves optimal printing with a speed of 100 mm/s and a resolution of 1440 DPI, with an accuracy of 160 µm. Further improvements in printing accuracy can be achieved by optimizing the printing distance and using enhanced hardware. Moreover, the use of plasma surface treatment on cross connectors enhances printing quality and reduces ink consumption.

Our research has successfully demonstrated the feasibility and effectiveness of using a cus-

tomized inkjet printer with an integrated vision system for the purpose of modifying the appearance of metallic interconnects in BIPV modules. Additionally, this work offers valuable information and guidance for original equipment manufacturers aiming to develop inkjet printers with vision systems. These findings open up promising avenues for the implementation of inkjet printing technology in BIPV production lines, providing enhanced flexibility, speed, and automation to optimize manufacturing processes in BIPV systems.

In the next chapter, we complement these results by researching the effects of using ink-coated metallic ribbons in the PV module stack of materials under weather stressors. We present a complete characterization analysis to understand the effects observed, develop mitigation strategies, and propose recommendations.

# 5 Stability of Black Interconnect Coatings for Solar Photovoltaic Module Applications

The work in this chapter is based on the following published article presented at the 11th edition of the Metallization and Interconnection Workshop for Crystalline Solar Cells (MIW):

- A. Borja Block, C. Barretta, A. Faes, A. Virtuani, A. Vlk, M. Ledinský, G. Oreski, C. Ballif, *Stability of Black Interconnect Coatings for Solar Photovoltaic Module Applications*, Solar Energy Materials and Solar Cells, 2023 [80].

## Abstract

Building-integrated photovoltaics (BIPV) are dual purpose, providing both energy and building functions. Aesthetics play a crucial role in the BIPV market, with increasing demand for uniformly colored modules for building skins. Manufacturers strive to mask, typically through expensive manual processes, the reflective metallic interconnects to obtain uniform module colors. Inks offer an automated alternative but must be implemented in the production line and remain stable, maintaining their appearance over time. In this chapter, three black metallic ribbons were tested: one commercially pre-coated and two coated with UV-curable inkjet printing. Accelerated UV-light exposure was applied according to IEC standards on coupons mimicking glass/backsheet (G/BS) samples including encapsulant with and without UV blockers. Additionally, one-cell modules with ink-coated ribbons were fabricated using a laboratory-designed automatic inkjet printer and exposed to accelerated UV aging. Results showed that the commercially available coated ribbon remained stable after 120 kWh/m$^2$ of UV exposure. However, UV-curable inkjet inks caused color changes in the encapsulant around metallic interconnects, regardless of the encapsulant used or the presence or not of UV blockers in the encapsulant. Ink #1 exhibited the largest color change after the UV-dose. Its main component, 2-phenoxyethyl acrylate (2-PEA), photodegraded and caused yellowing. An early sign of degradation with a slight increase of 22% in carbonyl index (CI) was observed after 15 kWh/m$^2$ of UV exposure. Encapsulants with UV blockers successfully mitigated 2-PEA photodegradation on G/BS laminates; however, color change occurred with ink #1 despite

their application.  Using this ink on PV modules results in color change, but the electrical performance remains relatively stable, with less than a 3% power loss after 360 kWh/m$^2$ of UV exposure.

## 5.1  Introduction

Climate change is one of the most pressing challenges facing our society today, and the building sector is a major contributor to greenhouse gas emissions. Buildings account for around 30% of global energy consumption and approximately one-third of global $CO_2$ emissions [174]. Building-integrated photovoltaic (BIPV) modules can be incorporated into the building envelope, for example on roofs, facades, and windows, to generate electricity while also providing shade, insulation, and other benefits. By generating electricity from renewable sources, buildings can reduce their dependence on fossil fuels and help mitigate the environmental impacts associated with traditional energy production [175]. BIPV modules can be designed in a range of shapes, sizes, and colors, enabling architects and designers to create visually stunning and energy-positive buildings. One important factor for BIPV acceptance by architects and house owners is the aesthetic of the active PV construction elements. In particular, the homogeneous appearance is of high importance even if the performance is reduced. The overall appearance of the modules, created by the mix of dark cells, metallic ribbons, and typically white backsheets, is frequently perceived as visually unappealing, complicating PV incorporation in the built environment [129]. In many cases, BIPV modules are still considered a non-aesthetic appendage by architects. As aesthetic is still a crucial point in the consumer decision of purchase [176], in recent years, several BIPV module manufacturers have attempted to mask the highly reflective metallic interconnects to minimize inhomogeneous patterns of solar modules and used black backsheets in place of white ones.

Metallic ribbons, connectors or interconnects play an important role in the construction of PV modules. These thin strips of metal are used to connect the individual solar cells in the module, allowing the current to flow from cell to cell and ultimately to the external electrical circuit. In addition to their functional role in the module, metallic ribbons can also contribute to its aesthetic appeal. Interconnect hiding is often achieved through expensive and inefficient manufacturing steps, such as applying colored strips or bands with manual positioning. A possible solution to modify the appearance of the metallic ribbons is to coat them with ink. However, the metallic ribbons come in different shapes, orientations, and sizes, depending on the module design and solar cells used; therefore, coating them is not straightforward. Inkjet is one of the best technologies able to cope with the requirements of accuracy, resolution, and flexibility to coat the bright metallic ribbons, even on top of the solar cells. Ink coated metallic ribbons could be a suitable solution to achieve the uniform appearance architects seek. Nevertheless, using ribbons precoated with black color on the production line has many challenges. They are stretched, bent, soldered and laminated at high temperatures (>300°C and  150°C respectively), all of which the black coating should withstand while maintaining the production line speed. Figure 5.1 depicts a black coated ribbon with non temperature resistant

coating after soldering. An alternative solution will be the coating of the interconnects by advanced inkjet printing after the stringing and soldering of the solar cell array. The curing of the ink should be fast, making UV curable inks an appropriate candidate.



**Figure 5.1:** Black coated ribbon without heat resistant coating after soldering. The coating burns and easily falls from the metallic ribbon leaving uncovered its highly reflective surface.

UV-curable inkjet inks are typically made of a mixture of monomers, oligomers, photoinitiators, colorants, and additives. These materials are well described by S. Magdassi et al. [173]. Monomers are small molecules that form the polymer backbone of the ink when exposed to UV light. Oligomers are larger molecules that polymerize to control the physical properties of the cured ink, such as hardness and flexibility. Photoinitiators are chemicals that are sensitive to UV light and are added to the ink to initiate the polymerization process when exposed to UV light. Colorants (e.g. pigments or dyes) are added to provide color to the ink, and additives such as surfactants and stabilizers are used to improve the ink's performance and stability. UV-curable inkjet inks can be formulated to work with a wide range of substrates, including paper, plastics, glass, metal, and ceramics, and can be customized for specific printing applications. However, there are many considerations to be taken into account when formulating a UV-curable inkjet ink (e.g. viscosity, surface tension, particle size, colorant type, cure speed, etc.) [177]. No UV-curable inkjet inks are specifically made for BIPV applications. To be compatible with PV applications, the ink should first wet and have good printing quality on cell and string interconnects, and then it should have strong adhesion not to be delaminated due to the shear stresses in the encapsulants during module lamination, ruining the aesthetic appearance. Finally, the ink should have long term stability as PV modules are subjected to long-term exposure weather stressors including humidity, temperature, and light, which are known to cause deterioration of polymer module materials such as backsheets and encapsulants [178].

Little is known about the stability of black ribbons in these conditions and the effects the black coatings could create in the PV modules. The components of the black ink could react with the materials of the PV modules and produce degradation. To date there are no specific requirements for colored ribbons for PV applications besides the common qualification tests used for PV modules such as IEC 61215 [72]. Few studies have tested the stability and requirements of black metallic ribbons for integrated PV applications [84], [85], [149]. The objectives of this research are to determine whether the black coatings are stable after a protocol based on UV light exposure tests for polymeric materials used by the PV industry [77], discuss the challenges of these products and understand the degradation mode observed focusing on a particular ink, exhibiting the most substantial color change among the tested samples.

**Table 5.1:** Black metallic ribbons investigated in this work. The initial two ribbons were coated with UV-curable inkjet ink, whereas the third ribbon was a commercially available black pre-coated metallic ribbon with a dispensing technique and ink that were not specified. All materials are commercially available components.

| Metallic ribbon # | Type | Dispensing technique | Ink info | Ribbon info |
|:---:|:---:|:---:|:---:|:---:|
| 1 | UV curable | Inkjet | Safety datasheet | Copper with Sn:Pb= 70:30-60:40 coating |
| 2 | UV curable | Inkjet | Safety datasheet | Copper with Sn:Pb= 70:30-60:40 coating |
| 3 | Unknown | Unknown | Technical specification | Copper with Sn:Pb= 70:30-60:40 coating |

## 5.2  Material and methods

We selected three different black metallic ribbons. One was commercially-available but with no information about the used coating, while the other two were coated in the laboratory with UV-curable inkjet commercial inks (see Table 5.1). The only available information for the inks used was the safety datasheet. One key advantage of inkjet UV-curable coated ribbons was their ability to be coated immediately after the soldering process. This eliminated the need for the coatings on metallic ribbons to withstand high temperatures, thereby avoiding any potential damage or degradation caused by extreme heat.

Depending on the compatibility of the inkjet equipment, the ribbons were coated manually or according to the dispensing technique suggested by the distributor. The curing process was carried out for ink #1 and #2 using a FireJet One UV 20 W lamp emitting at 395 nm with 4 passes at 100 mm/s with a substrate distance of 3 mm. The samples were subjected to light and temperature exposure according to IEC 62788-7-2 [77]. Assessing the stability of the coatings was necessary to understand the effect they will have on the PV module in the long-term. The characterization was performed with image processing visual inspection on all the samples.

A deeper study was carried out only with the ink that was known to produce the largest color change (ink #1) in one-solar cell PV modules according to previous investigation [85], and due to the challenge of investigating commercial components with undisclosed materials. The characterization techniques employed were attenuated total reflectance Fourier transform infrared spectroscopy (ATR-FTIR), UV-fluorescence imaging, thermo-desorption gas chromatography coupled to mass spectrometry (TD-GCMS) and Raman spectroscopy. Single solar cell mini-modules were manufactured employing ink #1 with the help of a laboratory-designed ribbon coating equipment to mask all the metallic ribbons, even the cell connectors at the top of the solar cell. The one solar cell mini modules were also exposed to the same protocol to assess, through electrical performance measurements (IV curve and electroluminescence), the effects of unstable coatings on PV modules.

**Table 5.2:** UVA+UVB dose applied to each sample in this work. Three different kinds of samples were used: G/BS coupons with coated ribbons and with ink components, pure ink components in small glass bottles and mini modules.

| Sample | UVA+UVB dose (kWh/m2) |
|---|---|
| **G/BS coupons** | 120 |
| **Pure ink components** | 1.5 and 15 |
| **One solar cell PV modules** | 360 |

### 5.2.1  Sample preparation

The stability and performance of the inks was tested on three levels under UV exposure (see Table 5.2): 1) Glass–backsheet (G/BS) laminates to investigate the interactions of all the inks with the encapsulants. 2) Individual ink #1 components to check the potential root causes for color change, because ink #1 produced the largest visual modifications. 3) Coated one solar cell PV modules to investigate the influence of ink #1 on the electrical performance.

**G/BS laminates**

After coating, the metallic ribbons were cut into 3 cm long stripes. They were then laminated at around 150°C in the conventional PV configuration glass-backsheet (G/BS) using solar glass (see Figure 5.2). Three different types of encapsulants were chosen, one made of ethylene vinyl acetate (EVA) and the other two based on polyolefin elastomer (POE), with and without UV blockers. The encapsulant with UV blockers had a transmittance of equal to or less than 30% for wavelengths ranging from 290 nm to 380 nm, while those without UV blockers had larger transmittance than 70% in the same range. The idea of comparing an encapsulant with UV blockers with encapsulant without UV blockers came from the hypothesis that they could mitigate the degradation observed with unstable inks. The final size of the G/BS laminates were 5 cm x 5 cm. Glass-glass (G/G) samples were not manufactured since recent investigations into G/G and G/BS samples showed similar effects after light exposure [84], [85], see Annex B. Furthermore, G/BS samples had the crucial advantage that they can be peeled to have access to the materials inside the laminates for further characterization.

Our study primarily centered on ink #1 to investigate the significant color change observed in this particular ink. Inks are complex mixtures containing various interacting substances, including undisclosed materials. To simplify our research, we generated samples similar to those depicted in Figure 5.2(B). Instead of using coated metallic ribbons, we laminated either ink flush or pure monomers droplets of ink #1 between the encapsulants. Ink flush is a liquid product designed for printhead maintenance and ink cleaning. In the case of ink #1, the primary component of the ink flush matches the main component of the ink itself, which is 2-phenoxyethyl acrylate (2-PEA). In this study, the ink flush and pure component primarily consisted of 2-phenoxyethyl acrylate. However, it's important to note that ink flush is not as pure as the standalone component. The decision to use ink flush was based on logistical
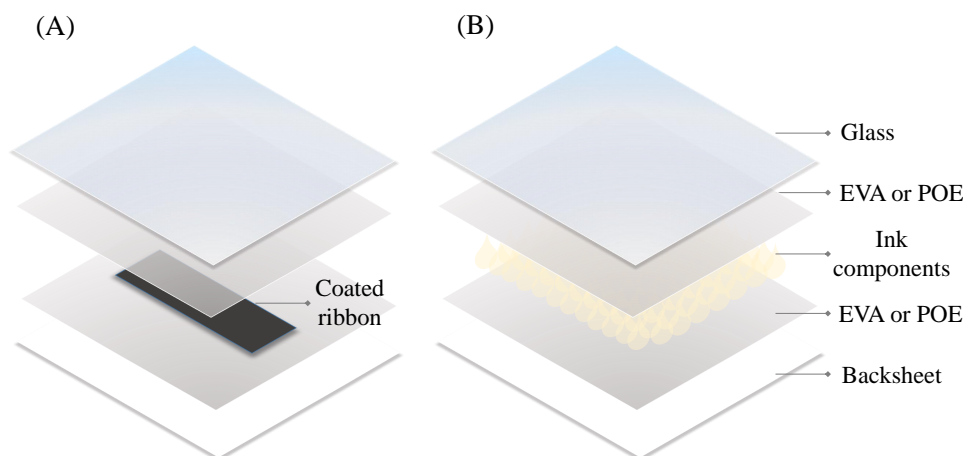
**Figure 5.2:** Typical sample configuration manufactured in this investigation. They were produced with either EVA or POE with or without UV blocker. (A) Sample with encapsulated coated ribbon, this type of sample was manufactured with all inks. (B) Sample with ink component, this type of sample was manufactured only with ink #1.

considerations and material availability. Furthermore, we replicated the same samples by laminating pure 2-PEA in the G/BS configuration, as depicted in Figure 5.2(B).

**Pure component degradation**

As previously mentioned, the inks are made with several components (i.e. monomers, oligomers, photoinitiators, colorants, and additives) that interact between themselves and with the materials of the substrate and surroundings. We isolated in small glass bottles the ink flush #1 and the pure molecule 2-PEA to investigate whether it played an important role on the degradation observed.

**Coated solar cell mini modules**

We investigated the effect of the ink #1 on a one solar cell G/BS mini module. Samples were prepared by first soldering the cell, subsequently the ribbons were coated with the help of the laboratory-developed inkjet ribbon coating equipment (RCE) that can coat ribbons even on top of the solar cells. The equipment consists of a customized inkjet printer specifically designed for coating laboratory samples. However, it offers scalability possibilities to industrial scale, allowing for the modification of the appearance of PV modules. It employs high-resolution actuators and image processing to detect cell connectors and interconnects with remarkable precision. After coating, the stringed solar cell was encapsulated and laminated with front solar glass, EVA, and a rear black backsheet. This was also performed with an uncoated cell (see Figure 5.3). The goal of these samples was to investigate the effect of an ink that produces

large color change on a PV module.
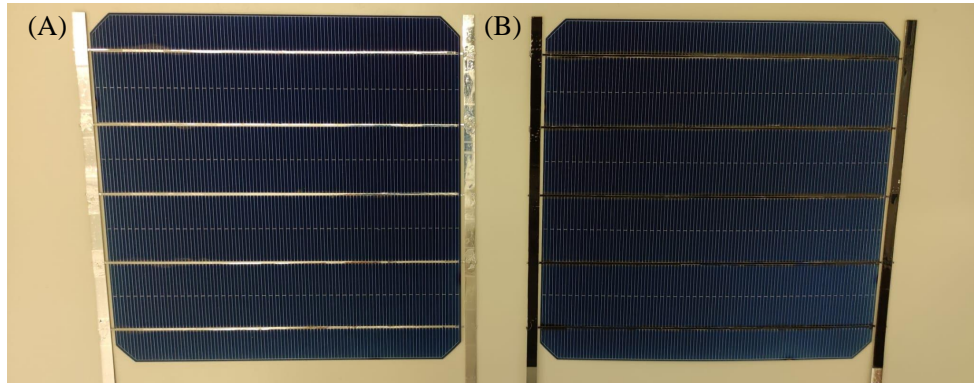


**Figure 5.3:** (A) Solar cell with uncoated ribbons and (B) solar cell with black coated ribbons. The high reflection of the uncoated ribbons can be observed.

### 5.2.2 Testing sequence

The samples followed a sequence based on IEC 62788-7-2 standard with A3 conditions [77]. They were placed inside a Q-Sun Xenon chamber (Q-SUN Model Xe-3) with a noon summer sunlight filter following the conditions of Table 5.3.

**Table 5.3:** Test conditions in the UV chamber according to IEC 62788-7-2 standard with A3 conditions.

| Condition | UVA+UVB dose (kWh/m$^2$) |
|---|---|
| **Irradiance** | 0.8 W/m$^2$ at 340 nm |
| **Relative humidity** | 20% |
| **UV intensity (UV-A + UV-B)** | 60 W/m$^2$ |
| **Chamber air temperature** | 65°C |
| **Black panel temperature** | 90°C |

The G/BS coupons were left in the chamber for a total of 2000 h, equivalent to roughly 120 kWh/m$^2$ of UVA + UVB, which corresponds approximately to 2 years of outdoor exposure in central Europe. The mini modules were aged for a total of 6000 h, and the pure component samples simply for 24 h and 10 days. This was because the degradation observed appeared very rapidly. The total UV dose was presented in Table 5.2.

### 5.2.3 Characterization techniques

The measurements performed in this work aim to assess the effects of the coatings in common PV materials under accelerated aging tests. In the case of PV modules, these impacts can be both aesthetic and on the electrical performance.

## Chapter 5. Stability of Black Interconnect Coatings for Solar Photovoltaic Module Applications

### Visual and UV-fluorescence imaging

Images of the samples were taken periodically with high illumination and resolution using a scanner machine. A software was developed using image processing to compare the RGB color coordinates' change in the sample previous to and after UV exposure, employing the CIEDE2000 formula [88]. While the sample is deteriorating, the program allows a relative change in color to be observed and calculated. Less stable inks will exhibit a greater color change ($\Delta$E). Further images were taken with UV-fluorescence imaging with a 365 nm UV LED flood light and a digital camera to assess polymer degradation [179].

### Attenuated total reflectance Fourier transform infrared spectroscopy (ATR-FTIR)

The G/BS laminates were peeled manually, and the chemical changes in the encapsulant and pure ink components were assessed with attenuated total reflectance (ATR) Fourier transform infrared (FTIR) spectroscopy. A Bruker Vertex 80 spanning the 400-4000 cm$^{-1}$ range with 64 scans in absorbance mode was used to collect the data. The background was collected on a clean ATR diamond crystal. Several measurements of each sample were taken in various spots and the data was then processed and normalized. The same process was followed with the polymerized pure ink components. The carbonyl index was calculated as shown in Equation 5.1 [180], [181]:

$$\text{Carbonyl index (\%)} = \frac{I_{1720}}{I_{2920}} \times 100 \tag{5.1}$$

### Thermo-desorption gas-chromatography coupled to mass-spectrometry (TD-GCMS)

The method was used to analyze the chemical processes that occur in samples containing ink #1 components. About 1 mg of reference and contaminated encapsulant with ink component materials were extracted from the G/BS laminates to qualitatively investigate the changes in the additive composition and formation of possible degradation products that took place during exposure. TD-GCMS experiments were carried out using a GC-MS QM2010 Ultra from Shimadzu equipped with a Pyrolyzator 3030D from Frontier laboratories. The encapsulant samples were heated up in the furnace of the pyrolyzator from 60°C to 320°C with a heating rate of 20°C/min and kept at 320°C for 3 minutes. The gases evolving from the encapsulants during this step were then carried into the GC using helium as carrier gas. The evolved substances were separated in the GC equipped with an Optima-5-Accent column, with length of 30 m and inner diameter of 0.25 mm. The interface between GC and pyrolyzator was kept at 300 °C, and thermal protocol in the GC was characterized by the following steps: (I) heating from 50°C to 90°C with a heating rate of 10°C/min, (II) isotherm at 90°C for 2 min, (III) heating from 90°C to 300°C with a heating rate of 10°C/min, (IV) isotherm at 300°C for 10 min. Each substance eluting from the column was then ionized using an ionization energy of 70 eV and

mass spectra were recorded in the range of m/z 50 – 800. The identification of the mass spectra was carried out by comparison with the NIST database.

**Raman spectroscopy**

Similarly, as ATR-FTIR, the G/BS laminates were peeled manually, and the chemical changes in the encapsulant were assessed. The Raman spectra were acquired using two Renishaw InVia confocal spectrometer using 785 nm laser as excitation source. Line map of the Raman spectra of the sample was taken using 100x Leica objective (numerical aperture NA = 0.90), dielectric rejection filter, and 1200 groves/mm diffraction grating. As a calibration sample, Raman line of crystalline silicon at 520.5 cm$^{-1}$ was used.

**IV curve and electroluminescence (EL)**

The one-sun IV curve and electroluminescence (EL) were measured on single solar cell mini modules to determine the difference between coated and uncoated PV modules after UV exposure. Standard tests conditions (25°C, Air Mass 1.5g, 1000 W/m$^2$) were followed with irradiance and temperature calibration correction using a PASAN solar simulator.

## 5.3 Results and discussion

The results are divided in five main sections. The first section examines the results of the digital images, color change and UV-fluorescence imaging. The second, third, and fourth includes the characterization of the investigated samples with ATR-FTIR, TD-GCMS, and Raman spectroscopy, respectively. Finally, the electrical performance of the mini modules is assessed.

### 5.3.1 Visual inspection

The G/BS laminates were scanned at 0 kWh/m$^2$ and at 120 kWh/m$^2$. Figure 5.4 presents the results of the color change ($\Delta$E) from the samples previous to and after degradation. Different encapsulants (e.g EVA or POE) showed no major effect on the color change perceived. The single most striking observation to emerge from the data comparison was that the color change only appeared on the UV curable inkjet inks, while not on the commercial black ribbons.

Ink #1 produced the largest color change, a yellow halo in the surroundings of the coated metallic interconnects appeared. This could indicate diffusion of ink components into the encapsulant and degradation. Ink #2 produced a milder but still noticeable color change. No increase in $\Delta$E was detected for ink #3. Surprisingly, the UV blocker encapsulant did not mitigate the color change effect for the black coatings in any case.

The G/BS laminates containing 2-PEA were photographed at ambient light and with UV-
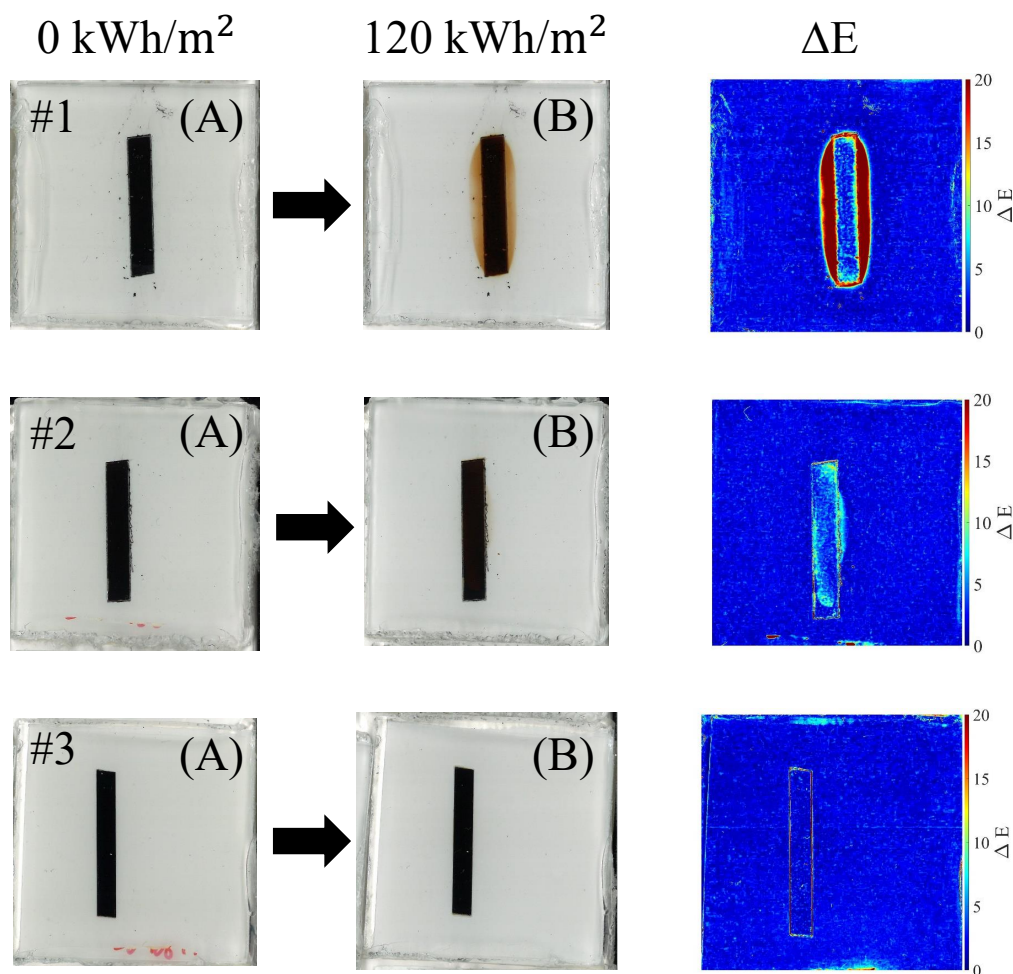
**Figure 5.4:** G/BS laminates before and after UV exposure for all studied inks (#1, #2 and #3). On the right, the image depicting a value of color change for each pixel between the two images. The image is generated by aligning image (A) and (B) to then calculate the color change ($\Delta$E) between them. (#1) Ink #1 made mainly of 2-PEA produces a yellow halo after 120 kWh/m$^2$ of UV exposure. (#2) UV curable ink #2 produces a mild but still noticeable color change. (#3) Commercial pre-coated metallic ribbon is stable after 120 kWh/m$^2$ of UV exposure.

fluorescence imaging to compare exposed and not exposed samples. Figure 5.5 shows the difference, while with ambient light all samples appear white (since the backsheet is white colored) with UV light an evident fluorescence is observed for the encapsulants without UV blockers. After exposure there might be chromophore formations in the 2-PEA component that produce fluorescence under UV light [182].

On samples with UV blockers and only 2-PEA, no color change was found. This suggests that encapsulants with UV blockers help preserving the major component of ink #1 (2-PEA). Even with UV blockers, yellowing happened in samples with coated metallic interconnects. This phenomenon might be explained by the deterioration of another ink components, potentially
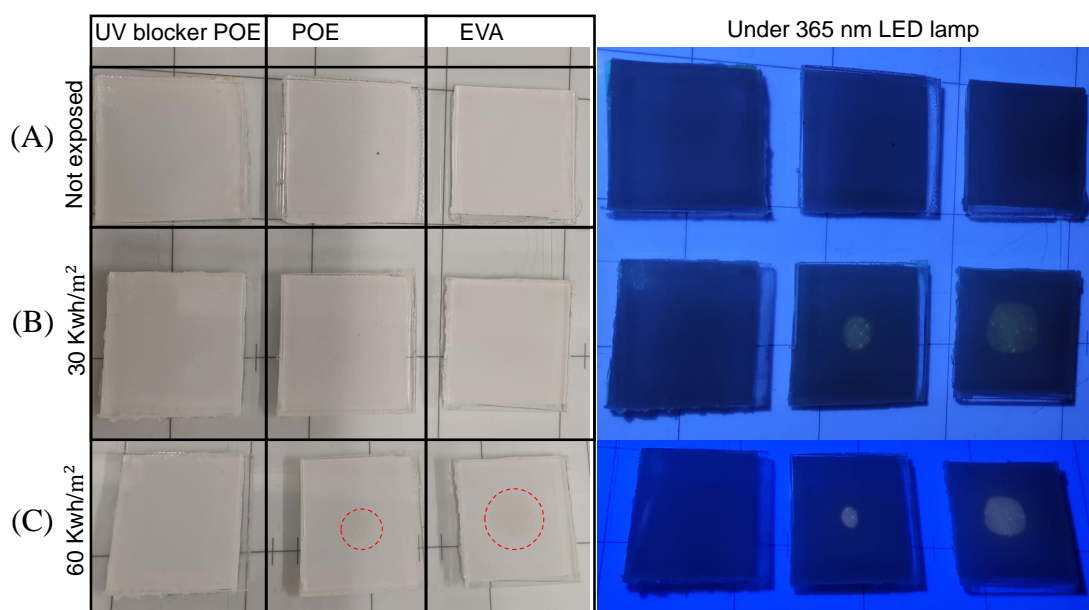
**Figure 5.5:** G/BS laminates with 2-PEA in between the encapsulant layers (see Fig. 5.2(B)). (A) Not exposed samples show no difference under UV-fluorescence imaging. (B) and (C), 30 kWh/m$^2$ and 60 kWh/m$^2$ respectively, highlighted in red dashed lines, a mild yellow color appear in the samples under an ambient light picture (left) and a slight increase in fluorescence is appreciated (right). The UV blocker mitigates the degradation.

with greater light wavelength exposure, temperature or humidity.

### 5.3.2 Attenuated total reflectance Fourier transform infrared spectroscopy (ATR-FTIR)

The peeled G/BS laminates and pure components were measured. In the case of the samples encapsulated with flush clear peaks corresponding to the 2-PEA appeared in the range of 1300 to 1100 cm$^{-1}$ (see Fig. 5.6). After the exposure of 120 kWh/m$^2$ of UV, no difference was appreciated in the ATR-FTIR spectra even when a change in color was observed for the sample with flush. The reference samples (samples without any ink component) did not show any major change in the spectra after exposure. The same effect happened with all encapsulants tested. The same measurement was performed on the samples with coated metallic ribbons, but no difference was observed in the spectra even for measurements in the regions presenting change in color. Several plausible explanations for these results exist. Firstly, the use of ATR-FTIR as a measurement technique presents a limitation in its surface sensitivity, as it can only probe a thin layer of material, typically around 0.5 and 2 µm [179]. Consequently, if the chemical changes of interest occur deeper within the sample and do not manifest on the surface, they may go undetected. Secondly, it is important to consider the composition of the samples. The encapsulant material constitutes the primary component, while the ink components are relatively minor in comparison. As a result, any significant changes

in the overall signal would be predominantly influenced by the encapsulant. Therefore, if the encapsulant remains relatively stable and unchanged, it becomes challenging to detect variations due to the limits of detection of the device and the overlapping bands present in the FTIR spectrum. Overall, these factors contribute to the difficulty in detecting certain chemical changes using ATR-FTIR in this context. The measurement's surface sensitivity and the dominant signal from the encapsulant pose challenges when attempting to identify subtle variations or shifts in the ink components.
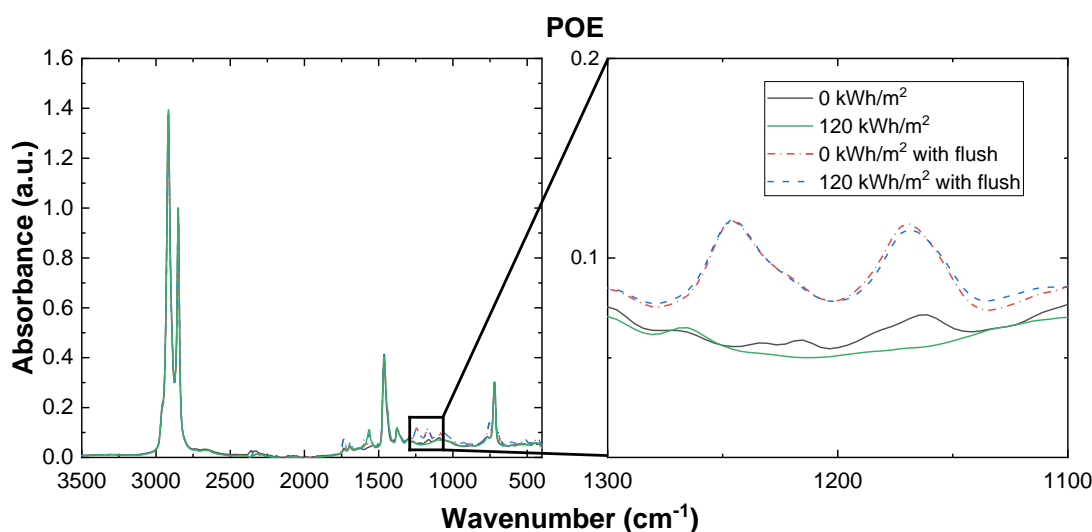


**Figure 5.6:** POE G/BS laminates subjected to exposure of 120 kWh/m$^2$, both with and without flush, before and after the exposure period. The red circular dashed lines show the region where the encapsulant was extracted. (A) Absorbance spectra from 3500 to 500 cm$^{-1}$ and (B) close up view from 1300 to 1100 cm$^{-1}$ with modified scale showing the peaks corresponding to 2-PEA. The data was normalized at 2850 cm$^{-1}$.

The pure component of the ink and flush, 2-PEA, polymerized after 1.5 kWh/m$^2$, and it turned yellow after 15 kWh/m$^2$. Figure 5.7 shows that there is a rise in the 1720 cm$^{-1}$ peak following degradation. This is due to the creation of carbonyl bonds in the substance, which are related to the oxidation of the molecule under UV light [183]. The carbonyl index (CI) was computed as shown in Equation 5.1, and it rose by 22% following the UV exposure of 15 kWh/m$^2$. We definitely see an increase in intensity in multiple peaks after degradation, indicating a possible production of carbon double bonds (C=C) throughout the ageing process [184]. The formation of polyconjugated carbon double bonds (C=C)$_n$ and carbonyl groups may be a significant contributory factor to the development of yellowness in the degraded 2-PEA, as it has been observed with other polymers [185]–[188]. When subjected to the protocol, the 2-PEA component undergoes both polymerization and photodegradation. Consideration can be given to aliphatic monomers as a potential alternative to 2-PEA, as they exhibit superior non-yellowing properties [173].
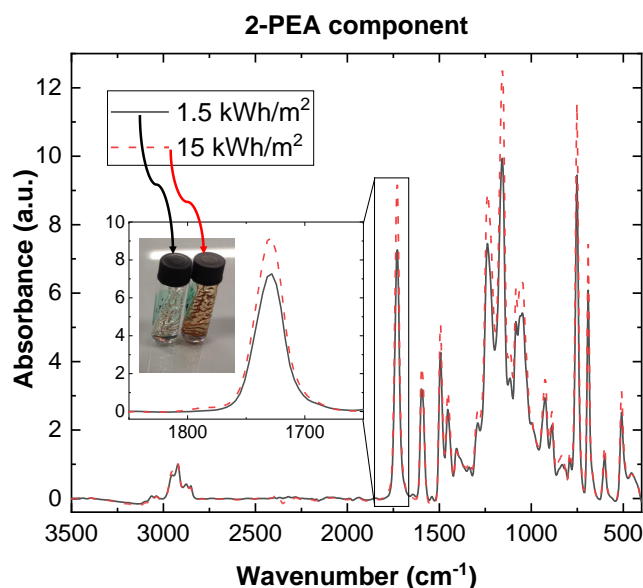
**Figure 5.7:** ATR-FTIR spectra in absorbance mode of the 2-PEA component after 1.5 kWh/m$^2$ and 15 kWh/m$^2$ of UV exposure. As it degrades the CI increases and the polymer becomes yellow. The data was normalized at 2850 cm$^{-1}$.

### 5.3.3 Thermo-desorption gas-chromatography coupled to mass spectrometry (TD-GCMS)

The results of TD-GCMS measurements can be seen in Figure 5.7(A). The chromatograms show presence of several peaks corresponding to substances that evolved during the thermo-desorption step from the encapsulants extracted from the G/BS laminates. The samples before the exposure to UV light showed presence of a residue of peroxide at about 6 min, crosslinking accelerator at about 17 min and hindered amine light stabilizer (HALS) at 29.8 min. Additionally, the sample with flush, showed presence of substances below 15 min that can be traced back to 2-PEA. Interestingly, the sample with flush that was exposed to 120 kWh/m$^2$ did not show presence of HALS, as can be seen in Figure 5.7(B). Typically, HALS protect the polymers from photo-oxidation trapping the carbon centered radicals by nitroxyl radicals [189]. In case of the sample laminated with the flush, the HALS might have acted not only to protect the encapsulant from photo-oxidation, but also to contrast the degradation processes taking place in the flush itself, thus accelerating the stabilizer's consumption. It is also possible that the stabilizer migrated during the exposure making the HALS undetectable [190].

### 5.3.4 Raman spectroscopy

The Raman spectroscopy measurements are presented in Figure 5.9. In order to analyze the peeled G/BS EVA samples with ink coated ribbons, a line scan was conducted across a peeled
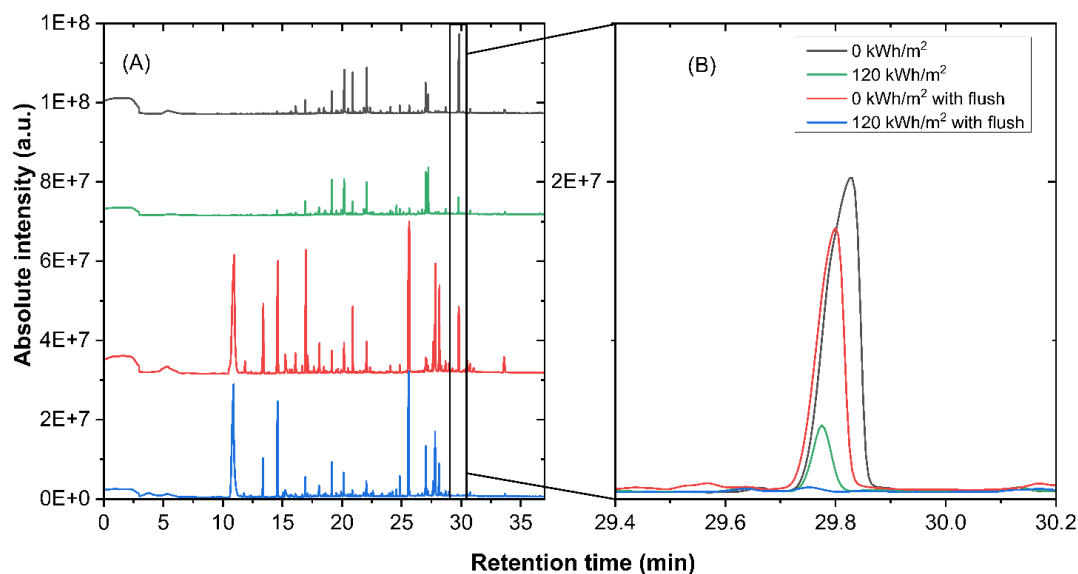
**Figure 5.8:** (A) TD-GCMS chromatograms of EVA extracted from G/BS samples in similar position as shown in the samples of Figure 5.6 with and without flush and (B) close up view rescaled from 29.4 min to 30.2 min showing peaks correspondent to hindered amine light stabilizer (HALS).

sample that was not subjected to UV exposure, as well as one after subjecting it to $120\,\mathrm{kWh/m^2}$ of UV exposure. The scan on the sample without exposure encompassed a range extending from the coated metallic interconnect into the encapsulant further away from it, as shown in Figure 5.9(B). An interesting observation is the consistent decrease in the intensity ratio between the 1000 and 1065 $\mathrm{cm^{-1}}$ peaks as the scan approaches regions further away from the ribbon.  These peaks are associated with 2-PEA compound and ethylene units of EVA [191], respectively. This observation suggests that the ink components undergo diffusion into the encapsulant material, resulting in a higher concentration in the immediate proximity of the metallic ribbon and a lower concentration in regions further away.  Numerous studies have analyzed the diffusion mechanisms of smaller organic molecules within a cross-linked polymer matrix at elevated temperatures [192], [193]. Given the widespread occurrence of this known phenomenon, these findings should not be considered particularly surprising. As for the UV-exposed sample, another line scan was performed. Unfortunately, it was not possible to measure the fully yellow material due to the masking effect of fluorescence, which hides the Raman peaks; therefore, the results are not presented in this work.

### 5.3.5   Electrical performance

The electrical performance measurements suggest that the investigated inks do not influence the power output of the modules.  There will be reduction in short circuit current ($I_{sc}$) due to shading losses if the coating is printed on top of the solar cell, but after ageing the loss of power will not increment considerably even with the diffusion of ink components into
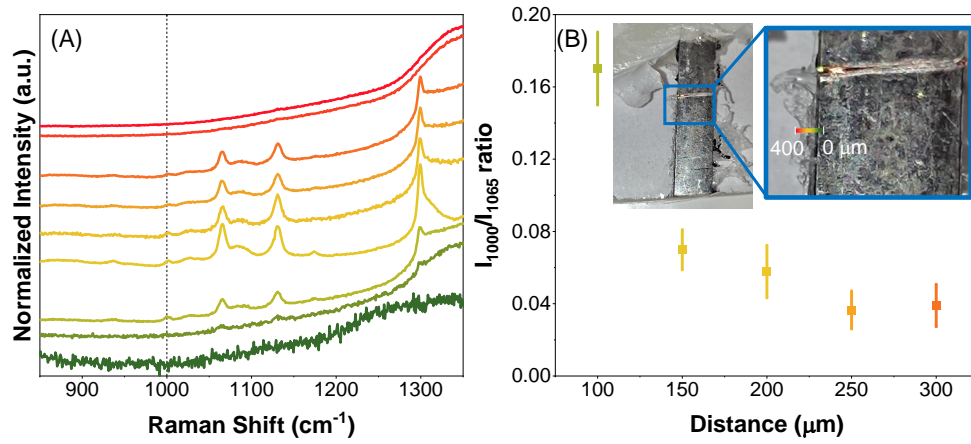
**Figure 5.9:** Raman spectra line scan of the EVA encapsulant inside a G/BS sample with coated ribbon with ink #1 without UV exposure. (A) Normalized intensity of the Raman shift on a line scan from 0 μm, in dark green, to 400 μm, in red. The vertical dashed line highlight the 1000 cm$^{-1}$ peak related to 2-PEA. (B) The ratio between the 1000 and 1065 cm$^{-1}$ peaks decreases as the distance increases, suggesting diffusion of 2-PEA into the encapsulant.

the encapsulant (see Fig. 5.10). Besides the IV curve we performed EL measurements, not reported here, that did not show any degradation. Upon UV light exposure the fluorescence from the degraded ink on the PV mini module becomes highly noticeable.
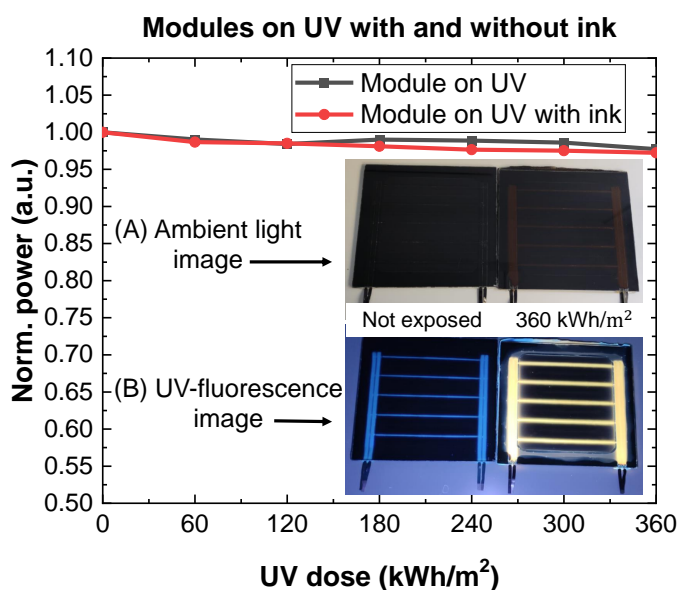
**Figure 5.10:** Normalized power of reference module without coated ribbons and coated module with ink #1 on UV exposure. It is important to note that the measuring equipment used has a reproducibility of ±1%, therefore minimal power loss in both cases is measured. (A) Ambient light image and (B) UV-fluorescence image were captured at two UV exposure levels: 0 kWh/m$^2$ and 360 kWh/m$^2$, revealing a significant increase in color change and fluorescence in the ink-coated modules.

## 5.4  Conclusions

In this investigation, the aim was to assess the long-term stability of black-coated metallic ribbons and their possible degradation effects. Three black metallic interconnects coated with different inks and encapsulated in a G/BS configuration were aged under light UV exposure with a protocol based on existing IEC standards. The commercially available coated ribbons remained stable after 120 kWh/m$^2$ of UV exposure. This investigation has identified that the studied UV-curable inkjet inks produce color changes in the portion of encapsulant surrounding the coated metallic interconnect. This, irrespective of the encapsulant used, and of the presence or not of UV blockers in the encapsulant. These findings cannot be necessarily generalized to all UV-curable inkjet inks.

In order to explain the observed color changes, we focused our investigation on ink #1, which produced the largest color change, and on its main component 2-PEA. From our observations, the 2-PEA component of the ink is photodegrading and contributing to the observed yellowing. This is proven with the slight increase of 22% in carbon index CI after 15 kWh/m$^2$ of UV exposure as observed from ATR-FTIR spectra. TD-GCMS measurements revealed that the HALS in the G/BS samples may have served not only to protect the encapsulant from photo-oxidation, but also to contrast the degradation processes taking place in the flush itself, thus accelerating the stabilizer's consumption. A different interpretation is that the stabilizer might have migrated during the exposure, making the HALS imperceptible. The findings of this study suggest that UV blocker encapsulants help mitigating the photodegradation of 2-PEA

on G/BS laminates, whereas they do not fully mitigate the degradation for the ink itself. It is possible, therefore, that other ink components contribute in a larger extent to the color change observed. However, we discourage the use of 2-PEA monomer for PV aesthetic applications and suggest the use of UV curable inks with aliphatic monomers, which have better non-yellowing properties, in combination with UV blocker encapsulants. The study is limited by the lack of information of undisclosed commercial ink components. In spite of its limitations, the study certainly adds to our understanding of the degradation of ink components on PV modules.

Additionally, the metallic ribbons of our one-cell modules were coated with the unstable ink #1 and aged under UV to assess the impact on aesthetics and electrical performance. The use of the investigated unstable ink would represent an aesthetical modification of color in the long-term demonstrating a potential long-term instability, but the electrical performance would be similar to a module without coated ribbons (less than 3% power loss after 360 kWh/m$^2$ of UV exposure).

A follow-up investigation would be that of designing a specific ink compatible with a commercial coating process for industrial scale PV modules, as no UV curable-inkjet inks made explicitly for coating the metallic interconnects of PV modules are apparently available, and the further study of several solutions provided by the market. This contributes to the understanding of the specific requirements needed for these coating layers.

In this chapter, we observed that some studied ink-coated metallic ribbons in the PV stack of materials under weather stressors produced a noticeable color change. However, there are no characterization techniques suitable to quantify the color change in BIPV modules. In the following chapter, we deal with common color characterization techniques and propose a suitable one for this field.

# 6 Accurate Color Characterization of Solar Photovoltaic Modules for Building Integration

The work in this chapter is based on the following article submitted to a journal and presented at the 40th European Photovoltaic Solar Energy Conference and Exhibition in Lisbon, 2023:

- A. Borja Block, J. Escarre Palou, A. Faes, A. Virtuani, C. Ballif, *Accurate Color Characterization of Solar Photovoltaic Modules for Building Integration,* Solar Energy, 2023 [82].

## Abstract

Accurate and reproducible color characterization is essential for colored building integrated photovoltaic (BIPV) products, both for manufacturing quality control and assessing long-term color stability. However, existing characterization techniques using colorimeters and spectrometers struggle to accurately determine color when a surface is behind a transparent layer like a solar PV laminate. In this chapter, we investigate different techniques and propose an innovative colorimeter to address this issue. Samples with varying transparent glass thicknesses and underlying colors are laminated and characterized using a scanner, an integrated sphere spectrometer, a commercial portable colorimeter, and the novel colorimeter. Results show that common scanners produce darker images and inaccurate color determination due to light losses in the glass. As glass thickness increases, reflectance decreases with the integrated sphere spectrometer and portable colorimeter. However, the novel colorimeter exhibits only minimal signal reduction. Bright colors experience more reflectance reduction with thicker glass than darker colors. All devices yield comparable results without the glass layer. The novel colorimeter, compensating for light losses, proves to be a suitable solution for accurately measuring color under glass laminates using reflected light. For example, it reduces the color change ($\Delta$E) from 57 (commercial portable colorimeter) to only 3 for an ivory colored glass laminate. This innovative tool has the potential to improve color characterization in BIPV products, enabling better manufacturing quality control and assessment of long-term color stability.

**Chapter 6.  Accurate Color Characterization of Solar Photovoltaic Modules for Building Integration**

## 6.1  Introduction

Building energy demand accounts for one-third of all final energy used globally [175]. By producing electricity on-site, integrated photovoltaic (PV) technologies play a significant role in reducing the energy demand of buildings. In addition, placing PV on buildings saves free land surface. Moreover, legislative initiatives such as the Building Energy Performance Directive [10] and the Directive on Renewable Energy [11] promote the incorporation of renewables in new constructions and renovations. Even if the building-integrated photovoltaic (BIPV) market is still niche, it has a huge growth potential as a result of global trends and of the impellent need to decarbonize the energy sector, integrating renewable energy sources in the built environment, focusing on energy efficiency and promoting heating with heat pumps. According to some projections, by end of 2030, the global market may be worth \$86.7 billion with a compound annual growth rate above 20% [194]. However, various constraints limit the incorporation of BIPV solutions into the built environment. These include: lack of standardization, evidence of long-term reliability of the products, tools to aid implementation (e.g. Building Information Modeling), smart interaction with the grid, and the low design flexibility [195].

BIPV products and projects heavily rely on aesthetics. Architects and other stakeholders in fact are often drawn to systems with distinctive design capabilities, in which a PV panel appearance is frequently, partially, or entirely modified. A key feature that building designers seek to tailor is color (see Figure 6.1). The color customization of PV modules can be achieved in different ways, for instance, by adopting digital ceramic printed (DCP) cover glasses, colored foils, and different coatings. Other technologies to produce colored PV modules have been developed and are described by H. Lee et al. [196]. Color characterization of a surface placed behind transparent front layer is essential for a wide range of applications such as glass for construction and colored parts for the automotive industry. In BIPV, it is fundamental to measure the color for quality control in production, color design, and to assess color changes after lamination or outdoor weather exposure.

Although many studies in the field of colored photovoltaic technologies focus on the performance of colored PV modules [196]–[198], to our knowledge, no study focuses on the color characterization techniques used and their limitations. There is still no standardized quantitative color characterization technique for PV modules. The academy and industry use common characterization techniques with devices such as colorimeters and integrated sphere spectrometers. These devices produce accurate reflectance measurements when the samples under investigation are positioned in the aperture of the integrating sphere or the colorimeter. In the case of integrated PV modules, the front layer is based on several-millimeter-thick glass, which creates measurement artefacts. The above-mentioned devices send a light probe through their aperture to then process the signal. A reduction in reflectance is observed due to the thickness of the transparent layer. Several authors have clearly described the problem of lateral light displacement losses due to the front glass [199], [200]. The colored layers (e.g. a foil or the inner face of a DCP glass) can be characterized in open-air before the lamination

**Figure 6.1:** (A) BIPV building made with a Solaxess nanotechnology white film. (B) With terracotta digital ceramic printing technology. Credit to Patrick Heistein. (C) Colored BIPV modules in a demonstrator in Bern. Courtesy of 3S Swiss Solar Solutions AG.

process, but color changes after the module lamination are frequently observed, as well as after a prolonged outdoor exposure. Therefore, it is critical to correctly measure the color for integrated PV applications to keep track of color changes in the long term and design colors effectively.

Precise color characterization is important for the industrialization of BIPV elements. This study proposes an innovative measurement technique to assess the reflected color of a specimen placed behind a transparent layer. In addition, we compare conventional measurement techniques to determine the color in PV modules. The main topics addressed are: a) artefacts of common color characterization techniques for BIPV elements, b) comparison of different commercially available devices, and c) presentation of an alternative method to reliably characterize color in glass laminates.

## 6.2   Approach and method

The methodological approach taken in this study started by preparing several samples with different glass thicknesses and colors. Both color coordinates and color change ($\Delta$E) between the samples are assessed using the different characterization techniques to compare and to determine the optimal solution. The International Commission on Illumination "Lab" (CIELab) color coordinates were calculated using the reflectance measured, the D65 illuminant [201] and the 10° observer [202]. Most devices already compute the color coordinates with internal data processing. The $\Delta$E was calculated with a MATLAB software according to

CIELABDE2000 formula [88]. More information about the color coordinates calculations can be found in Annex C.

### 6.2.1 Colored laminates

Samples with a wide variety of colors ranging from bright white to dark clay with various glass thicknesses were laminated as shown in Figure 6.2. The standard size of the samples was 7 cm by 7 cm.
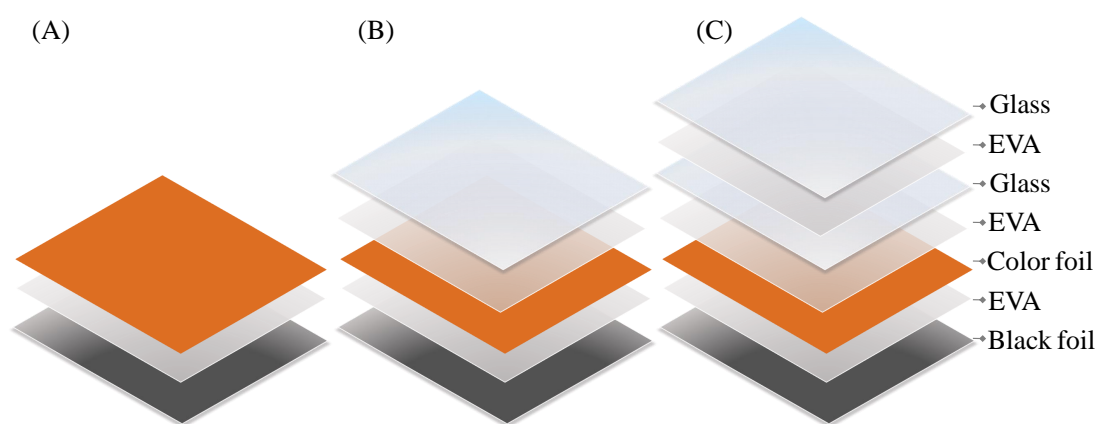


**Figure 6.2:** The materials used in the samples are commonly used in PV modules. (A) Sample without any glass cover used as reference. (B) Sample with one glass layer of 3.2 mm. (C) Sample with two glass layers of 3.2 mm laminated together to increase the thickness of the glass to 6.4 mm, because the only available glass was 3.2 mm thick. A black backsheet foil is used in the rear side of the samples to avoid background artefacts, because some of the color foils are not fully opaque in the visible spectra. All materials are laminated with ethyl vinyl acetate (EVA).

The samples were developed using flat solar-grade glass with a thickness of 3.2 mm and no surface treatment. To create the final laminates, a typical EVA lamination recipe was used with maximum temperature of 145°C and an approximate duration of 15 minutes. To increase the glass thickness, more glass layers (with a thickness of 3.2 mm) were bonded with EVA during the lamination process, because it was the only glass thickness available.

Depending on the foil used, the color may vary after lamination; however, the color shift is generally small or nonexistent. The samples of each hue have almost the same appearance under sunlight to the human eye regardless of the varying glass thicknesses and the presence or not of a cover glass. Figure 6.3 shows the samples beneath the sun.

The transmittance and reflectance of the solar glass layer of 3.2 mm and 6.4 mm including the
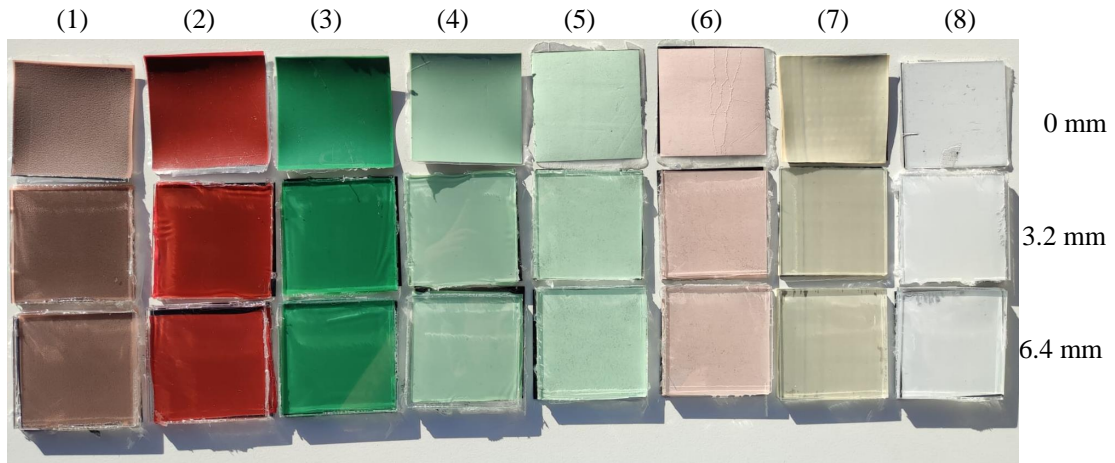
**Figure 6.3:** Digital camera picture of all of the samples used in this study under sunlight with uniform illumination. It includes eight types of colors with two glass thicknesses and without glass. Irrespective of the presence or not of a glass cover (and its thickness), for each color layer the human eye perceives very similar colors.

EVA bonding layer were measured. The 6.4 mm glass differs from the 3.2 mm glass by having a transmittance of 1.5% to 2% lower than the 3.2 mm glass in the visible spectrum (380 nm to 730 nm). More data related to the samples can be found in Chapter 2. To investigate the influence of the illuminated area while measuring with the novel colorimeter, several white colored (#8) squares samples with sides ranging from 20 cm to 10 cm were manufactured without glass, with 3.2 mm glass, and with 6.4 mm glass, as shown in Figure 6.4. Black opaque masks were utilized to cover the samples and measure regions as small as 1 cm x 1 cm.

### 6.2.2   Characterization techniques

The data were collected with conventional instruments used in industry and for research to analyse the appearance of the colored samples. These devices include a scanner, a portable colorimeter, an integrated sphere spectrometer, and the novel colorimeter developed. One could use a digital camera to retrieve the RGB coordinates, a method that we did not use in this work.

**Scanner**

Many researchers have utilized scanners to assess the appearance of modules by visual inspection [85], [149]. Visual inspection in photovoltaic research is a common characterization technique to evaluate the appearance of the samples. It is useful to determine changes that
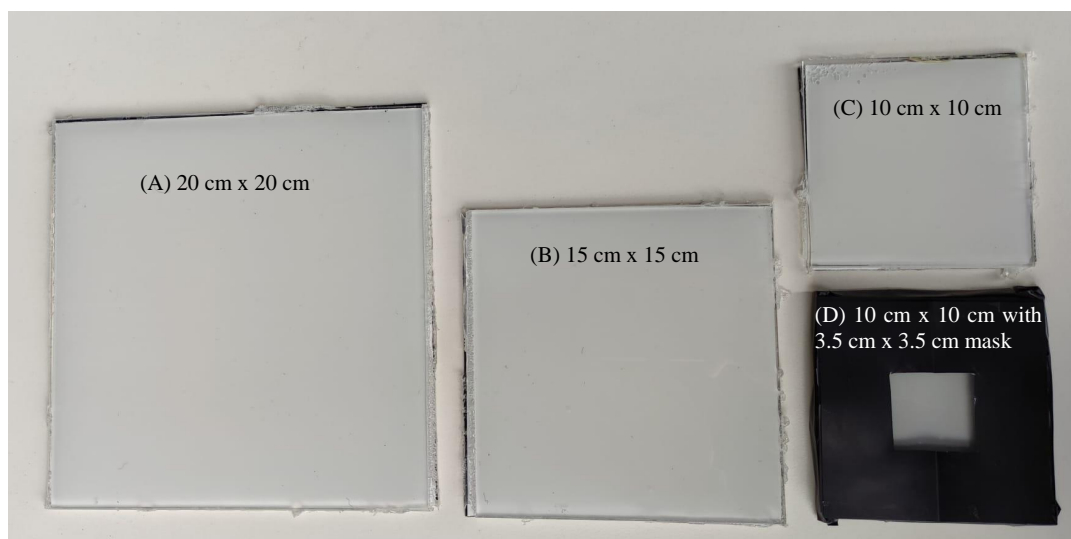
**Figure 6.4:** Picture of the larger samples with color white (#8). (A) 3.2 mm thick 20 cm x 20 cm sample. (B) 3.2 mm thick 15 cm x 15 cm sample. (C) 3.2 mm thick 10 cm x 10 cm sample. (D) 6.4 mm thick 10 cm x 10 cm sample with a 3.5 cm x 3.5 cm mask.

can appear such as bubbles, cracks, delamination, etc. Digital scanners (of the type that can be found in printers) can be used to perform a visual inspection of small-area samples. They are commonly utilized because the resolution and lightning can be consistent to compare samples before and after accelerated-aging tests. Scanner devices typically use line arrays of light sources and reproduce an image by moving the sensors over the full surface of the sample.

When performing visual inspection with a scanner on a glass laminate it is common to notice a darkening of the image (see Figure 6.6). Depending on the manufacturer, there could be different color corrections with internal processes that are unknown for the users. In the case of assessing colors, the result would be given in RGB coordinates with an unknown illuminant. For this investigation, a software was developed using image processing to calculate the color change between a reference color and the pixels or the region of interest [88]. A conventional scanner Canon imageRUNNER ADVANCE DX C5860i was used to measure the samples.

**Portable colorimeter**

The colorimeter used in this investigation was a portable X-Rite i1Pro Rev E collecting data from 380 nm to 730 nm with a sampling interval of 10 nm. In the present study, we will define it simply as colorimeter. Colorimeters employ a light source that shines momentarily into the sample before detecting its reflectance. Typically, various parameters may be changed, such as the color space, the range of the reflectance data, the observer (2° or 10°), the illuminant, and the sampling interval. Commercial colorimeters are usually compact portable devices

that can make the measurement in a few seconds. The initial procedure with this tool is to perform a calibration against a white reference sample. This is required to obtain a maximum reflectance value of 100%.

**Spectrometer**

Reflectance data for this study were collected also with an integrated sphere UV/VIS/NIR spectrometer Perkin Elmer Lambda 950. In this work, we will refer to this tool as spectrometer. Such equipment is capable of measuring transmittance and reflectance from 250 nm to 2500 nm. However, we focused our analysis on the visible range only. The device makes use of an integrating sphere, which helps capturing the light probe reflected from the sample. Differently from the colorimeter, which generates a light probe of varying wavelengths and rapidly recovers the reflectance, this instrument generates a scan of wavelengths with a chosen sampling interval. The reflection from each wavelength is stored. Prior to data collection, a calibration with a white reference (spectralon) and dark reference (no sample lid placed) is performed to have the maximum and minimum reflectance values. The reference data is later used to correct the reflectance of the measured samples. To perform a measurement, the sample is placed into the aperture of the integrated sphere and covered with the device's lid. The integrated sphere spectrometer measurements take longer than the colorimeter measurements. It might take up to 3 minutes per measurement depending on the wavelength range and sample interval. In this work, we focused on at the visible range and used a sampling interval of 10 nm.

**Novel colorimeter**

In this chapter, the term novel colorimeter will be used to describe the proposed characterization technique. The novel colorimeter detects the signal via an optical fiber. The signal is subsequently transferred and analyzed. The measurements are taken in real time and are completely dependent on the lighting. The illuminated area must be greater than the measuring spot. If the lighting is varied, then naturally, the reflectance measured will be altered. To characterize the samples and evaluate color, the probe, sample, and lighting should all be correctly positioned.

Figure 6.5 depicts the arrangement employed. A fiber optic spectrometer measuring in the visible range was positioned at 45° with respect to the samples. The lighting was achieved using a diffuse lamp with a visible spectrum signal similar to D65 (see Annex C).

The following steps were implemented to perform the measurements:

1. Turn on the lamp until the spectrum is stable (20 min).

2. Collect a dark measurement covering the aperture of the probe's spectrometer in order to calibrate the 0% reflectance.
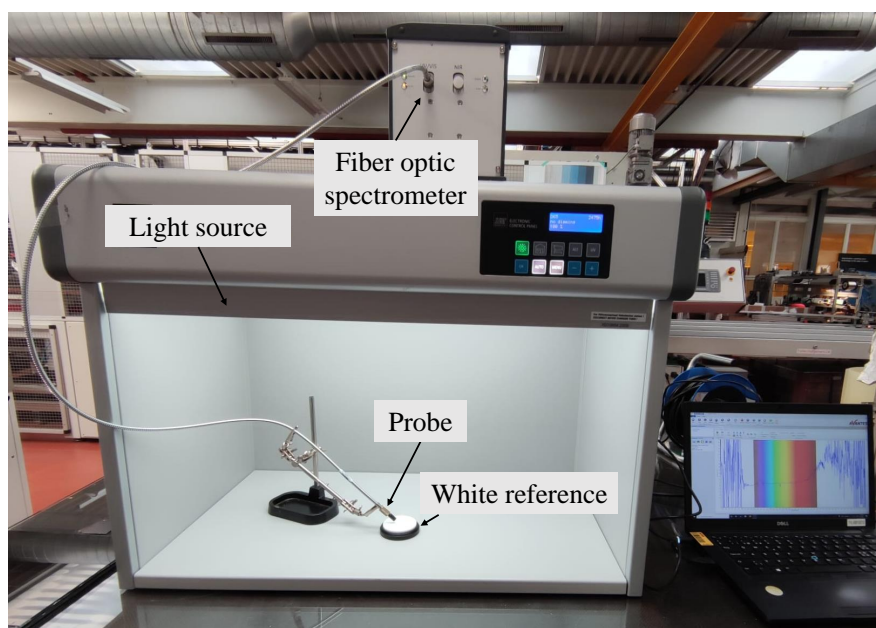
**Figure 6.5:** Image of the novel colorimeter components. It includes a fiber optics spectrometer positioned at 45° and a light source similar to D65.

3. Measure a white reference pointing the probe to the center of the spectralon to measure the 100% reflectance.

4. Position the sample inside the setup and perform measurement.

## 6.3 Results

The results are divided in four main sections. The first section examines the results of the digital images generated by the scanner. The second includes the characterization of the samples without glass and the third with glass respectively. Finally, the illumination area was investigated on white (#8) samples.

### 6.3.1 Digital imaging by scanning

Following the scanning of the samples, they are processed with the software that calculates the $\Delta$E of each pixel of the chosen picture with respect to a fixed color reference in RGB coordinates. The reference color is the scanned color of the colored foil without any glass layer. The color change rises as the thickness of the glass is increased. Figure 6.6 depicts the difference between a dark and a bright color.

The reason of the color change in scanned images is that the image produced is taken with a line scan, therefore the sample is never fully illuminated. A line light source moves generating the full image. Because of the presence of a transparent media (glass) - between the scan plane

**Figure 6.6:** Raw and processed scanner images with a dark sample (#2 red) and a bright sample (#6 pink). A low color difference ($\Delta$E) is shown as blue, and red as a high $\Delta$E. Since the reference is always the color without a glass layer itself, the first sample (sample without glass) always appears as dark blue. When the glass layer is increased the $\Delta$E increases and the sample appears red.

and the colored foil - the signal is reduced (by multiple optical reflections in the transparent medium) and the samples appe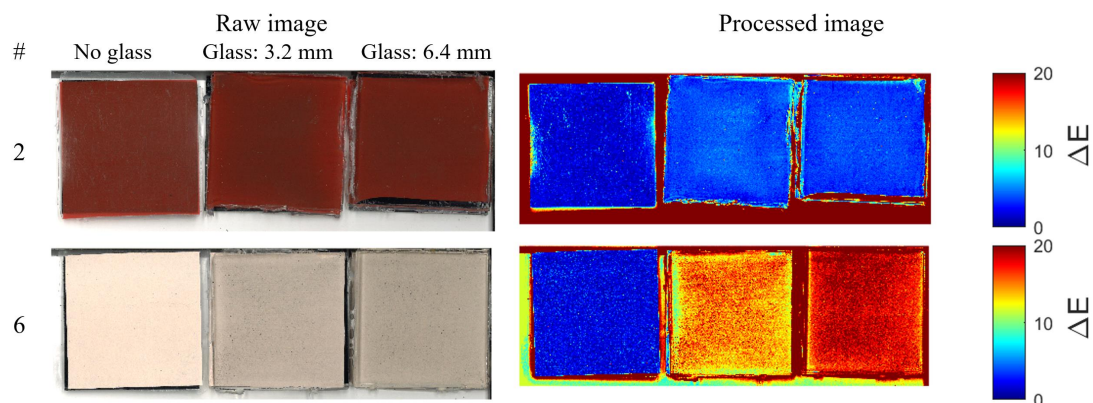ar darker. A high $\Delta$E is measured on bright samples and a low one on darker ones. Scanners are still useful to perform visual inspection in small samples to assess cracks, bubbles and other physical effects, but colors cannot be assessed properly when a transparent media is between the sample and scan plane. Moreover, PV modules are too large to fit into a typical scanner. If a scanner is used as a tool to measure the color change of a sample with transparent media, then it needs to be analyzed as relative color change and not as an absolute value. Some solutions could involve a color correction software with the use of image processing or the use of a different setup with a camera at a fix position with stable illumination of the full sample maintaining the camera parameters constant. If the samples are illuminated uniformly with large-area illumination a similar color would be perceived irrespective of the presence of the glass thickness (see Figure 6.3). If this condition is not fulfilled, the presence of the glass will introduce measurements artefacts that increase with increase glass thickness (see Figure 6.6).

### 6.3.2 Characterization of colored samples without front glass

We measured the reflectance of the samples without the presence of a glass layer. It was expected to see low color changes ($\Delta$E) between the devices. In Figure 6.7, we observe the reflectance for ivory and clay, a bright and a dark color. All curves showed similar appearances and intensities, but to quantitatively compare the devices the $\Delta$E was calculated between all

of the studied characterization devices, as it can be observed in Figure 6.8. We stress the fact that a $\Delta$E lower than 2 is barely noticeable to the human eye. We therefore use this value as a reference.
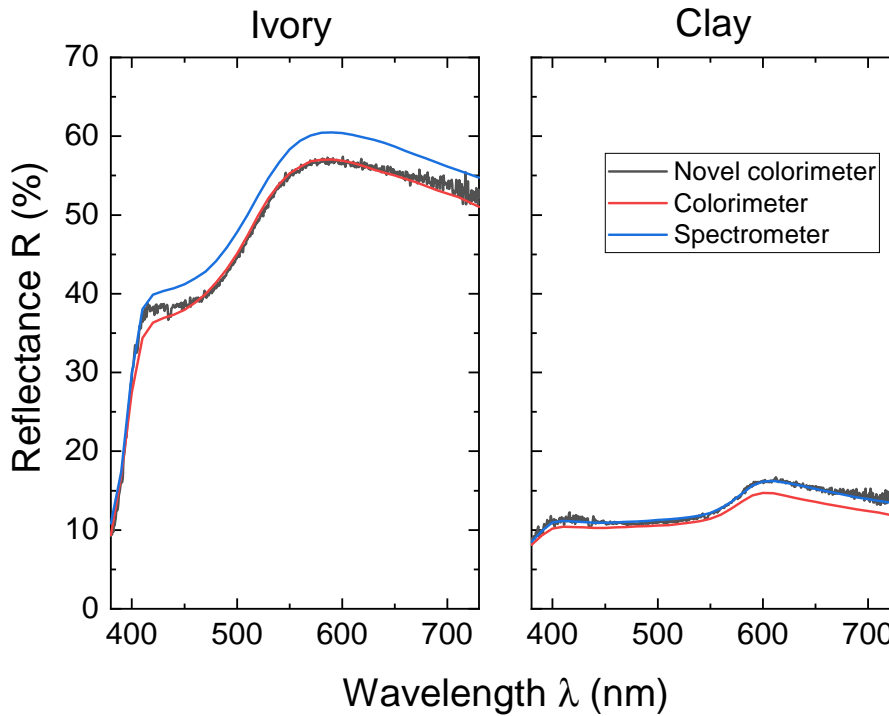


**Figure 6.7:** Reflectance of ivory and clay samples without glass measured with all the characterization equipment.

The devices measurements are comparable in most cases, with excellent results for bright colors. The spectrometer signal is always slightly higher than the colorimeter. The novel colorimeter performs in most cases in between the two other solutions, for bright color similarly as the colorimeter and for dark ones closer to the spectrometer data. In the case of dark colors, the $\Delta$E between the equipment is higher, being red the color with most discrepancies. Surprisingly, the greatest disparities are between the spectrometer and the colorimeter, and were observed for dark hues. The novel colorimeter and the spectrometer measured higher signals than the colorimeter, consequently the $\Delta$E is usually higher for this device.

### 6.3.3 Characterization of colored samples behind a glass

The reflectance was characterized on colored samples behind glass with the novel colorimeter, the spectrometer with integrated sphere and the commercial portable colorimeter. In this section, only the results with one bright and one dark color are included.

Figure 6.9 shows reflectance measurements taken with different characterization devices. What is interesting in this figure is the dramatic decrease in reflectance for the colorimeter

## ΔE between different devices
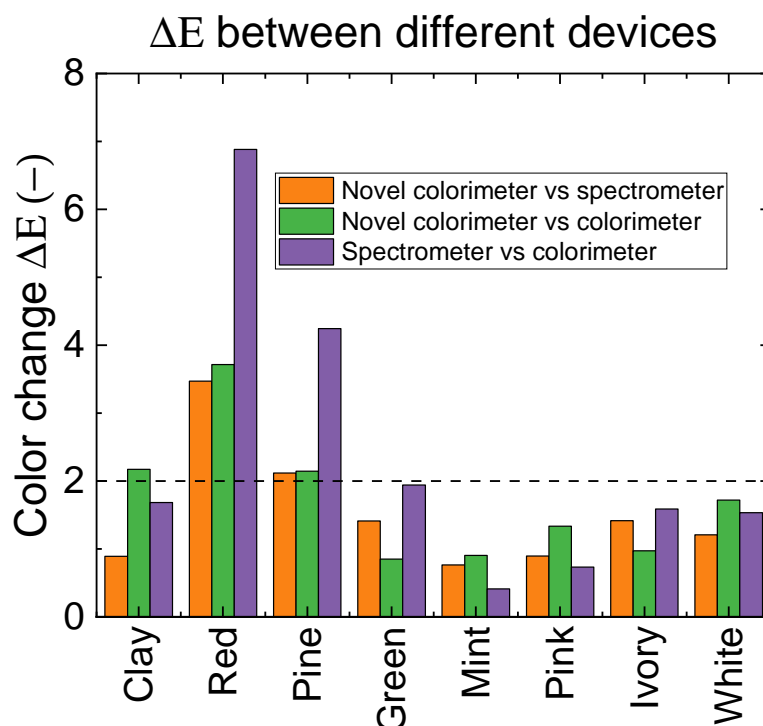


**Figure 6.8:** $\Delta$E of the samples without glass comparing all the characterization techniques. Note that the scale goes from 0 to 8. The dashed line at $\Delta$E=2 represent the limit of human eyes detection of color change.

and integrated sphere spectrometer measurements. The reflectance is expected to decrease with the increase in glass thickness. It is now understood that the measurement plane plays an important role in the reduction of the signal. Incorporating a glass layer into the samples shifts the measurement plane. In contrast to these characterization techniques, the novel colorimeter performs better, since the signal reduction is minimized. However, there is still a slight decrease in the signal when the glass thickness is increased. The glass layer on top of the samples causes light trapping of the ray reflected at a higher angle than the critical angle for which the light cannot escape the glass (for visible light the critical angle is 42°) and produce lateral trapping of the light, thus reducing the light reaching the detector [203].

Ivory color is an example of a color for which a strong signal decrease appears. This occurs because it is a bright color with high reflectance. The reflectance is then converted to produce the color on the screen or paper to have a visual representation of the results. Table 6.1 depicts how the color is according to the measured reflectance for each equipment.

It is observed how the signal and color change is almost maintained for the novel colorimeter while for the other equipment it decreases and a change of color to gray or black is clearly appreciated. The novel colorimeter reduced considerable the $\Delta$E compared to the other characterization tools. A possible explanation for the color change observed in the novel
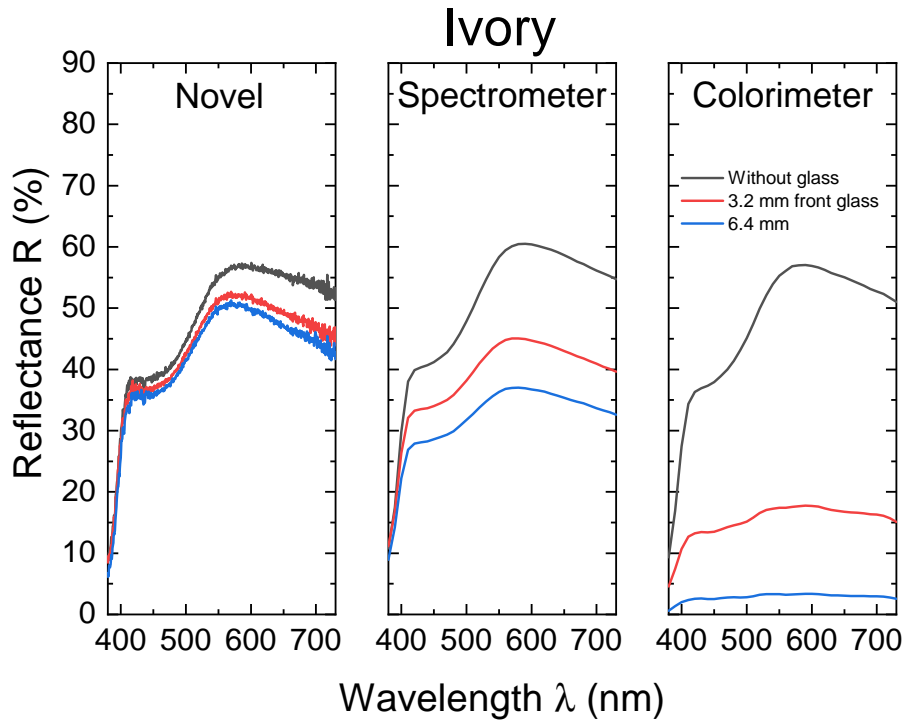
**Figure 6.9:** Reflectance curves in the visible range for the novel developed colorimeter, the integrated sphere spectrometer and the colorimeter for ivory color. It can be appreciated how the signal decreases for each device, as the glass thickness is increases.

colorimeter may be that indeed the glass properties are not exactly the same for 3.2 mm and 6.4 mm glass (see Chapter 2). Another possible explanation for this is that after lamination, depending on the colored foil used, the color could vary. However, for the human eye it is still challenging to notice the color difference between these samples.

Turning now to the experimental evidence on the darker colors, we observe the same reflectance decrease for the different devices but at a smaller magnitude. For the novel colorimeter the difference between the sample without glass and the thickest glass is only of 2.6 in $\Delta$E. Figure 6.10 exemplifies how the signal decrease in dark colors.

It can be appreciated how the signal decreases highly for the colorimeter and only slightly for the spectrometer and for the novel colorimeter. The reflectance of the novel colorimeter decreases with 3.2 mm glass, but it slightly increases from 3.2 mm to 6.4 mm glass. Interestingly, the reflectance was observed to slightly increase for dark colors (clay #1, red #2 and pine #3) from 3.2 mm to 6.4 mm glass when measuring with the novel colorimeter. Different effects may explain this. Firstly, by the physical properties of the transparent layers used shown in Chapter 2, and, secondly, by the reflections occurring in the glass itself. Other possible explanations may be the non-uniformity and instability of the lamp of the novel colorimeter, and the illumination entering from the sides of the glass. Table 6.2 depicts the calculated colors from the reflectance data.

**Table 6.1:** Ivory samples shown from RGB coordinates computed from the reflectance spectra for the devices studied. The colors were generated using the software "Paint". Note that depending on the characteristics of the display or paper is how the colors appear.

| Sample ID | Novel colorimeter | Spectrometer | Colorimeter |
|:---:|:---:|:---:|:---:|
| Ivory 0 mm | | | |
| Ivory 3.2 mm | | | |
| Ivory 6.4 mm | | | |
| $\Delta$E 0 mm vs 3.2 mm | 4.1 | 4.4 | 16.8 |
| $\Delta$E 0 mm vs 6.4 mm | 2.6 | 4.5 | 27.2 |
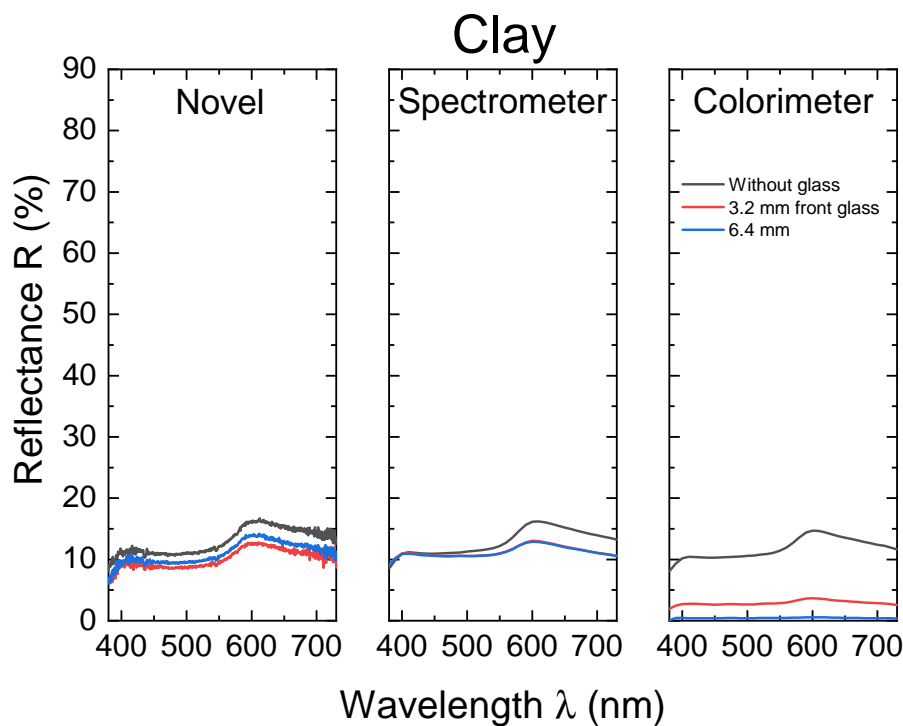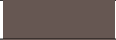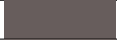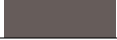


**Figure 6.10:** Reflectance curves in the visible range for the novel manufactured colorimeter, the integrated sphere spectrometer and the colorimeter for clay color.

In summary, these results shows that the decrease in signal is much higher for bright colors and lower for dark colors with glass layers. Figure 6.11 shows the calculated $\Delta$E for all the samples (no glass vs 6.4 mm). The strongest measurements artefacts introduced by the glass layers are observed with the handheld commercial colorimeter in first place, the integrated sphere in second place and, finally, the novel colorimeter is only slightly affected.

We observe that the $\Delta$E of the novel colorimeter are lower than the spectrometer and the same effect of higher $\Delta$E with bright colors appears. Let us remember that in the sunlight all the samples have a very similar appearance in color to the human eye (see Figure 6.3).

**Table 6.2:** Visual representation of the reflectance data plotted using a conversion into RGB coordinates for clay samples measured with the three devices. Again, the colorimeter measures the thick glass sample as black, and the spectrometer and novel colorimeter perform better with a $\Delta$E lower than 5 and 3 respectively for the thickest glass.

| Sample ID | Novel colorimeter | Spectrometer | Colorimeter |
|---|---|---|---|
| Ivory 0 mm | | | |
| Ivory 3.2 mm | | | |
| Ivory 6.4 mm | | | |
| $\Delta$E 0 mm vs 3.2 mm | 4.1 | 4.4 | 16.8 |
| $\Delta$E 0 mm vs 6.4 mm | 2.6 | 4.5 | 27.2 |

### 6.3.4 Illumination area of white colored samples with and without glass

A critical aspect of the newly developed colorimeter is the area of illumination, as this is the key difference with the other equipment. The visible light source must be stable over time and illuminate uniformly a large region. The illumination area required depends on the color and glass thickness of the sample. To determine the area that needs to be illuminated, squared samples such as the ones shown in Figure 6.4, with sides ranging from 20 cm to 10 cm were manufactured without glass, with 3.2 mm, and with 6.4 mm glass. Black opaque masks were used to cover the samples and measure smaller areas. The samples were built with bright white colored foil, because it produces higher light displacement, therefore it represents a case where there is a necessity for large area illumination. Figure 6.12 shows how the $\Delta$E increases when the illuminated area decreases.

When the glass is thicker a larger area needs to be illuminated to diminish the light trapping losses. In Figure 6.12, the 6.4 mm samples cross the $\Delta$E=2 reference established in this work at approximately 8 cm x 8 cm. The 3.2 mm samples cross it at 5 cm by 5 cm and the sample without any glass only increases in $\Delta$E when the measuring area is partially covered by the mask at very small area. This proves that when a transparent layer is used a good uniform illumination over a larger area will improve the measurements as the light is trapped over a long distance depending on the reflected color, the glass thickness and the glass surface.
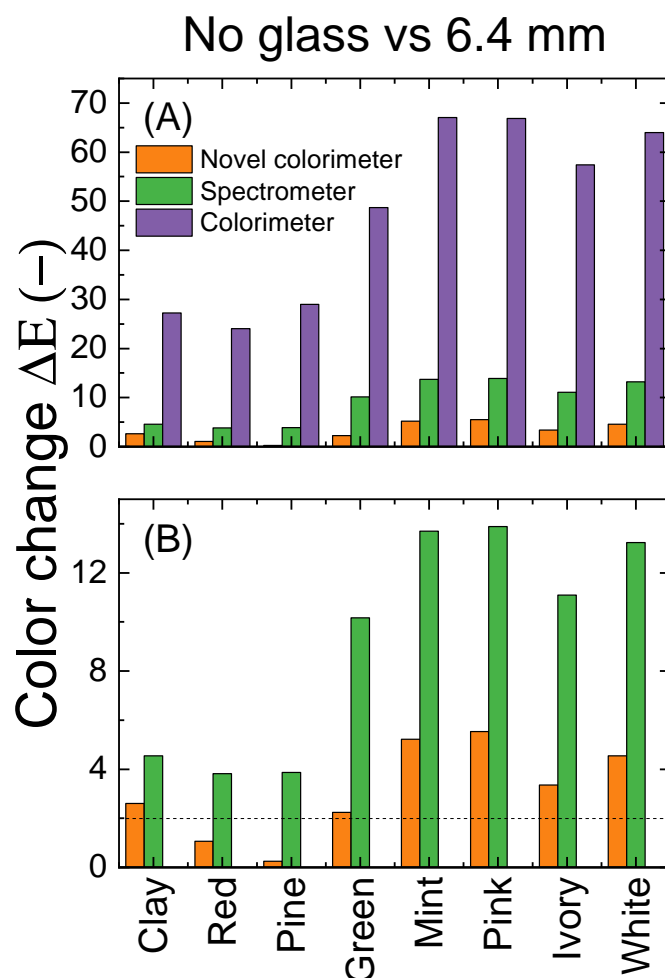
**Figure 6.11:** Comparison of $\Delta$E for all samples without glass against the 6.4 mm glass measured with the three characterization devices. (A) The colorimeter measured extremely high $\Delta$E for all colors, and it is observed how dark colors (i.e. clay #1, red #2 and pine #3) have lower $\Delta$E compared to bright colors (i.e. pink #6, ivory #7 and white #8). (B) Same graph as (A) with a lower scale in the $\Delta$E axis. A threshold of $\Delta$E=2 is placed as a dashed line just as a reference of perceivable color change for the human eye.
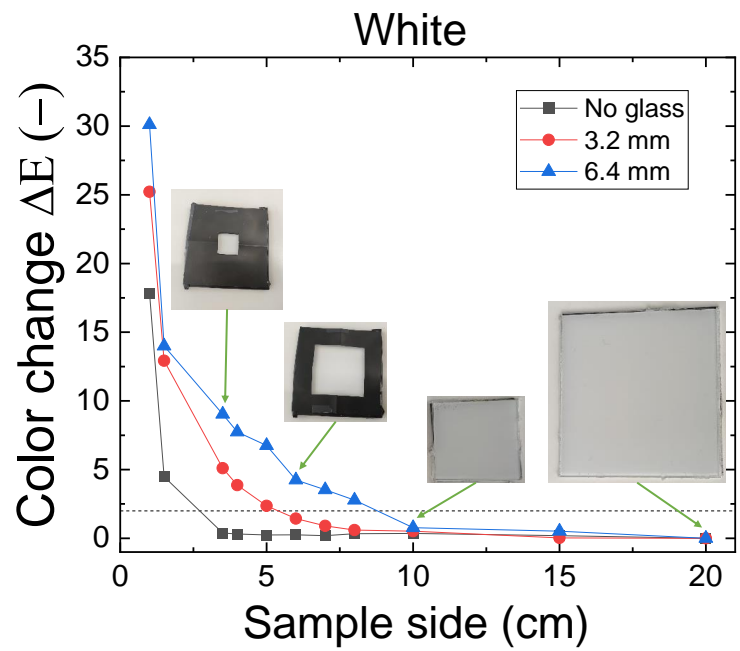
**Figure 6.12:** White-colored (#8) squared samples without glass, and placed behind a glass layer with a thickness of 3.2 mm and 6.4 mm, respectively. The sides of the squared samples vary from 20 cm to 10 cm and were measured with the novel colorimeter. For smaller area measurements black opaque masks were used. The reference color to calculate the $\Delta$E is the largest sample measurement for each glass thickness, that explains why at 20 cm of sample side the $\Delta$E=0.

## 6.4 Discussion

One of the main differences between the four characterizations techniques investigated in this work is the illumination area. While the scanner, the colorimeter, and the spectrometer use spot illumination, the novel colorimeter illuminates the entire sample. The glass layer act as a light guide because of the multiple reflections happening between the two different interfaces (glass/air and glass/colored sample). The lateral attenuation distance increase: (1) with the increasing glass thickness and (2) when the reflectance of the color sample is higher (i.e. for brighter colors). The following figure depicts how a localized light probe generated by devices such as the colorimeter and the spectrometer is scattered and trapped in the glass.
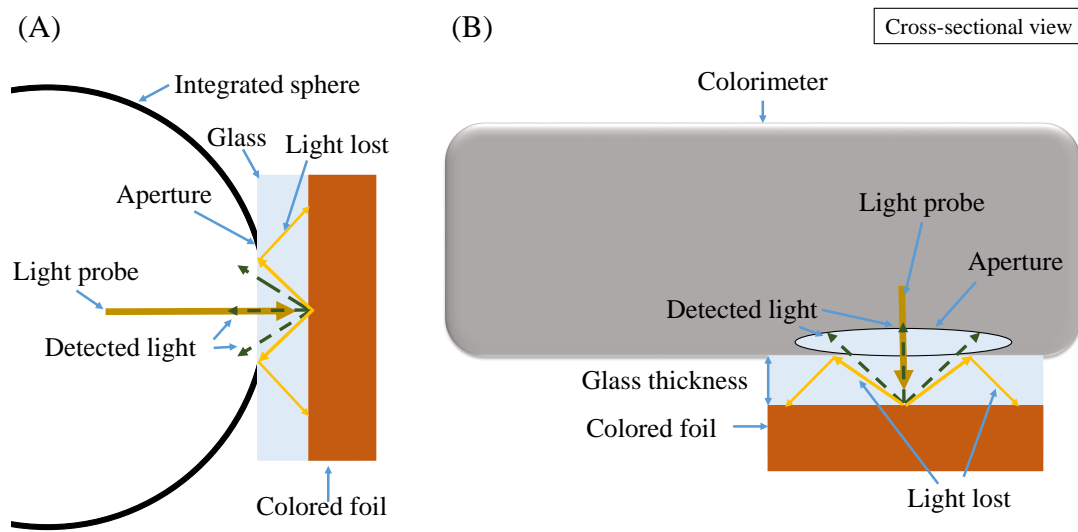


**Figure 6.13:** Simplified cross-sectional view of the common color characterization techniques with (A) Integrated sphere spectrometer and (B) conventional portable colorimeter. In both cases, the light probe goes through the transparent layer (usually glass for PV modules) and lateral displacement losses of light occur, producing measurement artefacts. A portion of the light signal is lost in multiple reflections in the glass and does not reach back to the instrument detector through the device aperture; creating artefacts. The artefacts are higher with increasing glass thickness.

The glass layer on top of the samples traps the light reflected at an angle greater than the critical angle ($\theta_c$= 42° for our case) for which the light cannot leave the glass and produces lateral trapping of the light (see Figure 6.14). The trapped light will not be detected for the colorimeter and the spectrometer causing artefacts in the reflection measurements. Snell's law (see Equations 6.1 and 6.2) describe how is the critical angle calculated for the glass/air interface being $n_1$ the refractive index of the air and $n_2$ of the glass respectively [203], [204].

$$n_1 \times \sin\theta_1 = n_2 \times \sin\theta_2 \qquad (6.1)$$

$$\theta_c = \arcsin \frac{n_1}{n_2} \tag{6.2}$$
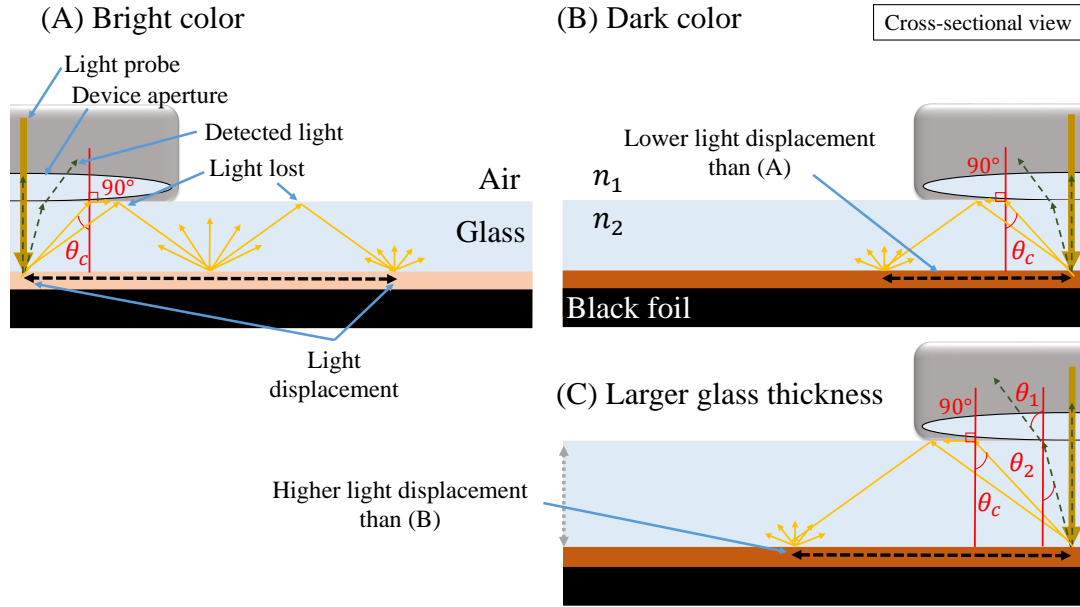


**Figure 6.14:** Cross-sectional schematic description of the multiple internal reflections taking place inside the glass that produce measurement artefacts of the colorimeter and spectrometer. (A) Bright color: The light probe enters the sample through the device aperture with a bright light color foil being displaced considerably due to the increased glass internal reflections. (B) Dark color: Light probe goes into a dark colored sample and it is displaced slightly. Because the reflectance of sample (A) is higher than (B) the light displacement is higher in (A) than (B). (C) Dark color with thicker glass: Same color as (B) but with larger glass thickness, when the glass is thicker the light displacement is larger. The displaced light in all cases does not cross the device aperture and is not detected causing measurement artefacts.

It is observed in Figure 6.14 that when there is a brighter color or thicker glass the light displacement is larger than with a darker color. Therefore, larger area illumination is needed for those cases in order to compensate the light trapping losses. The novel colorimeter, thanks to large-area illumination with a light source with spectra similar to D65, has minimal losses and is the most reliable measurement technique (see Figure 6.15). This helps to measure quantitatively the color coordinates and determine the color change of PV modules after the lamination process, accelerated-aging testing or outdoor exposure. The novel colorimeter measures in most cases in between the two other solutions, for bright color similarly as the colorimeter and for dark ones closer to the spectrometer. Whenever a colored solution is adopted in the laminate of a PV module, the newly proposed equipment allows to increase considerably the accuracy and reproducibility of the color characterization.

Several specific concerns exist for the novel assembled arrangement. The measurements are affected by the change in light outside the box because the box is open. A simple solution is
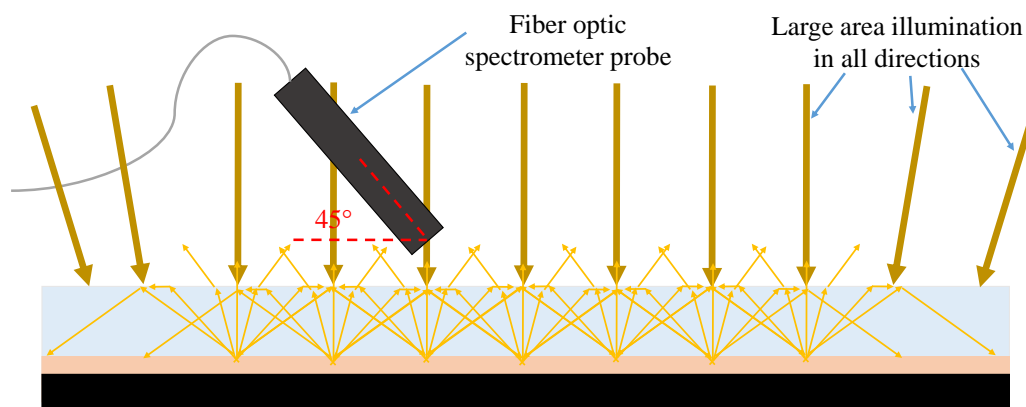
**Figure 6.15:** Novel colorimeter based on a fiber optic spectrometer with large area illumination. The multiple reflections in the glass compensate the light trapping in the glass. Note that the illumination comes in all directions since it is diffuse illumination.

to cover the box or to perform the calibration periodically if the white reference reflectance is no longer equivalent to 100% in the visible range. The main difference between the novel colorimeter and the other equipment is that the illuminated area includes the entire sample.

The use of large area illumination is not the only alternative to measure accurately the color under transparent media. Hergert et al. used an integrated sphere spectrometer and a white reference was laminated with the same cover glass to minimize deviations in their measurements [205]. This reduces artefacts, because the colored layer is not tangent to the integrated sphere. When the calibration is performed with the transparent layer the signal is lower which results in a correction of all the measured data. The drawback of this solution is that for every type of transparent layer a calibration reference sample should be manufactured. Another disadvantage of standard spectrometers based on integrated spheres, is that they are not portable, whereas a solution based on the novel colorimeter could be made portable.

An alternative to reduce the reflectance signal decrease is the use of larger integrating spheres. Wilson and Elsnert studied different colored glasses with various sizes of integrated spheres showing that the larger integrated sphere performed better than the small one [199]. When the integrating sphere is large, the transparent layer thickness influence is minimized. This alternative solution implies the use of expensive and not portable equipment.

The results in the current investigation show the decrease in signal for several devices. If we observe carefully how the reflectance decreases, we notice that there is close proportionality. The same effect was also observed by Rosillo et al. [206]. In their investigation, they calculated

the Yellowing Index (YI) in PV modules by measuring with a bifurcated fiber optic spectrometer with spot illumination. They concluded that there was proportionality between the sample's yellowness with and without different glasses. In their case, as they were calculating the YI and the absolute contribution of reflectance is cancelled, the decrease of reflectance was not important. To retrieve the color coordinates the absolute reflectance is necessary. However, if the physical properties of the sample materials are known, a modeling approach can be employed. When using common color characterization techniques, such as a portable colorimeter, corrections could be applied to its data retrieving the absolute reflectance.

This presented investigation is limited to samples with color foils laminated with conventional PV materials. DCP glasses, colored foils and solar cells were not studied, but the expected results should be similar, because the principle of having a colored layer placed behind a transparent media is the same. Another limitation of this study is the used glass and the small size of the samples. We used flat 3.2 mm low iron glass common for solar applications without any textured of special surface treatment. In the PV industry, it is common to use coatings such as anti-reflective coatings or special textures in the glass and this could affect the measurements. We plan to perform further work to investigate the impact that the glass surface may have on the color measured. Future work also involves the characterization of color on PV modules with a solar cell placed behind the color sample.

We believe that the field of application of the method and novel piece of equipment extend far beyond the PV industry and may find application in many other fields that make use of coloring solutions and glass, such as the glass, the building, and automotive industries. Therefore, the potential of the newly developed tool is considerable.

## 6.5   Conclusions

The aim of the present research was to examine conventional color characterization techniques used in the BIPV industry and to propose a solution for the artefacts measured in samples with color layers behind glass laminates. We investigated a common scanner, a portable commercial colorimeter, an integrated sphere spectrometer and the novel manufactured colorimeter.

The investigation has shown that common scanner machines cannot assess accurately colors in PV modules, because the light is trapped in the glass, which decreases the reflected signal and produces darker images, therefore altering an accurate color determination. The $\Delta$E between the samples with glass is lower for dark colors than for brighter ones. Scanner images are still useful devices to observe physical changes such as cracks, bubbles or relative change in color.

This study has demonstrated that the novel colorimeter assembled with a fiber optic spectrometer positioned at 45° with respect to the samples and using a uniform and stable D65 light source can perform reliable color measurements under glass laminates. We observe in

fact a high reflectance reduction with the integrated sphere spectrometer and the portable colorimeter when a glass layer is present between the colored sample and the propping head, as the glass thickness of the sample increases. The signal is only slightly decreased when using the novel colorimeter. Bright colors and thicker glass cross sections show a larger reflectance reduction with respect to darker colors and thinner glass cross sections. The measurements comparing the characterization techniques indicate that the novel colorimeter performs much better than the commercially available solutions, in terms of accuracy.

Further research should be carried out to improve the measurements performed by the novel colorimeter, moreover, the investigation of angle dependent colors, surface effects such as glass texture and anti-reflective coating, light sources and calibration procedures. The challenge now is to fabricate a portable novel colorimeter that measures reliably the color in commercial integrated PV modules. Such equipment, based on the presented investigation, would be certainly beneficial in color design, degradation assessment and quality control. Furthermore, the application of the tool extends far beyond the PV industry, and may find application in the glass, building and automotive industries. In the final chapter, we will summarize the findings of this thesis and engage in a discussion regarding potential avenues for further research activities aimed at advancing this investigation.

# 7 Discussion, Conclusions and Perspectives

With global temperatures already exceeding record values due to ongoing global warming, the impacts of climate change are becoming increasingly evident and are posing significant threats to both biodiversity and human safety in various regions. To mitigate these challenges, the transition to clean and renewable energy sources is imperative. PV energy stands out as a key contributor in this transition, thanks to its cost-effectiveness and minimal carbon footprint. Additionally, PV technology helps securing the energy supply locally, avoiding unreliable imports. However, a major challenge facing this technology is the space it requires. In countries with limited available land, the widespread deployment of PV systems clashes with other land uses. Even in larger countries, the installation of substantial solar farms on agricultural land is encountering growing resistance from both national and local governments due to conflicts over land usage. Integrated PV solutions, (e.g. agri-PV and BIPV), offer promising ways to overcome land availability issues. Nevertheless, these innovative approaches require specific conditions and creative solutions to become practical choices (for instance, colored BIPV).

In this thesis, our main focus was on BIPV technology, its environmental impact, and the incorporation of new materials like inks in the module's components. We conducted a complete analysis covering all stages of the manufacturing process, presenting a proof-of-concept equipment that could potentially be scaled up for mass production. We also examined the durability and compatibility of these materials, studied the degradation modes observed, and suggested ways to mitigate those issues. Finally, we explored various techniques for color characterization under transparent layers for quality control, degradation analysis and improved aesthetics over time. Figure 7.1 describes the topics explored in this thesis.

In Chapter 3, we analyzed the carbon intensity (CI) implications of installing PV systems on surfaces with sub-optimal orientations. The average values extracted from the probability distributions of PV system CI for various orientations and European countries reveal that for buildings, the CI is 35.8 $gCO_2$-eq/kWh with an optimal orientation (i.e. south-facing at the best tilt). For typical rooftop setups (assuming a 17% energy yield reduction due to misalignment compared to optimal exposure), this value slightly rises to 43 $gCO_2$-eq/kWh. Façades exhibit
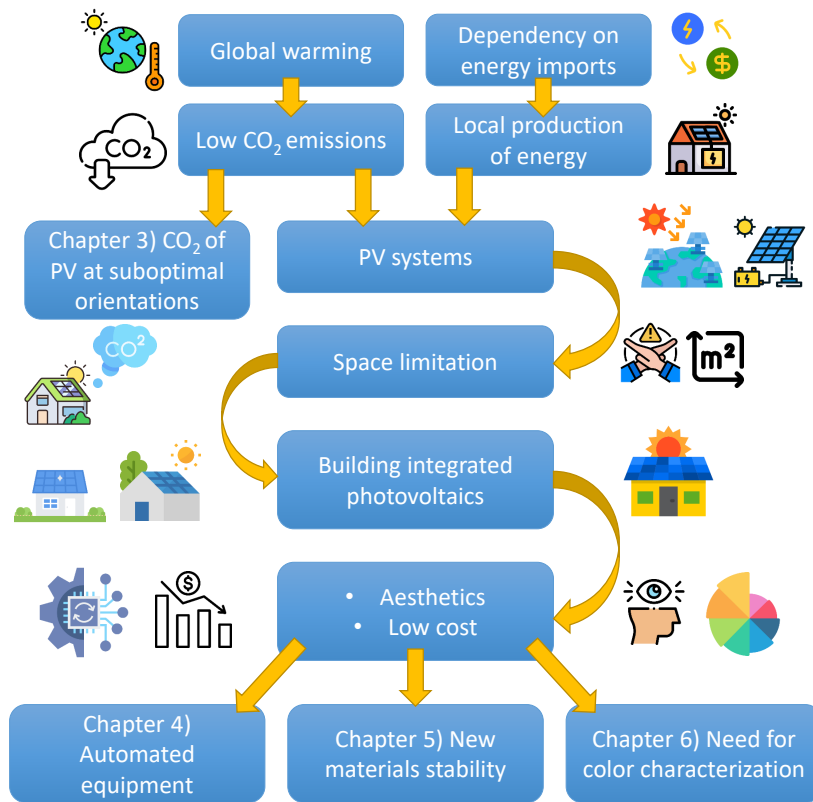
**Figure 7.1:** Schematic of the topics related to this thesis. It is motivated by the pressing issues of the energy crisis and global warming. PV energy is a standout solution due to its cost-effectiveness and minimal carbon footprint, a topic explored in Chapter 3. However, PV faces limitations regarding land availability. To address this, BIPV is a viable solution, but it comes with specific requirements, such as aesthetics and low cost. In Chapter 4, we introduce an automated tool for creating uniform color ribbons for PV modules, in Chapter 5, we explore the stability of the inks used, and in Chapter 6, we present an innovative approach to characterizing colors.

mean CI values of 51.4, 71, and 214 gCO$_2$-eq/kWh for south-, west-/east-, and north-facing orientations, respectively. These values are influenced by annual sunlight variations across different capital cities. To put this in context, these numbers should be contrasted with the average CI distribution of national electricity mixes, which was 374.5 gCO$_2$-eq/kWh (across all European countries in 2021). These findings indicate that integrating PV into façades, even on north-facing sides or the use colored solutions, would not penalize but rather support the transition toward a carbon-neutral electricity mix for most European countries, from a carbon balance perspective.

However, it is important to acknowledge that the analysis in Chapter 3 presents just a snapshot of the current scenario. Improving the study could be done by including BIPV cases, which encompass factors such as the reduction in carbon footprint achieved by replacing a building element and the reduction in energy yield of the PV system due to full building integration. The life-cycle analysis (LCA) of the bill-of-materials of the PV modules and the potential reduction

in $CO_2$ emissions could show a direction for the improvement of the PV technology. This kind of study could be extrapolated to other regions in the world. Naturally, it will be necessary to refine this work at regular intervals in the near future, where the greener-PV scenario (PV with reduced CI) is likely and would provide additional reasons to consider adopting colored PV solutions.

Chapter 4 presents a customized inkjet printer as a proof-of-concept for modifying the appearance of metallic interconnects in BIPV applications. We tackled significant aspects in equipment design and emphasized the essential calibration procedures needed for precise printing, incorporating a vision system. This calibration process effectively rectified distortions in the lens and corrected misalignments arising from mechanical tolerances. Our study establishes the feasibility of a customized inkjet printer as a tool for modifying metallic interconnects' appearance, even when directly applied to solar cell connectors and interconnects, regardless of size, orientation, or position, enabled by a vision system using image processing. Notably, the maximum power ($P_{max}$) output only experienced a 2% decrease after the coating step, mainly attributed to shading losses causing a reduction in short circuit current ($I_{sc}$). This reduction could be further mitigated with more capable hardware. Furthermore, our investigation reveals that optimal printing parameters can be determined by considering variables such as printing speed, DPI, specific hardware, printing fluid, and substrate used. The proposed equipment achieves optimal printing at a speed of 100 mm/s and a resolution of 1440 DPI, with an accuracy of 160 µm. Inkjet technology has demonstrated the desired attributes of flexibility, speed, and automation, making it suitable for integration into the BIPV production line.

Nonetheless, to adapt it for the production line several modifications are necessary. One approach involves coating the ribbons after soldering, once the array of solar cells is assembled. This process would need flipping or raising the array, detecting it, and applying a coating through a line array of printheads covering the module area in a single pass. The curvature of the soldered cells could produce coating artefacts, which could be mitigated by flattening the cells with suction vents. A practical approach to reduce vibrations would involve maintaining the vision, printing, and curing equipment in a static position while moving the array of solar cells on a conveyor belt. Overall, equipment performance could be improved through hardware modifications, taking into account the optimization of various subsystems and their interactions. Nowadays, due to changes in the technology and the ribbon number increase, the coating of cell interconnects has become less crucial, however, the proposed equipment offers the flexibility to coat the string interconnects too, which are still relevant, and even other areas of the module, such as the glass itself.

In Chapter 5 we assessed the long-term stability of black-coated metallic ribbons and their possible degradation effects. A protocol based on existing IEC standards (Annex B) was proposed and applied to several inks and precoated commercial ribbons. We observed color change in the encapsulant of laminates containing typical PV components with ink after UV exposure. An extensive study was performed to a specific UV-curable inkjet ink, which showed

the largest color change. The alteration was attributed to ink components diffusion into the encapsulant and its photodegradation. The main component of the ink, 2-phenoxyethyl acrylate (2-PEA), was identified as a contributor to the yellowing, which could be mitigated by using encapsulants with UV-blocking properties. While using this less stable ink might alter color aesthetics over time, indicating potential long-term instability, the electrical performance closely resembled modules without coated ribbons (less than 3% power loss after 360 kWh/m$^2$ of UV exposure). We advise against using the 2-PEA monomer for PV aesthetic applications and suggest the adoption of UV-curable inks containing aliphatic monomers, which exhibit better resistance to yellowing, combined with UV-blocking encapsulants.

Nowadays, even though precoated black metallic interconnect exist, they should withstand the production line requirements (e.g. soldering, stretching, bending, lamination, etc.). Moreover, there is an absence of studies addressing their potential long-term effects on the bill of materials for PV modules, coupled with a lack of information about the composition of these coatings. Besides, no commercial available inks exist for this application, the composition of commercial inks is not clear, and each ink is unique, adding challenges to the understanding of the degradation modes observed. Two follow-up activities should be considered: (1) designing a specific ink compatible with a commercial coating process for industrial scale PV modules and (2) the further study of several solutions provided by the market. The new ink should not only minimize the color changes observed under weather stressors, but also be compatible with PV module materials and printing equipment producing an aesthetic appearance.

Furthermore, the proposed screening protocol encounters some limitations. For instance, the extended duration required for UV indoor testing has led us to restrict the protocol to 60 kWh/m$^2$. However, this could lead to inks passing it and producing detrimental effects in the module after longer exposures (false positives). We recommend to extend the UV indoor exposure to minimum 240 kWh/m$^2$, besides the implementation of common IEC qualification tests (such as Damp Heat, Humidity Freeze, Thermal Cycling...). Moreover, we have set a threshold of 2≤ $\Delta$E using CIELABDE2000 standard. This threshold is arbitrary and relates to a perceivable color difference, nonetheless, it may be too strict and not relate directly to a rejection of the product by the customers. Therefore, we suggest that more studies and data are needed to find a suitable $\Delta$E threshold for the BIPV industry. This value should correspond to customer perception and industry risk tolerance. The development of UV indoor testing with a more accelerated technique would be beneficial for the main players in the PV field, however, we are aware of the challenges that this would imply. Additionally, it is important to note that this research lacks data on how the inks perform when exposed to real outdoor weather conditions due to time-frame constraints. Ideally, when assessing new materials for PV modules, they should undergo testing not only in controlled indoor environments but also in the actual installation location, closely replicating the real-world conditions, including the use of the final products.

Finally, in Chapter 6 we examined the conventional color characterization techniques used and proposed a solution to characterize the color behind transparent layers, such as glass in

the case of BIPV modules. This study has demonstrated that the novel colorimeter, which incorporates a fiber optic spectrometer positioned at 45° with respect to the samples and using a uniform and stable D65 large area illumination source can perform reliable color measurements under glass laminates. In contrast, we observed a significant decrease in reflectance when using the integrated sphere spectrometer and the portable colorimeter to measure similar samples. This reduction in reflectance became more pronounced as the thickness of the glass layer on the sample increases.

Our ongoing research efforts are dedicated to improve the measurements achieved by the novel colorimeter. Some subjects that are worth to explore are angle-dependent colors, surface effects such as glass texture and anti-reflective coatings, variations in light sources, and calibration procedures. Another interesting challenge is the development of a portable version of this novel colorimeter that could consistently and accurately measure color within commercially integrated PV modules. Such a tool, based on our research, could significantly contribute in color design, degradation assessment, and quality control processes in the BIPV field.

# A Chapter 3 Supplementary Material

**Figure A.1 and A.2** show examples of Integrated PV (IIPV or IPV) in buildings and infrastructures and, respectively, landscape-integrated PV.

**Table A.1** displays the same figures of Table 3.3 for the CI of PV normalized - for comparison - over the CI of the national electricity mix.

**Figure A.3** plots the carbon footprint of different power generation technologies, comparing the results optained for solar PV electricity in Europe (this work) to: i) fossil fuel-fired power stations; ii) various renewable electricity sources and nuclear. These figures are taken from Scarlat et al. [105]. Similar figures – with a distribution of values – are given in a recent fachsheet report by NREL [207].
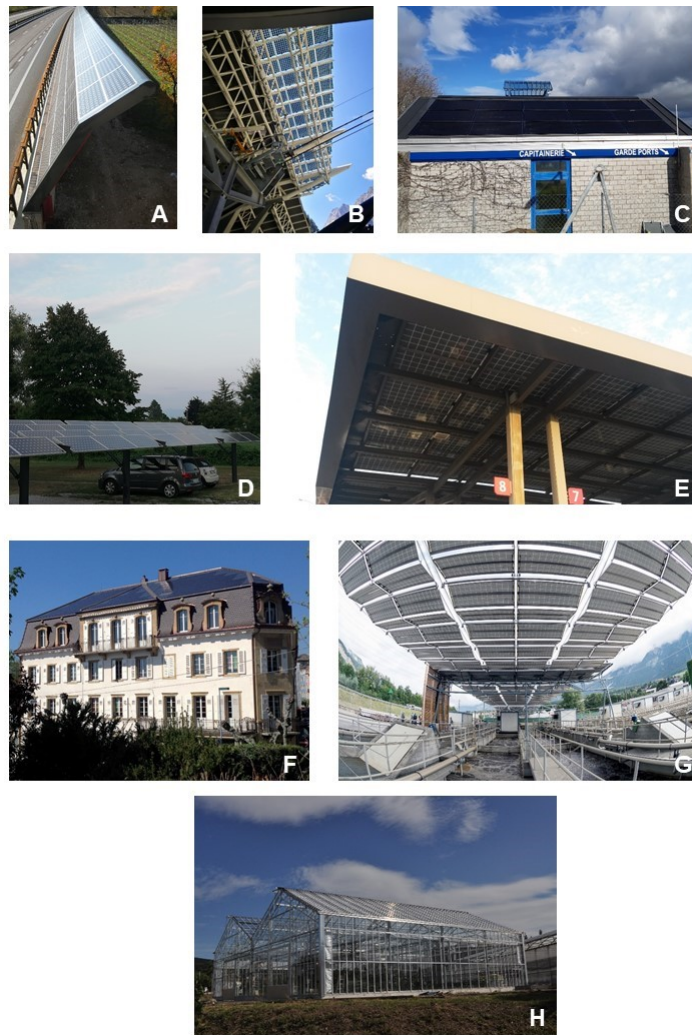
**Figure A.1:** Examples of Integrated-PV in Buildings and infrastructures. (A) PV noise barrier located along the A22 motorway and protecting the village of Marano (Trento, Italy); (B) Base Skyway Monte Bianco cable-car station in Courmayeur (Italy); (C) Harbour master's office buildings in Neuchâtel (Switzerland); (D) Solar car-park in Fiumicello (Trieste, Italy); (E) PV system integrated in the canopy of a petrol station in Dakar (Senegal); (F) BIPV system integrated into the roof of an historical building from 1880 in the old city of Neuchâtel (Switzerland); (G) PV plant covering a waste water treatment plant in Chur (Switzerland); (H) Solar plant integrated in the roof of a green-house in Derio (Spain). Credits: (A) Autostrade del Brennero Spa; (B) Giuseppe Virtuani; (C) Alessandro Virtuani; (D) Raffaella Lorenzi; (E) Alessandro Virtuani; (F) SolarAgentur; (G) DHP; (H) Tecnalia.

**Figure A.2:** Examples of landscape-integrated PV. (A) Agricultural-PV (Agri-PV) installation in Tressere (Perpignan, France); (B) Utility-scale plant in Somerset (UK); (C) Floating PV plant on an irrigation reservoir in Japan. Credits: (A) Sun'R, (B) WiseEnergy, (C) Ciel & Terre International).

## Appendix A. Chapter 3 Supplementary Material

**Table A.1:** values for the CI of PV (see Table 3.3) normalized over the CI of the national electricity mix. In the greener-PV scenario – a realistic target for 2030 and beyond - all figures are halved.

| Country code | Capital | CI elect. mix [%] | S-opta [%] | Flat roof *[idem]* | S-90° *[idem]* | W-90° *[idem]* | N-90° *[idem]* |
|---|---|---|---|---|---|---|---|
| AT | Vienna (48.2N, 16.4E) | 100 | 13.3 | 15.9 | 19.0 | 27.3 | 79.9 |
| BE | Brussels (50.8N, 4.4E) | 100 | 17.4 | 20.8 | 24.3 | 35.1 | 90.0 |
| BG | Sofia (42.6N, 24E) | 100 | 5.7 | 6.9 | 8.8 | 12.8 | 35.0 |
| CY | Nicosia (35.1N, 33.2E) | 100 | 3.2 | 3.7 | 5.3 | 7.0 | 24.3 |
| CZ | Prague (50N, 14.5E) | 100 | 6.8 | 8.1 | 9.6 | 13.8 | 38.1 |
| DE | Berlin (52.5N, 13.4E) | 100 | 9.2 | 11.2 | 12.8 | 18.9 | 51.0 |
| DK | Copenhagen (55.7N, 12.6E) | 100 | 25.2 | 30.6 | 34.5 | 49.1 | 139.6 |
| EE | Tallinn (59.4N, 24.8E) | 100 | 9.7 | 12.0 | 13.3 | 18.7 | 52.7 |
| EL | Athens (38N, 23.7E) | 100 | 3.3 | 3.7 | 5.5 | 6.6 | 24.5 |
| ES | Madrid (40.4N, 3.7W) | 100 | 9.1 | 10.9 | 13.7 | 19.6 | 74.2 |
| FI | Helsinki (60.2N, 24.9E) | 100 | 30.2 | 37.5 | 40.6 | 58.5 | 179.1 |
| FR | Paris (48.9N, 2.3E) | 100 | 36.7 | 44.1 | 51.7 | 76.2 | 203.8 |
| HR | Zagreb (45.8N, 16E) | 100 | 9.2 | 10.8 | 13.5 | 18.8 | 56.1 |
| HU | Budapest (47.5N, 19.1E) | 100 | 9.9 | 11.8 | 14.1 | 20.5 | 60.9 |
| IE | Dublin (53.3N, 6.3E) | 100 | 11.1 | 13.5 | 14.9 | 22.8 | 54.0 |
| IT | Rome (41.9N, 12.5E) | 100 | 7.8 | 9.2 | 11.7 | 16.3 | 57.3 |
| LV | Riga (56.9N, 24.1E) | 100 | 13.0 | 15.9 | 17.8 | 25.8 | 71.4 |
| LT | Vilnius (54.7N, 25.3E) | 100 | 13.5 | 16.0 | 18.8 | 27.0 | 72.3 |
| LU | Luxembourg (49.7N, 6.1E) | 100 | 11.7 | 13.7 | 17.0 | 23.6 | 60.9 |
| MT | Valletta (35.9N, 14.5E) | 100 | 5.4 | 6.1 | 9.1 | 11.0 | 41.1 |
| NL | Amsterdam (52.4N, 4.9E) | 100 | 8.9 | 10.7 | 12.4 | 17.4 | 46.8 |
| PL | Warsaw (52.2N, 21E) | 100 | 4.9 | 5.9 | 6.9 | 10.0 | 27.4 |
| PT | Lisbon (38.7N, 9.1W) | 100 | 8.1 | 9.3 | 12.9 | 16.8 | 59.6 |
| RO | Bucharest (44.4N, 26.1E) | 100 | 6.9 | 8.1 | 10.4 | 14.4 | 44.3 |
| SK | Bratislava (48.1N, 17.1E) | 100 | 10.0 | 11.9 | 14.4 | 20.8 | 61.7 |
| SI | Ljubljana (46N, 14.5E) | 100 | 12.1 | 13.9 | 18.3 | 23.3 | 70.6 |
| SE | Stockholm (59.3N, 18.1E) | 100 | 104.8 | 133.0 | 139.0 | 204.8 | 595.5 |
| IS | Reykjavik (64.1N, 21.9W) | 100 | 178.5 | 243.5 | 225.8 | 233.1 | 856.9 |
| NO | Oslo (59.9N, 10.6E) | 100 | 146.1 | 186.1 | 192.3 | 291.0 | 830.3 |
| CH | Bern (46.9N, 7.4E) | 100 | 44.5 | 52.9 | 63.3 | 93.7 | 263.1 |
| UK | London (51.5N, 0.1W) | 100 | 13.0 | 16.4 | 17.6 | 17.8 | 71.5 |
| UA | Kiev (50.4N, 30.5E) | 100 | 7.7 | 9.1 | 11.3 | 12.1 | 50.1 |
| RS | Belgrade (44.8N, 20.4E) | 100 | 3.7 | 4.3 | 5.4 | 7.7 | 23.0 |
| AL | Tirana (41.3N, 19.8E) | 100 | 122.1 | 142.9 | 183.8 | 262.1 | 851.7 |
| ME | Podgorica (42.4N, 19.3E) | 100 | 4.4 | 5.3 | 6.6 | 9.5 | 33.0 |
| TR | Istanbul (41N, 29W) | 100 | 5.1 | 5.8 | 8.1 | 10.3 | 33.6 |
| Mean (all) | - | 100 | 9.6 | 11.5 | 13.7 | 18.9 | 57.2 |
| Mean (greener-PV, 2030+) | | | 4.8 | 5.7 | 6.8 | 9.5 | 28.6 |
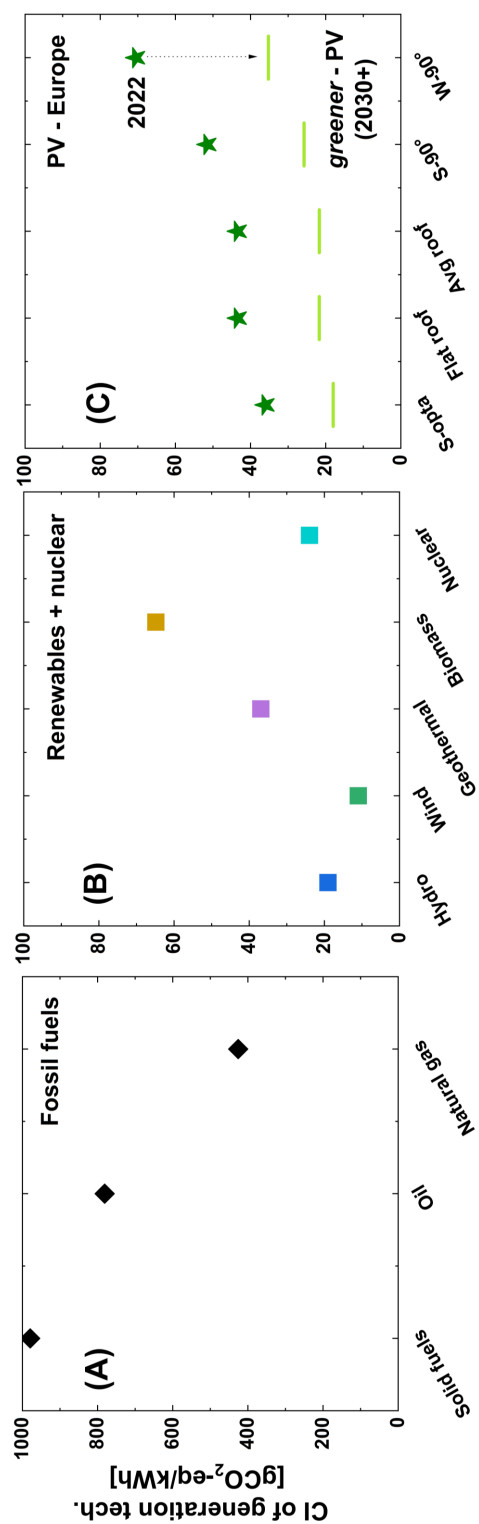
**Figure A.3:** How does solar PV compare to other generation technologies? Carbon footprint of different power generation technologies: (A) fossil fuel-fired power stations; (B) various renewable electricity sources and nuclear; (C) solar-PV (mean values for Europe) with 2022 values and projections for 2030 and beyond. The data in (A) and (B) are taken from [105], those in (C) from this work. The y-axis scale of chart (A) differs from those of (B) and (C).

# B | Ink Screening Protocol

The following annex is based on two publications, the former presented at the 38th European PV Solar Energy Conference and Exhibition, and the latter at the 8th World Conference on Photovoltaic Energy Conversion:

- A. Borja Block, A. Virtuani and C. Ballif, *Stability of Inks Used for Masking Metallic Interconnects in BIPV Modules*, 38th European PV Solar Energy Conference and Exhibition (EU PVSEC) Proceedings, 2021 [84].

- A. Borja Block, J. Escarre Palou, A. Virtuani and C. Ballif, *A Screening Protocol to Assess the Stability of the Inks Used To Mask Metallic Interconnects in BIPV Modules*, 8th World Conference on Photovoltaic Energy Conversion (WCPEC) Proceedings, 2022 [85].

A protocol was designed to screen the inks used to mask the metallic interconnects of PV modules. We applied it to coupons mimicking the structure of conventional glass-glass (G/G) and glass-backsheet (G/BS) structures encapsulated with EVA and POE (see Figure B.1).

The protocol involved two main sequences. One with DH + UV exposure (sequence A) and the other only with UV exposure (sequence B). The first proposed protocol is described in Figure B.2. It was based on IEC standards 61215 [72] and IEC 62788-7-2 [77] with A3 conditions as described in Chapter 2.

Initially, three inks were tested (see Table B.1) and among them only one passed the protocol. The pass or fail criteria was set to a $2 \leq \Delta E$ measuring with the advanced visual inspection software described in Chapter 2.

However, the screening protocol was modified due to two main reasons:

1. It did not provided insights into the adhesion of the ink with the metallic ribbons. For instance, ink #3 was stable and passed the protocol, however, it was easily scratchable and if the samples were not prepared carefully they were easily damaged.
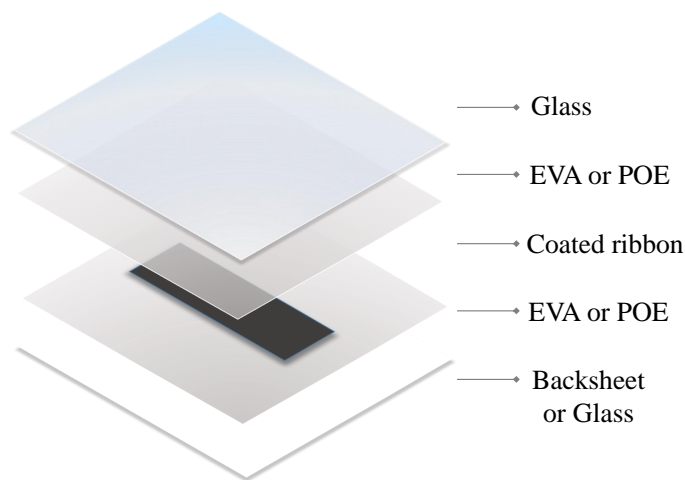
**Figure B.1:** The sample configurations to test the stability of the coating have a glass/glass (G/G) and glass/ backsheet (G/Bs) structure and are made with either EVA or POE as encapsulant
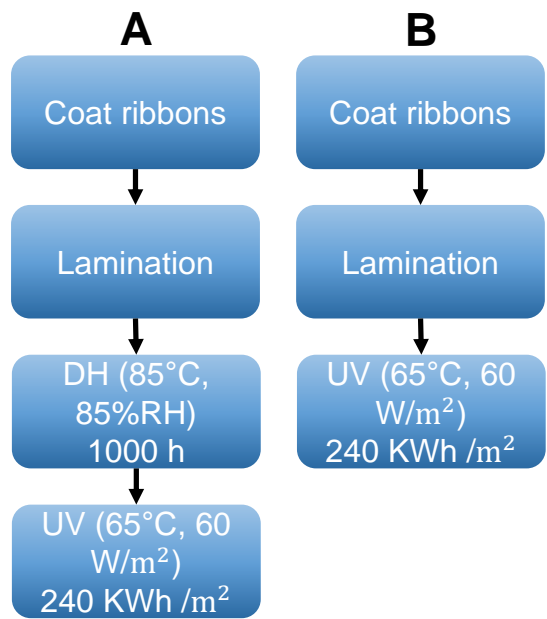


**Figure B.2:** Followed accelerated aging tests sequences. (A) Damp heat (DH) for 1000h and then ultraviolet (UV) exposure aiming for 240 KWh/m$^2$ and (B) only UV exposure for the same dose.

2. The duration of the protocol was 5000 hours (longer than 6 months). Due to the time consumption and logistics it was decided to be reduced.

This study showed no major differences between the G/G and G/BS configurations, neverthe-

**Table B.1:** Result of the protocol. Two inks failed the test due to color change.

| Ink # | Type | Dispensing technique | A (DH + UV) | B (UV) | Failure cause |
|---|---|---|---|---|---|
| 1 | UV curable | Inkjet | **Fail** | **Fail** | Yellowing |
| 2 | UV curable | Inkjet | **Fail** | **Fail** | Yellowing |
| 3 | Solvent based | Inkjet | Pass | Pass | - |

less, inks on G/G configuration produced a slightly lower $\Delta$E. The yellowing showed a larger spread in EVA than in POE, but it appeared in both cases. The protocol was modified reducing its duration by four times, as shown in Figure B.3. The adhesion was assessed considering the ASTM D3359 – 17 X cut tape test [208]. An "X" of 4 cm was carved on the not laminated coated ribbons with the aid of a sharp tool. As the ribbons were 8 cm by 0.5 cm there were acute angles in the direction of the longest side of metallic interconnect. The ribbons were fixed to a flat clean surface. Transparent pressure sensitive tape was cut in 8 cm pieces and glued manually with the help of pressure done by an eraser on top of the "X" avoiding bubble formation. After the tape was positioned, 1.5 min were waited before pulling the tape in the direction of the acute angles of the "X" as close as 180° as possible. The result was classified on 5 levels depending on the amount of coating that detaches the metallic interconnect surface.

The idea was to replicate the same effects from the previous protocol on a shorter period and to address the adhesion of the ink to the ribbon.
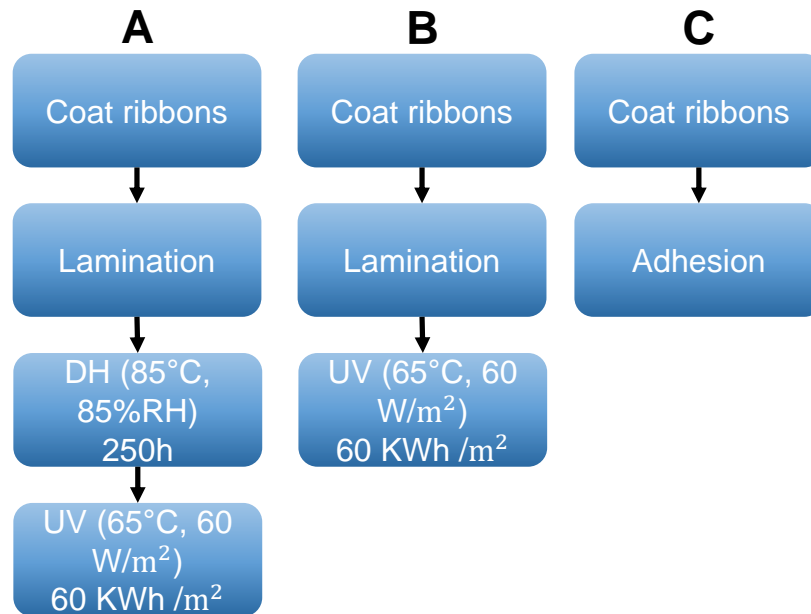


**Figure B.3:** Sequences of the screening protocol. (A) starts with DH followed by UV to investigate the effect of humidity in the samples. (B) involves only UV with the same dose as (A) of 60 kWh/m2. Sequence (C) tests the adhesion of the coating to the ribbon. All sequences are carried out in parallel.

4 new inks were tested as well, as shown in the Table B.2. All investigated inks that failed

**Table B.2:** Result of the improved protocol. Three inks failed the test due to color change or lack of adhesion to the metallic interconnects.

| Ink # | Type | Dispensing technique | A (DH+UV) | B (UV) | C (Adhesion) | Failure cause |
|---|---|---|---|---|---|---|
| 1 | UV curable | Inkjet | **Fail** | **Fail** | Pass | Yellowing |
| 2 | UV curable | Inkjet | Pass | Pass | Pass | - |
| 3 | Solvent based | Inkjet | Pass | Pass | **Fail** | Adhesion |
| 4 | UV curable | Inkjet | Pass | Pass | Pass | - |
| 5 | UV curable | Inkjet | **Fail** | **Fail** | **Fail** | Adhesion, yellowing |
| 6 | UV curable | Screen printing | Pass | Pass | Pass | - |
| 7 | UV curable | Screen printing | Pass | Pass | Pass | - |

sequence (A) also failed sequence (B). This led us to the conclusion that, for the investigated inks, the harsher criteria was UV exposure and the screening could have been performed only with sequence (B) and (C). The results from the previous protocol were observed, again, no clear differences were observed with G/G and G/BS configurations, and the failure causes were yellowing and poor adhesion. Due to these reasons, in Chapter 5, only indoor UV aging was performed. Ink #2 that failed the first protocol (see Figure B.2) and passed the second protocol (see Figure B.3) was a clear example that extensive UV exposure should be performed to ensure the color stability of these inks.

The screen printed inks that underwent testing successfully met the protocol criteria. However, integrating them into the production line would pose challenges relating to aligning stringed cells and managing soldering temperature. The proposed protocol sets only the minimum requirement coatings for masking metallic interconnects should pass. To ensure long-term stability, it is advisable to extend the accelerated aging tests. Additionally, we recommend to test the entire bill of materials under real outdoor conditions, ideally in full size samples. Furthermore, it is essential to take into consideration the specific manufacturing step within the production line where the coating application will take place. This consideration is important to meet all the coating requirements, such as accuracy, temperature resistance, printing speed, curing, adhesion, and more.

# C Color Coordinates Calculation from the Reflectance Spectra

Color coordinates can be computed using reflectance spectra. Apart from the reflectance data, the illuminant and color-matching functions are required to perform the computation. The light source is referred to as the illuminant and depending on it, the hue of the sample will vary. Standards exist that specify the relative spectral power values of the illuminants used in the calculations. In this work, we employed the D65 illuminant, which closely matches to normal noon light in Europe.

The color-matching functions are also given by the Commision International de l'Eclairage (CIE), and can change depending on the observer. Two main observers are proposed, 2° 1931 and 10° 1964. They refer to the observer's field of view when the experiments were performed. The three color-matching functions come from the sensitivity of the three types of cone cells of the human eye for different wavelengths [209]. Figure C.1 shows the color-matching functions according to both observers and the standard D65 illuminant.

The three main curves, x, y, and z from Figure C.1(A) are from both standards and relate to the human cone cells capable of processing different colors. The graph shows an increase in the intensity in the lower wavelengths of each curve from the standard 1964 10° with respect to the standard 1931 2°. As wavelengths higher than 700 nm are approached, the intensity is significantly reduced to nearby zero values. One reason why the intensity declines is that the human cone cells cannot detect wavelengths above 700 nm. In the same way, the human eye cannot perceive any intensity of wavelengths below 380 nm.

There are several color spaces available to quantitatively represent color. RGB coordinates, for example, are often employed to represent colors on a display. We mostly used CIELab coordinates in the presented investigation. Figure C.2 depicts a three-dimensional representation of it. "L" stands for lightness and can have values from 0 to 100, 0 being black and 100 white. When the "a" is positive, it is red, and when it is negative, it is green. The variable "b" can be either positive or negative; when positive, the color is yellow; when negative, the color is blue. The bigger the values are with respect from 0 the more saturated the color is.
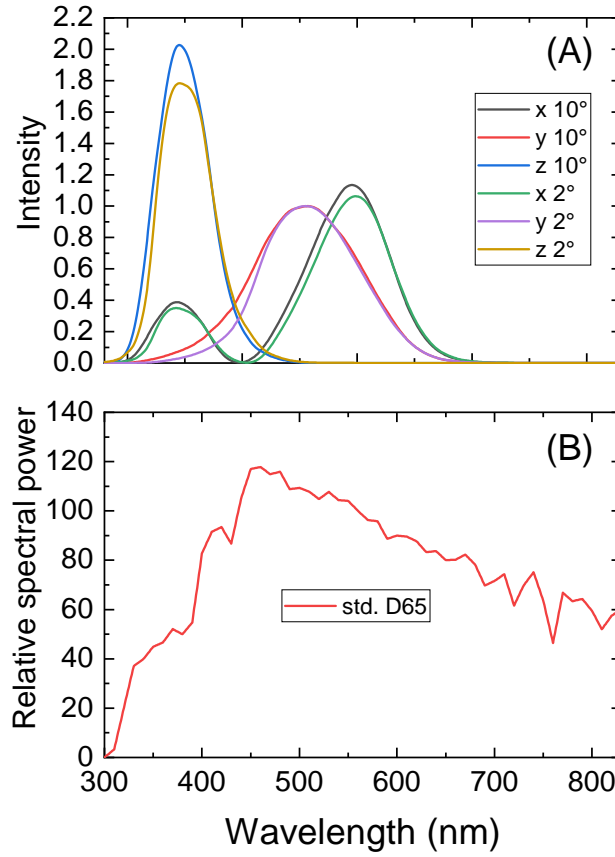
**Figure C.1:** (A) Color-matching functions of the 10° observer 1964 [202] and the 2° observer 1931 [210]. (B) Standard D65 corresponding to midday direct and diffuse sunlight in Europe [201].

The great majority of colorimeters and spectrometers already come with the option to calculate the color coordinates in the desired color space with the chosen illuminant and observer. The color coordinates were directly processed with the illuminant D65 and 10° observer with the used equipment, colorimeter, spectrometer and novel manufactured colorimeter. The following equations show how the XYZ coordinates can be calculated from reflectance data. The CIELab coordinated can be computed from them.

$$X = \frac{1}{N} \int_{\lambda_0}^{\lambda_1} \overline{x}(\lambda) I(\lambda) S(\lambda) d\lambda \tag{C.1}$$
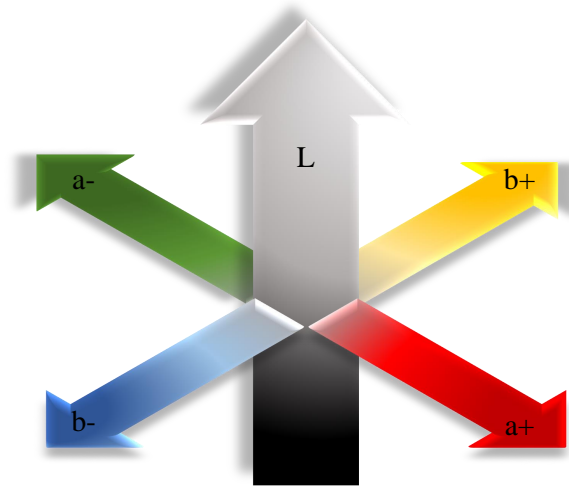
**Figure C.2:** Representation of CIELab color coordinates. L stands for lightness; the range of values go from 0 to 100. "a" (green to red) and "b" (blue to yellow).

$$Y = \frac{1}{N} \int_{\lambda_0}^{\lambda_1} \overline{y}(\lambda) I(\lambda) S(\lambda) d\lambda \qquad (C.2)$$

$$Z = \frac{1}{N} \int_{\lambda_0}^{\lambda_1} \overline{z}(\lambda) I(\lambda) S(\lambda) d\lambda \qquad (C.3)$$

$$N = \int_{\lambda_0}^{\lambda_1} \overline{y}(\lambda) I(\lambda) d\lambda \qquad (C.4)$$

Equations C.1, C.2, C.3 and C.4 are the formulas used to calculate color coordinates XYZ. L, a, and b can be computed from them. The color-matching functions are x($\lambda$), y($\lambda$), and z($\lambda$). I($\lambda$) stands for the illuminant and S($\lambda$) for the reflectance measurements of the samples. The values chosen for this work where D65 as illuminant and 10° observer.

The color change ($\Delta$E) can be calculated in the CIELab color space as the distance between points in a 3-dimensional space, but in this work we used software generated on MATLAB performing the calculation according to CIEDE2000 formula [88].

# Bibliography

[1]  C.-F. Schleussner, J. Rogelj, M. Schaeffer, *et al.*, "Science and policy characteristics of the Paris Agreement temperature goal", en, *Nature Climate Change*, vol. 6, no. 9, pp. 827–835, Sep. 2016, ISSN: 1758-678X, 1758-6798. DOI: 10.1038/nclimate3096. [Online]. Available: https://www.nature.com/articles/nclimate3096 (visited on 06/29/2023).

[2]  M.-C. Cordonier Segger, "Advancing the Paris Agreement on Climate Change for Sustainable Development", *Cambridge International Law Journal*, vol. 5, no. 2, pp. 202–237, 2016, ISSN: 23989173, 23989181. DOI: 10.4337/cilj.2016.02.03. [Online]. Available: https://www.elgaronline.com/view/journals/cilj/5-2/cilj.2016.02.03.xml (visited on 06/29/2023).

[3]  S. N. Seo, "Beyond the Paris Agreement: Climate change policy negotiations and future directions: Beyond the Paris Agreement", en, *Regional Science Policy & Practice*, vol. 9, no. 2, pp. 121–140, Jun. 2017, ISSN: 17577802. DOI: 10.1111/rsp3.12090. [Online]. Available: https://onlinelibrary.wiley.com/doi/10.1111/rsp3.12090 (visited on 06/29/2023).

[4]  "World Energy Transitions Outlook 2023: 1.5°C Pathway", International Renewable Energy Agency, Abu Dhabi, Tech. Rep., 2023. [Online]. Available: https://www.irena.org/Publications/2023/Jun/World-Energy-Transitions-Outlook-2023.

[5]  "Electricity Market Report 2023", English, IEA, Paris, Tech. Rep., 2023. [Online]. Available: https://www.iea.org/reports/electricity-market-report-2023.

[6]  "Bp Statistical Review of World Energy 2022", BP, Tech. Rep. 71st edition, 2022. [Online]. Available: https://www.bp.com/en/global/corporate/energy-economics/statistical-review-of-world-energy.html.

[7]  "Trends in PV Applications 2022", IEA International Energy Agency, Tech. Rep., 2022. [Online]. Available: https://iea-pvps.org/trends_reports/trends-2022/.

[8]  "Solar PV", IEA International Energy Agency, Paris, Tech. Rep., 2022. [Online]. Available: https://www.iea.org/reports/solar-pv.

[9]  "Snapshot of Global PV Markets 2023", IEA International Energy Agency, Tech. Rep., 2023. [Online]. Available: https://iea-pvps.org/snapshot-reports/snapshot-2023/.

**Bibliography**

[10]   *Directive (EU) 2018/844 of the European Parliament and of the Council of 30 May 2018 amending Directive 2010/31/EU on the energy performance of buildings and Directive 2012/27/EU on energy efficiency, ("Energy Performance in Building Directive"),* May 2018. [Online]. Available: https://eur-lex.europa.eu/legal-content/EN/TXT/?uri=uriserv: OJ.L_.2018.156.01.0075.01.ENG.

[11]   *Directive (EU) 2018/2001 of the European Parliament and of the Council of 11 December 2018 on the promotion of the use of energy from renewable sources ("RED II Directive"),* Dec. 2018. [Online]. Available: https://eur-lex.europa.eu/legal-content/EN/TXT/?uri= uriserv:OJ.L_.2018.328.01.0082.01.ENG&toc=OJ:L:2018:328:TOC.

[12]   S. Kim and S. Kim, "Economic Feasibility Comparison between Building-Integrated Photovoltaics and Green Systems in Northeast Texas", en, *Energies,* vol. 16, no. 12, p. 4672, Jun. 2023, ISSN: 1996-1073. DOI: 10.3390/en16124672. [Online]. Available: https://www.mdpi.com/1996-1073/16/12/4672 (visited on 06/29/2023).

[13]   H. Gholami, H. N. Røstvik, and D. Müller-Eie, "Holistic economic analysis of building integrated photovoltaics (BIPV) system: Case studies evaluation", en, *Energy and Buildings,* vol. 203, p. 109 461, Nov. 2019, ISSN: 03787788. DOI: 10.1016/j.enbuild. 2019.109461. [Online]. Available: https://linkinghub.elsevier.com/retrieve/pii/ S0378778819315907 (visited on 06/29/2023).

[14]   A. Ghosh, "Potential of building integrated and attached/applied photovoltaic (BIPV / BAPV) for adaptive less energy-hungry building's skin: A comprehensive review", en, *Journal of Cleaner Production,* vol. 276, p. 123 343, Dec. 2020, ISSN: 09596526. DOI: 10.1016/j.jclepro.2020.123343. [Online]. Available: https://linkinghub.elsevier.com/ retrieve/pii/S0959652620333886 (visited on 06/29/2023).

[15]   M. Kryszak and L. W. Wang, "The value of aesthetics in the BIPV roof products segment: a multiperspective study under European market conditions", en, *Energy Sources, Part A: Recovery, Utilization, and Environmental Effects,* pp. 1–22, Aug. 2020, ISSN: 1556-7036, 1556-7230. DOI: 10.1080/15567036.2020.1807656. [Online]. Available: https://www.tandfonline.com/doi/full/10.1080/15567036.2020.1807656 (visited on 06/29/2023).

[16]   Q. Li, L. Zhu, Y. Sun, L. Lu, and Y. Yang, "Performance prediction of Building Integrated Photovoltaics under no-shading, shading and masking conditions using a multi-physics model", en, *Energy,* vol. 213, p. 118 795, Dec. 2020, ISSN: 03605442. DOI: 10.1016/j.energy.2020.118795. [Online]. Available: https://linkinghub.elsevier.com/ retrieve/pii/S0360544220319022 (visited on 06/29/2023).

[17]   K. Kurokawa and I. of Electrical and Electronics Engineers, Eds., *Proceedings of 3rd World Conference on Photovoltaic Energy Conversion: joint conference of 13th PV Science & Engineering Conference: 30th IEEE PV Specialists Conference: 18th European PV Solar Energy Conference: Osaka International Congress Center "Grand Cube", Osaka, Japan, 11-18 May, 2003.* [Osaka?], Japan: WCPEC-3 Organizing Committee, 2003,

Meeting Name: Kōki Denryoku Kōka no Kiso to Ōyō ni kansuru Shinpojūmu OCLC: ocm55977323, ISBN: 978-4-9901816-0-4 978-4-9901816-1-1 978-4-9901816-2-8.

[18] J. Hernández-Moro and J. Martínez-Duart, "Analytical model for solar PV and CSP electricity costs: Present LCOE values and their future evolution", en, *Renewable and Sustainable Energy Reviews*, vol. 20, pp. 119–132, Apr. 2013, ISSN: 13640321. DOI: 10.1016/j.rser.2012.11.082. [Online]. Available: https://linkinghub.elsevier.com/retrieve/pii/S136403211200696X (visited on 06/29/2023).

[19] M. T. Patel, R. Asadpour, M. Woodhouse, C. Deline, and M. A. Alam, "LCOE*: Rethinking LCOE for Photovoltaic Systems", in *2019 IEEE 46th Photovoltaic Specialists Conference (PVSC)*, Chicago, IL, USA: IEEE, Jun. 2019, pp. 1711–1713, ISBN: 978-1-72810-494-2. DOI: 10.1109/PVSC40753.2019.8980486. [Online]. Available: https://ieeexplore.ieee.org/document/8980486/ (visited on 06/29/2023).

[20] A. Luque and S. Hegedus, Eds., *Handbook of Photovoltaic Science and Engineering*, en, 1st ed. Wiley, Dec. 2010, ISBN: 978-0-470-72169-8 978-0-470-97470-4. DOI: 10.1002/9780470974704. [Online]. Available: https://onlinelibrary.wiley.com/doi/book/10.1002/9780470974704 (visited on 06/30/2023).

[21] K. Branker, M. Pathak, and J. Pearce, "A review of solar photovoltaic levelized cost of electricity", en, *Renewable and Sustainable Energy Reviews*, vol. 15, no. 9, pp. 4470–4482, Dec. 2011, ISSN: 13640321. DOI: 10.1016/j.rser.2011.07.104. [Online]. Available: https://linkinghub.elsevier.com/retrieve/pii/S1364032111003492 (visited on 06/29/2023).

[22] T. James, A. Goodrich, M. Woodhouse, R. Margolis, and S. Ong, "Building-Integrated Photovoltaics (BIPV) in the Residential Sector: An Analysis of Installed Rooftop System Prices", Tech. Rep. NREL/TP-6A20-53103, 1029857, Nov. 2011, NREL/TP–6A20–53 103, 1 029 857. DOI: 10.2172/1029857. [Online]. Available: https://www.osti.gov/servlets/purl/1029857/ (visited on 08/08/2023).

[23] A. K. Shukla, K. Sudhakar, P. Baredar, and R. Mamat, "Solar PV and BIPV system: Barrier, challenges and policy recommendation in India", en, *Renewable and Sustainable Energy Reviews*, vol. 82, pp. 3314–3322, Feb. 2018, ISSN: 13640321. DOI: 10.1016/j.rser.2017.10.013. [Online]. Available: https://linkinghub.elsevier.com/retrieve/pii/S1364032117313862 (visited on 10/03/2023).

[24] N. M. Kumar, K. Sudhakar, M. Samykano, and V. Jayaseelan, "BIPV Market Growth: SWOT Analysis and Favorable Factors", in *2018 4th International Conference on Electrical Energy Systems (ICEES)*, Chennai: IEEE, Feb. 2018, pp. 412–415, ISBN: 978-1-5386-3695-4. DOI: 10.1109/ICEES.2018.8443227. [Online]. Available: https://ieeexplore.ieee.org/document/8443227/ (visited on 06/29/2023).

[25] M. Pagliaro, R. Ciriminna, and G. Palmisano, "BIPV: merging the photovoltaic with the construction industry: Merging photovoltaic with the construction industry", en, *Progress in Photovoltaics: Research and Applications*, vol. 18, no. 1, pp. 61–72, Jan. 2010, ISSN: 10627995. DOI: 10.1002/pip.920. [Online]. Available: https://onlinelibrary.wiley.com/doi/10.1002/pip.920 (visited on 06/29/2023).

# Bibliography

[26] V. Shaw and M. Hall, "Chinese PV Industry Brief: 50 GW plan for rooftop, BIPV", *PV Magazine*, Mar. 2022. [Online]. Available: https://www.pv-magazine.com/2022/03/11/chinese-pv-industry-brief-50-gw-plan-for-rooftop-bipv/.

[27] ICARES, "BIPV market and stakeholder analysis", Tech. Rep., Jul. 2019. [Online]. Available: www.bipvboost.eu.

[28] PVsites, "Sustaining the BIPV market growth", [Online]. Available: https://www.pvsites.eu/project/expected-impacts/.

[29] H. C. Curtius, "The adoption of building-integrated photovoltaics: barriers and facilitators", en, *Renewable Energy*, vol. 126, pp. 783–790, Oct. 2018, ISSN: 09601481. DOI: 10.1016/j.renene.2018.04.001. [Online]. Available: https://linkinghub.elsevier.com/retrieve/pii/S0960148118304087 (visited on 08/08/2023).

[30] C. Ballif, L.-E. Perret-Aebi, S. Lufkin, and E. Rey, "Integrated thinking for photovoltaics in buildings", en, *Nature Energy*, vol. 3, no. 6, pp. 438–442, Jun. 2018, Number: 6 Publisher: Nature Publishing Group, ISSN: 2058-7546. DOI: 10.1038/s41560-018-0176-2. [Online]. Available: https://www.nature.com/articles/s41560-018-0176-2 (visited on 10/10/2023).

[31] D. D. B. Mesquita, J. Lucas De S. Silva, H. S. Moreira, M. Kitayama, and M. G. Villalva, "A review and analysis of technologies applied in PV modules", in *2019 IEEE PES Innovative Smart Grid Technologies Conference - Latin America (ISGT Latin America)*, Gramado, Brazil: IEEE, Sep. 2019, pp. 1–6, ISBN: 978-1-5386-9567-8. DOI: 10.1109/ISGT-LA.2019.8895369. [Online]. Available: https://ieeexplore.ieee.org/document/8895369/ (visited on 06/29/2023).

[32] J. Jean, M. Woodhouse, and V. Bulović, "Accelerating Photovoltaic Market Entry with Module Replacement", en, *Joule*, vol. 3, no. 11, pp. 2824–2841, Nov. 2019, ISSN: 25424351. DOI: 10.1016/j.joule.2019.08.012. [Online]. Available: https://linkinghub.elsevier.com/retrieve/pii/S2542435119304155 (visited on 06/29/2023).

[33] S. Ghosh and R. Yadav, "Future of photovoltaic technologies: A comprehensive review", en, *Sustainable Energy Technologies and Assessments*, vol. 47, p. 101 410, Oct. 2021, ISSN: 22131388. DOI: 10.1016/j.seta.2021.101410. [Online]. Available: https://linkinghub.elsevier.com/retrieve/pii/S2213138821004203 (visited on 06/29/2023).

[34] O. Arriaga Arruti, "Investigation and Mitigation of Moisture- and Potential-Induced Degradation Mechanisms of Silicon Heterojunction Solar Cells and Modules", en, Jul. 2023, Publisher: Lausanne, EPFL. DOI: 10.5075/EPFL-THESIS-10268. [Online]. Available: http://infoscience.epfl.ch/record/303762 (visited on 07/20/2023).

[35] A. Joshi, A. Khan, and A. Sp, "Comparison of half cut solar cells with standard solar cells", in *2019 Advances in Science and Engineering Technology International Conferences (ASET)*, Dubai, United Arab Emirates: IEEE, Mar. 2019, pp. 1–3, ISBN: 978-1-5386-8271-5. DOI: 10.1109/ICASET.2019.8714488. [Online]. Available: https://ieeexplore.ieee.org/document/8714488/ (visited on 06/29/2023).

[36] T. Panda, S. Sadhukhan, S. Acharyya, *et al.*, "Impact of multi-busbar front grid patterns on the performance of industrial type c-Si solar cell", en, *Solar Energy*, vol. 236, pp. 790–801, Apr. 2022, ISSN: 0038092X. DOI: 10.1016/j.solener.2022.03.051. [Online]. Available: https://linkinghub.elsevier.com/retrieve/pii/S0038092X22002171 (visited on 06/29/2023).

[37] J. Walter, M. Tranitz, M. Volk, C. Ebert, and U. Eitner, "Multi-wire Interconnection of Busbar-free Solar Cells", en, *Energy Procedia*, vol. 55, pp. 380–388, 2014, ISSN: 18766102. DOI: 10.1016/j.egypro.2014.08.109. [Online]. Available: https://linkinghub.elsevier.com/retrieve/pii/S1876610214013344 (visited on 06/29/2023).

[38] T. Borgers, E. Voroshazi, J. Govaerts, J. Szlufcik, and J. Poortmans, "Multi-wire interconnection technologies weaving the way for back contact and bifacial PV modules", in *2016 IEEE 43rd Photovoltaic Specialists Conference (PVSC)*, Portland, OR, USA: IEEE, Jun. 2016, pp. 3580–3583, ISBN: 978-1-5090-2724-8. DOI: 10.1109/PVSC.2016.7750339. [Online]. Available: http://ieeexplore.ieee.org/document/7750339/ (visited on 06/29/2023).

[39] N. Chen and A. Ebong, "Towards 20% efficient industrial Al-BSF silicon solar cell with multiple busbars and fine gridlines", en, *Solar Energy Materials and Solar Cells*, vol. 146, pp. 107–113, Mar. 2016, ISSN: 09270248. DOI: 10.1016/j.solmat.2015.11.020. [Online]. Available: https://linkinghub.elsevier.com/retrieve/pii/S0927024815006042 (visited on 06/29/2023).

[40] V. Benda and L. Černá, "PV cells and modules – State of the art, limits and trends", en, *Heliyon*, vol. 6, no. 12, e05666, Dec. 2020, ISSN: 24058440. DOI: 10.1016/j.heliyon.2020.e05666. [Online]. Available: https://linkinghub.elsevier.com/retrieve/pii/S2405844020325093 (visited on 06/29/2023).

[41] G. Oreski and G. Wallner, "Delamination behaviour of multi-layer films for PV encapsulation", en, *Solar Energy Materials and Solar Cells*, vol. 89, no. 2-3, pp. 139–151, Nov. 2005, ISSN: 09270248. DOI: 10.1016/j.solmat.2005.02.009. [Online]. Available: https://linkinghub.elsevier.com/retrieve/pii/S0927024805000668 (visited on 06/29/2023).

[42] M. Kempe, "Encapsulant Materials for PV Modules", en, in *Photovoltaic Solar Energy*, A. Reinders, P. Verlinden, W. Van Sark, and A. Freundlich, Eds., Chichester, UK: John Wiley & Sons, Ltd, Jan. 2017, pp. 478–490, ISBN: 978-1-118-92749-6 978-1-118-92746-5. DOI: 10.1002/9781118927496.ch43. [Online]. Available: https://onlinelibrary.wiley.com/doi/10.1002/9781118927496.ch43 (visited on 06/29/2023).

[43] O. Hasan and A. Arif, "Performance and life prediction model for photovoltaic modules: Effect of encapsulant constitutive behavior", en, *Solar Energy Materials and Solar Cells*, vol. 122, pp. 75–87, Mar. 2014, ISSN: 09270248. DOI: 10.1016/j.solmat.2013.11.016. [Online]. Available: https://linkinghub.elsevier.com/retrieve/pii/S0927024813006004 (visited on 06/29/2023).

[44]   A. S. Sarkın, N. Ekren, and Ş. Sağlam, "A review of anti-reflection and self-cleaning coatings on photovoltaic panels", en, *Solar Energy*, vol. 199, pp. 63–73, Mar. 2020, ISSN: 0038092X. DOI: 10.1016/j.solener.2020.01.084. [Online]. Available: https://linkinghub. elsevier.com/retrieve/pii/S0038092X20300918 (visited on 06/29/2023).

[45]   N. Shanmugam, R. Pugazhendhi, R. Madurai Elavarasan, P. Kasiviswanathan, and N. Das, "Anti-Reflective Coating Materials: A Holistic Review from PV Perspective", en, *Energies*, vol. 13, no. 10, p. 2631, May 2020, ISSN: 1996-1073. DOI: 10.3390/en13102631. [Online]. Available: https://www.mdpi.com/1996-1073/13/10/2631 (visited on 06/29/2023).

[46]   A. Syafiq, V. Balakrishnan, M. S. Ali, *et al.*, "Application of transparent self-cleaning coating for photovoltaic panel: a review", en, *Current Opinion in Chemical Engineering*, vol. 36, p. 100 801, Jun. 2022, ISSN: 22113398. DOI: 10.1016/j.coche.2022.100801. [Online]. Available: https://linkinghub.elsevier.com/retrieve/pii/S2211339822000119 (visited on 06/29/2023).

[47]   A. Grosjean, A. Soum-Glaude, P. Neveu, and L. Thomas, "Comprehensive simulation and optimization of porous SiO2 antireflective coating to improve glass solar transmittance for solar energy applications", en, *Solar Energy Materials and Solar Cells*, vol. 182, pp. 166–177, Aug. 2018, ISSN: 09270248. DOI: 10.1016/j.solmat.2018.03.040. [Online]. Available: https://linkinghub.elsevier.com/retrieve/pii/S0927024818301508 (visited on 06/29/2023).

[48]   L.-z. Zhang, A.-j. Pan, R.-r. Cai, and H. Lu, "Indoor experiments of dust deposition reduction on solar cell covering glass by transparent super-hydrophobic coating with different tilt angles", en, *Solar Energy*, vol. 188, pp. 1146–1155, Aug. 2019, ISSN: 0038092X. DOI: 10.1016/j.solener.2019.07.026. [Online]. Available: https://linkinghub.elsevier. com/retrieve/pii/S0038092X19306887 (visited on 06/29/2023).

[49]   M. Fathi, M. Abderrezek, and M. Friedrich, "Reducing dust effects on photovoltaic panels by hydrophobic coating", en, *Clean Technologies and Environmental Policy*, vol. 19, no. 2, pp. 577–585, Mar. 2017, ISSN: 1618-954X, 1618-9558. DOI: 10.1007/s10098-016-1233-9. [Online]. Available: http://link.springer.com/10.1007/s10098-016-1233-9 (visited on 06/29/2023).

[50]   K. Isbilir, F. Lisco, G. Womack, A. Abbas, and J. M. Walls, "Testing of an Anti-Soiling Coating for PV Module Cover Glass", in *2018 IEEE 7th World Conference on Photovoltaic Energy Conversion (WCPEC) (A Joint Conference of 45th IEEE PVSC, 28th PVSEC & 34th EU PVSEC)*, Waikoloa Village, HI: IEEE, Jun. 2018, pp. 3426–3431, ISBN: 978-1-5386-8529-7. DOI: 10.1109/PVSC.2018.8547272. [Online]. Available: https://ieeexplore.ieee. org/document/8547272/ (visited on 06/29/2023).

[51]   C. Ballif, F.-J. Haug, M. Boccard, P. J. Verlinden, and G. Hahn, "Status and perspectives of crystalline silicon photovoltaics in research and industry", en, *Nature Reviews Materials*, vol. 7, no. 8, pp. 597–616, Mar. 2022, ISSN: 2058-8437. DOI: 10.1038/s41578-022-

00423-2. [Online]. Available: https://www.nature.com/articles/s41578-022-00423-2 (visited on 04/12/2023).

[52] E. Biyik, M. Araz, A. Hepbasli, *et al.*, "A key review of building integrated photovoltaic (BIPV) systems", en, *Engineering Science and Technology, an International Journal*, vol. 20, no. 3, pp. 833–858, Jun. 2017, ISSN: 22150986. DOI: 10.1016/j.jestch.2017.01.009. [Online]. Available: https://linkinghub.elsevier.com/retrieve/pii/S2215098616309326 (visited on 06/29/2023).

[53] T. Chen, Y. An, and C. K. Heng, "A Review of Building-Integrated Photovoltaics in Singapore: Status, Barriers, and Prospects", en, *Sustainability*, vol. 14, no. 16, p. 10 160, Aug. 2022, ISSN: 2071-1050. DOI: 10.3390/su141610160. [Online]. Available: https://www.mdpi.com/2071-1050/14/16/10160 (visited on 06/29/2023).

[54] M. Pelle, E. Lucchi, L. Maturi, A. Astigarraga, and F. Causone, "Coloured BIPV Technologies: Methodological and Experimental Assessment for Architecturally Sensitive Areas", en, *Energies*, vol. 13, no. 17, p. 4506, Jan. 2020, Number: 17 Publisher: Multidisciplinary Digital Publishing Institute, ISSN: 1996-1073. DOI: 10.3390/en13174506. [Online]. Available: https://www.mdpi.com/1996-1073/13/17/4506 (visited on 10/06/2023).

[55] P. Bonomo, A. Chatzipanagi, and F. Frontini, "Overview and analysis of current BIPV products: new criteria for supporting the technological transfer in the building sector", *VITRUVIO - International Journal of Architectural Technology and Sustainability*, no. 1, p. 67, Dec. 2015, ISSN: 2444-9091. DOI: 10.4995/vitruvio-ijats.2015.4476. [Online]. Available: http://polipapers.upv.es/index.php/vitruvio/article/view/4476 (visited on 06/29/2023).

[56] "Innovative Solution for Building Integrated Photovoltaics", *Proceedings of CISBAT 2013 Cleantech for Smart Cities and Buildings*, L.-E. Perret-Aebi, P. Heinstein, V. Chapuis, *et al.*, Eds., 2013, Meeting Name: CISBAT 2013 Place: Lausanne, Switzerland Publisher: EPFL Solar Energy and Building Physics Laboratory (LESO-PB).

[57] V. Neder, S. L. Luxembourg, and A. Polman, "Efficient colored silicon solar modules using integrated resonant dielectric nanoscatterers", en, *Applied Physics Letters*, vol. 111, no. 7, p. 073 902, Aug. 2017, ISSN: 0003-6951, 1077-3118. DOI: 10.1063/1.4986796. [Online]. Available: https://pubs.aip.org/apl/article/111/7/073902/34714/Efficient-colored-silicon-solar-modules-using (visited on 08/08/2023).

[58] C. Jiang, G. Zhang, Z. Hong, *et al.*, "Colored Silicon Heterojunction Solar Cells Exceeding 23.5% Efficiency Enabled by Luminescent Down-Shift Quantum Dots", en, *Advanced Materials*, vol. 35, no. 6, p. 2 208 042, 2023, ISSN: 1521-4095. DOI: 10.1002/adma.202208042. [Online]. Available: https://onlinelibrary.wiley.com/doi/abs/10.1002/adma.202208042 (visited on 10/16/2023).

# Bibliography

[59]    C. Ji, Z. Zhang, T. Masuda, Y. Kudo, and L. J. Guo, "Vivid-colored silicon solar panels with high efficiency and non-iridescent appearance", en, *Nanoscale Horizons*, vol. 4, no. 4, pp. 874–880, 2019, ISSN: 2055-6756, 2055-6764. DOI: 10.1039/C8NH00368H. [Online]. Available: http://xlink.rsc.org/?DOI=C8NH00368H (visited on 08/08/2023).

[60]    H. Wang, H. A. Dewi, T. M. Koh, A. Bruno, S. Mhaisalkar, and N. Mathews, "Bifacial, Color-Tunable Semitransparent Perovskite Solar Cells for Building-Integrated Photovoltaics", en, *ACS Applied Materials & Interfaces*, vol. 12, no. 1, pp. 484–493, Jan. 2020, ISSN: 1944-8244, 1944-8252. DOI: 10.1021/acsami.9b15488. [Online]. Available: https://pubs.acs.org/doi/10.1021/acsami.9b15488 (visited on 08/08/2023).

[61]    X. Li, R. Xia, K. Yan, *et al.*, "Semitransparent Organic Solar Cells with Vivid Colors", en, *ACS Energy Letters*, vol. 5, no. 10, pp. 3115–3123, Oct. 2020, ISSN: 2380-8195, 2380-8195. DOI: 10.1021/acsenergylett.0c01554. [Online]. Available: https://pubs.acs.org/doi/10.1021/acsenergylett.0c01554 (visited on 08/08/2023).

[62]    A. Soman and A. Antony, "Colored solar cells with spectrally selective photonic crystal reflectors for application in building integrated photovoltaics", en, *Solar Energy*, vol. 181, pp. 1–8, Mar. 2019, ISSN: 0038092X. DOI: 10.1016/j.solener.2019.01.058. [Online]. Available: https://linkinghub.elsevier.com/retrieve/pii/S0038092X19300702 (visited on 08/08/2023).

[63]    SUNAGE, *Winter World*, Jul. 2023. [Online]. Available: https://sunage.ch/en/projects-facade.

[64]    M. Pelle, F. Causone, L. Maturi, and D. Moser, "Opaque Coloured Building Integrated Photovoltaic (BIPV): A Review of Models and Simulation Frameworks for Performance Optimisation", en, *Energies*, vol. 16, no. 4, p. 1991, Jan. 2023, Number: 4 Publisher: Multidisciplinary Digital Publishing Institute, ISSN: 1996-1073. DOI: 10.3390/en16041991. [Online]. Available: https://www.mdpi.com/1996-1073/16/4/1991 (visited on 10/13/2023).

[65]    *LÍNEA 100 MW Líneas de producción llave en mano de módulos fotovoltaicos*. [Online]. Available: https://www.mondragon-assembly.com/es-mx/solar-automation-solutions/turnkey-lines-for-pv-module-manufacturing/100-mw-line/ (visited on 07/26/2023).

[66]    R. A. Agathokleous and S. A. Kalogirou, "Status, barriers and perspectives of building integrated photovoltaic systems", en, *Energy*, vol. 191, p. 116 471, Jan. 2020, ISSN: 03605442. DOI: 10.1016/j.energy.2019.116471. [Online]. Available: https://linkinghub.elsevier.com/retrieve/pii/S0360544219321668 (visited on 08/08/2023).

[67]    P. D. T. O'Connor and A. Kleyner, *Practical Reliability Engineering*, en, 1st ed. Wiley, Dec. 2011, ISBN: 978-0-470-97982-2 978-1-119-96126-0. DOI: 10.1002/9781119961260. [Online]. Available: https://onlinelibrary.wiley.com/doi/book/10.1002/9781119961260 (visited on 08/08/2023).

[68]    D. Kececioglu, *Reliability engineering handbook. 1*, eng. Lancaster, Penn: DEStech Publ, 2002, ISBN: 978-1-932078-00-8.

[69] E. Annigoni, "Reliability of photovoltaic modules:from indoor testing to long-term performance prediction", en, May 2018, Publisher: Lausanne, EPFL. DOI: 10.5075/EPFL-THESIS-8672. [Online]. Available: http://infoscience.epfl.ch/record/255400 (visited on 08/08/2023).

[70] M. Köntges, S. Kurtz, C. Packard, U. Jahn, K. A. Berger, and K. Kato, *Performance and reliability of photovoltaic systems: subtask 3.2: Review of failures of photovoltaic modules: IEA PVPS task 13: external final report IEA-PVPS*, eng. Sankt Ursen: International Energy Agency, Photovoltaic Power Systems Programme, 2014, ISBN: 978-3-906042-16-9.

[71] *IEC 61730-1:2023 Photovoltaic (PV) module safety qualification - Part 1: Requirements for construction*, 2023.

[72] *Terrestrial photovoltaic (PV) modules: design qualification and type approval. Part 2, Test procedures = Modules photovoltaïques (PV) pour applications terrestres : qualification de la conception et homologation. Partie 2, Procédures d'essai*, en, Edition 2.0. 2021, OCLC: 1292019353, ISBN: 978-2-8322-9394-2.

[73] *IEC TS 63209-2 ED1: Extended-stress testing of photovoltaic modules – Part 2: Component materials and packaging*, 2021.

[74] I. E. Commission, *IEC 60050 (191): International Electrotechnical Vocabulary, Chapter 191: Dependability and quality of service*, 1990.

[75] A. C. Oliveira Martins, "Glass-free lightweight PV building elements: solutions to minimize weight and maximize durability", en, Jan. 2019, Publisher: Lausanne, EPFL. DOI: 10.5075/EPFL-THESIS-9149. [Online]. Available: http://infoscience.epfl.ch/record/262815 (visited on 08/08/2023).

[76] L. Gnocchi, "The role of Encapsulants in the long-term performance of advanced Crystalline Silicon Glass-Glass PV modules", en, Jun. 2022, Publisher: Lausanne, EPFL. DOI: 10.5075/EPFL-THESIS-9385. [Online]. Available: http://infoscience.epfl.ch/record/294600 (visited on 08/08/2023).

[77] *IEC TS 62788-7-2: Measurement procedures for materials used in photovoltaic modules - Part 7-2: Environmental exposures - accelerated weathering tests of polymeric materials*, 2017.

[78] R. Siddiqui, R. Kumar, G. K. Jha, *et al.*, "Comparison of different technologies for solar PV (Photovoltaic) outdoor performance using indoor accelerated aging tests for long term reliability", en, *Energy*, vol. 107, pp. 550–561, Jul. 2016, ISSN: 03605442. DOI: 10.1016/j.energy.2016.04.054. [Online]. Available: https://linkinghub.elsevier.com/retrieve/pii/S0360544216304601 (visited on 08/09/2023).

[79] C. R. Osterwald and T. J. McMahon, "History of accelerated and qualification testing of terrestrial photovoltaic modules: A literature review", en, *Progress in Photovoltaics: Research and Applications*, vol. 17, no. 1, pp. 11–33, Jan. 2009, ISSN: 10627995, 1099159X. DOI: 10.1002/pip.861. [Online]. Available: https://onlinelibrary.wiley.com/doi/10.1002/pip.861 (visited on 08/09/2023).

## Bibliography

[80]   A. Borja Block, C. Barretta, A. Faes, *et al.*, "Stability of black interconnect coatings for solar photovoltaic module applications", *Solar Energy Materials and Solar Cells*, vol. 262, p. 112 540, Oct. 2023, ISSN: 0927-0248. DOI: 10.1016/j.solmat.2023.112540. [Online]. Available: https://www.sciencedirect.com/science/article/pii/S0927024823003616 (visited on 10/13/2023).

[81]   A. Virtuani, A. Borja Block, N. Wyrsch, and C. Ballif, "The carbon intensity of integrated photovoltaics", en, *Joule*, S2542435123004002, Oct. 2023, ISSN: 25424351. DOI: 10.1016/j.joule.2023.09.010. [Online]. Available: https://linkinghub.elsevier.com/retrieve/pii/S2542435123004002 (visited on 10/17/2023).

[82]   A. Borja Block, J. Escarre Palou, A. Faes, A. Virtuani, and C. Ballif, "Accurate color characterization of solar photovoltaic modules for building integration", en, *Solar Energy*, vol. 267, p. 112 227, Jan. 2024, ISSN: 0038092X. DOI: 10.1016/j.solener.2023.112227. [Online]. Available: https://linkinghub.elsevier.com/retrieve/pii/S0038092X23008617 (visited on 12/04/2023).

[83]   A. Borja Block, A. Faes, A. Virtuani, and C. Ballif, "Customized Inkjet Equipment for Coating Metallic Interconnects of BIPV Modules", *submitted to the Journal of Manufacturing Processes*, 2023.

[84]   A. Borja Block, A. Virtuani, and C. Ballif, *STABILITY OF INKS USED FOR MASKING METALLIC INTERCONNECTS IN BIPV MODULES*. Sep. 2021.

[85]   A. Borja Block, J. Palou, A. Faes, A. Virtuani, and C. Ballif, *A SCREENING PROTOCOL TO ASSESS THE STABILITY OF THE INKS USED TO MASK METALLIC INTERCONNECTS IN BIPV MODULES*. Sep. 2022.

[86]   B. Derby, "Inkjet Printing of Functional and Structural Materials: Fluid Property Requirements, Feature Stability, and Resolution", en, *Annual Review of Materials Research*, vol. 40, no. 1, pp. 395–414, Jun. 2010, ISSN: 1531-7331, 1545-4118. DOI: 10.1146/annurev-matsci-070909-104502. [Online]. Available: https://www.annualreviews.org/doi/10.1146/annurev-matsci-070909-104502 (visited on 06/05/2023).

[87]   I. E. Commission, "IEC 60904-3:2019: Photovoltaic devices - Part 3: Measurement principles for terrestrial photovoltaic (PV) solar devices with reference spectral irradiance data", 2016.

[88]   G. Sharma, W. Wu, and E. N. Dalal, "The CIEDE2000 color-difference formula: Implementation notes, supplementary test data, and mathematical observations", en, *Color Research & Application*, vol. 30, no. 1, pp. 21–30, Feb. 2005, ISSN: 0361-2317, 1520-6378. DOI: 10.1002/col.20070. [Online]. Available: https://onlinelibrary.wiley.com/doi/10.1002/col.20070 (visited on 02/21/2023).

[89]   "100% Renewable Europe: How To Make Europe's Energy System Climate-Neutral Before 2050", SolarPower Europe and LUT University, Tech. Rep., 2020. [Online]. Available: www.solarpowereurope.org/insights/market-outlooks/100-renewable-europe-study.

[90] P. Eiffert, "Non-Technical Barriers to the Commercialization of PV Power Systems in the Built Environment", NREL, Technical NREL/TP-550-31976, Jan. 2003.

[91] A. Chatzipanagi, F. Frontini, and A. Virtuani, "BIPV-temp: A demonstrative Building Integrated Photovoltaic installation", en, *Applied Energy*, vol. 173, pp. 1–12, Jul. 2016, ISSN: 03062619. DOI: 10.1016/j.apenergy.2016.03.097. [Online]. Available: https://linkinghub.elsevier.com/retrieve/pii/S0306261916304299 (visited on 04/12/2023).

[92] E. Sánchez and J. Izard, "Performance of photovoltaics in non-optimal orientations: An experimental study", en, *Energy and Buildings*, vol. 87, pp. 211–219, Jan. 2015, ISSN: 03787788. DOI: 10.1016/j.enbuild.2014.11.035. [Online]. Available: https://linkinghub.elsevier.com/retrieve/pii/S0378778814009669 (visited on 04/12/2023).

[93] P. Redweik, C. Catita, and M. Brito, "Solar energy potential on roofs and facades in an urban landscape", en, *Solar Energy*, vol. 97, pp. 332–341, Nov. 2013, ISSN: 0038092X. DOI: 10.1016/j.solener.2013.08.036. [Online]. Available: https://linkinghub.elsevier.com/retrieve/pii/S0038092X13003460 (visited on 04/12/2023).

[94] H. Gholami and H. N. Røstvik, "Economic analysis of BIPV systems as a building envelope material for building skins in Europe", en, *Energy*, vol. 204, p. 117 931, Aug. 2020, ISSN: 03605442. DOI: 10.1016/j.energy.2020.117931. [Online]. Available: https://linkinghub.elsevier.com/retrieve/pii/S0360544220310380 (visited on 04/12/2023).

[95] P. Defaix, W. van Sark, E. Worrell, and E. de Visser, "Technical potential for photovoltaics on buildings in the EU-27", en, *Solar Energy*, vol. 86, no. 9, pp. 2644–2653, Sep. 2012, ISSN: 0038092X. DOI: 10.1016/j.solener.2012.06.007. [Online]. Available: https://linkinghub.elsevier.com/retrieve/pii/S0038092X12002186 (visited on 04/12/2023).

[96] S. Nowak, M. Gutschner, D. Ruoss, P. Togweiler, and T. Schoen, "Potential for Building Integrated Photovoltaics", IEA, Tech. Rep. IEA-PVPS T7–4, 2002. [Online]. Available: https://iea-pvps.org/wp-content/uploads/2020/01/rep7_04.pdf.

[97] "Schweizer Hausdächer und -fassaden könnten jährlich 67 TWh Solarstrom produzieren", Press-release, Apr. 2019. [Online]. Available: www.bfe.admin.ch/bfe/de/home/news-und-medien/medienmitteilungen/mm-test.msg-id-74641.html (visited on 05/11/2022).

[98] "Detailanalyse des Solarpotenzials auf Dächern und Fassaden» Swiss Solar Report", Tech. Rep., Aug. 2020. [Online]. Available: www.swissolar.ch/fileadmin/user_upload/Swissolar/Top_Themen/Detailanalyse_Solarpotenzial_Schweiz.pdf (visited on 05/11/2022).

[99] L. Middelhauve, L. Girardin, F. Baldi, and F. Maréchal, "Potential of Photovoltaic Panels on Building Envelopes for Decentralized District Energy Systems", *Frontiers in Energy Research*, vol. 9, p. 689 781, Oct. 2021, ISSN: 2296-598X. DOI: 10.3389/fenrg.2021.689781. [Online]. Available: https://www.frontiersin.org/articles/10.3389/fenrg.2021.689781/full (visited on 04/12/2023).

# Bibliography

[100] D. Anderegg, S. Strebel, and J. Rohrer, "Photovoltaik Potenzial auf Dachflächen in der Schweiz", de, Jul. 2022, Medium: 55,application/pdf Publisher: ZHAW Zürcher Hochschule für Angewandte Wissenschaften. DOI: 10.21256/ZHAW-2425. [Online]. Available: https://digitalcollection.zhaw.ch/handle/11475/25310 (visited on 04/12/2023).

[101] J. Remund, S. Albrecht, and D. Stickelberg, "Das Schweizer PV-Potenzial basierend auf jedem Gebäude", Meteotest-SwissSolar, Tech. Rep. [Online]. Available: www.swissolar.ch/fileadmin/user_upload/Swissolar/Top_Themen/Solarpotenzial_CH_JanRemund.pdf (visited on 05/11/2022).

[102] L. Grüter, S. Probst, and L. Konersmann, *Solarstrom auf Infrastrukturanlagen und Konversionsflächen.* [Online]. Available: https://f.hubspotusercontent40.net/hubfs/7195893/Studie%20InfraSolaire_Endbericht.pdf (visited on 11/11/2022).

[103] I. Schillig, B. Previsic, F. Egli, L. Hälg, M. Schreiber, and M. Schwary, *Alpenstrom jetzt!* [Online]. Available: https://www.kulturen-der-alpen.ch/fileadmin/user_upload/Dokumente/Downloads/Studien___Publikationen/Alpenstrom_jetzt.pd (visited on 11/11/2022).

[104] *PV-GIS.* [Online]. Available: https://ec.europa.eu/jrc/en/pvgis.

[105] N. Scarlat, M. Prussi, and M. Padella, "Quantification of the carbon intensity of electricity produced and used in Europe", en, *Applied Energy*, vol. 305, p. 117 901, Jan. 2022, ISSN: 03062619. DOI: 10.1016/j.apenergy.2021.117901. [Online]. Available: https://linkinghub.elsevier.com/retrieve/pii/S0306261921012149 (visited on 04/12/2023).

[106] M. A. Curran, "Life Cycle Assessment: a review of the methodology and its application to sustainability", en, *Current Opinion in Chemical Engineering*, vol. 2, no. 3, pp. 273–277, Aug. 2013, ISSN: 22113398. DOI: 10.1016/j.coche.2013.02.002. [Online]. Available: https://linkinghub.elsevier.com/retrieve/pii/S2211339813000221 (visited on 04/12/2023).

[107] E. C. for Standardization, *DIN EN ISO 14040: Environmental Management – Life Cycle Assessment – Principles and Framework (ISO 14040: 2006)*, 2006.

[108] E. C. for Standardization, *DIN EN ISO 14044: Environmental Management – Life Cycle Assessment – Requirements and Guidelines*, 2006.

[109] E. C. .-. J. R. C. .-. I. for Environment and Sustainability, *International Reference Life Cycle Data System (ILCD) Handbook Recommendations for Life Cycle Impact Assessment in the European Context*, First. Luxembourg, 2011.

[110] R. Frischknecht, P. Stolz, G. Heath, M. Raugei, P. Sinha, and M. de Wild-Scholten, "Methodology Guidelines on Life Cycle Assessment of Photovoltaic 2020", IEA, Tech. Rep. IEA-PVPS T12-18: 2020, 2020.

[111] J. Fritsche, C. Olson, A. Wade, *et al.*, "Product Environmental Footprint Category Rules (PEFCR): Photovoltaic Modules Used in Photovoltaic Power Systems for Electricity Generation: Version 1.1", Tech. Rep., 2019.

[112]   A. Müller, L. Friedrich, C. Reichel, S. Herceg, M. Mittag, and D. H. Neuhaus, "A comparative life cycle assessment of silicon PV modules: Impact of module design, manufacturing location and inventory", en, *Solar Energy Materials and Solar Cells*, vol. 230, p. 111 277, Sep. 2021, ISSN: 09270248. DOI: 10.1016/j.solmat.2021.111277. [Online]. Available: https://linkinghub.elsevier.com/retrieve/pii/S0927024821003202 (visited on 04/12/2023).

[113]   R. Frischknecht and L. Krebs, "Environmental life cycle assessment of electricity from PVsystems", IEA-PVPS, Tech. Rep., 2021.

[114]   R. Frischknecht, *Umweltfussabdruck Photovoltaikstrom Update 2020*, Jul. 2019.

[115]   V. Fthenakis and E. Leccisi, "Updated sustainability status of crystalline silicon-based photovoltaic systems: Life-cycle energy and environmental impact reduction trends", en, *Progress in Photovoltaics: Research and Applications*, vol. 29, no. 10, pp. 1068–1077, Oct. 2021, ISSN: 1062-7995, 1099-159X. DOI: 10.1002/pip.3441. [Online]. Available: https://onlinelibrary.wiley.com/doi/10.1002/pip.3441 (visited on 04/12/2023).

[116]   J. C. Goldschmidt, L. Wagner, R. Pietzcker, and L. Friedrich, "Technological learning for resource efficient terawatt scale photovoltaics", en, *Energy & Environmental Science*, vol. 14, no. 10, pp. 5147–5160, 2021, ISSN: 1754-5692, 1754-5706. DOI: 10.1039/D1EE02497C. [Online]. Available: http://xlink.rsc.org/?DOI=D1EE02497C (visited on 04/12/2023).

[117]   G. Saevarsdottir, T. Magnusson, and H. Kvande, "Reducing the Carbon Footprint: Primary Production of Aluminum and Silicon with Changing Energy Systems", en, *Journal of Sustainable Metallurgy*, vol. 7, no. 3, pp. 848–857, Sep. 2021, ISSN: 2199-3823, 2199-3831. DOI: 10.1007/s40831-021-00429-0. [Online]. Available: https://link.springer.com/10.1007/s40831-021-00429-0 (visited on 04/12/2023).

[118]   X. Li, K. J. Chalvatzis, and D. Pappas, "China's electricity emission intensity in 2020 – an analysis at provincial level", en, *Energy Procedia*, vol. 142, pp. 2779–2785, Dec. 2017, ISSN: 18766102. DOI: 10.1016/j.egypro.2017.12.421. [Online]. Available: https://linkinghub.elsevier.com/retrieve/pii/S1876610217361714 (visited on 04/12/2023).

[119]   R. Frischknecht, *Personal communication*, Nov. 2022.

[120]   "Report: A life-cycle model of Chinese grid power and its application to the life cycle impact assessment of primary aluminium", Tech. Rep. [Online]. Available: https://international-aluminium.org/wp-content/uploads/2021/03/Life-Cycle-Model-of-Chinese-Grid-Power-Application.pdf (visited on 11/20/2022).

[121]   K. Feng, K. Hubacek, Y. L. Siu, and X. Li, "The energy and water nexus in Chinese electricity production: A hybrid life cycle analysis", en, *Renewable and Sustainable Energy Reviews*, vol. 39, pp. 342–355, Nov. 2014, ISSN: 13640321. DOI: 10.1016/j.rser.2014.07.080. [Online]. Available: https://linkinghub.elsevier.com/retrieve/pii/S1364032114005322 (visited on 04/12/2023).

[122] A. Virtuani and L. Morganti, "Profitability of Solar Photovoltaic Projects: A Sensitivity Analysis of Performance Loss Curves and Operation and Maintenance Expenses", en, *Solar RRL*, p. 2 200 663, Nov. 2022, ISSN: 2367-198X, 2367-198X. DOI: 10.1002/solr. 202200663. [Online]. Available: https://onlinelibrary.wiley.com/doi/10.1002/solr. 202200663 (visited on 04/12/2023).

[123] B. Santos, "CEA-INES unveils 566 W HJT solar module with low carbon footprint", Jan. 2023. [Online]. Available: www.pv-magazine.com/2023/01/17/cea-ines-unveils-565-w-hjt-solar-module-with-low-carbon-footprint (visited on 01/31/2023).

[124] *Greenhouse gas emission intensity of electricity generation*, 2020. [Online]. Available: https://www.eea.europa.eu/ims/greenhouse-gas-emission-intensity-of-1 (visited on 09/11/2022).

[125] A. Moro and L. Lonza, "Electricity carbon intensity in European Member States: Impacts on GHG emissions of electric vehicles", en, *Transportation Research Part D: Transport and Environment*, vol. 64, pp. 5–14, Oct. 2018, ISSN: 13619209. DOI: 10.1016/ j.trd.2017.07.012. [Online]. Available: https://linkinghub.elsevier.com/retrieve/pii/ S1361920916307933 (visited on 04/12/2023).

[126] B. Tranberg, O. Corradi, B. Lajoie, T. Gibon, I. Staffell, and G. B. Andresen, "Real-time carbon accounting method for the European electricity markets", en, *Energy Strategy Reviews*, vol. 26, p. 100 367, Nov. 2019, ISSN: 2211467X. DOI: 10.1016/j.esr.2019.100367. [Online]. Available: https://linkinghub.elsevier.com/retrieve/pii/S2211467X19300549 (visited on 04/12/2023).

[127] A. Fairbrother, H. Quest, E. Özkalay, *et al.*, "Long-Term Performance and Shade Detection in Building Integrated Photovoltaic Systems", en, *Solar RRL*, vol. 6, no. 5, p. 2 100 583, May 2022, ISSN: 2367-198X, 2367-198X. DOI: 10.1002/solr.202100583. [Online]. Available: https://onlinelibrary.wiley.com/doi/10.1002/solr.202100583 (visited on 04/12/2023).

[128] A. Virtuani and D. Strepparava, "Modelling the performance of amorphous and crystalline silicon in different typologies of building-integrated photovoltaic (BIPV) conditions", en, *Solar Energy*, vol. 146, pp. 113–118, Apr. 2017, ISSN: 0038092X. DOI: 10.1016/ j.solener.2017.02.035. [Online]. Available: https://linkinghub.elsevier.com/retrieve/pii/ S0038092X17301287 (visited on 04/12/2023).

[129] J. Escarré, H.-Y. Li, L. Sansonnens, *et al.*, "When PV modules are becoming real building elements: White solar module, a revolution for BIPV", in *2015 IEEE 42nd Photovoltaic Specialist Conference (PVSC)*, Jun. 2015, pp. 1–2. DOI: 10.1109/PVSC.2015.7355630. [Online]. Available: https://ieeexplore.ieee.org/abstract/document/7355630/authors# authors (visited on 10/06/2023).

[130] G. De Carne, G. Buticchi, Z. Zou, and M. Liserre, "Reverse Power Flow Control in a ST-Fed Distribution Grid", *IEEE Transactions on Smart Grid*, vol. 9, no. 4, pp. 3811–3819, Jul. 2018, ISSN: 1949-3053, 1949-3061. DOI: 10.1109/TSG.2017.2651147. [Online]. Available: https://ieeexplore.ieee.org/document/7812791/ (visited on 04/12/2023).

[131]  P. Mohammadi and S. Mehraeen, "Challenges of PV Integration in Low-Voltage Secondary Networks", *IEEE Transactions on Power Delivery*, vol. 32, no. 1, pp. 525–535, Feb. 2017, ISSN: 0885-8977, 1937-2408. DOI: 10.1109/TPWRD.2016.2556692. [Online]. Available: http://ieeexplore.ieee.org/document/7457324/ (visited on 04/12/2023).

[132]  S. Fatima, V. Püvi, and M. Lehtonen, "Review on the PV Hosting Capacity in Distribution Networks", en, *Energies*, vol. 13, no. 18, p. 4756, Sep. 2020, ISSN: 1996-1073. DOI: 10.3390/en13184756. [Online]. Available: https://www.mdpi.com/1996-1073/13/18/4756 (visited on 04/12/2023).

[133]  F. R. Segundo Sevilla, D. Parra, N. Wyrsch, M. K. Patel, F. Kienzle, and P. Korba, "Techno-economic analysis of battery storage and curtailment in a distribution grid with high PV penetration", en, *Journal of Energy Storage*, vol. 17, pp. 73–83, Jun. 2018, ISSN: 2352152X. DOI: 10.1016/j.est.2018.02.001. [Online]. Available: https://linkinghub.elsevier.com/retrieve/pii/S2352152X17302591 (visited on 04/12/2023).

[134]  R. Luthander, J. Widén, J. Munkhammar, and D. Lingfors, "Self-consumption enhancement and peak shaving of residential photovoltaics using storage and curtailment", en, *Energy*, vol. 112, pp. 221–231, Oct. 2016, ISSN: 03605442. DOI: 10.1016/j.energy.2016.06.039. [Online]. Available: https://linkinghub.elsevier.com/retrieve/pii/S0360544216308131 (visited on 04/12/2023).

[135]  J. Seuss, M. J. Reno, R. J. Broderick, and S. Grijalva, "Improving distribution network PV hosting capacity via smart inverter reactive power support", in *2015 IEEE Power & Energy Society General Meeting*, Denver, CO, USA: IEEE, Jul. 2015, pp. 1–5, ISBN: 978-1-4673-8040-9. DOI: 10.1109/PESGM.2015.7286523. [Online]. Available: http://ieeexplore.ieee.org/document/7286523/ (visited on 04/12/2023).

[136]  J. Holweger, L. Bloch, C. Ballif, and N. Wyrsch, "Mitigating the impact of distributed PV in a low-voltage grid using electricity tariffs", en, *Electric Power Systems Research*, vol. 189, p. 106763, Dec. 2020, ISSN: 03787796. DOI: 10.1016/j.epsr.2020.106763. [Online]. Available: https://linkinghub.elsevier.com/retrieve/pii/S0378779620305666 (visited on 04/12/2023).

[137]  Y. Zhang, T. Ma, and H. Yang, "Grid-connected photovoltaic battery systems: A comprehensive review and perspectives", en, *Applied Energy*, vol. 328, p. 120182, Dec. 2022, ISSN: 03062619. DOI: 10.1016/j.apenergy.2022.120182. [Online]. Available: https://linkinghub.elsevier.com/retrieve/pii/S03062619022014398 (visited on 04/12/2023).

[138]  R. Luthander, J. Widén, D. Nilsson, and J. Palm, "Photovoltaic self-consumption in buildings: A review", en, *Applied Energy*, vol. 142, pp. 80–94, Mar. 2015, ISSN: 03062619. DOI: 10.1016/j.apenergy.2014.12.028. [Online]. Available: https://linkinghub.elsevier.com/retrieve/pii/S0306261914012859 (visited on 04/12/2023).

[139]  H. Kikusato, Y. Fujimoto, S.-i. Hanada, *et al.*, "Electric Vehicle Charging Management Using Auction Mechanism for Reducing PV Curtailment in Distribution Systems", *IEEE Transactions on Sustainable Energy*, vol. 11, no. 3, pp. 1394–1403, Jul. 2020, ISSN:

1949-3029, 1949-3037. DOI: 10.1109/TSTE.2019.2926998. [Online]. Available: https://ieeexplore.ieee.org/document/8770121/ (visited on 04/12/2023).

[140] R. Fachrizal, U. H. Ramadhani, J. Munkhammar, and J. Widén, "Combined PV–EV hosting capacity assessment for a residential LV distribution grid with smart EV charging and PV curtailment", en, *Sustainable Energy, Grids and Networks*, vol. 26, p. 100 445, Jun. 2021, ISSN: 23524677. DOI: 10.1016/j.segan.2021.100445. [Online]. Available: https://linkinghub.elsevier.com/retrieve/pii/S2352467721000163 (visited on 04/12/2023).

[141] "The potential of energy citizens in the European Union", CE-Delft, Tech. Rep., 2016. [Online]. Available: https://cedelft.eu/wp-content/uploads/sites/2/2021/04/CE_Delft_3J00_Potential_energy_citizens_EU_final.pdf (visited on 11/23/2022).

[142] M. Gržanić, T. Capuder, N. Zhang, and W. Huang, "Prosumers as active market participants: A systematic review of evolution of opportunities, models and challenges", en, *Renewable and Sustainable Energy Reviews*, vol. 154, p. 111 859, Feb. 2022, ISSN: 13640321. DOI: 10.1016/j.rser.2021.111859. [Online]. Available: https://linkinghub.elsevier.com/retrieve/pii/S1364032121011266 (visited on 04/12/2023).

[143] European Commission. Joint Research Centre., *Energy communities: an overview of energy and social innovation.* eng. LU: Publications Office, 2020. [Online]. Available: https://data.europa.eu/doi/10.2760/180576 (visited on 04/12/2023).

[144] C. Ferrara, H. Wilson, and W. Sprenger, "Building-integrated photovoltaics (BIPV)", en, in *The Performance of Photovoltaic (PV) Systems*, Elsevier, 2017, pp. 235–250, ISBN: 978-1-78242-336-2. DOI: 10.1016/B978-1-78242-336-2.00008-2. [Online]. Available: https://linkinghub.elsevier.com/retrieve/pii/B9781782423362000082 (visited on 06/02/2023).

[145] R. J. Yang and P. X. Zou, "Building integrated photovoltaics (BIPV): costs, benefits, risks, barriers and improvement strategy", en, *International Journal of Construction Management*, vol. 16, no. 1, pp. 39–53, Jan. 2016, ISSN: 1562-3599, 2331-2327. DOI: 10.1080/15623599.2015.1117709. [Online]. Available: http://www.tandfonline.com/doi/full/10.1080/15623599.2015.1117709 (visited on 06/06/2023).

[146] M. Mantysalo, V. Pekkanen, K. Kaija, *et al.*, "Capability of inkjet technology in electronics manufacturing", in *2009 59th Electronic Components and Technology Conference*, San Diego, CA, USA: IEEE, May 2009, pp. 1330–1336, ISBN: 978-1-4244-4475-5. DOI: 10.1109/ECTC.2009.5074185. [Online]. Available: http://ieeexplore.ieee.org/document/5074185/ (visited on 06/06/2023).

[147] J. Miettinen, V. Pekkanen, K. Kaija, *et al.*, "Inkjet printed System-in-Package design and manufacturing", en, *Microelectronics Journal*, vol. 39, no. 12, pp. 1740–1750, Dec. 2008, ISSN: 00262692. DOI: 10.1016/j.mejo.2008.02.014. [Online]. Available: https://linkinghub.elsevier.com/retrieve/pii/S0026269208001171 (visited on 06/06/2023).

[148] Y. Liu, H. Zhu, L. Xing, Q. Bu, D. Ren, and B. Sun, "Recent advances in inkjet-printing technologies for flexible/wearable electronics", en, *Nanoscale*, vol. 15, no. 13, pp. 6025–6051, 2023, ISSN: 2040-3364, 2040-3372. DOI: 10.1039/D2NR05649F. [Online]. Available: http://xlink.rsc.org/?DOI=D2NR05649F (visited on 06/06/2023).

[149] C. Schiller, S. Hoffmann, M. Jahn, A. De Rose, and M. Heinrich, "Fully Black and Reliable PV Modules with a Cost-Effective Inkjet Coating of Cell Strings", en, *8th World Conference on Photovoltaic Energy Conversion; 790-796*, 7 pages, 7429 kb, 2022, Artwork Size: 7 pages, 7429 kb Medium: application/pdf Publisher: WIP. DOI: 10.4229/WCPEC-82022-3DV.1.1. [Online]. Available: https://www.eupvsec-proceedings.com/proceedings?paper=51570 (visited on 06/12/2023).

[150] V. Borja Ramírez and A. Ramírez Reivich, *Innovación de producto*, Spanish, 2006.

[151] A. A. Castrejón-Pita, E. S. Betton, N. Campbell, *et al.*, "FORMULATION, QUALITY, CLEANING, AND OTHER ADVANCES IN INKJET PRINTING", en, *Atomization and Sprays*, vol. 31, no. 4, pp. 57–79, 2021, ISSN: 1044-5110. DOI: 10.1615/AtomizSpr. 2020034559. (visited on 06/06/2023).

[152] M. A. Shah, D.-G. Lee, B.-Y. Lee, and S. Hur, "Classifications and Applications of Inkjet Printing Technology: A Review", *IEEE Access*, vol. 9, pp. 140 079–140 102, 2021, ISSN: 2169-3536. DOI: 10.1109/ACCESS.2021.3119219. [Online]. Available: https://ieeexplore. ieee.org/document/9565892/ (visited on 06/06/2023).

[153] T. M. Eggenhuisen, Y. Galagan, A. F. K. V. Biezemans, *et al.*, "High efficiency, fully inkjet printed organic solar cells with freedom of design", en, *Journal of Materials Chemistry A*, vol. 3, no. 14, pp. 7255–7262, 2015, ISSN: 2050-7488, 2050-7496. DOI: 10.1039/C5TA00540J. [Online]. Available: http://xlink.rsc.org/?DOI=C5TA00540J (visited on 06/06/2023).

[154] M. Ritchie, *Print quality requirements for single-pass inkjet printing – the whole picture*. [Online]. Available: https://www.xaar.com/media/1303/print-quality-white-paper.pdf.

[155] XAAR, *A Guide to Industrial Inkjet*. [Online]. Available: https://www.xaar.com/media/2533/xaar-inkjet-guide-eng4.pdf.

[156] R. Schmitt, T. Pfeifer, C. Mersmann, and A. Orth, "A method for the automated positioning and alignment of fibre-reinforced plastic structures based on machine vision", en, *CIRP Annals*, vol. 57, no. 1, pp. 501–504, 2008, ISSN: 00078506. DOI: 10.1016/j. cirp.2008.03.128. [Online]. Available: https://linkinghub.elsevier.com/retrieve/pii/S000785060800098X (visited on 06/06/2023).

[157] W.-Y. Chang, J.-W. Hsu, and B.-Y. Hsu, "3D Scanning System of Structured Light for Aiding Workpiece Position of CNC Machine Tool", in *2018 IEEE International Conference on Advanced Manufacturing (ICAM)*, Yunlin: IEEE, Nov. 2018, pp. 388–391, ISBN: 978-1-5386-5609-9. DOI: 10.1109/AMCON.2018.8614757. [Online]. Available: https://ieeexplore.ieee.org/document/8614757/ (visited on 06/06/2023).

**Bibliography**

[158] N. Chen, X. Men, X. Han, X. Wang, J. Sun, and H. Chen, "Edge detection based on machine vision applying to laminated wood edge cutting process", in *2018 13th IEEE Conference on Industrial Electronics and Applications (ICIEA)*, Wuhan: IEEE, May 2018, pp. 449–454, ISBN: 978-1-5386-3758-6. DOI: 10.1109/ICIEA.2018.8397759. [Online]. Available: https://ieeexplore.ieee.org/document/8397759/ (visited on 06/06/2023).

[159] X. Li, W. Liu, Y. Pan, H. Li, X. Ma, and Z. Jia, "A monocular-vision-based contouring error detection method for CNC machine tools", in *2018 IEEE International Instrumentation and Measurement Technology Conference (I2MTC)*, Houston, TX, USA: IEEE, May 2018, pp. 1–6, ISBN: 978-1-5386-2222-3. DOI: 10.1109/I2MTC.2018.8409552. [Online]. Available: https://ieeexplore.ieee.org/document/8409552/ (visited on 06/06/2023).

[160] H. Li, B. Zhu, Z. Chen, and X. Zhang, "Realtime in-plane displacements tracking of the precision positioning stage based on computer micro-vision", en, *Mechanical Systems and Signal Processing*, vol. 124, pp. 111–123, Jun. 2019, ISSN: 08883270. DOI: 10.1016/j.ymssp.2019.01.046. [Online]. Available: https://linkinghub.elsevier.com/retrieve/pii/S0888327019300627 (visited on 06/06/2023).

[161] G. R. Bradski and A. Kaehler, *Learning OpenCV: computer vision with the OpenCV library* (Software that sees), eng, 1. ed., [Nachdr.] Beijing: O'Reilly, 2011, ISBN: 978-0-596-51613-0.

[162] J.-Y. Bouguet, *Camera Calibration Toolbox for Matlab*, Language: en, May 2022. DOI: 10.22002/D1.20164. [Online]. Available: https://data.caltech.edu/records/20164 (visited on 06/20/2023).

[163] A. Geiger, F. Moosmann, O. Car, and B. Schuster, "Automatic camera and range sensor calibration using a single shot", in *2012 IEEE International Conference on Robotics and Automation*, St Paul, MN, USA: IEEE, May 2012, pp. 3936–3943, ISBN: 978-1-4673-1405-3 978-1-4673-1403-9 978-1-4673-1578-4 978-1-4673-1404-6. DOI: 10.1109/ICRA.2012.6224570. [Online]. Available: http://ieeexplore.ieee.org/document/6224570/ (visited on 06/06/2023).

[164] Z. Zhang, "A flexible new technique for camera calibration", *IEEE Transactions on Pattern Analysis and Machine Intelligence*, vol. 22, no. 11, pp. 1330–1334, Nov. 2000, ISSN: 01628828. DOI: 10.1109/34.888718. [Online]. Available: http://ieeexplore.ieee.org/document/888718/ (visited on 06/20/2023).

[165] J. Heikkila and O. Silven, "A four-step camera calibration procedure with implicit image correction", in *Proceedings of IEEE Computer Society Conference on Computer Vision and Pattern Recognition*, San Juan, Puerto Rico: IEEE Comput. Soc, 1997, pp. 1106–1112, ISBN: 978-0-8186-7822-6. DOI: 10.1109/CVPR.1997.609468. [Online]. Available: http://ieeexplore.ieee.org/document/609468/ (visited on 06/20/2023).

[166] A. Notenboom, D. Bruijnen, E. Homburg, R. V. Molengraft, L. V. Bedem, and M. Steinbuch, "Mechatronic design of an active printhead alignment mechanism for wide format printing systems", en, *Mechatronics*, vol. 17, no. 2-3, pp. 109–120, Mar. 2007,

ISSN: 09574158. DOI: 10.1016/j.mechatronics.2006.10.001. [Online]. Available: https://linkinghub.elsevier.com/retrieve/pii/S0957415806001152 (visited on 06/06/2023).

[167]  T. Wang, J. Zhang, J. Dong, S. Pan, and L. Zheng, "A Method for Generating Spray Trajectory of a Shoe Sole Based on Laser Vision", in *2019 IEEE 4th International Conference on Image, Vision and Computing (ICIVC)*, Xiamen, China: IEEE, Jul. 2019, pp. 36–39, ISBN: 978-1-72812-325-7. DOI: 10.1109/ICIVC47709.2019.8981040. [Online]. Available: https://ieeexplore.ieee.org/document/8981040/ (visited on 06/06/2023).

[168]  R. Szeliski, *Computer Vision: Algorithms and Applications* (Texts in Computer Science), en. London: Springer London, 2011, ISBN: 978-1-84882-934-3 978-1-84882-935-0. DOI: 10.1007/978-1-84882-935-0. [Online]. Available: https://link.springer.com/10.1007/978-1-84882-935-0 (visited on 06/06/2023).

[169]  M. Yuda, Z. Xiangjun, S. Weiming, and L. Shaofeng, "Target accurate positioning based on the point cloud created by stereo vision", in *2016 23rd International Conference on Mechatronics and Machine Vision in Practice (M2VIP)*, Nanjing, China: IEEE, Nov. 2016, pp. 1–5, ISBN: 978-1-5090-2764-4. DOI: 10.1109/M2VIP.2016.7827268. [Online]. Available: http://ieeexplore.ieee.org/document/7827268/ (visited on 06/06/2023).

[170]  S. Byun and M. Kim, "Real-Time Positioning and Orienting of Pallets Based on Monocular Vision", in *2008 20th IEEE International Conference on Tools with Artificial Intelligence*, Dayton, OH, USA: IEEE, Nov. 2008, pp. 505–508, ISBN: 978-0-7695-3440-4. DOI: 10.1109/ICTAI.2008.124. [Online]. Available: http://ieeexplore.ieee.org/document/4669816/ (visited on 06/06/2023).

[171]  T. Jiang, X. Cheng, H. Cui, C. Shi, and Y. Li, "Dual-camera-based method for identification and location of scattered self-plugging rivets for robot grasping", en, *Measurement*, vol. 134, pp. 688–697, Feb. 2019, ISSN: 02632241. DOI: 10.1016/j.measurement.2018.11.017. [Online]. Available: https://linkinghub.elsevier.com/retrieve/pii/S0263224118310716 (visited on 06/06/2023).

[172]  R. C. Gonzalez and R. E. Woods, *Digital image processing*, eng, Fourth edition, global edition. New York, NY: Pearson, 2018, ISBN: 978-1-292-22304-9.

[173]  S. Magdassi, Ed., *The chemistry of inkjet inks*. Singapore ; Hackensack, NJ: World Scientific, 2010, OCLC: ocn473429224, ISBN: 978-981-281-821-8.

[174]  *Buildings - Energy System*, en-GB. [Online]. Available: https://www.iea.org/energy-system/buildings (visited on 10/12/2023).

[175]  R. Renewables now, "REN21 - 2022 - Renewables 2022 Global Status Report", Tech. Rep., 2022.

[176]  S. A. Awuku, A. Bennadji, F. Muhammad-Sukki, and N. Sellami, "Myth or gold? The power of aesthetics in the adoption of building integrated photovoltaics (BIPVs)", en, *Energy Nexus*, vol. 4, p. 100 021, Dec. 2021, ISSN: 27724271. DOI: 10.1016/j.nexus.2021.100021. [Online]. Available: https://linkinghub.elsevier.com/retrieve/pii/S2772427121000218 (visited on 03/27/2023).

[177] A. Hancock and L. Lin, "Challenges of UV curable ink-jet printing inks – a formulator's perspective", en, *Pigment & Resin Technology*, vol. 33, no. 5, pp. 280–286, Oct. 2004, ISSN: 0369-9420. DOI: 10.1108/03699420410560470. [Online]. Available: https://www.emerald.com/insight/content/doi/10.1108/03699420410560470/full/html (visited on 03/30/2023).

[178] W. Gambogi, Y. Heta, K. Hashimoto, *et al.*, "Weathering and durability of PV backsheets and impact on PV module performance", N. G. Dhere, J. H. Wohlgemuth, and K. W. Lynn, Eds., San Diego, California, United States, Sep. 2013, 88250B. DOI: 10.1117/12.2024491. [Online]. Available: http://proceedings.spiedigitallibrary.org/proceeding.aspx?doi=10.1117/12.2024491 (visited on 05/31/2023).

[179] Y. Lyu, A. Fairbrother, J. H. Kim, *et al.*, "Fluorescence imaging analysis of depth-dependent degradation in photovoltaic laminates: insights to the failure", en, *Progress in Photovoltaics: Research and Applications*, vol. 28, no. 2, pp. 122–134, Feb. 2020, ISSN: 1062-7995, 1099-159X. DOI: 10.1002/pip.3212. [Online]. Available: https://onlinelibrary.wiley.com/doi/10.1002/pip.3212 (visited on 06/06/2023).

[180] R. Satoto, W. S. Subowo, R. Yusiasih, Y. Takane, Y. Watanabe, and T. Hatakeyama, "Weathering of high-density polyethylene in different latitudes", en, *Polymer Degradation and Stability*, vol. 56, no. 3, pp. 275–279, Jun. 1997, ISSN: 01413910. DOI: 10.1016/S0141-3910(96)00213-3. [Online]. Available: https://linkinghub.elsevier.com/retrieve/pii/S0141391096002133 (visited on 05/24/2023).

[181] M. S. Salim, D. Ariawan, M. F. Ahmad Rasyid, R. Mat Taib, M. Z. Ahmad Thirmizir, and Z. A. Mohd Ishak, "Accelerated Weathering and Water Absorption Behavior of Kenaf Fiber Reinforced Acrylic Based Polyester Composites", *Frontiers in Materials*, vol. 7, p. 26, Feb. 2020, ISSN: 2296-8016. DOI: 10.3389/fmats.2020.00026. [Online]. Available: https://www.frontiersin.org/article/10.3389/fmats.2020.00026/full (visited on 05/24/2023).

[182] G. Oreski, S. Pötz, A. Omazic, *et al.*, "Reliability of Electrically Conductive Adhesives", ISBN: 3-936338-50-7. [Online]. Available: https://www.eupvsec-proceedings.com/proceedings?fulltext=p%C3%B6tz&paper=46359.

[183] C. Decker and K. Zahouily, "Photodegradation and photooxidation of thermoset and UV-cured acrylate polymers", en, *Polymer Degradation and Stability*, vol. 64, no. 2, pp. 293–304, May 1999, ISSN: 01413910. DOI: 10.1016/S0141-3910(98)00205-5. [Online]. Available: https://linkinghub.elsevier.com/retrieve/pii/S0141391098002055 (visited on 05/25/2023).

[184] F. Liu, L. Jiang, and S. Yang, "Ultra-violet degradation behavior of polymeric backsheets for photovoltaic modules", en, *Solar Energy*, vol. 108, pp. 88–100, Oct. 2014, ISSN: 0038092X. DOI: 10.1016/j.solener.2014.06.027. [Online]. Available: https://linkinghub.elsevier.com/retrieve/pii/S0038092X14003260 (visited on 05/31/2023).

[185] F. Pern and A. Czanderna, "Characterization of ethylene vinyl acetate (EVA) encapsulant: Effects of thermal processing and weathering degradation on its discoloration", en, *Solar Energy Materials and Solar Cells*, vol. 25, no. 1-2, pp. 3–23, Jan. 1992, ISSN: 09270248. DOI: 10.1016/0927-0248(92)90013-F. [Online]. Available: https://linkinghub.elsevier.com/retrieve/pii/092702489290013F (visited on 05/31/2023).

[186] G. Oreski and G. Wallner, "Evaluation of the aging behavior of ethylene copolymer films for solar applications under accelerated weathering conditions", en, *Solar Energy*, vol. 83, no. 7, pp. 1040–1047, Jul. 2009, ISSN: 0038092X. DOI: 10.1016/j.solener.2009.01.009. [Online]. Available: https://linkinghub.elsevier.com/retrieve/pii/S0038092X09000115 (visited on 05/31/2023).

[187] A. Krauklis and A. Echtermeyer, "Mechanism of Yellowing: Carbonyl Formation during Hygrothermal Aging in a Common Amine Epoxy", en, *Polymers*, vol. 10, no. 9, p. 1017, Sep. 2018, ISSN: 2073-4360. DOI: 10.3390/polym10091017. [Online]. Available: http://www.mdpi.com/2073-4360/10/9/1017 (visited on 06/12/2023).

[188] J. Segurola, N. S. Allen, M. Edge, A. McMahon, and S. Wilson, "Photoyellowing and discolouration of UV cured acrylated clear coatings systems: influence of photoinitiator type", en, *Polymer Degradation and Stability*, vol. 64, no. 1, pp. 39–48, Apr. 1999, ISSN: 01413910. DOI: 10.1016/S0141-3910(98)00169-4. [Online]. Available: https://linkinghub.elsevier.com/retrieve/pii/S0141391098001694 (visited on 02/15/2023).

[189] N. S. Allen and M. Edge, "Perspectives on additives for polymers. Part 2. Aspects of photostabilization and role of fillers and pigments", en, *Journal of Vinyl and Additive Technology*, vol. 27, no. 2, pp. 211–239, May 2021, ISSN: 1083-5601, 1548-0585. DOI: 10.1002/vnl.21810. [Online]. Available: https://onlinelibrary.wiley.com/doi/10.1002/vnl.21810 (visited on 06/05/2023).

[190] G. Haacke, F. F. Andrawes, and B. H. Campbell, "Migration of light stabilizers in acrylic/melamine clearcoats", *JCT, Journal of coatings technology*, vol. 68, pp. 57–62, 1996.

[191] C. Peike, T. Kaltenbach, K.-A. Weiß, and M. Koehl, "Non-destructive degradation analysis of encapsulants in PV modules by Raman Spectroscopy", en, *Solar Energy Materials and Solar Cells*, vol. 95, no. 7, pp. 1686–1693, Jul. 2011, ISSN: 09270248. DOI: 10.1016/j.solmat.2011.01.030. [Online]. Available: https://linkinghub.elsevier.com/retrieve/pii/S0927024811000444 (visited on 06/08/2023).

[192] A. Ahmad, S.-H. Li, and Z.-P. Zhao, "Insight of organic molecule dissolution and diffusion in cross-linked polydimethylsiloxane using molecular simulation", en, *Journal of Membrane Science*, vol. 620, p. 118 863, Feb. 2021, ISSN: 03767388. DOI: 10.1016/j.memsci.2020.118863. [Online]. Available: https://linkinghub.elsevier.com/retrieve/pii/S0376738820314381 (visited on 07/26/2023).

**Bibliography**

[193]  B. Mei, T.-W. Lin, G. S. Sheridan, C. M. Evans, C. E. Sing, and K. S. Schweizer, "How Segmental Dynamics and Mesh Confinement Determine the Selective Diffusivity of Molecules in Cross-Linked Dense Polymer Networks", en, *ACS Central Science*, vol. 9, no. 3, pp. 508–518, Mar. 2023, ISSN: 2374-7943, 2374-7951. DOI: 10.1021/acscentsci. 2c01373. [Online]. Available: https://pubs.acs.org/doi/10.1021/acscentsci.2c01373 (visited on 07/26/2023).

[194]  C. Anil and P. Eswara, *Building Integrated Photovoltaics (BIPV) Market - 2030*, English, Allied Market Research, Sep. 2021. [Online]. Available: https://www.alliedmarketresearch. com/building-integrated-photovoltaic-market (visited on 03/13/2023).

[195]  SUPSI, "Standardization, performance risks and identification of related gaps for a performance-based qualification in BIPV", Tech. Rep., 2019.

[196]  H. Lee and H.-J. Song, "Current status and perspective of colored photovoltaic modules", en, *WIREs Energy and Environment*, vol. 10, no. 6, e403, 2021, Number: 6 _-eprint: https://onlinelibrary.wiley.com/doi/pdf/10.1002/wene.403, ISSN: 2041-840X. DOI: 10.1002/wene.403. [Online]. Available: https://onlinelibrary.wiley.com/doi/abs/ 10.1002/wene.403 (visited on 10/06/2023).

[197]  B. Riedel, P. Messaoudi, Y. B. Assoa, *et al.*, "Color coated glazing for next generation BIPV: performance vs aesthetics", *EPJ Photovoltaics*, vol. 12, R. Kenny and J. M. Serra, Eds., p. 11, 2021, ISSN: 2105-0716. DOI: 10.1051/epjpv/2021012. [Online]. Available: https://www.epj-pv.org/10.1051/epjpv/2021012 (visited on 03/04/2023).

[198]  C. Kutter, B. Bläsi, H. Wilson, *et al.*, "Decorated Building-Integrated Photovoltaic Modules: Power Loss, Color Appearance and Cost Analysis", en, *35th European Photovoltaic Solar Energy Conference and Exhibition; 1488-1492*, 5 pages, 3529 kb, 2018, Artwork Size: 5 pages, 3529 kb Medium: application/pdf Publisher: WIP. DOI: 10.4229/ 35THEUPVSEC20182018-6AO.8.6. [Online]. Available: https://userarea.eupvsec.org/ proceedings/35th-EU-PVSEC-2018/6AO.8.6/ (visited on 10/12/2023).

[199]  H. R. Wilson and M. Elstner, "Spot Landing: Determining the Light and Solar Properties of Fritted and Coated Glass", en, *Challenging Glass Conference Proceedings*, 203–212 Pages, May 2018, Artwork Size: 203-212 Pages Publisher: Challenging Glass Conference Proceedings. DOI: 10.7480/CGC.6.2134. [Online]. Available: https://proceedings. challengingglass.com/index.php/cgc/article/view/105 (visited on 02/16/2023).

[200]  D. Milburn and K. Hollands, "An experimental investigation of thick-sample effects in the measurement of directional-hemispherical transmittance of advanced glazing materials", en, *Solar Energy*, vol. 57, no. 4, pp. 261–275, Oct. 1996, ISSN: 0038092X. DOI: 10.1016/S0038-092X(96)00090-4. [Online]. Available: https://linkinghub.elsevier.com/ retrieve/pii/S0038092X96000904 (visited on 02/16/2023).

[201]  International Commission on Illumination (CIE), *CIE standard illuminant D65*. DOI: 10.25039/CIE.DS.hjfjmt59. [Online]. Available: https://cie.co.at/datatable/cie-standard-illuminant-d65 (visited on 02/25/2023).

[202] International Commission on Illumination (CIE), *CIE 1964 colour-matching functions , 10 degree observer.* DOI: 10.25039 / CIE.DS.sqksu2n5. [Online]. Available: https: //cie.co.at/datatable/cie-1964-colour-matching-functions-10-degree-observer (visited on 02/25/2023).

[203] F. A. Jenkins and H. E. White, *Fundamentals of optics*, 4th ed. New York: McGraw-Hill, 1976, ISBN: 978-0-07-032330-8.

[204] M. Born, E. Wolf, and A. B. Bhatia, *Principles of optics: electromagnetic theory of propagation, interference, and diffraction of light*, Seventh (expanded) anniversary edition, 60th anniversary edition. Cambridge: Cambridge University Press, 2019, ISBN: 978-1-108-76991-4.

[205] F. Hergert, R. Thyen, and V. Probst, "High Performance CIS Solar Modules in Brilliant Colours", *The Gazette, Hobart (News Corp Australia, Sidney)*, vol. 6, 2010.

[206] F. Rosillo and M. Alonso-García, "Evaluation of color changes in PV modules using reflectance measurements", en, *Solar Energy*, vol. 177, pp. 531–537, Jan. 2019, ISSN: 0038092X. DOI: 10.1016/j.solener.2018.11.039. [Online]. Available: https://linkinghub.elsevier.com/retrieve/pii/S0038092X18311393 (visited on 03/04/2023).

[207] "Life Cycle Greenhouse Gas Emissions from Electricity Generation: Update", NREL, Fact sheet, 2021. [Online]. Available: www.nrel.gov/docs/fy21osti/80580.pdf.

[208] D01 Committee, "Test Methods for Measuring Adhesion by Tape Test", en, ASTM International, Tech. Rep. DOI: 10.1520/D3359-09E02. [Online]. Available: http://www.astm.org/cgi-bin/resolver.cgi?D3359-09E2 (visited on 02/15/2023).

[209] M. D. Fairchild, *Color appearance models* (The wiley-IS&T series in imaging science and technology), Third edition. Chichester, West Sussex: John Wiley & Sons, Inc, 2013, ISBN: 978-1-118-65309-8 978-1-118-65310-4 978-1-118-65311-1.

[210] CIE, "CIE 1931 colour-matching functions, 2 degree observer", International Commission on Illumination, Tech. Rep., 2019. DOI: 10.25039 / CIE.DS.xvudnb9b. [Online]. Available: https://cie.co.at/datatable/cie-1931-colour-matching-functions-2-degree-observer (visited on 02/25/2023).

# Publication list

Updated: 4.12.2023

## Publications as first author

- A. Borja Block, A. Faes, A. Virtuani and C. Ballif, *Customized Inkjet Equipment for Coating Metallic Interconnects of BIPV Modules,* submitted to the Journal of Manufacturing Processes, 2023.

- A. Borja Block, C. Barretta, A. Faes, A. Virtuani, A. Vlk, M. Ledinský, G. Oreski and C. Ballif, *Stability of Black Interconnect Coatings for Solar Photovoltaic Module Applications,* Solar Energy Materials and Solar Cells, 2023.

- A. Borja Block, J. Escarre Palou, A. Faes, A. Virtuani and C. Ballif, *Accurate Color Characterization of Solar Photovoltaic Modules for Building Integration,* Solar Energy, 2023.

- A. Borja Block, J. Escarre Palou, A. Virtuani and C. Ballif, *A Screening Protocol to Assess the Stability of the Inks Used To Mask Metallic Interconnects in BIPV Modules,* 8th World Conference on Photovoltaic Energy Conversion (WCPEC) Proceedings, 2022.

- A. Borja Block, A. Virtuani and C. Ballif, *Stability of Inks Used for Masking Metallic Interconnects in BIPV Modules,* 38th European PV Solar Energy Conference and Exhibition (EU PVSEC) Proceedings, 2021.

## Publications as co-author

- A. Virtuani, A. Borja Block, N. Wyrsch and C. Ballif, *The carbon intensity of integrated photovoltaics,* Joule, 2023.

- H. Quest, A. Virtuani, L. Gnocchi, A. Borja Block, N. Wyrsch and C. Ballif, *Decoupling performance gains of Silicon Hetero-Junction bifacial modules,* 8th World Conference on Photovoltaic Energy Conversion (WCPEC) Proceedings, 2022.

# Conference and Workshop Presentations

- A. Borja Block, J. Escarre Palou, A. Faes, A. Virtuani and C. Ballif, *Optimized Color Characterization for Solar Photovoltaic Laminates*, oral presentation at the 40th European PV Solar Energy Conference and Exhibition (EU PVSEC), Lisbon, Portugal, 2023.

- A. Borja Block, C. Barretta, A. Faes, A. Virtuani, A. Vlk, M. Ledinsk, G. Oreski and C. Ballif, *Stability of Black Interconnect Coatings for Solar Photovoltaic Module Applications*, visual presentation at the 11th Metallization and Interconnection Workshop for Crystalline Solar Cells (MIW), Neuchâtel, Switzerland, 2023.

- A. Borja Block, J. Escarre Palou, A. Virtuani and C. Ballif, *A Screening Protocol to Assess the Stability of the Inks Used To Mask Metallic Interconnects in BIPV Modules*, visual presentation at the 8th World Conference on Photovoltaic Energy Conversion (WCPEC), Milan, Italy, 2022.

- A. Borja Block, A. Virtuani and C. Ballif, *Stability of Inks Used for Masking Metallic Interconnects in BIPV Modules*, visual presentation at the 38th European PV Solar Energy Conference and Exhibition (EU PVSEC), online, 2021.

# Alejandro **BORJA BLOCK**

**Phone : +41 78 825 33 36**
**Email: alexborja95@gmail.com**

## EDUCATION

**École Polytechnique Fédérale de Lausanne (EPFL)**
2019 - 2023
Ph.D student in Photovoltaics and Thin-Films Laboratory (PV-Lab)

**Universidad Nacional Autónoma de México (UNAM)**
2014 - 2019
Mechatronic engineering (GPA 9.5/10)
Student mobility at the Czech Technical University in Prague (Spring 2018)
Development of management skills specialization

## WORK EXPERIENCE

**RESEARCH SCIENTIST**
**École Polytechnique Fédérale de Lausanne (EPFL)**
October 2019–November 2023

Module and reliability group: Dr. Alessandro Virtuani and Dr. Antonin Faes

Industrial partner: 3S Swiss Solar Solutions AG (7 months internship) under Philipp Wälchli supervision.

Topic: research on the reliability and characterization of colored photovoltaic (PV) module technologies.

- Manufacturing and characterization of PV modules.
- Performance of accelerated ageing tests based on the Qualifications Tests defined in the industry standard IEC 61215.
- Prototype design and manufacturing for innovative experimental applications with automation.
- Design and implementation of experimental protocols.
- Monitoring station maintenance and software support.
- Teaching activities and academic projects supervision.
- Participation in EU and Swiss projects.

**INTERN**
**Centro de Ingeniería Avanzada (CIA)**
2017–2018
Project: CASA UNAM
- Automation activities in collaboration with the science museum UNIVERSUM.
- Prototype manufacturing for exhibitions with sensors interactivity.

## SKILLS AND EXPERTISE

- Team work.
- Project planning.
- Analytical and creative thinking.
- Problem solving.
- Social skills.

- C# (OOP, APIs, image processing).
- MATLAB.
- General software skills (Python, LabVIEW, C, C++).
- Office.
- Data analysis.

## LANGUAGES

**Spanish**: Native    **English**: Advanced/Professional    **French**: Advanced    **German**: Basic    171